POLITECNICO DI MILANO

FACOLTA' DI INGEGNERIA INDUSTRIALE
Corso di Laurea Magistrale in Mechanical Engineering

Development of an optimal sensor placement algorithm and modal analysis of a turbine blade by means of OBR optical-fiber strain sensor

Relatore: Prof. Paolo Emilio Lino Maria PENNACCHI
Correlatore: Ing. Gabriele CAZZULANI

Tesi di laurea di:
Martina CHIEPPI
Matr. 833992
Andrea COLOMBO
Matr. 833178

Anno Accademico 2015 - 2016

Contents

Abstract

Most of turbomachines failures are the result of blades uncontrolled vibration. Due to the aerodynamic forcing that they undergo, a resonant vibrating behaviour can occur. The knowledge of blades displacement modal-shapes allows to be aware of such critical condition and to proceed in more suitable blade designs.

For this purpose, in this thesis an innovative method has been developed to reconstruct displacement modal-shape starting from local strains. The measurement system is based on the Optical Backscatter Reflectometer (OBR) fiber-optic technology, which generates a *continuous* strain measure.

After the definition of the *optimal* fiber arrangement by means of a dedicated *genetic algorithm*, the acquired fiber strains are transformed into the displacements of the whole surface of a bi-dimensional thin plate, without employing the commonly used Displacement Strain Transformation (DST)-matrix method. The result is a displacement modal shapes reconstruction which does not require for any Finite Element (FE)-models of the analysed structure.

Then, displacement modal-shapes of a 3D-printed blade model will be experimentally obtained relying on a proper three-dimensional DST-matrix strain conversion method. To conclude, a totally new approach will be explained in order to achieve a FE-model independent result.

Instrumentation criticisms, which arises due to its application in dynamic measurements, will be highlighted and solved.

Keywords

OBR; optical fiber; mode shapes reconstruction; sensor placement optimisation; genetic algorithm; turbine blade; strain to displacement conversion; DST matrix.

Sommario

Gran parte dei cedimenti che si verificano nelle turbomacchine sono la conseguenza della vibrazione incontrollata delle pale. A causa del forzamento aerodinamico cui sono sottoposte, infatti, può innescarsi una loro vibrazione in *risonanza*. Conoscere le *forme modali* di spostamento delle pale stesse permette di prevedere se una tale situazione possa verificarsi, dando quindi la possibilità di agire progettualmente per evitare questa circostanza.
Al fine di ottenere questi parametri modali è stato sviluppato un metodo innovativo. La ricostruzione delle forme modali di spostamento dell'intera superficie strumentata si basa sull'utilizzo della tecnologia a fibra ottica OBR, che misura in modo continuo le deformazioni subite dalla fibra stessa lungo tutta la sua lunghezza.
Dopo aver determinato il percorso *ottimale* lungo cui disporre la fibra, ottenuto grazie all'implementazione di un opportuno *algoritmo genetico*, le deformazioni misurate sono rielaborate per ottenere il campo di spostamento superficiale di una piastra bi-dimensionale. Questo processo è condotto senza fare affidamento a simulazioni numeriche, a differenza di quello generalmente proposto in letteratura attraverso la matrice DST.
Successivamente, le forme modali di spostamento di un prototipo di pala ottenuto con stampa 3D saranno ottenute facendo affidamento al metodo DST opportunamente sviluppato. Come conclusione verrà proposto un approccio completamente nuovo al fine di raggiungere anche sulla struttura tridimensionale il medesimo risultato senza avvalersi dell'uso di un modello FEM.
Le criticità riguardanti il sistema di acquisizione, sorte a causa del suo impiego nel monitoraggio di fenomeni dinamici, saranno messe in evidenza e verranno proposte le rispettive soluzioni.

Parole chiave

OBR; fibra ottica; ricostruzione forme modali; ottimizzazione disposizione fibra; algoritmo genetico; pala di turbina; conversione delle deformazioni in spostamenti; matrice DST.

List of Figures

List of Tables

Chapter 1

Introduction

Vibrational issues concerning turbomachinery blades are one of the most significant engineering challenges.
It is of common knowledge that these particular structures operate in critical conditions: in addition to the *stationary* load which they are exposed to and designed for, they are distressed by a continuous *dynamic* forcing that can cause their dangerous and uncontrolled vibration.
This occurrence arises from the nature of the fluid-stream, that crosses alternately statoric and rotoric stages spreading through blade channels. This results in unsteady pressure-fields above blade surfaces. As a matter of fact, the main sources of such behaviour are the interaction among the outgoing-flow from *stationary* rows and rotors (and vice-versa), together with other particular phenomena such as stalls or boundary layer detachments, that are generally consequence of start-up or off-design operations.

When a dynamic load acts on a structure, the structure response may consist in *dangerous* displacements. Direct consequences of such phenomena are, among the others, blades-tip hammering and fatigue crack propagation, that usually led to catastrophic machines-failures involving high risk for operators and huge economical losses.
Generally, such dangerous displacements are achieved when the structure is vibrating according to one of its *resonances* and it is worsen by the typical low damping of the blade structure. This occurs whenever arises a sort of *coupling* among the properties of the force and of the structure. It means that both the *frequency* and the *shape* of the forcing pressure-field must be in agreement with a blade *modal-shape* and its *eigenfrequency.*
If the blades *modal-parameters* are known, it is possible to predict if that critical *coupling* occurs. As a first consequence, blade or machine design can be *tuned* to get rid of such event.

As it can be understood, an accurate reconstruction of the blade mode-shapes is needed to point out the capability of the pressure-field to introduce *dangerous energy* into the system. As a matter of fact, a complete and *spatially-continuous* knowledge of structure modal-shapes makes possible to highlight the blade-areas where the force can really introduce energy into the system. Practically this permits to compute the *Jacobian* of the force on the structure, which allows to understand the response of a structure under forcing, and so its level of *criticality*. Currently, it is extremely difficult to reconstruct accurate and *continuous* turbine blade vibration shapes. Since the source of blades dynamic excitement is a three-dimensional continuous pressure-field, it is fundamental to estimate the displacement mode-shape concerning the blade surface in the most *complete* manner.

According to the previous sentences, the first purpose in performing modal analysis in the turbomachinery field is the blade design completion. Blades have to be *efficient* but even mechanically resistant. During their design, it is fundamental to verify that no resonant responses can occur while the machine is operating. Such a behaviour must be avoided both during steady-state operations, and during the start-up and shut-down procedures.

Usually the blade-design step relies on FE-models and numerical simulations, able to estimate the Frequency Response Function (FRF) of the blade under exam. Nevertheless, experimental measurements on prototypes have to be performed in order to determine the real modal parameters of the blade itself and the machine. Generally the FE-based design and the experimental tests, both concerning the single element, both the whole assembly, are repeated in an iterative procedure in order to guarantee coherence and robustness in design. In addition to this, if a real-time mode-shape monitoring system is implemented, the acquired data could be employed to continuously update and upgrade the structure numerical model. Nowadays, the main criticism according to this approach is represented by the limits of traditional in-machine measurement systems used in turbomachines.

Another important purpose of blade modal-analysis depends on the necessity to perform a proper fatigue assessment. The knowledge of the blades FRFs permits to be aware of their high-cycle fatigue resistance. As already explained, the resulting dynamic response and the associated stresses of an excited structure depend on its natural frequencies, on its modal shapes, on its own energy dissipation mechanism and on the exciting force properties. A particularly risky condition in terms of High Cycle Fatigue (HCF) failure is the so called *resonant fatigue*. In this loading condition the structure is forced according to one of its resonances, and serious consequences can occur.

As a consequence, it would be interesting to develop a real-time monitoring

system in order to immediately highlight possible structural modifications (e.g. a fatigue crack nucleation). Such a technological improvement would be of great relevance for turbomachinery components, considering the consequences in the case of their failure.
The so called *health monitoring* techniques attempts to collect and compare experimental data concerning the structure behaviour at different time instants. As a matter of fact, when a structure gets damaged or altered, its modal parameters (eigenvectors and eigenfrequencies) change. As a result, theoretically it would be possible to monitor its *health* and organize the maintenance just looking at its modal properties. Nowadays, no measurement system is claimed to perform an effective *health monitoring* in the turbomachines field. The possibility to reconstruct the complete vibrating-shape would improve this technique.

In this thesis work it will be proposed an innovative methodology in order to carry out blades modal-shape determination. Their estimation will be performed in the most reliable and *spatially-continuous* manner exploiting the potentialities of a new measurement system.

The innovative LUNA ODiSI-B v4 system *reads* the informations coming from an optical-fiber arranged above the structure and processes them into localised *strains*. The employed sensor is a common optical fiber, that is *transformed* into a strain-sensor directly by the interrogator, according to the LUNA OBR-technology. Differently from strain measurements commonly obtained through Fiber Bragg Grating (FBG)-based optical fibers, some advantages immediately arise among the others.

While the fibers employed by LUNA ODiSI-B are cheap and commonly available, sensors for FBG interrogators are generally designed according to consumer needs and requires for costly technological operations.
Furthermore, the measure *spatial-resolution* of the employed system is at least one order of magnitude higher than the FBG one. The *continuous* nature of LUNA OBR sensor represents an enormous advantage with respect to the traditional measurement instruments. This potentiality becomes a critical advantage especially in the turbomachinery field, where it is fundamental to reconstruct the modal-shapes in the most *continuous* manner along the fluid-interaction surface.
Actually, the measurement-*continuity* of the proposed technology can also be exploited in many other fields, as smart-structures and aerospace applications.

The high chemical and mechanical compatibility of optical-fibers with many materials is a convenient characteristic. This suggests promising possibilities of embedding fiber solutions, in order to develop innovative in-machine acquisition systems.

Being a new technology and still under development, it is not exempt from criticisms. Furthermore, it must be stated that LUNA ODiSI-B output-reliability in not guaranteed when monitoring *dynamic* phenomena. The Control Unit (CU) is designed for static measurement applications. For this reason, all the signal-related issues will be deeply investigated and analysed.

By dealing with optical fiber measurements, one of the most critical tasks that have to be faced consists in the *translation* of surface measured *strains* into surface *displacements*. Indeed in the turbomachines, the mode-shapes have to be reconstructed in terms of displacement to permit the comparison among the *shape* of the forcing pressure-field and blades *eigenvectors*.

A noticeable effort will be performed in order to implement an original method to obtain such a result, totally avoiding to rely on any FE-analysis help, as generally suggested by literature. In the proposed method, displacements are obtained just by re-elaborating the measured strain-fields, just accounting for physical correlations. As a result, the developed strain-to-displacement procedure is strongly different from the traditionally applied solutions.

To numerically reconstruct the measured strain-fields that have to be processed, some thoughts have been dedicated to data import and signal-cleaning, without forgetting the pseudo-automatic procedure to ease the gathering of the informations about fiber real spatial-path.

A further important aspect proper of this research project concerns the Optimal Sensor Placement (OSP) algorithm that has been developed in order to determine the *optimal* fiber arrangement above the structure to best acquire and reconstruct a specific set of targeted vibrating mode-shapes. A *genetic algorithm* is implemented for this purpose.

The proposed innovative optimization algorithm aims to exploit the *continuity* of the OBR sensor measurement to best reconstruct the blade mode-shapes and to compensate the criticisms proper of the LUNA ODiSI-B system.

Some criteria are thought to solve all the physical constraints concerning the fiber placement. This represents an important step, since solutions to manage a continuous sensor placement are totally absent in literature.

To best understand the issues and clearly evidence the criticisms concerning each theme explained before, a large part of the work has been performed accounting for a simpler bi-dimensional geometry than a real turbine blade.

The methodology initially developed for a simple plate, can be applied to many other planar thin-structures resulting to be particularly suitable for aerospace and fluid-interactive structures. After having developed the strain-to-displacement method and carried out a complete investigation of the LUNA system, a more complex geometry will be approached.

A 3D-printed model of a real turbomachine blade will be used to perform the final analysis. Conclusions referred to the particular problems occurred when dealing with a full three-dimensional structure will be explained, coupled to their solutions.

The thesis is organized as follows:

- In chapter 2 the most common blade modal-shapes measurement techniques are described. The OBR technology is presented and a short comparison with the FBG system is performed. Then, the traditional *strain-to-displacement* translation method is explained. Finally, a brief summary concerning the State-of-the-Art optimal sensor placement (OSP) algorithms is reported;

- In chapter 3 the proposed OSP method, dealing with the fiber placement optimization issue and the *strain-to-displacement* conversion, is introduced and disclosed. At the end, the complete procedure to obtain the displacement mode-shapes of the whole surface starting from the acquired fiber strains is depicted;

- In chapter 4 and chapter 5, the experimental set-up is described for both the two-dimensional and three-dimensional structures and the signal processing procedure is examined. All the resulting considerations regarding the LUNA ODiSI-B signal analysis are illustrated here;

- After reporting in chapter 6 the experimental results concerning the reconstructed plate modal-shapes, in chapter 7 the theory of the three-dimensional case-study is explained. The experimental results concerning the 3D-printed blade shape reconstruction, processed through a devised DST-matrix method, are shown. Finally, the possible solution to perform an effective extraction of blade mode-shapes without relying on a FE-model is discussed.

Chapter 2

State of the art

The focal point of this essay touches three branches of the engineering research. The logical path that has been followed to carry out a successful blade modal analysis employing the innovative chosen sensor, required a know-how proper of different research fields. The final result is achieved thanks to the interaction among them and the implementation of engineering solutions proper of different areas. For that, it is fundamental to examine what literature offers in order to best approach the study case, adopt the right techniques, understand the criticisms and improve better technological routines than existing ones.
The actual chapter has been divided into three main sections:

1. Blade vibration analysis;
2. Turbomachinery measurement sensors;
3. Sensor positioning optimization algorithm.

2.1 Modal analysis

First of all it can be useful recall some general physical principles regarding the structure vibrations.
According to the modal approach, structure dynamics can be expressed by the superimposition of an infinite number of space-time dependent functions. In the most general case, according to a Cartesian frame of reference, the vectorial function $\bar{u}$ collects the displacements along the $x,\ y,\ z$ directions that a material point undergoes at a time instant t.

$$\bar{u}(x,y,z,t) = \sum_{i=1}^{\infty} G_i(x,y,z) \cdot q_i(t)$$

Where the function $G_i(x, y, z)$ is called *shape function* of the mode i, while the function $q_i(t)$ is its modal amplitude. Shape functions are intrinsic *properties* of the system and directly depends on geometry and constraints. Modal amplitudes are computed according to system forcing and determines its dynamic response.

The evaluation of the shape function of each mode can be performed analytically, numerically or experimentally. An analytical formulation can be computed for simple geometries, else a computational modal analysis (CMA) or experimental modal analysis (EMA) is required. In these last two cases, two simplifications occur. The amount of mode shapes that compose the response $\bar{u}$ is a *finite* number and the G_i function spatial continuity is no longer kept. Thus, the term *shape function* is replaced by the term *eigenvector*, and the number of modes taken into account is finite and case dependent. In the case of a Computational Modal Analysis (CMA), the structure is divided in a number of small *finite elements*. Each element has some vertexes, called *nodes*. Vector $\bar{u}$ will be no longer a direct function of space, but it will be function of nodes Degree of Freedom (DoF) N, so:

$$\bar{u}(t)_{N\times 1} = [\Phi]_{N\times n}\, \bar{q}(t)_{n\times 1}$$

where n is the total amount of modes considered.

Recently, mode-shapes estimation and their real-time monitoring has become one of the most interesting challenges in the engineering field, especially when dealing with lightweight structures and structures with aerodynamic-forces interaction: airplane wings, helicopter rotors, wind turbine blades and power-production turbine blades.

The capability to determine structure modal-shapes is fundamental especially when a modification of its vibrating behaviour directly influences the performances of the whole system. Furthermore, the possibility to be aware in real-time of these changes is necessary to employ advanced vibration reduction techniques and to enhance aerodynamic performances. Thus, the development of effective methods to better reconstruct vibrating mode-shapes is a technological key challenge.

In this scenario, the attempt to develop a methodology to experimentally reconstruct the blade vibrations with high accuracy is perfectly aligned with the current dynamic researches.

2.1.1 Turbomachinery blade vibrations

As explained in chapter 1, the blade modal analysis is fundamental to be aware regards the dynamic behaviour of the turbomachine. The better is the knowledge of the modal shape, the better is:

1. The capability to predict the locations of possible energy introduction. This permits to evidence which fluidynamic-forces interactions could become critic for the blade structure;
2. The reconstruction of the effects of eventual cracks in the modal shapes and, with a proper real-time methodology, a fatigue crack evolution control;
3. The reliability of FE model validation, in particular with complex geometry or inhomogeneous material parameters in the structure.

In this sense it is evident the importance of a good measurement system, permitting the monitoring of a large number of sensors. This aims to have an high spatial resolution in the modal acquisition. A sensor with a considerable spatial-measurement discretisation can be called a *continuous sensor*. The need of a continuous sensor becomes even more relevant where the structure presents space dependant physical parameters or material characteristics, that means space-dependant damping and stiffness.

The dynamic loads, causing the blade vibrations, arise from various sources and can be generally classified as time and space dependant forces [1].

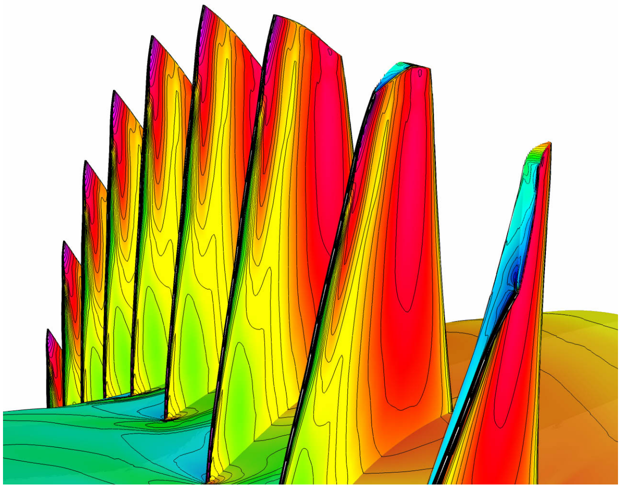

Figure 2.1: Example of pressure distribution along compressor rotor-blades

Ideally, turbomachine blades, when assumed as isolated profiles, are subjected to a static pressure field with a certain distribution in space, along the span and along the profile: the stator blades are statically loaded in the absolute frame of reference, while in the rotor blades the pressure can be considered *static* in its relative frame of reference. Actually, in a real machine the blades are not isolated aerodynamic profiles but are assembled in rows and stages. As a result, a dynamic pressure exciting-field is overlapped to the static pressure field. The static pressure forcing field is represented in Figure 2.2. The forces that blades withstand are, practically, both static and dynamic.

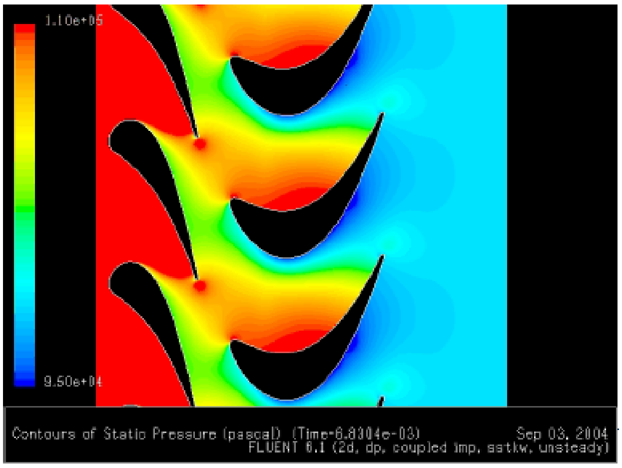

Figure 2.2: Example of pressure field interaction among rows

The dynamic load is caused mainly by two different phenomena: time non-uniformities of pressure, that born in the actual stage, and spatial non-uniformity of pressure, that are produced by the previous one. As a matter of facts, assuming to consider the rotating frame of a rotor, the flow inside the blades channel will be unsteady in the case of non-uniform inlet flow, and this causes aerodynamic forcing. The pressure inside the channel becomes a scalar field dependant on time. Practically all spatial non uniformities in the channels of a stage create a non uniform inlet flow for the following one. In turbomachinery, each spatial non-uniformity is translated into a time non-uniformity, due to the sequence of rotating and stationary *frames* in the machine. This is clear always in Figure 2.2, where the interaction among rotor and stator rows of the stage is evidenced.
Sources of spatial non uniformities, which are converted in dynamic loads for the following stage, are:

- Blade pressure non uniformity distribution along the meridional coordinate in the duct, necessary for an energy exchange fluid-blade;

- The pressure field depends on the radial coordinate in the duct due to radial equilibrium law, necessary for an energy exchange fluid-blade;
- Blade wakes;
- Shock waves;
- Vortical structure: secondary flows, clearance flows, Von Karman street;
- Stall and boundary layer separation.

Generally the frequency of the forces created by spatial non uniformities is related to the *blade passing frequency.* The *blade passing frequency* for the stator is the frequency of the machine rotation multiplied for the number of rotor blades. *Vice-versa* for the rotor the *blade passing frequency* is the frequency of the machine rotation multiplied for the number of stator blades.

Sources of time non-uniformities, those are dynamic loads for the stage where the time non-uniformities are originated, are:

- rotating stall: a periodic reduction in the flow rate and a fluctuation on the incidence angle, the characteristic frequency is in the range of 50-100 Hz;
- surge, characterized by a low characteristic frequency around 5-20 Hz;
- transient effects due to turbomachine regulations (flow rate, rpm regulation, valves);
- stall and boundary layer separations;
- periodic blade and machine vibrations alter the cascade properties (pitch, stagger, etc...) so periodic alteration in the interaction between flow and cascade appear. These unfavourable interaction produces the so called *aereo elastic forces* and can cause a self-exciting flutter vibrations (vibrations related to the natural frequencies of the blades).

To conclude, it is clear that in the turbomachine design a blade mechanical analysis is strictly necessary and an optimum modal analysis to verify the dynamic response of the blades since the pressure field and so the lift on the blade is deeply time dependant. In the turbomachines, for example in jet engines or in compressors and turbines due to the risk of a possible catastrophic failures, it is fundamental to understand both the cause of the vibrations and the response of the blades to different dynamic loadings.

The knowledge of the FRF of the blades gives the possibility to understand what are the most critical dynamic phenomena, by comparing the natural frequencies with the exciting ones. In addition to this, a good reconstruction of the mode shapes raises the possibility to manage the issue of the introduction of energy for each forcing harmonic and increases the capability to understand the source of instabilities given by the interaction between the blade vibration and the flow fields. The practical and most common consequence of the dynamic excitations in the turbomachinery is the fatigue failures:

- High-cycle-fatigue: generally related to aerodynamic forces at high frequencies (excitation at blade passing frequency or high natural structure frequencies), issue usually related to a flutter o self excited vibration;
- Low-cycle-fatigue: result of the cycles of start and stop. Generally a problem related to the compressor and turbine disk loaded with centrifugal forces;
- Termo-mechanic fatigue: due to the stresses caused by the expansion of different hot components during the start-up and the shut-down.

2.1.2 Mathematical models and computational finite element modelling methods

A single free-standing blade can be considered as a pre-twisted cantilever beam with an asymmetric aerofoil cross-section mounted at a stagger angle on a rotating disk. The vibration characteristics of such a blade are always coupled between the two bending modes in the flapwise and chordwise directions and the torsion mode. Coupled bending-torsion vibrations occur when the centre of flexure does not concide with the centroid as in the airfoil blade cross-section and the vibrations are coupled between the two bending modes beacuse of the pre-twist. The classical Euler-Bernoulli beam with cantilever boundary conditions for bending vibration and Saint-Venant's non circular rod for torsional vibration are the starting points for the blade vibration solutions. The result will be more realistic if second order effects are included in the model: stiffening effect due to centrifugal loading during the rotation, disk shear deformations, rotary inertia, cross-section warping, root fixing, Coriolis accelerations and pre-stressing effect due to the temperature gradients. Many types of turbomachine blade cannot be adequately dealt with by mean theories since they contain complex shapes: typical example are blades both twisted and tapered between the root and the tip. In this case it is essential to use plate and shell theories to accurately model such rotating, pre-twisted,

shell-like structures [2].
In fact with the modern computing power, the best way to perform vibration analysis is with the finite element method. FE-model can be made to approximate blade geometries with the right boundary conditions, and then can be loaded to simulate real life operational conditions. It is possible use FE-model for static but also for dynamic analysis, in this sense it is possible calculate the modal parameters of a FE-model and so predict the frequency dynamic response of the real structure. Finite element analysis takes a real structure and approximates it by breaking it into a number of discrete elements with a finite number of degrees of freedom. In a free vibration analysis the number degrees of freedom of a given model corresponds to the number of natural frequency modes that can be extracted, which in most cases is more than is necessary.
Traditionally there are different approaches to model the blades and the cascade of a turbomachine [3]:

- The simplest model is the blade-alone model (the rotor is not included in the geometry). This approach reduces the run time but has a limited accuracy, in particular the blade alone solution tends to be stiffer and present higher resonances that the real assembly (rotor is supposed infinitely rigid and the nodes on the bottom of the blade are considered as completely constrained);

- An alternative to model the boundary conditions of the blade is to fix the sector boundary nodes in all degrees of freedom. In this case the rotor is included in the model as part of the blade. So part of the elasticity of the rotor is considered, but the model still ignore the real elastic properties of the rotor. However it is possible to reach a good prediction of the resonances, with an error less than 2% [3];

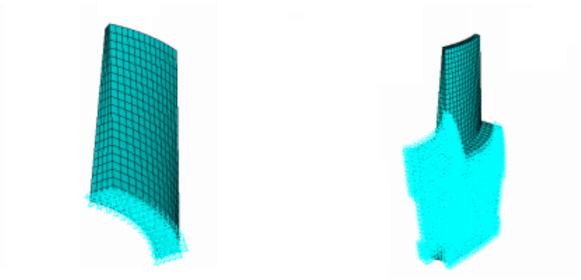

Figure 2.3: Comparison among modelling strategies: blade-alone and blade-rotor models

- There is the possibility to model a full 360 degree rotor by using cyclic symmetry without the modelling of the full rotor but just using the symmetry property. This approach permits to study the complete interaction between the rotor and the flow, and in particular the interaction between the rotor vibrations and the blade ones. The blade frequencies are solved corresponding to a particular disk mode or nodal diameter. Different rotor nodal diameters cause the blade mode shapes and the frequencies to change;

- The most complex analysis deals with a complete blade assembly model. Really this approach present different kind of models: generally the blade assembly model is classified in eight categories divided in two main groups,“fixed-free” or “disk not completely rigid”, [3]. In the first category the disk is sufficiently rigid to not affect the vibration characteristics of the blades. In each of these two groups there are free-standing, finite blade group, continuous blade group, finite/continuous blade group. This last approach permits to consider important parameters as the number of blades, blade connections and the stiffness of the shrouding. In particular, usually in the analysis of a complete stage it is necessary consider that the disk influences the dynamic behaviour of the blades: additional natural frequencies are added by the consideration in the model of the disk as a real flexible part of the structure. In addition to this,in the case of packeted assembly, where a group of blades are connected by shrouding, many more natural frequencies and modes exist, and these cannot be seen by a simple single beam model. This is due to the fact that a group of blades behave as a system and are coupled through the shrouding. So practically a complete blade assembly model can be essential in a machine analysis.

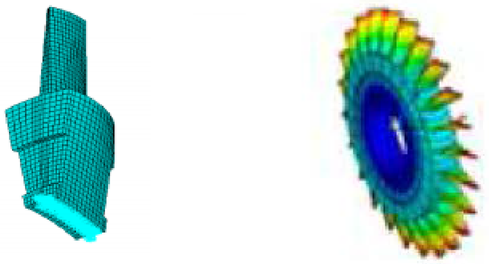

Figure 2.4: Comparison among modelling strategies: cyclic-symmetry and complete-assembly models

2.1.3 Traditional evaluation of blade design based on modal analysis

Traditionally, a blade design is evaluated by using the Campbell Diagram to point out the dynamic behaviour of the machine.

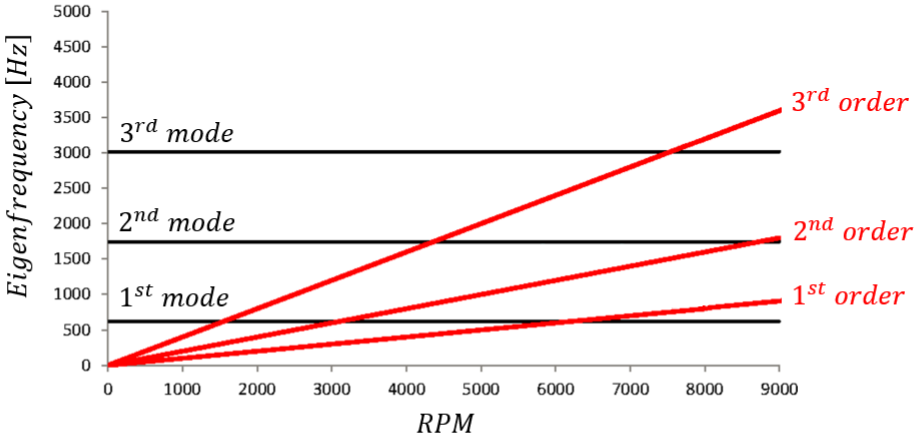

Figure 2.5: Example of Campbell diagram

The Campbell diagram describes the relationships between the natural frequencies and the rotor speed. It is also called interference diagram. On the horizontal axis there is the machine speed, while the vertical one shows the natural frequencies. The diagonal lines are called driver lines or engine orders, and represent the potential disturbances that could affect the rotating blades. The horizontal lines corresponds to the modes. The crossing between the mode and driver lines represents a potential resonant response. This representation has the limitation to consider the criticism related to the dynamic response dependant just on the correspondence between the exciting frequency, related to the rotor speed, and the natural frequencies. This approach completely neglects the physical principle of the *Jacobian*, the real dynamic response is the result of the comparison between the modal shapes and the exciting force shape. It is not just a matter of frequencies, but even of *Jacobian* determination, so energy introduction. This aspect is totally omitted in the Campbell diagram. Actually the Campbell diagram omission is just the consequence of the inability of the traditional measurement techniques to reconstruct the modal shapes of the blades. Thus, it is not possible to calculate the complete and exact *Lagrangiana* term. The main issue, in the traditional modal analysis, is the limitation given by an high level of discretization in the modal shape measurement: generally, with

the conventional measurement instruments described previously, the modal shapes are known just in few points, or even just in the blade tip.
Confirming what is written previously, it is experimentally demonstrated that not all the *resonant excitations* create a significant amplification in the structure displacement response [4]. This can be ascribed to the omission in the Campbell diagram of the *Jacobian* estimation, practically to the modal shapes reconstruction neglect. It is not sufficient to verify that resonance frequency is excited, it is necessary to investigate the capability of the forcing fluid interaction to introduce energy in the blade vibration. For this reason an accurate and complete modal reconstruction of the blade is so fundamental.

An innovative way to explain failures and develop reliable designs is presented by Murari [4], a new method called SAFE diagram to evaluate the dynamic behaviour of the packeted bladed disk assembly. This method is used to analyse the machine with a complete blade assembly model. This type of diagram evaluates not just the interferences in terms of resonances, but it compares the shape of the exciting harmonic with the normal mode shape of my structure. So the innovative aspect of this diagram is the possibility to consider the real shape of the exciting force, modelled as continuous in the space. It is no more necessary the approximation of the exciting force in a punctual discrete lift force. In the SAFE diagram the comparison between the force shape distribution on the blade, given but the pressure field, and the modal shapes excited is fundamental. As a result, it is able to define the energy introduction for each shape of excitation in each mode of the machine. For this reason it is so successfully used to calculate the dynamic stresses and complete the fatigue assessment, explaining the typical turbomachine failures.

The real limitation to the use of the SAFE diagram is the capability to experimentally reconstruct the modal shapes. If the experimental measures are not able to reconstruct the modal shape, the SAFE diagram can not be calculated. The diagram can be easily calculated with the resulting data of a complete FE-model, but the real machine is obviously different from the modelled one. An analysis based just on the FE-model can be restrictive, due to the inevitable FE-model approximations, numerical errors and the difficulty to include all the effects of the components interaction, the stiffening effects due to even the centrifugal force and so on. To apply the SAFE diagram to the real structure, with all the effects neglected in the FE-model and with the blade potential physical characteristic variations during the machine work, is necessary be able to reconstruct experimentally the modal shapes. This is not permitted by the traditional measurement instruments, there is a necessity of a continuous sensor.

2.2 Traditional blade vibration experimental measurement techniques

The experimental analysis of structural vibration has always proven to be a major contributor to understand and control many vibration related phenomena that occur in practice.

The vibration test are carried out mainly in two manners: pre-determined excitation and in-machine measurements.

- In a pre-determined excitation the conditions are controlled, the acquired informations are detailed and the time test is usually short. Typical approach is measure the FRF in discrete physical points, exciting the structure in a fixed points or in different fixed points (Single Input Multilple Output (SIMO) or Multiple Input Multiple Output (MIMO)). The frequency range of excitement is known and decided a priori. Traditionally the FRF is analysed as mobility, typical shape excitation is stepped-sine or broad-band excitation and typical measurements are piezoelectric accelerometers (attached measurements) and Laser Doppler Velocimeter (LDV)(not attached measurements), explained even in recent literature: [5] (2016) and [6] (2015);
- For in-machine rotor blade vibration, the traditional methods involve the use of strain gauges or frequency modulated grids. More recently, however, non-contact spatial whole field vibration measurement techniques have been adapted to measure rotating components. Traditional in-machine measurement techniques:
  - The classical strain gauges have limited spatial resolution, load effects, multiple connective wires;
  - In frequency-modulated grid measurements, it is possible to determine the amplitude of the blade tip position variation, through a small permanent magnet mounted to the blade tip that induces an alternating electromagnetic voltage in a winding installed in the machine casing. The limits of this technique are in the number of blade detectable and in the strong restriction in the modal shape reconstruction:it is practically impossible determine the modal shape of the blades;
  - A possible alternative, in particular for the in-machine measurement, is a whole-field measurement techniques, characterized by a non-contact nature: the holographic interferometric-based measurements, pulsed holography and time-averaged holographic images

([7], [8]). The criticism is related to the fact that the blades are enclosed in the machine, so it is difficult use this techniques in turbomachinery;

- Radial tip-timing techniques give information regards the presence of a delay or advance in the time passing tip, caused by the vibration of the blade considered. The installation on the tip of the blade of a transmitter is necessary. It is a non-contact probe, and is all the data acquired are based on the comparison between the tip passage frequency with the hypothetical no-vibrations one. The main problem is the difficulty to extract reliable information if the direction of the inclination of the mode shapes is not tangential, so for the torsional modes and the coupled modes are problematic. In addition to this, as in the frequency modulated grid measurements, it is impossible to define the mode shapes, just eigenvalues informations. Finally the radial tip-timing techniques require expensive machine modifications to locate the receiver in the casing;
- LDV sensors: they are non-contact devices and they measure the frequency shift due to Doppler effect to obtain a time-resolved measurement of the target velocity. They are characterized by spatially discrete points of measurements, but it possible to choose where the measurement has to be performed. However the critical issues are the necessity of a line-of-sight, similarly to the holographic images but less critical. It is possible use LDV systems just on early stages, where there is an optical access. In this measurement technique two alternatives are possible: Eulerian approach with a probe laser beam parallel or perpendicular to the axis of the machine or Lagrangian approach with a circular tracking LDV system where a dual mirror scanning makes a probe laser beam moving in a circular path in order to follow a fixed point on the rotor, a digital encoder is attached to the rotation shaft and control the position of the shaft itself. The first alternative has the problem of short time acquisition available while the second one is an open loop controlled system where is not possible verify the position of the laser beam [4].

2.3 Optical-fiber strain sensing

The conclusion of the previous paragraphs is the clear need of a complete displacement shape reconstruction. The necessity to define the modal shapes with a sufficient spatial discretization, in order to perform a satisfactory modal analysis, is common to many application fields (smart structures, tooling machines, air-plane wings, space-reflectors) but it is peculiar of the turbomachinery field. The main limit of the efficacy of the blades modal analysis is the inadequacy of the traditional measurement instruments in the modal shape reconstruction. As previously described, the traditional instruments are not able to measure a complete displacement field of the blades, in laboratory experimental set up but especially in-machine measures. This means inability to determine the modal shapes and, as a result, the inability to define the real level of criticism of an exciting pressure disposition (aereodynamic and fluidynamic excitation) and the inability to calculate the SAFE diagram from the experimental data. A different measurement instrument can be able to go beyond the traditional measures limits: a fiber optical strain sensor. A fiber optic sensor is an instrument that uses optical fiber as the sensing element. Generally the fiber sensors use a strain Experimental Modal Analysis (EMA) approach, so the displacements are calculated from the strain data acquired.
The general attractive characteristics of the optical fiber technology are [9]:

- Reduced size of the sensor: so small areas of the surface will be occupied by the mounted fiber, in the non-embedded use of the fiber;
- Generally, wide frequency bandwidth operation permitted;
- Since their dielectric nature, the immunity to electromagnetic interference is achieved and no electrical pathway is created within the host structure. No protection is required for lightning and various forms of electromagnetic interference so the fiber technology figures prominently in their selection for civil, aeronautic and aerospace applications;
- Usually low level noise in the output signals and high signal to noise ratio;
- The capability to measure several parameters simultaneously: strain and temperature. The two effects have to be properly distinguished.

The general attractive characteristics of the optical fiber technology particularly required in the turbomachinery applications [9]:

- The high resistance to corrosion and fatigue, typical problems of turbomachinery components;
- Typical long term stability, favourable in all the applications with heat transfer or temperature variations (a typical example are the turbines and the compressors);
- The fiber has a very low load effect: small cross section, small concentrated mass, small stiffening effects. This means a good attitude of the fiber sensor for the lightweight structures measures;
- Compatibility with the most part of composite materials and low detrimental effects on mechanical properties of host structure. So the fiber is very adapted fo the embedded applications, particularly interesting in the turbomachinery. Effectively the possibility to embed the fiber in the blade profile during the blade manufacturing permits to perform in-machine measures without any distortion in the fluid-surface interaction. No wires and no surface irregularities on the blade profile will be present with an embedded fiber sensor. So the dynamic force on the blade, imposed by the fluid motion in the duct, is preserved and not influenced by the presence of the measurement instrument, while the fiber is protected from the fluid flux.

2.3.1 Traditional fiber sensor: FBG

Many optical fiber deformation instruments are present, for instance the fiber technology based on Brillouin scattering. Nevertheless the most common fiber sensor for dynamic acquisitions is the FBG. An FBG consists in a distributed Bragg reflector with a short segment of optical fiber core with a modified refraction index, with a certain periodicity ([10], [11], [12]). The length related to the periodicity of this spatial discontinuity defines the wavelength that is reflected and not transmitted. The Bragg grating behaves as a wavelength-specific dielectric mirror. The wavelength that is reflected depends on the discontinuities in the refraction index created by the Bragg grating in the core. The spatial periodicity of the grating, manufactured in the core fiber, is unequivocally correlated to the frequency of the waves reflected: if the periodicity changes due to a deformation of the fiber, the reflected waves change. If the original Bragg grating period is modified by a deformation (a strain related to a certain stress or a temperature strain) the spectrum of the filter changes (the filter is the Bragg grating itself). In this way the reflected wavelength depends on the strain, so we are able to measure the deformation of a structure by analyse the shift in frequency of the reflected wavelengths. Practically, the fiber is made integral (mechanically rigidly fixed) in respect to the surface of interest. So the light is injected in the fiber with a wide frequency range content and it is necessary detect what frequencies are reflected. In particular for an homogeneous strain field across the sensor's length, a linear relationship exists between the strain and the variation of the wavelength peak. So, finally, the changes in the harmonics contained in the signal transmitted by the fiber give the information regards the structure deformations. So the points where the FBG sensor is able to measure are just the locations of the Bragg gratings: the FBG behaves as wavelength-specific reflectors just in a certain number of points, decided at priori during the production of the fiber. As a result the FBG is a discrete strain sensor, with a certain number of measurements points.

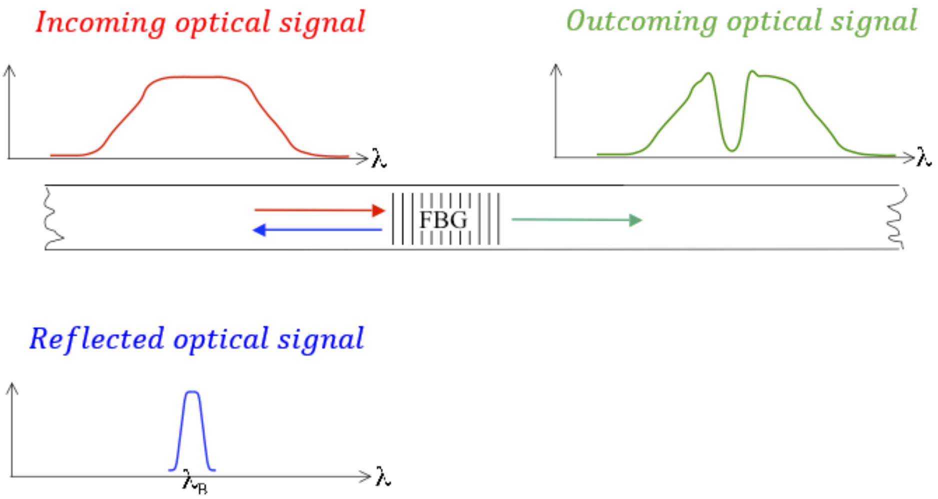

Figure 2.6: Fiber Bragg Grating principle

2.3.2 Innovative fiber sensor: OBR

This innovative measurement system bases on the Optical Backscatter Reflectometer (OBR) technology to make a common optical-fiber a distributed strain and temperature sensor. The main company to produce such a technologically advanced device is LUNA Innovations Inc.

LUNA's software, when combined with the OBR, transforms the standard telecom-grade fiber into a high spatial-resolution strain and temperature sensor. The OBR uses Swept Wavelength Interferometry (SWI) to measure the Rayleigh backscatter as a function of length in optical fiber with high spatial resolution. An external stimulus (like a strain or temperature change) causes temporal and spectral shifts in the local Rayleigh backscatter pattern. The OBR measures these shifts and scales them to give a distributed temperature or strain measurement.

Both OBR than FBG sensor are strain detectors but the physical principles used to measure and the measure characteristics are very different. Generally a fiber optic sensor is illuminated with laser light, it behaves as an optical fingerprint that changes in a repeatable and predictable way in proportion to changes in strain or temperature. So the idea of put a light in the fiber and detect what happens to this light in order to analyse the fiber structure changes and so of the deformation of the material where it is attached, is the same both in OBR than in FBG. However the differences in the measure procedure are significant. The basic concept exploited by the OBR is that an usual and standard optical fiber reflects small amounts of light randomly due to a random spatial pattern fixed into the core fiber when it is manufactured due to the non-crystalline nature of fused silica. This reflected light is known as Rayleigh scatter. LUNA sensing systems measure and record the amplitude and phase of this scattered light as a function of distance down the fiber with microns of spatial resolution. When the fiber is stretched or compressed, this pattern is also stretched or compressed. These changes are measured by comparing to the scatter pattern measured in a baseline state and the scatter pattern in the deformed state. So the software proceeds always with a first measure of the baseline state pattern and then acquires the scatter pattern in the fiber deformed shape. This procedure is completely automatic and controlled by the LUNA control unit (CU). Strain can be calculated along a straight length of fiber with large gage lengths even if the strain across the gage length is non-uniform. This ability to measure with large gage lengths even in the presence of a non-uniform strain field is unique to distributed Rayleigh scatter sensing with LUNA fiber sensing systems. In OBR system is necessary an initial non-measured length: the fiber sensor length is the length of the actual sensor available for making measurements not including this initial section of non-measuring strain relief.

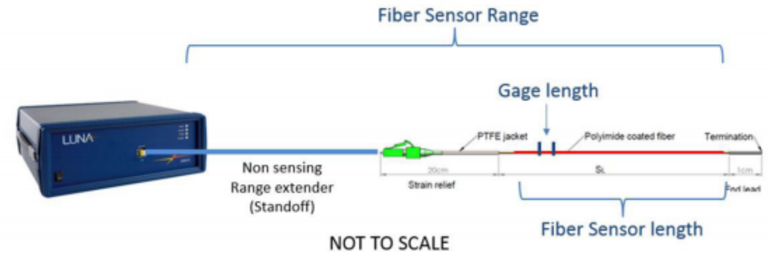

Figure 2.7: OBR measurement system layout

2.3.3 OBR and FBG comparison

Although OBR and FBG are both distributed fiber optic sensing systems, the main and basilar difference concerns in the effective physical measurement instrument: the natural random discontinuities of the core material for the OBR and the manufactured artificial Bragg grating imposed to the FBG fiber core. However this is not the unique difference: even their implementations are very different.
Advantages of OBR technology:

- The fiber used in an FBG system has to be custom designed and manufactured while the OBR sensors are made from standard unaltered optical fiber. This means a consistent difference in costs and availability of sensors;
- A Bragg grating is situated at a specific location on the fiber optic cable and this position defines the sensor location. Thus in an FBG system the number of sensors and spacing of sensors is determined by the number and location of Bragg gratings, etched into the cable whereas with OBR the entire fiber is a sensor. So in this sense the OBR can be assimilated to a continuous sensor, while the FBG is a spatial discrete detector. Obviously this is an enormous advantage for the application of the OBR in respect to the FBG in the blade modal analysis, where the reconstruction of the complete and continuous modes shapes is so fundamental;
- The location of Bragg gratings cannot be altered in the field and has to be decided at priori. In addition to this for FBG systems the number of sensors per fiber is limited. So the OBR technology can be considered more flexible and it is favourable for the embedded application due to the possibility to change the spatial resolution in post-processing (the *sensing locations* are not defined a-priori). Even this attitude of OBR to the embedded application makes this technology particularly appropriate to the turbomachinery field where is necessary avoid eventual disturbances to the fluid field next the blade surface;
- The FBG has a strong limit regards the Bragg grating length (sensor length), if the length increases the non-linearity becomes too much affective. The non- linearity is typical problem of FBG.

Critical aspects of OBR technology:

- The frequency range where OBR guarantees its correct working principles is much narrow than in the FBG technology. So, currently, the in the

OBR is not used in dynamic applications. Its dynamic behaviour is not well-known. Nevertheless the dynamic application presents promising development prospects. Many researches are trying to increase the performance of the OBR technology even at higher frequency.

- The OBR results depend on two consequential measurements (baseline state pattern and scatter pattern fiber deformed shape),while in FBG the output spectrum (locations of peaks in frequencies domain of the reflected harmonics) before the deformation is a nominal data gives in the data sheet of the fiber. So the uncertainty of an OBR measure could be higher than the FBG one.

- The OBR sensor requires the acquisition ODiSI system. So a complex and patented control unit is needed. Generally the FBG sensor with its control unit system is a more run-in technology, with a simpler data output post processing. The LUNA CU is yet not so comfortable in the fieldwork, on the other side the OBR fiber itself is however economic.

2.3.4 Traditional Strain to Displacement conversion method

When optical sensors are applied to the structure, the informations acquired are local strains. As previously explained, in the turbomachinery the mode shapes have to be determined in terms of displacements. This necessity is common to many other engineering fields. An important issue is the choice of the method to convert strains into displacements.
In literature, [10] and [13], the problem is generally closed by a FE-based approach. Traditionally the applied *strain-to-displacement* methodology is the Displacement-Strain-Transformation (DST) matrix, [12] and [14]. This approach is widely employed and strongly relies on the FE-model output. Given a set of experimentally measured data, no physical correlations are accounted to perform the transformation. The missing informations to transform the strains comes from a mathematical re-elaboration of the whole FE-analysis output, in particular the modes determined by the numerical model. This procedure permits to reconstruct the displacement values starting from the few experimental informations collected. None integrations are implemented, a simple *matrix operation* is able to convert the *vector* of the acquired strains to the *vector* of the desired displacement.
The numerical modelling of the structure dynamic response have to provide n mode shapes, a vector of m strain values and a vector of N discrete displacements. The m strain values are the FE model strains related to the strain-Degrees of Freedom (DoFs) which will be measured, while the FE model

N discrete displacements-DoFs are the ones associated to the locations of the desired displacements. The strain and displacement fields of the excited structure can be expressed, according to the modal approach, in the following matrix notation:

$$\begin{aligned} \bar{\epsilon}(t)_{m\times 1} &= [\Psi]_{m\times n}\ \bar{q}(t)_{n\times 1} \\ \bar{u}(t)_{N\times 1} &= [\Phi]_{N\times n}\ \bar{q}(t)_{n\times 1} \end{aligned} \tag{2.1}$$

Where $\Psi_{m\times n}$ is the *strain modal matrix* that accounts for m strain informations referred to each strain-DoF , $\Phi_{N\times n}$ is the *displacement modal matrix* that accounts for the overall set of N displacement-DoFs. Both consider n modes. Since the modal amplitude vector $q(t)$ is the same for the strain and the displacement field [10], it is possible to use the mode shape matrices Φ and Ψ to calculate a transformation matrix which connects the nodal displacement field $\bar{u}(t)$ with the *measured* strain field $\bar{\epsilon}(t)$.

$$\begin{aligned} \bar{u}(t)_{N\times 1} &= [\Phi]\ \left([\Psi]^T\ [\Psi]\right)^{-1}\ [\Psi]^T\ \bar{\epsilon}(t)_{m\times 1} \\ &= DST_{N\times m}\ \bar{\epsilon}(t)_{m\times 1} \end{aligned} \tag{2.2}$$

Remember that N is the overall amount of displacement-DoFs of the FE-model and m is the number of measured strains. Each strain measurement must be performed so to acquire a real value that is assigned to a FE-model strain-DoF. Practically the DST matrix permits to reconstruct the final displacement of bi-dimensional and three-dimensional surfaces, starting just from a restricted number m measured strains.

Practically the DST matrix is the *strain-to-displacement* method traditionally applied to re-elaborate experimental strains. Its main limitation is the clear strong dependence on the FE model. To properly convert the strain acquisitions to displacement informations, a reliable and accurate FE model is needed. Other criticisms will be deeply investigated in the entire description of the work thesis. The mathematical passages to calculate the DST matrix in case of three-dimensional structures and superficial measured strains will be explained in chapter 7

In literature, the mathematical integration of experimental strains is performed just in very simple mono-dimensional structures.

2.4 The Optimal Sensor Placement algorithm

The problem of determining the optimal geometric configuration of a sensor network, that maximizes the accuracy of the target estimates has a great importance in a multitude of scenarios. In particular, optimal placement techniques play a significant role in enhancing the quality and reducing the uncertainty of measured modal parameters during a vibration based health monitoring or, more in general, during the modal analysis of a complex structure. In this sense, optimal sensor placement OSP techniques are really interesting in turbomachinery applications: the blade modal shape reconstruction, as previously said, is fundamental to understand the possible critical load distribution on the blades, to monitor the blade health or to calculate the SAFE diagram experimentally. Defined a certain number of available sensor to be placed or imposed any other limitation about sensors arrangement, the OSP algorithm is run: it can really improve the blade modes experimental reconstruction, increasing accuracy of the results and providing a robust measurement system.

In the years, a number of approaches have been developed: some based on intuitive or heuristic placement, others employing systematic optimisation methods.

In literature a number of algorithms are proposed that, starting from some considerations based on the numerical model of the structure, generate a set of *significant positions* to be monitored, in order to obtain as much *modal informations* of the structure as possible. Thus, a quite accurate FE model must be available. OSP techniques have as main purpose to improve the experimental determination of the values of the required set of un-knowns: in modal analysis, the modal shapes. In this scenario, with the help of a computational modal analysis (CMA) output the sensing positions that will permit, in a real experimentation, to obtain the most significant set of data to achieve modal shapes best reconstruction are chosen. As a matter of facts, shape reconstruction has to be optimum both in the numerical simulation based on the FE model, but especially in the final experimental results. For this reason it is fundamental to understand both which sensor network can provide *ideally* more informations for the shape determination, both which configuration can improve signal quality in the experimental acquisition, both which sensor configuration is less affected by FE-model errors.

Practically, OSP procedure has two further simultaneous targets: to guarantee results quality both in the case of discrepancies among experimentation and

FE analysis output and in the case of noise affecting the experimental data. To resume, the final purposes of an OSP algorithm applied to modal analysis, are:

- Increase the quality of the modal shape reconstruction;
- Decrease the uncertainty of the general results;
- Evaluate the number of sensor really necessary;
- Optimize the sensor network according to the chosen measurement system, so to generate a configuration that reduces the eventual disturbances and respects the proper set-up limitations;
- Reduce the effects of the uncertainties in FE model parameters, on which OSP must be however based.

A number of parameters have been historically developed in order to lead the OSP procedure:

- Effective Indipendence (EFI) approach, [15], [16] and its derivations, [17];
- Kinetic Energy (KE) approach [15] and Strain Energy (SE) approach;
- Entropy Based (EB) approach, [18];
- Modal Assurance Criterion (autoMAC) approach;
- Mean Squared Error (MSE) approach;

These parameters can be used to find the best sensor positioning in whichever unknown variable could be the scope of the experimental measure. Obviously these indices can be investigated to find the best sensor configuration in case of mode shapes research, modal analysis.
The presented parameters can be able to provide an *heuristic* solution to the OSP problem. Alternatively they can be inserted in the definition of a *cost function*. This *cost function* represents the potentiality of the sensor configurations. The *cost function* has to be generally maximized to find the final OSP answer.

The indices shown, when elaborated in *heuristic methods* are able to offer an *unique* optimal sensors configuration starting from the entire set of position that can be physically observed. So they can point out directly just one set of *significant* degrees of freedom that must be simultaneously monitored.

They generally assure an *unequivocal* best sensor network arrangement. No iterations or function maximization are needed.

The methods including a function maximization can be defined as *systematic methods*. These algorithms just provide a numerical value that characterize a specific transducers configuration and allow to *rank* it with respect to another one, and require a sort of *iterative* approach. They can be considered as quality-ranking *methods* and converge to a *solution* after a number of iterations. As previously explained, the *quality* of each configuration is quantized using EFI, KE ,SE and so on. In this last scenario, it is necessary to follow a somehow defined logic to propose the candidate configurations to process
In literature many approaches are proposed, some of them are reported:

- Monte Carlo (MC) method, [16], is a full random approach. A random configuration is proposed, then its *quality* index is computed. At each attempt just the best arrangement is kept without *learning* anything from the previous one;

- Simulated Annealing (SA) algorithm, [19] (2013), is an optimization code analogous to the physical process of annealing, where a material is reheated to its melting point and subjected to a controlled cooling process that recrystallises its micro-structure formation, eventually improving the materials properties. Similarly, the ultimate goal of the SA algorithm is to determine a global optimal solution to a problem that is governed by an objective function. It proceeds with a sequence of iterations. At each iteration, the algorithm randomly finds a new configuration in the vicinity of its neighbours. The radius of the random search is proportional to the annealing temperature at that time. Normally, the newly generated solution is constrained by a set of boundary conditions such as the upper and lower bounds. Next, this solution is compared to the previous configuration based on the objective function value. The better solution is always accepted, while the weaker solution is accepted only if a randomly generated number (0,1) is greater than a proper probability value p. This method includes a *random* component in the research of the solution, however it has suitable criteria to converge to the best solution;

- Discrete optimization scheme based on artificial bee colony similarity, [20] (2015). This approach is proposed to reach the best sensor disposition for component health monitoring. The method to search the desired configuration is based to the minimization of a cost function, formulated as a combination of EFI informations and MSE check. Nevertheless the parameter to be optimized is no longer free to vary in a continuous space but is limited to specific knots in the search space;

- Genetic Algorithm (GA) method, [21], [14], [22], [16] and [23](2016). *Generation after genaration* the GA tends to maximize the value of a sensor-configuration quality-index, called *fitness function*. At each iteration the configuration is modified taking into account which *genetic characteristic* is more significant to achieve the best output, favouring the *reproduction* of that trait. This kind of cost function maximization guarantees a good convergence and convenience.

Practically all the last three described optimization algorithms are different methods to maximize a cost function. In these cases the primary issue is define correctly the cost function in relation to the desired scope of the optimization.

2.4.1 Effective Independence criterion

One of the most widely employed method to judge the optimality of a sensor network arrangement is the Fischer Information Matrix (FIM). In the earliest approach, Kammer [24](1990) proposed the EFI method to quantify the contributions of response measurements so that the modal states of targeted modes can be optimally observed. The EFI method classifies sensor locations based on the quantified informations on observing target modes and eliminates less significant locations from the candidates. Practically this approach is able to search the best set of DoFs locations from all the candidate locations in the structure. The goal of the EFI is to retain as much information as possible about the dynamic behaviour of a structural system while reducing the number of sensors through maximization of the Fisher information [25](2014).
Historically the EFI method is employed to maximize the accuracy of the estimation of a general unknown parameter: it has a mathematical background, whichever unknown parameters has to be determined. First of all, it is necessary to dispose of a reasonably good estimate of the unknown parameter vector that it is attempting to identify with the proper sensor configuration. This unknown vector in modal analysis scenario contains the modal parameters of the modes of interest. Secondly, are considered N available locations where m sensors can be applied, so the issue can be resumed into finding the m out of N responses that contain the most informations about the modal system-parameters, and that result to be maximally sensitive in any change in their values.
Considering the problem of the unknown-variables estimation, the covariance of the vector of parameter-estimates satisfy the relation (Nahi and Wallis,

1968; Sage and Melsa, 1971):

$$E\left[\theta - \hat{\theta}^T\right] > Q(t)^{-1} \tag{2.3}$$

In Equation 2.3, $\hat{\theta}$ is the estimator of the parameters-vector, while θ is the exact values of the unknown variables. The right-hand side of 2.3 is called Cramer-Rao lower bound. This formulation states that the error in the estimation made with $\hat{\theta}$ of θ has a minimum. If this minimum is maximized, the possible error in the estimation is reduced. The Cramer-Rao limit depends on the sensor data, so it depends on the sensor network configuration. What is searched is the configuration that maximizes the Cramer-Rao limit. All these considerations are valid for any type of unknown variable. Starting from any set of data that are somehow dependant on these variables, the problem can be always closed.
$Q(T)$ is called Fischer information matrix (FIM), therefore its *maximisation* would provide the minimum possible value of the covariance of the estimation error. The meaning of *FIM matrix maximization* os generally referred to the maximization of a certain norm, such as the trace norm. To better understand the real meaning of the Equation 2.3, the FIM represents the amount of *informations* about the unknown parameter that every possible sensor position has in its time history. Mathematically it is possible to define the FIM as the matrix containing the derivatives of all the the N-sensor available responses (where N is the total amount of monitorable DoFs of the structure), with respect to the unknown vector parameters.

$$Q(T) = \int_0^T \frac{(\frac{\partial H}{\partial \theta})^T (\frac{\partial H}{\partial \theta})}{\psi(t)^2 dt} \tag{2.4}$$

Where $\psi(t)$ is the noise variance on the experimental data and $H(\theta, t)$ is the vector $m \times 1$ containing the measured time histories of each sensor, that have to be dependant on the unknown parameters and on the time: in modal analysis $H(\theta, t)$ is the vector of the time signals dependant on the modal parameters θ, coherently with the modal approach theory. So it is possible describe $H(\theta, t)$ as:

$$H(\theta, t)_{m\times 1} = S_{N\times N}\ \bar{u}(t)_{N\times 1} \tag{2.5}$$

Where S is the *selector* matrix, a diagonal matrix with unity in the position r if the r^{th} DoF is measured. The matrix S is used to *select* the m sensor locations among the N available. Practically the definition of the matrix S is the final scope of the OSP algorithm.
In particular a single term of the Fischer matrix can be written as:

$$q_i(t) = \int_0^T (\frac{\partial H}{\partial \theta_i})^2 dt \tag{2.6}$$

From this last equation, 2.6, arises the meaning of FIM: it represents the dependence of the acquired signal $H(t)$ on the single unknown θ_i, considering the time interval T of the measurements. If are chosen the m time histories out of N, with the maximum $q_i(t)$ for all the θ_i required, are found the best locations for the m sensor.

Heuristically one should place the sensor in such a location that the time history obtained in that position is most sensitive to any changes in the parameter θ_i. Hence, it is really the slope of $H(\theta_i, t)$ with respect to θ_i that needs to be maximized. Slope means *dependence*. However, since only the absolute magnitude of the slope is of interest, it is more logical to maximize $(\frac{\partial H}{\partial \theta_i})^2$. This means maximize the determinant of the matrix $Q(t)_{m\times m}$ with a proper choice of m sensors.

The EFI method can be simply applied to the modal analysis.
In the logical path followed below it is assumed to deal with displacement measurement systems. The logical path that should be followed when monitoring other quantities is conceptually the same.
The starting point of this approach is the availability of the full modal matrix $\Phi_{N\times N}$, that contains all the available measurable DoFs. In is provided by a FE analysis. The purpose is again the determination of the best m locations, among the N DoFs available. Considering the results of the computational modal analysis (CMA), Φ contains the eigenvectors. Each column refers to a mode, each row to DoFs displacements, rotations and coordinates, those can be measured. Some target modes are selected to be optimally detected, so it is necessary define a-priori the n the modal shapes to estimate. So Φ is a $N \times n$ matrix. Considering the general equation 2.6, if the unknown vectors are the eigenvectors, the FIM formulation can be simplified. The signal time history vector can be described as:

$$H(\theta, t)_{m\times 1} = S_{N\times N}\ \bar{q}(t)_{N\times 1}\ [\Phi]_{N\times n} \tag{2.7}$$

As consequence, per each set of m sensors (a set of sensor is a sensor-network configuration), Equation 2.4 can be reduced to (according to **??**):

$$Q = [\phi^T \phi] \tag{2.8}$$

In this way the FIM is no more time-dependant, due to the modal-approach introduction that separates the spatial contribution to the temporal one. Practically, for each set of m locations it is possible to calculate the $\det(Q)$ employing just FE model data. If the determinant of the FIM is zero, the columns of the modal matrix (i.e. the target modes) are linearly dependent. Therefore, the purpose of the EFI method is to select the best DoFs (to place the sensors) which maximizes the determinant of the FIM. This method permits to estimate the quality of a sensor positioning just being aware of which are the unknowns, which is the analytical relation between the measurable DoFs data and the un-knowns and FE model preliminary values. An interesting application of the EFI index is presented in [26] (2011), where the EFI informations are ranked in a cost function and a proper genetic algorithm proceeds to maximize it. Another approach is described in [20] (2012), in these case an iterative elimination of *less important* possible sensor positions is performed. In this way the *importance* of the locations is properly judged by using EFI index.

2.4.2 Kinetic Energy and Strain Energy criterion

In 1997, [27], the KE method was proposed to determine a sensor configuration that maximizes the kinetic energy of the system. This approach is similar to the EFI method. A reliable comparison can be analysed in the article [17] (2005). The main difference is that the KE-approach purpose is to find sensor placements which maximizes the measure of the kinetic energy of the structure rather than the determinant of the FIM Q [17]. The basic idea underlying the KE algorithm is to achieve a sensor positioning that maximize the energy of the signal acquired. The positive consequence is the guarantee to have an high signal to noise ratio in the experimental acquisition. The disadvantage is that the OSP algorithm based on the maximization of KE tends to concentrate sensors where the predicted displacement as a maximum amplitude: this excludes the anti-nodes of the modal shapes. The same procedure and the same considerations can be repeated using strains instead of displacements (SE method). The KE and the SE methods permit to maximize the energy contained in the acquired signal and can increase the quality of experimental analysis, but they are not able to provide satisfactory data to optimize the complete modal shape reconstruction.

2.4.3 Entropy Based criterion

In the 1999 [28] a new criterion to optimize the sensor positioning is presented: the EB method, a statistical methodology with the scope to extract from the measured data the most information about the parameters of the structure. The optimality principle for the sensor locations is based on entropy information, which represents a measure of the uncertainty of the model parameters. A Bayesian statistical method helps to calculate the uncertainty related to the un-known parameters, then the entropy measure is minimized over the set of possible sensor configurations using a genetic algorithm. This method, generally, is particular suitable to minimize the number of necessary sensors.

2.4.4 autoMAC criterion

Carne and Dohrmann (1995) introduced the idea to calculate the correlation between the target mode shapes and defined the sensor set that minimizes the off diagonal term of correlation matrix. This approach is related to the calculation of the autoMAC matrix, with the CMA modes. The main purpose in exploiting this criterion is to maximize the capability to distinguish the different modal shapes and avoid misunderstanding in the modes definition. It is particularly important in the optimization that involves many modes simultaneously and with geometrically complex structure.

2.4.5 Mean Squared Error criterion

To evaluate the quality of the modal shape reconstruction, the most immediate and representative index is the MSE.

$$MSE_i = \frac{1}{N}\sum_{k=1}^{N}(\hat{\phi}_{k,\ i} - \phi_{k,\ i})^2 \tag{2.9}$$

Where MSE_i is the error calculated with respect to the single i mode shape. $\hat{\phi}_{k,\ i}$ is the k^{th} value of the eigenvector as computed by the FE software, and $\phi_{k,\ i}$ is the eigenvector value reconstructed by using just the m candidate sensor positions available. N is the overall number of displacement-DoFs. It is evident that FE modal analysis output is claimed to be *exact*. The MSE index gives exactly the same information of another parameter called Modal Assurance Criterion (MAC),[26](2008) and [19](2013).

$$MAC_i = \frac{\phi_i^T \phi_i}{(\phi_i^T \phi_i)(\phi_i^T \phi_i)} \tag{2.10}$$

2.4.6 Genetic Algorithm

To understand the meaning and the potentiality of GA, it is necessary to reference the Darwinian process of natural selection, that was defined by Darwin itself as the *principle by which each slight variation of a trait [of a specie], if useful, is preserved.* According with this evolutionary theory, individuals best adapted to their environments are more likely to survive and reproduce. As long as there are differences between them and that differences are heritable, there will be an inevitable selection of the individuals with the most advantageous traits. If that favourable genetic traits are heritable, the differential reproductive success leads to a progressive evolution of a specie, that will be characterized by that particular *feature*.

The fundamental concepts of reproduction, chromosomal crossover, occasional mutation of genes and natural selection process are reflected in the different stages of the GA.

The algorithm (see 2.12 for rapid consultation) is started by selecting the candidate set of Design Variables (DVs). Their value is initialized either randomly or heuristically, in order to create an initial population, composed by a certain number of individuals. Then the initial population is encouraged to evolve over generations to produce new designs, which are fitter. The quality (or *fitness*) of each design is evaluated according to an Objective Function (ObF), the fitness function, which must be formulated in relation to the specific optimization problem. By historical definition, the optimal design corresponds to the maximum of this objective function.

To implement the GA, it is necessary to set up a general *coding system* for the representation of the DVs. Most commonly the numerical DVs are coded according to binary basis (Figure 2.8). However the binary coding logic can be arbitrary, as long as univocal. Each Design Variable (DV) is coded into a *gene* (which corresponds to a binary sequence composed by a certain number of digits, or bits). The set of coded DVs that compose an individual is then *joined* into a single *chromosome*, which is a binary sequence of $number_{of}bits * number_{of}DV$ digits.

The reproduction process, which involves the *crossover* of the chromosomes of two individuals is commonly performed *cutting* them in a random position and exchanging one of the cut extremities. What is built are the chromosomes of the two offspring (Figure 2.9).

After the crossover, one or more bit of the sequence can randomly and occasionally *mutate*, switching its value. The mutation, which occurs after crossover, can introduce both a great improvement in the offspring fitness, both a drop of its value. GA gene mutation, introducing something absolutely new in the genetic make-up of an offspring, reduces the risk of stagnation of solution in local maxima (or minima).

The last step is a decoding process (Figure 2.10), to turn back to decimal entries.

The *natural selection process* is involved during the choice of the two parents that will be part of the crossover. Before the coding process, to each individual of the population is assigned a *fitness* value, depending on the *fitness function* that has been chosen to be employed. The fitness function is generally in the form: $fitness = f(DV_1, DV_2, ...)$. Problem constraints are generally managed by introducing a penalty on the fitness value. If an

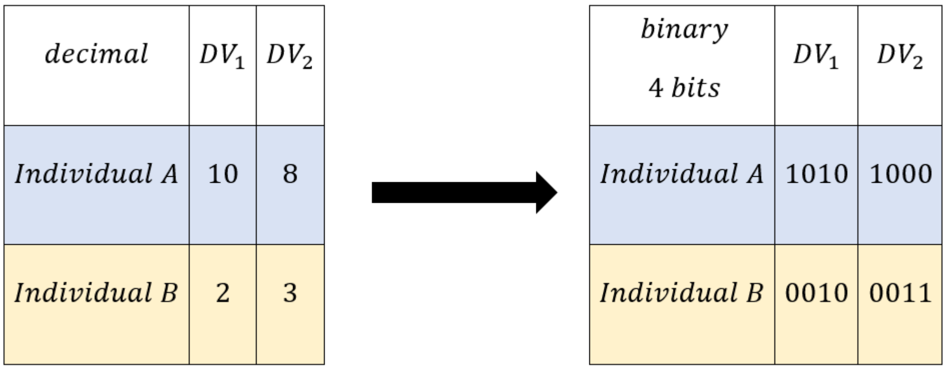

decimal	DV_1	DV_2
Individual A	10	8
Individual B	2	3

binary 4 bits	DV_1	DV_2
Individual A	1010	1000
Individual B	0010	0011

Figure 2.8: Binary coding process

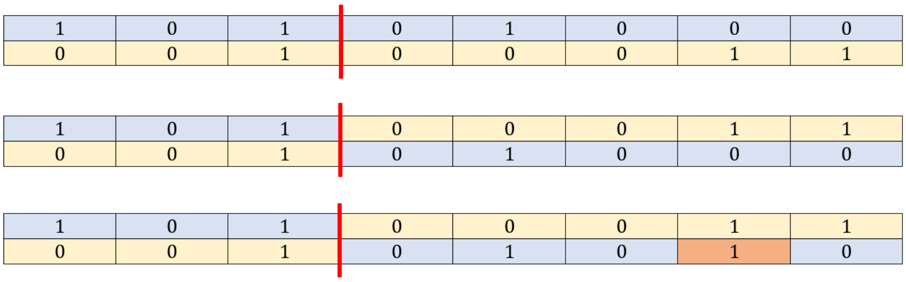

1	0	1	0	1	0	0	0
0	0	1	0	0	0	1	1

1	0	1	0	0	0	1	1
0	0	1	0	1	0	0	0

1	0	1	0	0	0	1	1
0	0	1	0	1	0	1	0

Figure 2.9: Crossover process with mutation

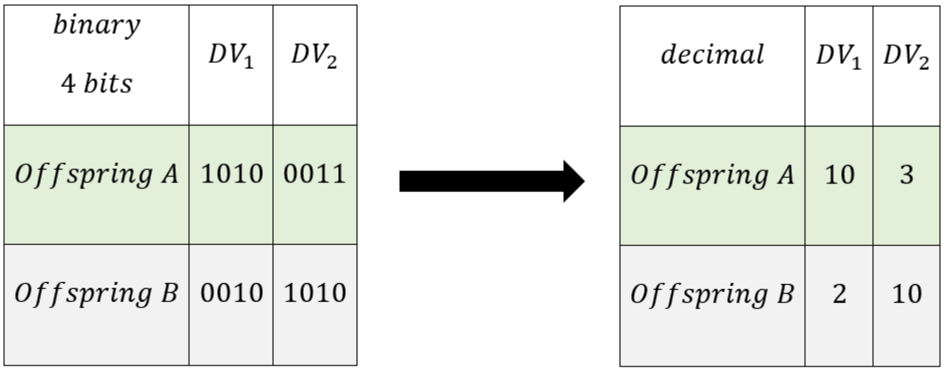

binary 4 bits	DV_1	DV_2
Offspring A	1010	0011
Offspring B	0010	1010

decimal	DV_1	DV_2
Offspring A	10	3
Offspring B	2	10

Figure 2.10: Binary decoding process

individual contains one or more DVs whose values do not respect the imposed limits, it is added a weighted increment to the calculated fitness, depending on the relevance of the violation. This will block, or limit, the reproduction of a not admissible solution.

The parents selection process can be compared to the spin of the wheel of Fortune. The wheel is split in as many parts as the number of individuals. Each slice is as large as the fitness value of that individual. To perform a reproduction, two spins are required, as two parents are needed to generate two sons. It is evident that, the higher is the individual fitness, the higher will be the probability to be chosen for crossover (Figure 2.11). At the end

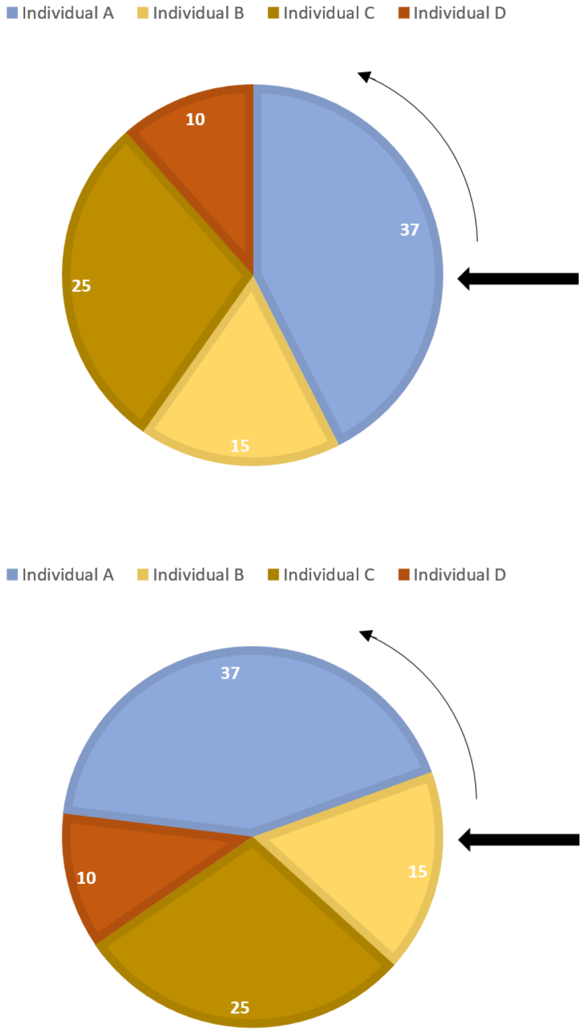

Figure 2.11: Parents selection for crossover: first and second wheel spin

of the whole process, once are generated as much offspring as parents, the cycle starts again. The offspring of the previous cycle become the parents of the new one, and so on, till *convergence*. An useful improvement is the so called *discarding* process. The fitness of each son is evaluated, and then it is compared to the one of parents. Will compose the next population only the individuals with the best fitness value.

The world of GA is extremely wide and under continuous development: a number of improvement can be introduced at each step, aiming to faster the convergence to the optimal solution and avoiding the risk to relapse into local maxima (or minima). GA convergence is strongly affected by algorithm parameters indeed:

- Number of sections of the chromosome exchanged during crossover;
- Number of individuals considered;
- Number of bits for coding;
- Criterion employed to select parents for reproduction;
- Criterion employed to stimulate mutation;
- Probability of an offspring to withstand a genetic mutation;
- Probability of two selected parents to undergo crossover, respect to the eventuality to pass directly to the next generation.

In conclusion, it does not exist a general *right* or *wrong* manner to employ a GA. Different choices directly reflects in convergence speed. The meaning of *convergence* in a GA-based optimization process is not rigorous. The termination condition that sanction when to *stop* the cycle is defined depending on problem requirement, and generally is reached when:

- The minimum criteria is satisfied, but generally, being the fitness objective-value unknown, is difficult to be formalized;
- A maximum number of generation is reached, but no idea on the quality of the solution can be given;
- The allocated resources-budget (*i.e.: time, money, ...*) is terminated;
- No more noticeable improvements at next generation, but just a local maxima (or minima) can be confused with an absolute one.

Generally, multiple considerations are done before claiming that solution is reached.

For the sake of completeness, a very little digression will follow on the theoretical background that stays behind GA. A GA is not based on a deterministic strategy: so why its solution evolves till *convergence*? The schema theorem [29] is the basis of the proof that a rightly tuned GA *works*.

A schema is a set of bits that are repeated in the same position in a certain number of individuals. The order of that schema is the overall number of bits by which it is composed, its length is the distance (in terms of number of digits) among the first and the last specific bit that compose the schema itself. In a primitive population live different schemas, which tend to survive or be suppressed, generation after generation, because of the action of crossover and mutation. The very conclusion of the theorem states that *a short, low-order and high (i.e. above average) fitness schema increases exponentially [its appearance in more and more individuals] generation by generation.* If a schema has these requirements, it will be the *building-box* of the final solution. This principle assures that if an infinitely large population is considered, the real *convergence* of solution to a maxima will be reached. However, given the stochastic component of the process, the required number of generations remains unknown.

In the light of what said previously, the structure of a GA is synthesized as follow, Figure 2.12.

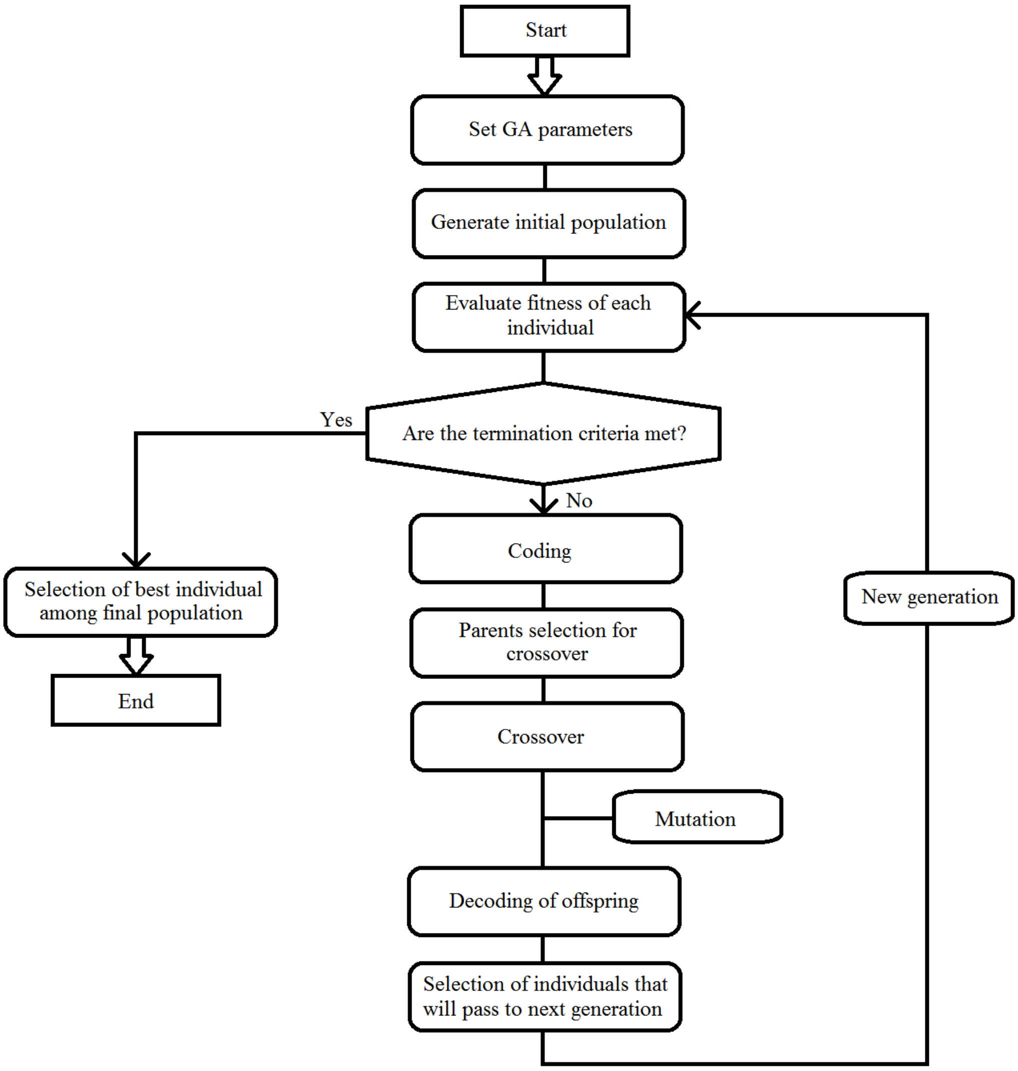

Figure 2.12: GA logical structure

The specific content of each block will be extensively treated in chapter 3, explaining how tasks are performed and the involved choices.

Chapter 3

Proposed Optimal Sensor Placement method and numerical mode-shapes reconstruction

3.1 Introduction

This section pursues the entire process of the *optimal sensor placement* (OSP). Here it will be explained how the optimal fiber arrangement has been determined and the steps that has been followed.
MathWorks MATLAB and Dassault Systèmes Abaqus FE-software will been employed.

One of the main tasks of this essay is to reconstruct the vibrating mode-shapes of a specific structure starting from surface strain measurements. To best achieve this result, the fiber must be arranged in the most convenient way.
To perform an OSP procedure, some knowledge about the *expected* measurement output is necessary. As a matter of fact, it is required to understand a-priori whenever a fiber configuration is suitable or not in order to success in the shape reconstruction purpose.
To understand where the optical fiber sensor has to be placed, a *virtual simulation* of the measurement process must be performed.
To perform such a simulation, the surface modal strain-fields (not acquired yet) have to be *virtually* generated by a *computational modal analysis* (CMA). Then, several *candidate* fiber arrangements are produced. Each one of those

specific configurations will be *tested* in order to discover if the fiber can provide enough information to well reconstruct the shape of the deformed surface.

The various candidate configurations to be tested are generated by a *genetic algorithm*. The quality of each proposed arrangement is ranked thanks to a dedicated *composite cost function*.
The GA *drives* the optimisation of the configuration aiming to maximise the shapes reconstruction quality without violating any physical constraint concerning the optical-fiber sensor.

Being the measurement output a strain measure, to obtain the structure displacements a *strain-to-displacement* (StD) procedure have to be implemented. This goal is achieved without relying on any FE-based data as suggested by literature with the DST-matrix method, instead.

To simplify the readability, pre-processing will be treated schematically. The whole optimal sensor placement procedure involves the following steps:

- Case-study definition, section 3.2;
- Strain theory and bi-dimensional thin plate assumption, section 3.3;
- Strain-to-displacement translation procedure, section 3.5;
- Computational modal analysis with FE software and data import in MathWorks MATLAB environment, section 3.4;
- Development of a GA suitable to optimize fiber arrangement on the plate, section 3.6;
- Analysis of results to determine how to definitively arrange the sensor, section 3.7;

3.2 Case-study definition

All the considerations that will be carried out starting from this section are formulated considering a specific simplified case. In the truth, no strong assumptions are made except for the restriction to a bi-dimensional model to describe the geometry under exam. This allows to analytically streamline the problem of the Strain to Displacement (StD) conversion and well comply with the simple experimental case considered.
The analysis will focus on a thin Polycarbonate (PC) cantilever plate, clamped on one of its short sides.

Material data-sheet and layout are described in Table 3.1 and Figure 3.1. The suspended area measures 700x145x5mm. In practice, the clamp is built by two thick steel plates bolted together and clamping the thin plate. This constraint is assumed to be *infinitely rigid*.

Table 3.1: Polycarbonate data-sheet

-	quantity	unit
Density	1.21	g/cm^3
Young modulus	2200	MPa
Poisson ratio	0.37	–

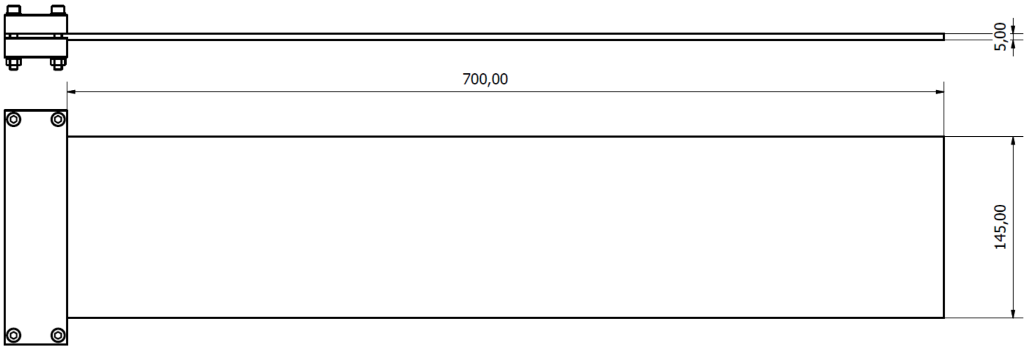

Figure 3.1: Polycarbonate plate layout

There are several reasons that stays behind the choice of these specific features.

First of all, the purpose to resemble a *turbine blade*, together with the possibility to well comply the bi-dimensional thin-plate assumptions and well accommodate a ∼2m length fiber.

Secondly, the need of having an high number of eigenfrequencies below 200 Hz, so that the OBR fiber acquisition system can work in the most reliable way. This allows to perform a fiber arrangement optimisation over a wide range of effectively measurable modes. The acquisition system, being designed for quasi-static applications, does not allow high frequency monitoring: to optimise fiber arrangement accounting for those modes is meaningless.

3.3 Strain theory and bi-dimensional thin plate

3.3.1 Strain theory

When a solid body is subjected to external actions, it deforms, producing internal strains and stresses. The deformation depends on the geometrical configuration of the body, on applied loads and on the mechanical properties of its material.

Consider an elastic body of any general shape subjected to external loads which are in equilibrium, and consider a Cartesian frame of reference defined by x, y, z. Applying this action over the body it deforms, and each of its points has small elastic displacements.

A generic point has the coordinates x_0, y_0 and z_0 in its initial undeformed state. After deformation, this point has moved into a new position, and its coordinates have became the following: $x_1 = x_0 + u$, $y_1 = y_0 + v$ and $z_1 = z_0 + w$, where u, v and w are projections of the displacement vector of the point on the coordinate axes x, y and z. In the most general case, u, v and w are functions of x, y, z and time.

The term *deformation of a body* so refers to the relative displacements experienced by the *points* of the body itself. Every particle K in the body corresponds to a position X. When the body is deformed, the particle K moves from P, defined by the vector $\bar{X} = (x_0, y_0, z_0)$ to a new position p, defined by $\bar{x} = \chi(\bar{X}, t) = (x_1, y_1, z_1)$. The function $\chi(\bar{X}, t)$ is called *mapping function* and describes the motion of a continuum. It is a continuous and differentiable function of space and time, which implies that cracks and voids do not open or close during the deformation. If the displacement of every particle in the body is known, the deformed configuration κ can be built from the undeformed configuration κ_0.

In the Lagrangian description, the displacement $\bar{u} = (u, v, w)$ is expressed as:

$$\bar{u}(\bar{X}, t) = \chi(\bar{X}, t) - \bar{X} = \bar{x} - \bar{X}$$

From this point on, time dependence will be no more mentioned. The deformation of a body can be measured in terms of the strain tensor E, which is defined such that it gives the change in the square of the length of the material vector $d\bar{X}$ passing from κ_0 to κ_1. $d\bar{X}$ is the vector connecting two points in the undeformed configuration, $d\bar{x}$ is the vector connecting the two points in the deformed one. By definition of E:

$$2d\bar{X} \cdot E \cdot d\bar{X} = d\bar{x} \cdot d\bar{x} - d\bar{X} \cdot d\bar{X} \tag{3.1}$$

Consider Figure 3.2 to visualize analytical steps.

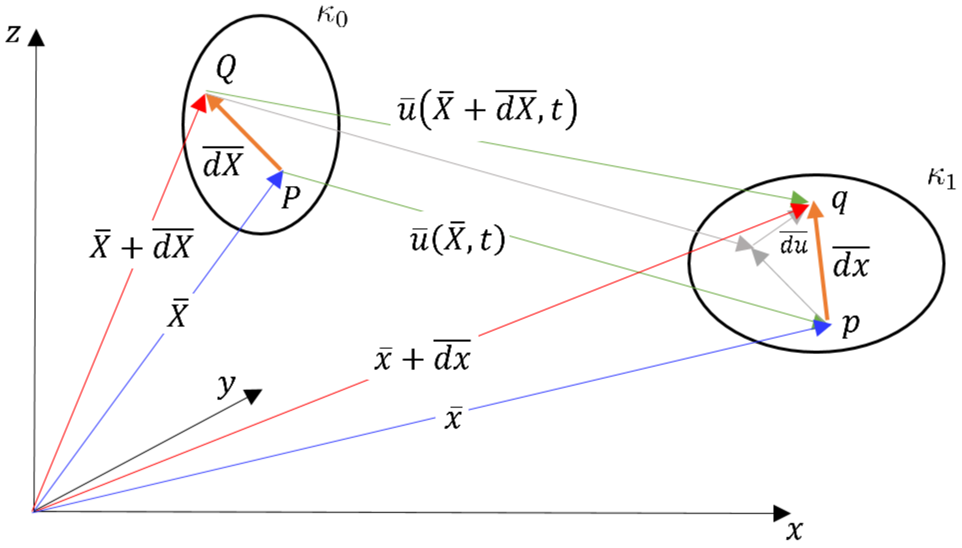

Figure 3.2: Strain definition

The components of the displacement vector for the particle Q can be expressed by:

$$\bar{u}(\bar{X}+\bar{dX}) = \bar{u}(\bar{X}) + \bar{du} \tag{3.2}$$

where $\bar{du}$ is the relative displacement vector, which represents the relative displacement of q with respect to p in the deformed configuration. Now consider:

$$\begin{aligned} \bar{x}+\bar{dx} &= \bar{X}+\bar{dX}+\bar{u}(\bar{X}+\bar{dX}) \\ \bar{dx} &= \bar{X}-\bar{x}+\bar{dX}+\bar{u}(\bar{X}+\bar{dX}) \\ &= -\bar{u}(\bar{X})+\bar{dX}+\bar{u}(\bar{X}+\bar{dX}) \\ &= \bar{dX}+\bar{du} \end{aligned} \tag{3.3}$$

For an infinitesimal element $\bar{dX}$, and assuming continuity on the displacement field, it is possible to approximate the displacement vector for the neighboring particle Q (Equation 3.2) using a Taylor series expansion around point P and neglecting higher-order terms, as stated by the following correlation:

$$\begin{aligned} \bar{u}(\bar{X}+\bar{dX}) &= \bar{u}(\bar{X}) + \bar{du} \\ &\approx \bar{u}(\bar{X}) + \nabla\bar{u}\cdot\bar{dX} \end{aligned} \tag{3.4}$$

where ∇ is the gradient operator. Thus, Equation 3.3 becomes:

$$\begin{aligned} d\bar{x} &= d\bar{X} + d\bar{u} \\ &\approx d\bar{X} + \nabla\bar{u}\cdot d\bar{X} \\ &\approx d\bar{X}\cdot(I+\nabla\bar{u}) \end{aligned} \tag{3.5}$$

Stated these correlations, the 3.1 becomes:

$$\begin{aligned} 2d\bar{X}\cdot E\cdot d\bar{X} &= d\bar{x}\cdot d\bar{x} - d\bar{X}\cdot d\bar{X} \\ &= d\bar{X}\cdot(I+\nabla\bar{u})\cdot[d\bar{X}\cdot(I+\nabla\bar{u})] - d\bar{X}\cdot d\bar{X} \\ &= d\bar{X}\cdot[(I+\nabla\bar{u})\cdot(I+\nabla\bar{u})^T - I]\cdot d\bar{X} \end{aligned} \tag{3.6}$$

where E is the *Green-Lagrange strain tensor*, defined as:

$$E = \frac{1}{2}\Big[\nabla\bar{u} + (\nabla\bar{u})^T + \nabla\bar{u}\cdot\nabla\bar{u}^T\Big] \tag{3.7}$$

Note that the strain tensor is symmetric, $E = E^T$. The strain tensor defined in Equation 3.7 is called *finite strain tensor*. If the displacement gradients are so small that their squares and products are negligible, the 3.7 becomes:

$$E = \frac{1}{2}\Big[\nabla\bar{u} + (\nabla\bar{u})^T\Big] \tag{3.8}$$

that is named *infinitesimal strain tensor*. Its components can be seen as:

$$e_{ij} = \frac{1}{2}\Big[\frac{\partial u_i}{\partial x_j} + \frac{\partial u_j}{\partial x_i}\Big] \tag{3.9}$$

Using the notation $x_1 = x$, $x_2 = y$, and $x_3 = z$, and $u_1 = u$, $u_2 = v$, $u_3 = w$, the infinitesimal strain components become:

- $\epsilon_{xx} = \frac{\partial u}{\partial x}$, $\epsilon_{yy} = \frac{\partial v}{\partial y}$, $\epsilon_{zz} = \frac{\partial w}{\partial z}$;
- $\epsilon_{xy} = \frac{1}{2}[\frac{\partial u}{\partial y} + \frac{\partial v}{\partial x}] = \frac{1}{2}\gamma_{xy}$;
- $\epsilon_{xz} = \frac{1}{2}[\frac{\partial u}{\partial z} + \frac{\partial w}{\partial x}] = \frac{1}{2}\gamma_{xz}$;
- $\epsilon_{yz} = \frac{1}{2}[\frac{\partial v}{\partial z} + \frac{\partial w}{\partial y}] = \frac{1}{2}\gamma_{yz}$;

3.3.2 Bi-dimensional thin plate

Plates are plane structural elements with a small thickness with respect to the other two dimensions [30]. Plates can be modelled according to the action they withstand: uniform bending moment or in-plane membranal loads. The case under exam has the aim to resemble a strongly simplified turbine blade, whose loading condition better fits the first occurrence, since pressure field acts normally to blade surface.

Kirchhoff's plate bending theory takes advantage of the dimensional length-scale difference to reduce the complexity of a full three-dimensional solid mechanics problem. All stress, strain and displacement components can be expressed by the deflection w of the plate mid-plane, which is a function of the two coordinates in the plane: $w = f(x, y)$.

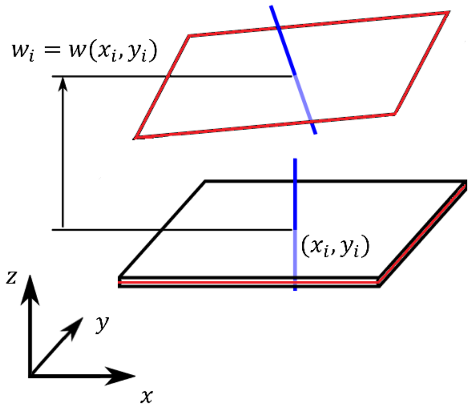

Figure 3.3: Thin-plate theory

Consider a plate in which the xy plane coincides with the plate's mid-plane and the z coordinate is perpendicular to it and directed upward. Thin plate bending theory is valid under the following conditions:

- The material of the plate is elastic, homogeneous, and isotropic;
- No external loads (membranal or normal) are applied;
- The plate is initially flat, thickness t is small and constant;
- The deflection w of the mid-plane is *small* with respect to thickness. The slope of the deflected surface is therefore very small;

- The straight lines initially normal to the mid-plane before bending, remain *straight* and *normal* to the mid-surface during the deformation;

- The *thickness* of any element composing the plate is not altered during deformation;

These hypothesis imply that:

- The mid-plane remains unstrained after bending: u and v displacements of points lying on the mid-plane are null;

- The thickness-normal strain in null: $\epsilon_z = \frac{\partial w}{\partial z} = 0$. It shows that w is independent from z. Each point lying along the same mid-plane normal undergo the same w;

- The transverse shear strains, γ_{zx} and γ_{zy} are zero, because straight and normal-to-mid-plane lines remain so;

Remind that u, v, w denote the total displacements of a point along the x, y, z coordinates. From the most general point of view, a generic material-point i occupying the position x_i, y_i, z_i in the undeformed plate, moves to the position $x_i + u, y_i + v, z_i + w$ in the deformed configuration.

Under the considerations stated above, each parameter can be expressed just as a function of w. It represents both the displacement of the generic point i along z, both the plate mid-plane deflection.
It can be easily seen in Figure 3.4 that:

- $\varphi_x = \frac{\partial w}{\partial x}$ and $\varphi_y = \frac{\partial w}{\partial y}$;

- $u = -z \cdot \varphi_x = -z\frac{\partial w}{\partial x}$ and $v = -z \cdot \varphi_y = -z\frac{\partial w}{\partial y}$, being z the distance from the mid-plane and the point i in the undeformed configuration, so: $z = \frac{t}{2}$ if the point is on the surface. Displacements u and v are null on mid-plane;

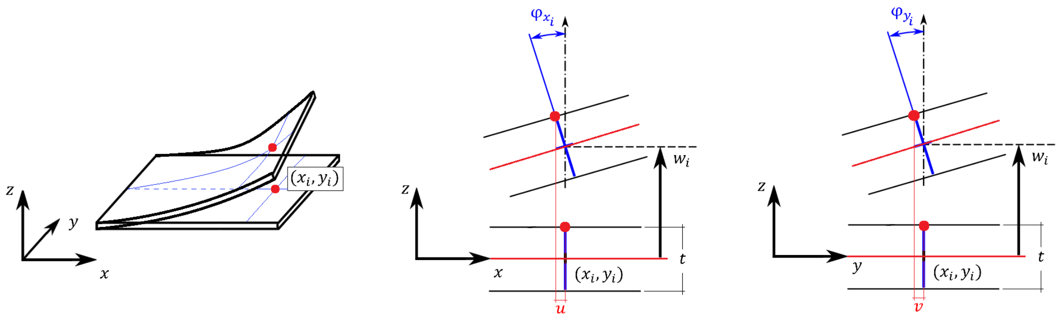

Figure 3.4: Thin-plate theory nomenclature

In the light of these considerations, the infinitesimal strain components become:

- $\epsilon_{xx} = \frac{\partial u}{\partial x} = -z\frac{\partial^2 w}{\partial^2 x}, \quad \epsilon_{yy} = \frac{\partial v}{\partial y} = -z\frac{\partial^2 w}{\partial^2 y}, \quad \epsilon_{zz} = \frac{\partial w}{\partial z} = 0;$
- $\epsilon_{xy} = \frac{1}{2}[\frac{\partial u}{\partial y} + \frac{\partial v}{\partial x}] = \frac{1}{2}[-z\frac{\partial^2 w}{\partial x \partial y} - z\frac{\partial^2 w}{\partial x \partial y}] = -z\frac{\partial^2 w}{\partial x \partial y} = \frac{1}{2}\gamma_{xy};$
- $\epsilon_{xz} = \frac{1}{2}[\frac{\partial u}{\partial z} + \frac{\partial w}{\partial x}] = \frac{1}{2}\gamma_{xz} = 0;$
- $\epsilon_{yz} = \frac{1}{2}[\frac{\partial v}{\partial z} + \frac{\partial w}{\partial y}] = \frac{1}{2}\gamma_{yz} = 0;$

3.4 Computational Modal Analysis and data import

To perform an optimal sensor placement procedure (OSP), is essential to dispose of a FE-model of the structure under exam, to have an available set of data that can simulate the output of a real measurement session. Once the model has been created, the FE software must perform a computational modal analysis, in order to determine which displacement and strain *mode-shapes* are expected to appear in the examined frequency range.

The numerical results must be then imported into the processing environment, in order to be prepared for the following steps.

3.4.1 Computational Modal Analysis

A 3D finite element model has been created in Dassault Systèmes Abaqus 6.13.

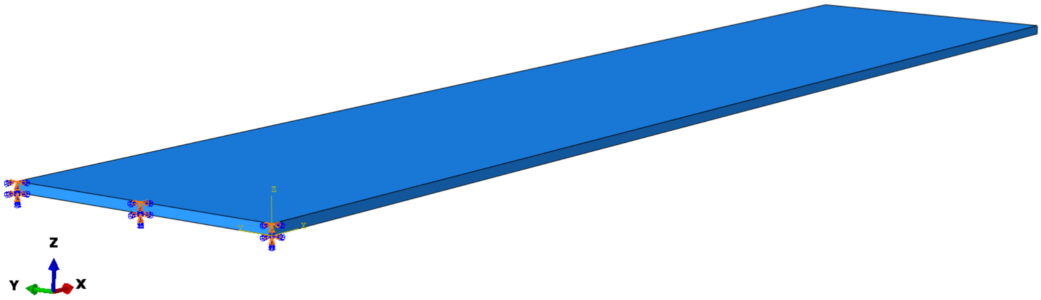

Figure 3.5: FE plate model

The plate dimensions are the same of Figure 3.1. The plate material is modelled as purely elastic, isotropic and not damped. Its specifications are in Table 3.1.

Problem boundary conditions consist in a clamp, which *sets* to zero rotations and displacements on the visible short side, as in Figure 3.5.

The mesh is *structured*. It is built by a number of $2.5mm \times 2.5mm$, hexahedral, 8-node linear bricks (element type: C3D8). Each node of this mesh element type has three DoFs. Calculations will be performed by full integration, with a second order accuracy level. It is mandatory to consider that mesh size (i.e. relative distance among nodes) is chosen to be coherent with strain gauges spacing inside optical fiber. Strain-eigenvector will be referred to nodes, so nodes are assumed in the OSP algorithm to *coincide* with fiber measurable locations.

The numerical analysis aims to extract all the displacement and strain *eigenvectors* within a certain frequency range (within 0 and $200Hz$).
Displacement eigenvectors are automatically normalized with respect to their maximum displacement value.

For each vibrational mode a report output file is generated. It contains, among the others, the nodal displacements along x, y and z directions with respect to the undeformed configuration (the *displacement-eigenvectors*), and all the nodal strain values according to the definitions in subsection 3.3.1 (the *strain-eigenvectors*).

3.4.2 Data import

A MATLAB script is created, aiming to *read* the previously generated output report-files and *generate* the set of variables needed to proceed the OSP procedure. More in detail:

- The nodes coordinates;
- The indices of the nodes on surface and on mid-plane;
- The displacement-eigenvectors associated to these nodes (their u, v and w displacements);
- The strain-eigenvectors associated to these nodes and the strain-DoFs of interest (ϵ_x, ϵ_y and γ_{xy}).

To provide some examples, the components of a *torsional* and a *flap-wise* strain and displacement eigenvector are presented below:

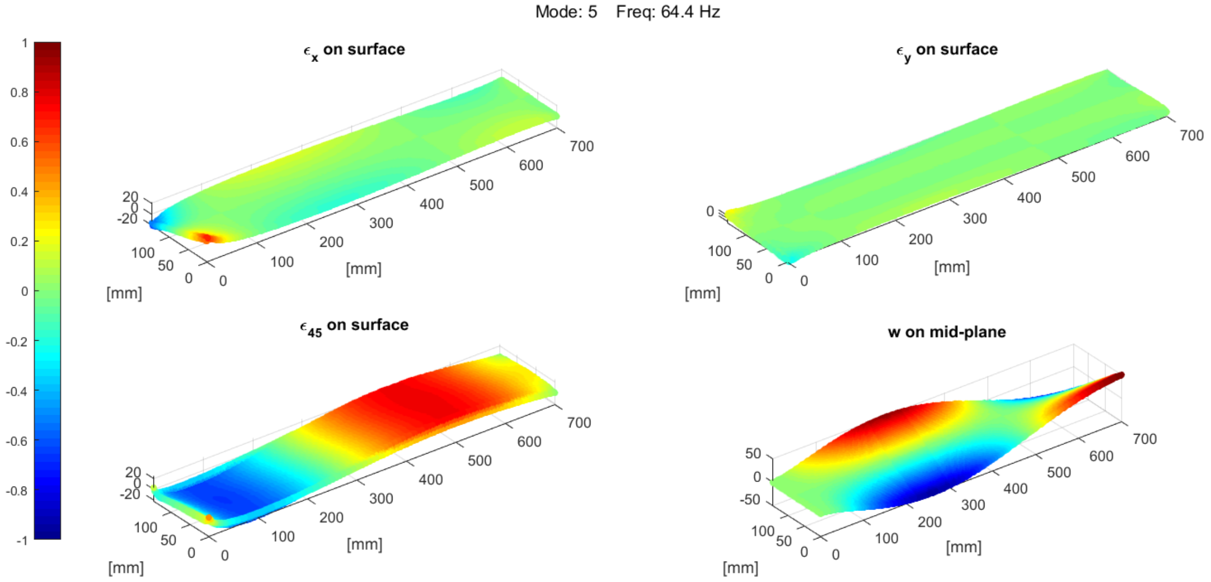

Figure 3.6: 5^{th} PC thin-plate vibrating mode

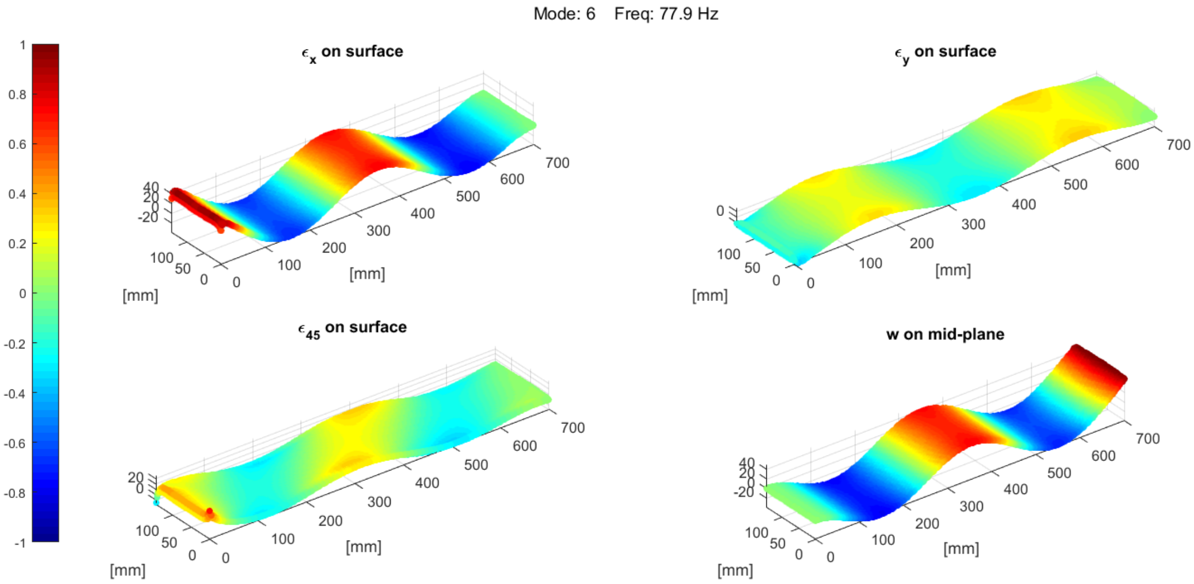

Figure 3.7: 6th PC thin-plate vibrating mode

3.5 Implemented method for Strain to Displacement translation

The purpose of this work is to find an effective way to evaluate the plate surface deflection w having available just the superficial strain fields, the ones actually measured by the optical fiber sensor. Given the consistency of the thin-plate assumptions, surface w corresponds to the *mid-plane* displacement field $w = f(x, y)$.
To perform the strain-to-displacement translation, an effort has been carried out to avoid exploiting any kind of external aid coming from the use of a FE-software, as is generally suggested in literature, instead.

Even if the optimal sensor placement process is necessarily based on somehow *artificially generated* data (i.e. *produced* by a FE software, so potentially any kind of information can be obtained), it must be noted that all the informations employed in this optimal sensor placement OSP algorithm will be absolutely coherent with the ones that in the real experimentation can be obtained. Strain data from *FE*-analysis are required just to *simulate* the informations that would be available in a real experimental session.

A set of considerations that must be taken into account to better understand these concepts are listed below:

- Optical fiber sensors (both OBR and FBG) are transducers that evaluate the *longitudinal* strain that each one of their *embedded gauges* undergo. These sensors generate an *unidimensional* information, exactly as resistive strain-gauges do. In a real fiber-based measurement is obtained a set of numerical values that figures how much a *specific* portion of the fiber has been *stretched*;

- If the optical-fiber (OF) is fixed on a surface, each on of its portions provides the strain that *locally* the surface undergoes, along the direction in which the Optical Fiber (OF) lies. The OF can be obviously placed with the desired orientation. It is the additional knowledge of its spatial arrangement that give sense to the measure itself;

- If the purpose is to attain *displacements* from measured surface *strains*, and the accuracy of this reconstructed displacement field is the main goal, the optimal sensor placement procedure aims to arrange the OF sensor so that, *after* the strain-to-displacement transformation (StD), the deformed surface can best fit the *exact* one. As a matter of fact, given the same input data, different StD procedures led to different quality shape reconstructions.

In conclusion:

- Measurements that will be performed are *strain* measurements. The local strain value (generated by the FE-software in pre-processing, or by the OF equipment in real monitoring) must be followed by an *external* information concerning fiber arrangement and orientation, point by point;

- The number of possible OF orientations impacts on the choice of the strain-to-displacement procedure and the final result;

- The OSP algorithm has to determine the best fiber arrangement just relying on the superficial strain fields generated by the FE-software. The strain-to-displacement transformation function here employed must be the same that will be used when dealing with real measurements.
  Fiber arrangement is optimized depending on the useful informations it can provide *after* their translation from surface-strains into displacements.
  Fiber distribution is *optimal* according to the strain-conversion procedure that will be followed.

Under the light of these facts, the StD problem arises not only during post-processing, but the whole conversion procedure must be taken into account also during optimal sensor placement process. OSP output will determine where the fiber must pass and its orientation.

To extrapolate w, a re-elaboration of the measured strains is required. Differently from what literature proposes (to rely on the DST-matrix method), to perform this task it has been assumed that detaching from FE-analysis data is a more suitable approach. The amount of uncertainties that implicitly affects a computational modal analysis are acknowledged to be a considerable source of error. For that reason, a new approach totally free from *numerical* help has been developed. In order to close the strain-to-displacement problem a direct integration of measured strain fields will be performed.
In this section, a physical approximation has however been introduced because well comply with the bi-dimensional geometry under exam and simplify the strain-displacement physical correlations. In a full three-dimensional structure, the StD problem can however be closed just relying on physical approximation-free correlations, see chapter 7 for further explanations.

Surface strains that arise in a thin plate can be summarized in ϵ_x, ϵ_y, γ_{xy}, or by another three-directional strain information set. Each one of them can be directly connected to w by integration.

From a simplified point of view, as for resistive strain-gauges, to fix a strain-sensor on a surface means to measure the relative displacement among *two* points. It is assumed that, under the assumption of small displacements, once the sensor is placed along one direction, the component of measured strain produced by small displacements in the other directions, are neglected.

To dispose the fiber just along x or y axis of the plate to exclusively obtain ϵ_x or ϵ_y fields and proceed in their integration ($\epsilon_x = -z\frac{\partial^2 w}{\partial^2 x}$ or $\epsilon_y = -z\frac{\partial^2 w}{\partial^2 y}$) in order to obtain the surface displacement led to misleading results.

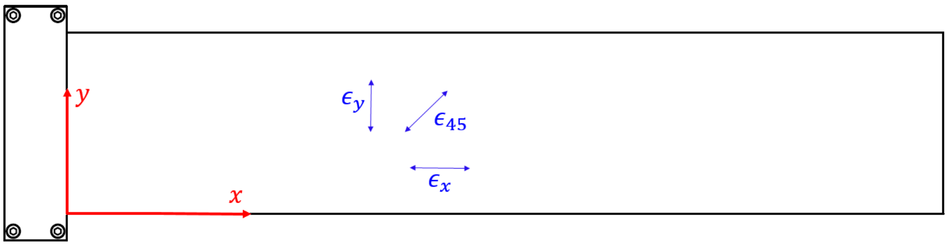

Figure 3.8: Strain nomenclature on the bi-dimensional plate, upper view

To integrate $\gamma_{xy} = -2z\frac{\partial^2 w}{\partial x \partial y}$ led to far better outputs, as explained in the following paragraphs and by Figure 3.15. It must be noticed that the shear planar strain cannot be measured directly, but it can be locally evaluated by a re-elaboration of the measured ϵ_x, ϵ_y, ϵ_{45}, obtained fixing the fiber in the right directions, as in Figure 3.8. These three directions are in this case chosen arbitrarily. In each on-surface measurement any set of at least three strain informations allows to be manipulated in order to calculate γ_{xy}:

$$\begin{bmatrix} \epsilon_x \\ \epsilon_y \\ \gamma_{xy} \end{bmatrix} = \begin{bmatrix} cos^2\theta_1 & sin^2\theta_1 & cos\theta_1\ sin\theta_1 \\ cos^2\theta_2 & sin^2\theta_2 & cos\theta_2\ sin\theta_2 \\ cos^2\theta_3 & sin^2\theta_3 & cos\theta_3\ sin\theta_3 \end{bmatrix}^{-1} \begin{bmatrix} \epsilon_{\theta_1} \\ \epsilon_{\theta_2} \\ \epsilon_{\theta_3} \end{bmatrix}$$

With the previous formulation, given ϵ_{θ_1}, ϵ_{θ_2} and ϵ_{θ_3}, γ_{xy} is extracted. As a matter of facts, an higher number of strain fields can be accounted together. In this case the physical problem would be overdetermined. In order have a solution, the problem must be approached through a minimisation strategy relying on a pseudo-inverse matrix approach.
Actually, the strain directions involved should be determined by the optimisation process itself. This because a different set of strain fields can deeply affect the reconstruction of γ_{xy}, due to the interpolation procedure that occurs. As already stated, in this scenario the measurement directions has been defined a-priori, to reduce the computational effort and considering the practical complexity in arrange the fiber with the exact orientation.

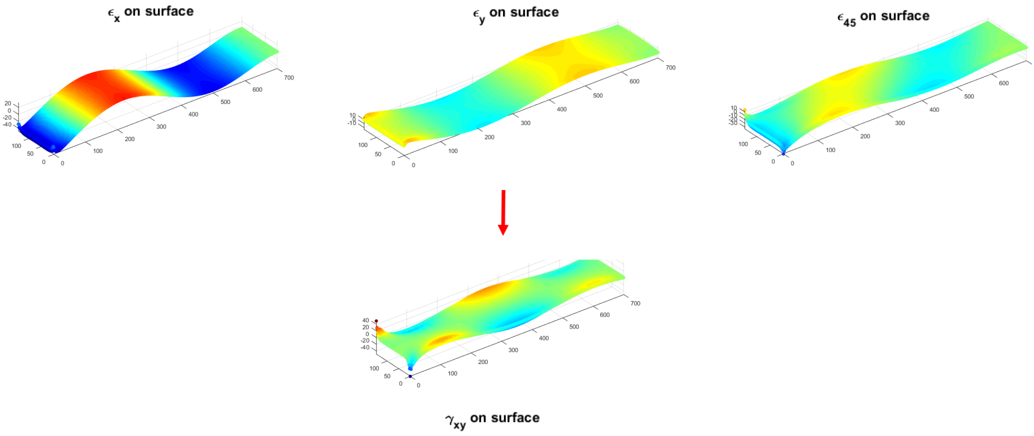
ϵ_x on surface

ϵ_y on surface

ϵ_{45} on surface

γ_{xy} on surface

Figure 3.9: γ_{xy} reconstruction from ϵ_x, ϵ_x and ϵ_{45} - 4th mode

Strain measurements are local, and it is not possible to monitor each point of the surface in the three directions together. What is physically available are some values of ϵ_x, ϵ_y, ϵ_{45} in some distinct locations. Interpolations are required to obtain three continuous strain fields all over the plate surface.

To integrate γ_{xy} has two advantages. As a matter of fact, the availability of three surface strain fields give a *complete* knowledge of the bi-dimensional strain condition. Computing γ_{xy} as $\gamma_{xy} = f(\epsilon_x, \epsilon_y, \epsilon_{45})$ means to attribute to the planar shear strain field the capability to *represent* a good *index* of the surface strain state. Furthermore, being ϵ_x, ϵ_y, ϵ_{45} extended over the surface by interpolation, the evaluation of γ_{xy} smooths possible errors.
So, once ϵ_x, ϵ_y, ϵ_{45} are available in the whole domain (x, y), γ_{xy} field is calculated as:

$$\gamma_{xy} = \frac{\epsilon_{45} - cos(45°)^2\epsilon_x - sin(45°)^2\epsilon_y}{sin(45°)cos(45°)} \tag{3.10}$$

Displacement field w can be evaluated integrating in space:

$$\gamma_{xy} = -2z\frac{\partial^2 w}{\partial x \partial y} \tag{3.11}$$

where z is half of the plate thickness.
Integration is performed numerically. A centred-difference numerical scheme is adopted. An uniform spacing calculation grid is generated: subscript i is referred to x direction, subscript j is referred to y direction. This method implies the following derivative discretization:

$$\begin{aligned}
\frac{\partial^2 w}{\partial x \partial y}|_{x_i,y_j} &= \frac{\partial}{\partial x}\frac{\partial w}{\partial y}|_{x_i,y_j} \\
&\approx \frac{\partial}{\partial x}(\frac{w_{i,j+1} - w_{i,j-1}}{y_{j+1} - y_{j-1}})|_{x_i} \\
&\approx \frac{w_{i+1,j+1} - w_{i-1,j+1}}{(x_{i+1} - x_{i-1})(y_{j+1} - y_{j-1})} - \frac{w_{i+1,j-1} - w_{i-1,j-1}}{(x_{i+1} - x_{i-1})(y_{j+1} - y_{j-1})} \\
&\approx \frac{w_{i+1,j+1} - w_{i-1,j+1} - w_{i+1,j-1} + w_{i-1,j-1}}{4\Delta x \Delta y} = -\frac{\gamma_{xy}(x_i, y_j)}{2z}
\end{aligned} \tag{3.12}$$

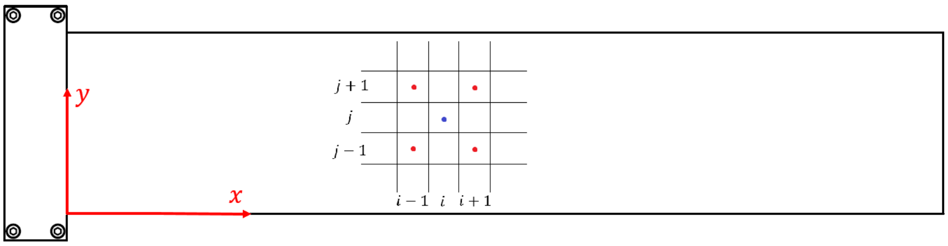

Figure 3.10: Numerical integration stencil for γ_{xy}

The integration process requires for Boundary Conditions (BCs). While BCs along y direction in $x = 0$ are easily imposable due to clamp, so $w(x_1, y_j) = 0$ and $w(x_2, y_j) = 0$ $\forall j$, it is more difficult to impose the BCs along x direction in $y = 0$ (or $y = W$), where conditions of null moment about x and null shear force must be respected. In order to *generate* the required BCs along this direction, a first preliminary integration which takes into account just the available informations about ϵ_x to extract w, is carried out. In this way a sort of *initialisation* of the displacement field is performed.

It must be stated that the effectiveness of this procedure is strictly related to the optimisation process. Being this integration procedure taken into account directly into the optimal sensor placement algorithm, it comes that the *optimal* fiber arrangement generated will be implicitly able to provide the best compromise in term of informations to perform both the integrations, so that the final result (i.e. the shape reconstruction) is achieved in the most precise way.

Thus, the numerical discretization scheme for $\epsilon_x = -z\frac{\partial^2 w}{\partial^2 x}$ is:

$$\frac{\partial^2 w}{\partial^2 x}|_{x_i, y_j} \approx \frac{w_{i+1,j} - 2w_{i,j} + w_{i-1,j}}{\Delta x^2} = -\frac{\epsilon_x(x_i, y_j)}{z} \tag{3.13}$$

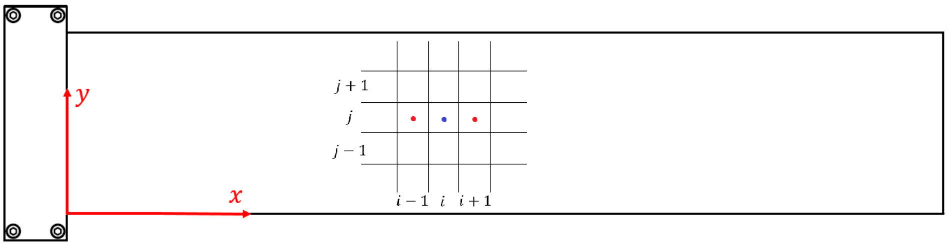

Figure 3.11: Numerical integration stencil for ϵ_x

The required BCs for ϵ_x integration are known.
In the truth, it is useless an integration of ϵ_x on the whole spatial domain, because this procedure is required just to provide a substitute of the missing BCs along x dimension. Being the complete strain field ϵ_x produced by data interpolation, at this specific step it has been decided to calculate w just around $y = \frac{W}{2}$, instead of $y = 0$ or $y = W$, to avoid meaningless w values caused by ϵ_x singularities on boundaries (W is plate width). Because of this choice, γ_{xy} integration with respect to the y-variable will start from the *middle-band* of the plate.

This particular procedure exploits the optimisation process of which it will be part, to implicitly respect the physical BCs. Being the main fiber-arrangement quality-index a comparison among the reconstructed mode-shape and the *ideal* one (i.e. the one generated by FE software), it comes that the fiber configuration that will be chosen will be able to provide the set of strain informations that, processed together, permit a displacement field reconstruction coherent with the *exact* one. It means that physical BCs has been respected.

Once $w(x_i, y_i)$ is known $\forall x_i, y_j$ thanks to the proposed method, it is interpolated on the surface to reconstruct $w = w(x, y)$. No u or v field are computed, because in this context it is assumed to consider just the mid-plane deflection, in which they are null.

So, summarizing:

- Available strain data are: ϵ_x, ϵ_y, ϵ_{45} in some distinct location on plate surface;
- Strain data are interpolated on surface in order to generate three continuous strain fields: $\epsilon_x = \epsilon_x(x, y)$, $\epsilon_y = \epsilon_y(x, y)$, $\epsilon_{45} = \epsilon_{45}(x, y)$;
- $\gamma_{xy} = \gamma_{xy}(x, y)$ is computed;
- Plate surface is gridded by uniform integration mesh of $n \times m$ calculus nodes: $i = 1, ..., n$ and $j = 1, ..., m$. BCs are known in $i = 1$ and $i = 2$: $w(x_1, y_j) = 0$ and $w(x_2, y_j) = 0 \ \forall j$;
- w is calculated by ϵ_x integration just in the *central-band*, advancing along x. Elaborating Equation 3.13 are obtained: $w_{i,\frac{m}{2}}$, $w_{i,\frac{m}{2}-1}$, $w_{i,\frac{m}{2}+1}$ $\forall i$;
- w is calculated by γ_{xy} integration, advancing along x, from $i = 2$ to $i = n - 1$. Per each i step, integration starts in the middle of the plate

and proceeds along y on *left* and *right* sides. Elaborating Equation 3.12 as needed is obtained:

- The $w_{i+1,j-1}$ value, for $j = \frac{m}{2} - 1, \frac{m}{2} - 2, ..., 2$;
- The $w_{i+1,j+1}$ value, for $j = \frac{m}{2} + 1, \frac{m}{2} + 2, ..., m - 1$;

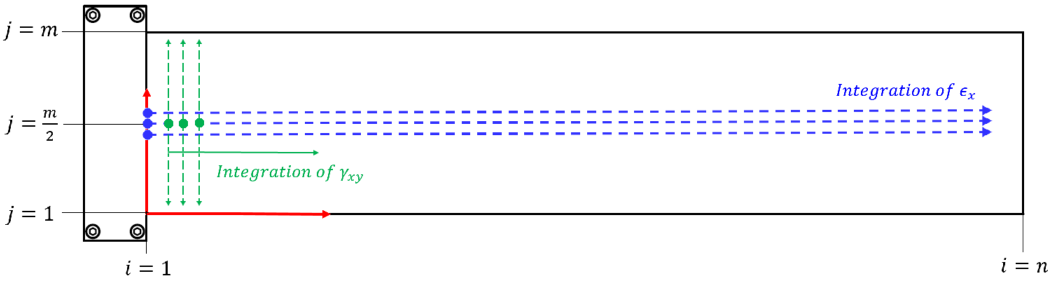

Figure 3.12: Numerical integration procedure

- w is known $\forall x_i, y_j$: w is interpolated to reconstruct $w = w(x, y)$;

Figure 3.13 is an example of the integration input and output.

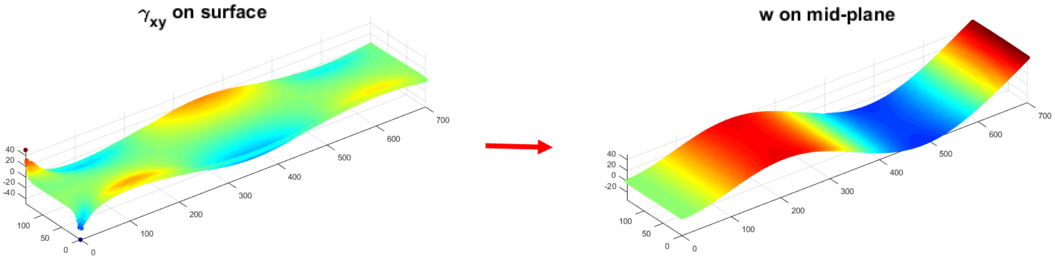

Figure 3.13: w displacement computed from γ_{xy} - 4^{th} mode

Just to remark what previously said about the choice of the *integration strategy*, an example is shown here below. Both the configurations are the result of the implemented OSP algorithm (explained in the following section) when used to *place* strain-gauges or FBG-fibers instead of OBR ones. In both the cases, all the parameters were the same (number of sensors, constrains and termination conditions) except for gauges orientation and strain fields integration. In the first case, sensors can be placed by the algorithm just along x direction and they can measure anything else than ϵ_x. In the second case, even ϵ_y and ϵ_{45} are monitored, to reconstruct γ_{xy}.

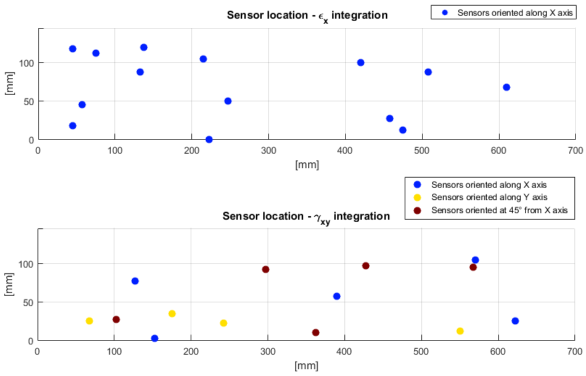

Figure 3.14: Difference among integration strategies: ϵ_x vs γ_{x_y}

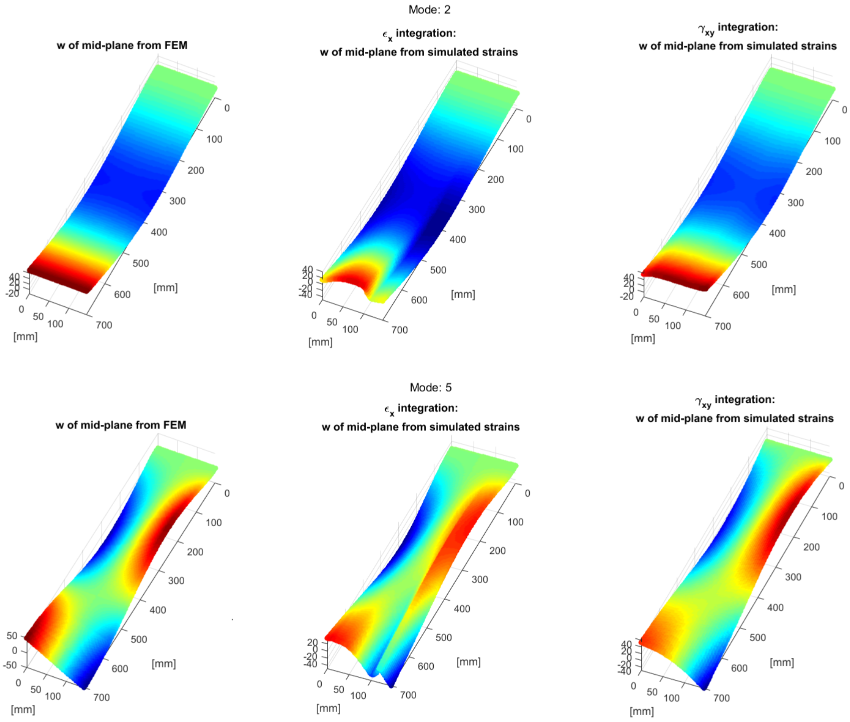

Figure 3.15: Difference among integration strategies: ϵ_x vs γ_{x_y}

In the first case, the integration accounts for ϵ_x only. It proceeds along x without *considering* any information coming from the other directions. This produce an irregular displacement fields and can give sensed results only if the plate geometry has a predominant dimension (in this case, length $\approx$ 5 width).

3.6 Genetic Algorithm implementation

Some theoretical considerations about GA can be found in subsection 2.4.6. Here below will be treated under the practical point of view how the GA has been implemented.

Due to the conceptual similarity, two different algorithms have been developed, each one referred to a different measurement system. In this case-study, an OBR strain fiber sensor has been employed. However, an *FBG strain fiber-sensor* and a *resistive strain-gauges* optimal sensor placement algorithms are made available.
Some considerable differences that arises in this scenario have to be highlighted:

- FBG optical-fibers allows to locate a reduced amount of strain sensors. However, allows to place them without *geometrical* constraints: just the sensitive parts have to be fixed. GA locates fiber-gauges as they were each other physically independent.

- OBR optical-fiber contains a very large amount of embedded gauges: to exploit the maximum amount of informations, the most of the fiber must be fixed on the component surface. This advantage is followed by huge complications. GA must place the fiber considering to deal with a *continuous* device and its physical constraints.

The fiber-sensor *continuity* is a tricky constraint to be dealt with. No kind of suggestion has been found in literature concerning how to manage such a particular aspect, especially when it has to be handled with a genetic algorithm. As a consequence, some innovative procedures have been implemented according to this fact.
To discuss about GA implementation, after a brief introduction, will be followed a step-by-step approach.

3.6.1 Introduction

As already stated, in the case of OBR optical-fiber it is necessary to optimize the arrangement of the whole fiber (i.e. where it passes and its orientation), not only of a small amount of its sections. The amount of DoFs of the problem (in terms of possible different configurations) is extremely wide. Furthermore, it is necessary that the optimal sensor placement algorithm provides an optimal output configuration which complies the strict geometrical constraints (i.e.: *continuity*, *length*, *curvature radius*, etc...) that are required to guarantee the possibility to fix the fiber in the real experimentation and obtain high-quality interrogator outputs.

When a proposed fiber configuration does not match even just one of the imposed constraints, configuration fitness is set to zero. If the configuration is geometrically consistent, depending on the strain data it can provide it is computed its fitness value.

It is necessary to develop a *fiber-placement algorithm* that works *inside* the GA, and *tracks* a potentially valid path for the fiber starting from a reduced number of encoded DVs. This approach permits to produce *valid* sensor arrangements at each generation, depending on a fixed logic. As a matter of fact, too many constraints exist to allow the survival of whichever valid configuration after a crossover if the whole fiber-path is encoded. For these reasons, the genetic coding and crossover procedure will *not* involve the whole fiber arrangement, but just a set of *outstanding* positions. These points, which represent the genes of each individual and build the chromosome, will be *connected* in a taught deterministic manner, providing when processed by the fiber-placement algorithm the complete configuration.
The individual fitness is computed accounting for the informations available by the complete configuration, instead.

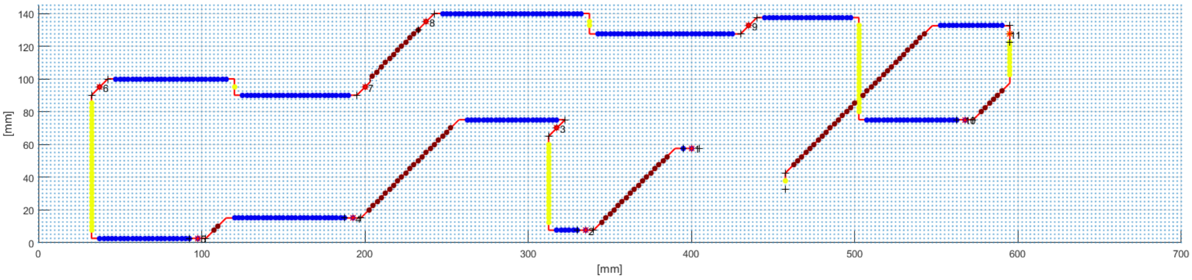

Figure 3.16: Example of fiber configuration

Being the connection strategy deterministically dependent on the relative position and orientation of the *outstanding* locations, the *genetic heritability* of fiber arrangement is guaranteed among generations.

In the case of an FBG optical-fiber sensor or a resistive strain-gauges instrumentation, the same algorithm can be applied, except for the absence of the fiber-placement algorithm. The previously called *outstanding locations* represent directly the locations to be monitored.

3.6.2 Chromosome structure, choice of parameters and first population start-up

Each individual of the population is characterized by a set of particular values of design variables DVs. The value of each DV will be encoded into a *gene*. The assembly of all the *genes* constructs the *chromosome*. In this specific case the DVs consist in a number of *outstanding locations* and their *orientations*.

As explained, the optimal sensor placement algorithm needs for FE-based data to run. Half of the chromosome represents *positions*, half *orientations*. The position is represented by the index of the mesh-node which falls in that spot, the orientation by a scalar value whose meaning is defined a-priori. The DVs of each individual will be collected in the *population matrix*.

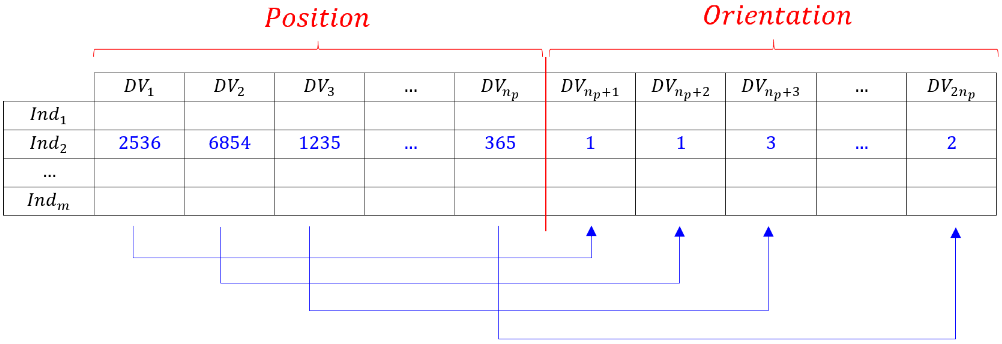

	DV_1	DV_2	DV_3	...	DV_{n_p}	DV_{n_p+1}	DV_{n_p+2}	DV_{n_p+3}	...	DV_{2n_p}
Ind_1										
Ind_2	2536	6854	1235	...	365	1	1	3	...	2
...										
Ind_m										

Figure 3.17: Individual structure - Population matrix

A number of considerations have been carried out to determine the best parameter compromise to run the GA. Here below are stated just the final values. To properly work, the GA requires for:

- The number of outsanding locations n_p (or the number of gauges available in the case an FBG optical-fiber or a resistive strain-gauges instrumentation is used). This will build $2n_p$-genes individuals. n_p has been set to 14: this permits to withstand the fiber length constraint. As a matter of fact, a larger value does not allow to successfully run the previously called fiber-placement routine.

- The number m of individuals. The parameter is set to 100, a good compromise among calculation time and genetic variability;

- The number of bits for coding. The parameter is set to 15, the minimum to encode univocally all the possible values of DVs;

- The probability of mutation, set to 0.4%. Because the mutation introduces a random *modification* of the chromosome, a small value can introduce *positive* variations, while a larger value can totally *destroy* the chromosome structure generating a random sequence of bits;

To well *initialize* the GA, additional specific informations are required about the employed sensor itself and the optimisation target.
Among the other sensor-dependent parameters, it must be set the *maximum* fiber length that the algoritmh can *place* above the surface and the curvature radius to be respected at bends. These constraints depend both on the physical limits of the optical-fiber, both, as it will be clearer later, on the need to obtain high-quality interrogator outputs.
Last but not least it is obviously necessary to chose the target-modes of optimisation, that must be determined within a *valid* frequency bandwidth. As a matter of facts, the main criticism to be remarked stays in the nature of the acquisition system. Interrogator output reliability is not guaranteed by manufacturer when LUNA is employed in dynamic environments. LUNA ODiSI-B V.4 hardware and software are developed to monitor static or quasi-static phenomena. For that, strong issues must be faced concerning the signal quality, especially at high forcing frequencies. Modes above $200Hz$ will be for that not considered into optimisation because not measurable.
Besides acquisition system limitations, some thought has to be carried out about the sensor itself. The OBR optical-fibers are slightly modified commercial-grade fibers. As known (see chapter 2) they are assimilable to *light-ducts*.

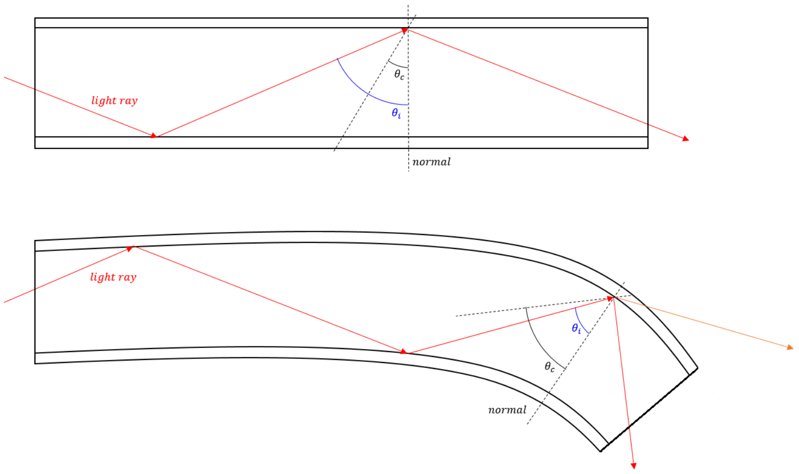

Figure 3.18: Signal loss due to fiber bending

The electromagnetic radiation flows inside fiber core thanks to the continuous reflection produced by reflection-index shift in correspondence of the core-cladding interface. Light is totally reflected inside the core if the *incidence* angle θ_i of light ray is higher than the *critical* angle θ_c (value given by the coupling of glass core and polymeric cladding). Incidence angle and critical angle are values relative to surface normal. If locally, due to micro or macro-bending or surface irregularities even in terms of refraction index, the light approaches the interface with a *wrong* inclination, total reflection does not occur and signal strength attenuates. Generally, it is suggested to keep a minimum bending radius higher than fifteen times the fiber diameter. With a $10mm$ bending radius, exploiting a fiber-fault locator, can be clearly seen the laser light loss. It tends to disappear above $25mm$ curvature radius. However, such a large bend does not allow a good fiber arrangement. The little signal lost caused by bends of $10mm$ radius is accepted.
Figure 3.19 shows the *signal amplitude* as function of fiber-length, as *seen* by the interrogator. The back-ground case has a curvature radius of $\sim 5mm$, the front one has a curvature radius of $10mm$ instead. The yellow and the red lines determines the fiber *sensing-length*.
The main consequence to this signal attenuation is the progressive unreliability of the transducer output. It can be noticed that the *qualty* of each single time-step concerning the last part of the fiber tends to be really worse than initial section. These concepts will be deeply investigated in section 5.3.
As a consequence, even if the theoretical length of exploitable fiber is about $1800mm$, the final optimal sensor placement algorithm will be run considering just $1500mm$.

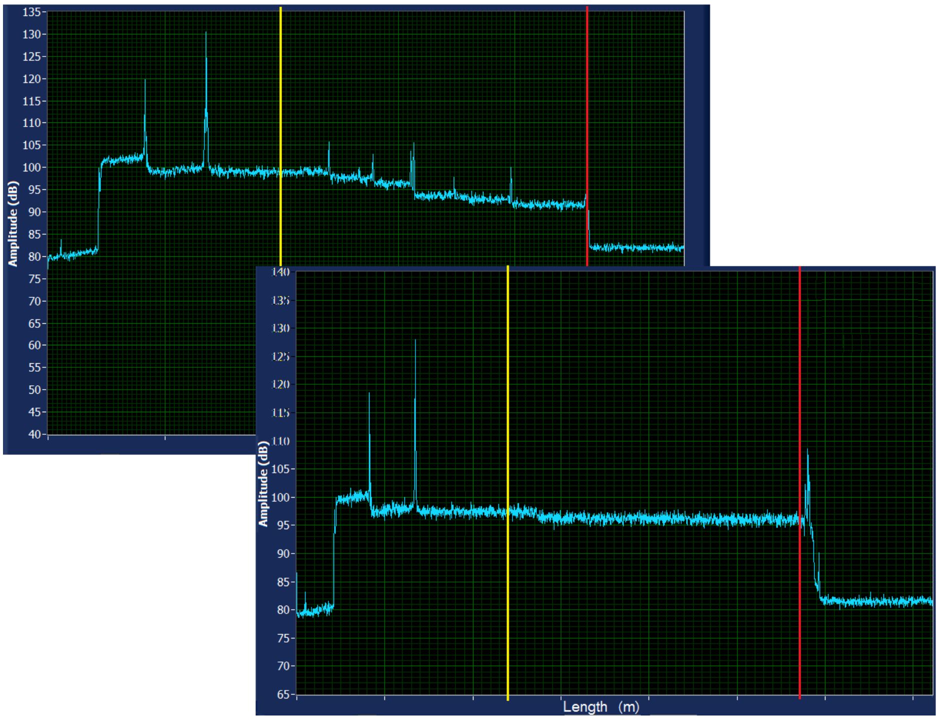

Figure 3.19: Signal amplitude comparison among different fiber curvature radius

It has also been assumed that strong strain offsets might worsen the measurement quality. The heavy strain local field that arises next to clamp reduces the reliability of the signal coming from that segment.
To prevent this occurrence, is set as constraint a minimum distance from clamp, quantified in $30mm$.

Summarizing the considerations stated above, additional informations provided to GA to run are:

- The target-modes for optimisation. The algorithm has been run to optimise fiber arrangement in order to best reconstruct the shapes of modes: 2, 3, 4, 5, 6, 7, 9. This is the real modes-ordering with respect to the ones computed by the FE-simulation. This issue is given by the FE-analysis eigenfrequencies calculation error, evidenced by a fast experimental check performed on a preliminary case-study plate thanks to the use of accelerometers;

- The maximum fiber length that can be effectively arranged, set to $1500mm$, and the minimum curvature radius, set to $10mm$;

- The minimum relative distance among each outstanding position is set to $10mm$ as the minimum curvature radius allowed in fiber placing. The minimum gap among each one of these location and edges is $10mm$ too. Among them and the clamp is $30mm$ to avoid interferences with deformations given by clamp closure;

- The minimum overall number of sensors that are required along x, y and $\angle_x$ 45°, set to 3 per each direction to allow *strain-surfaces* interpolations;

The population is initialised generating a starting random population matrix.It is generated an individual at time: are randomly produced a set of locations and their respective orientations. If the generated set of DVs is consistent with constraints and when processed by the fiber placement algorithm, subsection 3.6.3, can be proposed a valid arrangement, the individual takes part to the initial population. This is done till reaching the amount m of wanted individuals.

3.6.3 Fiber Placement Algorithm

This stage is built up by two consequent steps and each population individual is processed once at time. In a first instance, the n_p outstanding locations are reordered in a thought manner, so that they can be consequentially connected. Then, depending on their relative position, each outstanding location is physically connected to the next, in such a manner that the fiber passes on the surface just moving in the three direction of interest (along x, y and $\angle_x$ 45°), avoiding complex and intersecting or meaningless routes. Only at the end of this procedure the measurement process can be *simulated*, the strain data re-elaborated and the fitness computed.

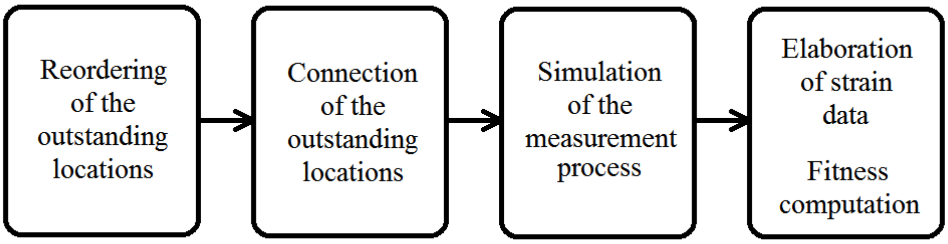

Figure 3.20: Logic of fiber placement algorithm

A main point is that this step is *deterministic*. A set of subsequent locations, if have the same position and the same orientation, will be always connected in the same manner.

The *ordering-process* must be necessarily driven by an external a-priori criteria. Each time it is processed a set of n_p, the algorithm divides the geometry along x and y directions in a number of *sections* depending on initial user input.This choice must be performed in order to *homogeneously* arrange the fiber on the available surface. An higher number of subdivisions along a direction can make this direction predominant with respect to the other, influencing the results. This subdivision could be even managed directly by the GA, but due to computational time limits it has been not implemented.

A number of different *ordering strategies* are then produced per each individual according to the geometry subdivision. This imply that different orderings can provide different sequences and, at the end, very different fiber configurations.
Here below a clarifying example:

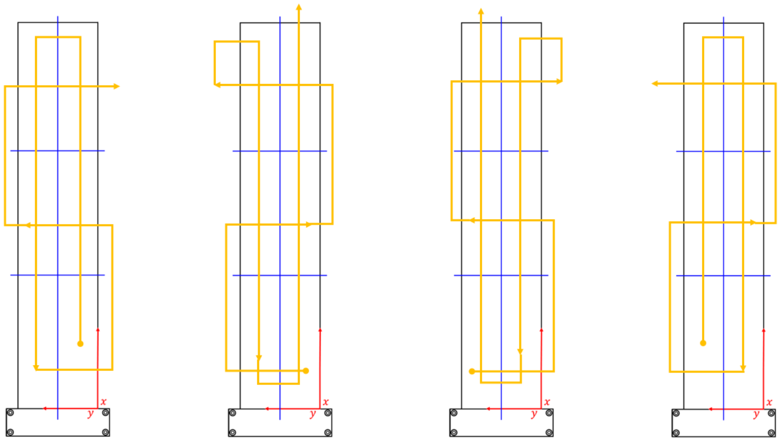

Figure 3.21: Ordering logic - example of four produced sequences

Such an high number of different orderings is required even because the ordering procedure itself can exclude one or more outstanding location whenever it cannot be connected with the other, owing to the contrast with an ordering constraint. These constraints depend on the imposed minimum curvature radius and a large set of further physical limitations concerning fiber nature. Outstanding locations reordering is performed aiming to not favour output fiber-arrangements that can collide with practical constraints. Furthermore, during this step has been taken into account many other expedients capable to propose the most convenient ordering (in terms of connection logic, so path-smoothness, fiber length, etc...) in prospect of the following point-connection step.

The *point-connection* algorithm processes whichever set of previously generated set of ordered positions. It takes into account their orientation and connects iteratively each spot with the next one. It aims not only to dispose the connecting fiber along the three meaningful directions, but also try to exploit the most thought path, in terms of number of bends and curvature angles. Per each couple of points to be connected, it determines the best way to *pass through* them. This is done generating a number of different paths and at last depending on the features of each one of them, it chooses which is the best to be used. The procedure will be clarified by the image just below, fig. 3.22.

First of all are determined the *anchor-points* $(1, 2, 3, 4)$, that states how the fiber must cross the two locations n_{p_1} and n_{p_2}. Anchor-points are required both for this step, both to smooth an eventual fiber curvature radius next to the outstanding positions. Fiber will connect always anchor-point 2 and 3. Then three configurations are built: the best one will reduce the number of curves and minimize the curvature angles.

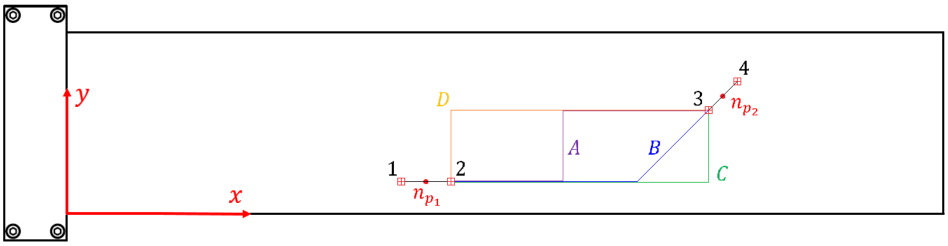

Figure 3.22: Point-connection logic

It is evident that, among the four candidate connections, the most suitable one is *B*.

The output of the whole procedure is a set of positions and directions. They represent the zones covered by the fiber. The strain values that will be considered as available data to rank the actual configuration are the ones that correspond to the whole amount of highlighted locations (Figure 3.23). The fiber-gauges in correspondence of configuration angles are excluded from that set of positions, depending on the minimum radius defined as input. This to be as much coherent as possible with the data that would be available in real experimentation if the configuration is chosen as the definitive one.

With a $10mm$ curvature radius imposed at bends, such a configuration can be obtained. Filled points corresponds to the locations whose strain value is considered for mode shape reconstruction. Colour represent the direction of measurement.

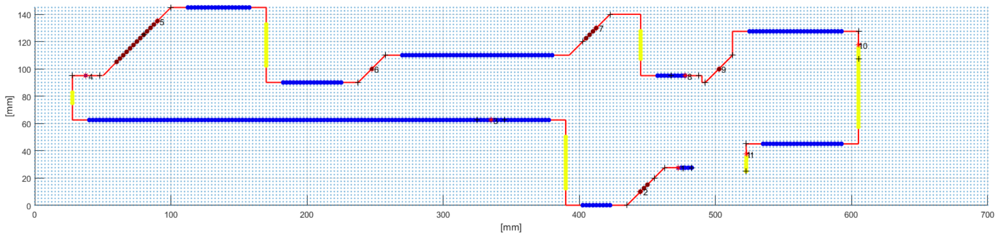

Figure 3.23: Example of fiber configuration

As stated, per any individual of the population are generated many different outstanding-positions orderings. Consequently, per each individual are built a number of different complete fiber-arrangements. To determine the best configuration among them, it must be computed the value of the fitness function, the index of *quality* of the fiber placement. It depends on the data that each configuration can *provide*. At this step, the set of informations that the proposed arrangement can provide according to its path comes directly form the strains of CMA: practically, here is simulated the measurement process.

Just the best configuration is now considered. It means that the individual DVs are physically reordered according to its ordering. This is to favour the following crossover step. Practically, the line of the population-matrix corresponding to the individual under exam is rewritten so that the outstanding locations (and the respective orientations) are placed in the right order. Then the value of the fitness is assigned to the individual, to allow the comparison among the whole population and chose the items to crossover in the next steps.

This procedure must be performed for all the individuals before proceeding to coding, crossover, etc... .

3.6.4 Cost function definition and configuration robustness

Any fiber arrangement produced can be considered acceptable or not.

If the generated configuration exceeds the maximum length, or contains an overall number of strain information that does not suffice to interpolate the strain field (i.e. less than three strain values per each direction), the configuration is not acceptable. It means that its fitness value is not really computed but is set a-priori next to zero.

If the configuration is considered to be valid, it must be ranked by the computation of a fitness function. Making reference to section 2.4, the cost function has been composed aiming to maximize the accuracy of the reconstructed mode shape, employing different quality indexes and weighting the signal quality loss caused by the bending of the fiber.

The final cost function aims to guide the the optimization-code to generate the fiber configuration able to:

- Increase the quality of modal shape reconstruction for the selected modes;
- Provide suitable and unequivocal modal parameters;
- Compensate the measurement system issues detected and, as a consequence, improve the signal quality of the experimental acquisition;
- Guarantee the robustness of the output with respect to the uncertainties of FE model;
- Guarantee the robustness of the output with respect to the acquisition system faults;
- Compensate and reduce the errors introduced by the strain-to-displacement procedure: the modal-shape reconstruction is based on the post-processing of strain acquired data. The mathematical sequence of interpolations and integrations introduce inevitably errors, the OSP algorithm has to consider this occurrence and minimize it. It is fundamental understand that:
  1. Given a certain StD procedure, a different fiber arrangement give different modal shape reconstructions;
  2. The same fiber positioning, with different *strain to displacement* procedure, will give different modal shape reconstructions.

If the optimal sensor placement code satisfies all these requirements, the final result will be an experimentally well-reconstructed series of modal shapes, with an high spatial discretization and a low dependence on the FE model used. In its complete formulation, the *fitness function* is:

$$Fitness = \left\{ MSE_{weighted} \left[1 + \left(1 - \frac{\det FIM_{fiber}}{\det FIM_{global}} \right) + \right. \right.$$
$$\left. \left. + AutoMAC_{criticity\ coefficient} + \left(1 - \frac{bends_{min}}{bends_{fiber}} \right) \right] \right\}^{-1} \tag{3.14}$$

where:

- $MSE_{weighted} = \sum(MSE_{mode_i} \cdot weight_{mode_i})$, where i represents the indexes of the modes on which the optimisation is running, and MSE is the Mean Squared Error among the i-mode mid-plane w displacement, generated by the FE-analysis, and the reconstructed w shape evaluated by the strain-to-displacement transformation, starting from the *simulated* strain data.
  To basically recall the general formula of MSE:

  $$MSE_{mode_i} = \frac{1}{\tilde{N}} \sum_{k=1}^{\tilde{N}} (\hat{\phi}_{k,i} - \phi_{k,i})^2 \tag{3.15}$$

  where $\hat{\phi}$ is the *exact* eigenvector, ϕ is the reconstructed one from the available data and $\tilde{N}$ is the overall amount of DoFs accounted in the numerical calculation. As previously described, in the plate modal-analysis the mode shapes are identified by the mid-plane w displacement, so the MSE definition, for the single i-mode, becomes:

  $$MSE_{mode_i} = \frac{1}{N} \sum_{k=1}^{N} (\hat{w}_{k,i} - w_{k,i})^2 \tag{3.16}$$

  where $\hat{w}$ is the *exact* modal i-shape given by the complete FE-analysis, while w is the result of the reconstruction performed from *simulated* strain-data considering just the informations contained in the m monitored DoFs. N are the DoFs of interest lying on mid-plane. The *weight* is an user-defined numerical coefficient. The MSE is the fundamental keystone of the constructed cost function: in the measure simulation-code it evaluates, for each set of m sensor considered, the capability to describe with high quality definition the modes of the structure. It

is the fundamental part of the fitness because able to *evaluate* all the mathematical passages present in the experimental post-processing: if the fiber-sensor optimal placement algorithm is guided by MSE, surely the fiber configuration is chosen since it gives the *right* informations with respect to the interpolation and integration processes faced in the StD transformations. MSE parameter is a global index of the quality of the final mode shapes reconstruction: it practically resumes and judges *all* the processes, from the measurement to the final mode shape description.
Nevertheless, the limitations in considering just the MSE as quality-parameter are the following:

- Inability to define *a-priori* the more *interesting* locations where to embed the fiber. In this sense the use of MSE as unique fitness parameter would give a final result strictly dependant on the interpolation functions and *strain-to-displacement* method chosen;
- Complete inadequacy to take into account LUNA acquisition system limits and to compensate the dependence of the optimization algorithm from the FE-model;
- Inability to guarantee a desirable and satisfactory value of MSE_i for each single mode, it gives a *mean* estimate of the general quality over the all modes;
- Inability to highlight whenever the reconstructed shapes of two modes risk to be *confounded* each-other

So to obtain a reliable and optimal result it is necessary to add to the MSE other criteria and parameters to guide the optimization.

- $\left(1 - \frac{\det FIM_{fiber}}{\det FIM_{global}}\right)$: this part of the fitness-function presses the optimisation code to place the fiber-gauges in those locations which contains, *a-priori*, the *most meaningful* strain informations. The code will search the configuration with the $detFIM_{fiber}$ closest to the $detFIM_{global}$ (section 2.4). This last term somehow represents the maximum global amount of *informations* regarding the strain modal-shapes. When dealing with a strain-sensors optimal placement problem, the formula of the FIM concerning the modal-approach is:

$$Q = FIM = [\psi^T \psi] \tag{3.17}$$

where ψ is the strain modal-matrix.
The $\det(FIM_{fiber})$ is computed considering just the DoFs accounted by

the specific fiber configuration, while $\det(FIM_{global})$ is computed once and includes all the strain-DoFs of the system. It is required just to have a *reference* value.

The use of a FIM-related parameter adds to the cost-function a *contribution* that depends on the *pure* informations potentiality *included* inside each monitored position.

The importance of the FIM approach has a deep mathematical meaning. To understand the procedure, all the rigorous steps are explained in section 2.4.

Actually, the meaning of the proposed FIM method can be clarified by some logical steps. A well known property of the modal-matrix is the following:

$$\psi^T_{\tilde{m}\times n}\,\psi_{\tilde{m}\times n} = I \tag{3.18}$$

As a consequence:

$$\det\left(\psi^T_{\tilde{m}\times n}\,\psi_{\tilde{m}\times n}\right) = 1 \tag{3.19}$$

where $\tilde{m}$ is the number of all the strain-DoFs in the complete three-dimensional FE-model. It has to be noticed that the term $\hat{m}$ will be considered as the *global* number of strain-DoFs that can be potentially measured (for instance, the ones that lies on the surface of the structure). The FIM index in the cost function has the aim to identify the best m DoFs in terms of strains, out of the set of $\hat{m}$ to be monitored, in order to obtain the *most meaningful* informations to reconstruct the entire modal-shape of the structure.

As a matter of fact, to search these m locations is equivalent to delve the set of m DoFs which guarantees that:

$$\psi_{m\times n} \cong \psi_{\tilde{m}\times n} \tag{3.20}$$

The optimum $\psi_{m\times n}$ has ideally to include the most of the *informations* proper of $\psi_{\tilde{m}\times n}$. Practically, to guarantee the Equation 3.20 an efficient method is to find a set of m DoFs capable to equal the determinants of the two matrices $\psi_{m\times n}$ and $\psi_{\tilde{m}\times n}$ or a re-elaboration of them.

To proceed, it is more suitable to make reference to Equation 3.19. Therefore, to make $\psi_{m\times n}$ *as more equal as possible* to $\psi_{\tilde{m}\times n}$, according to Equation 3.19 and Equation 3.20 it must be found the conditions that assure:

$$\det\left(\psi^T_{m\times n}\,\psi_{m\times n}\right) \cong 1 \tag{3.21}$$

Practically, this means to maximize $\det(\psi^T_{m\times n}\;\psi_{m\times n})$. The matrix $[\psi^T_{m\times n}\;\psi_{m\times n}]$ is, in this scenario, the FIM that characterise a specific fiber configuration in a sensor-placement problem concerning modal

analysis.
In this way it is evident the deep meaning in using the maximization of the $\det(FIM_{fiber})$ as a parameter to guide the sensor-positioning optimization. In the case of an optical-fiber, the m locations are the strain-DoFs *covered* by the fiber-gauges.
To resume, the value of $\det(FIM_{fiber})$ permits to quantify the amount of *useful informations* regarding the *whole* modal-shape, *included* inside the m measured strains along the fiber.
The effective-independence method is intrinsically and totally independent from the measurement simulation step and so from interpolations and the strain-to-displacement procedure. It can be a useful complementary index to be accounted together with the MSE. The FIM computation is determined just through the FE-simulation data: the $FIM_{fiber_{m\times m}}$ is computed with the strain-eigenvectors given by the FE-model, considering just the m strain-DoFs in correspondence of the fiber path.
In conclusion, while the $MSE_{weighted}$ parameter evaluates the *final result* just in terms of displacement mode-shapes reconstruction and accounting also for interpolations and integrations, the $\left(1-\frac{\det FIM_{fiber}}{\det FIM_{global}}\right)$ index gives a quantitative estimation about the importance just in terms of *strain-information contribution* that a specific candidate fiber arrangement can provide.

- $autoMAC_{criticity\ coefficient}$: the autoMAC matrix is generally computed in modal analysis before proceeding in measurements. It provides interesting and useful indexes concerning the sensor positioning. Its evaluation is completely based on FE model data. As stated, the main purpose in including autoMAC informations inside the cost function is to maximize the capability to distinguish among different acquired modal shapes and avoid misunderstandings in the modes definition. autoMAC can be used to find whether a certain measurement point is effective or produce spatial aliasing calculation: for each fiber configuration, the autoMAC calculation is capable to evidence the reliability of results of an eventual EMA implemented with that fiber configuration. Practically the autoMAC verifies if the modal shapes reconstructed according to the locations considered are easy to be distinguished. Concretely the autoMAC computation entails the determination of a matrix, if the targeted modes are n the dimensions of the autoMAC matrix is $n \times n$:

$$autoMAC_{i,j} = \frac{|\phi_i^T\ \phi_j|^2}{(\phi_i^T\ \phi_j)^T \cdot (\phi_i^T\ \phi_j)} \tag{3.22}$$

where ϕ_i and ϕ_j are the eigenvectors composed by just the monitored DoFs and each term $autoMAC_{i,j}$ represents the cross-correlation between the i-mode and the j-mode: if this correlation is considerably high, the couple of modes has a serious possibility to be confused in the experimental analysis. This is not so critical if the two modes, with an higher possibility to be not discerned, are sufficiently *distant* in the frequency domain. The real dangerous case is when the *autoMAC* between the i-mode and the j-mode can not be approximated to zero and the i-mode and the j-mode are two consequential modes in frequency domain: this means that there is the concrete possibility to confuse this two modes during the experimental post-processing. In addition to this, the higher is the uncertainty of the FE model, the higher is the possibility of *shifts* and errors in the FE model resonances calculation. As a consequence higher is the importance of the autoMAC computation. To conclude, a satisfactory configuration is the configuration with an autoMAC matrix as similar as possible to an *identity matrix* I, with zero off-diagonal terms.

In the OSP algorithm implemented, the autoMAC information is used to search and evidence *critical situations*. The conditions shown below have been classified as hazardous. For each of those a specific provision is taken and the proper fitness modification is imposed. The fitness penalty introduced in the cost function calculation is represented by the $autoMAC_{criticity\ coefficient}$ in the general formula of the fitness. Whenever a couple of modes has an $autoMAC_{i,j}$ value higher than 0.35, there is a *criticism*. These criticisms occur when it exists, at least:

- A couple of modes i and j (with neighbouring frequencies) with an $autoMAC_{i,j}$ value higher than 0.5 is considered as a *strongly* critical case. For that the $autoMAC_{criticity\ coefficient}$ penalty is fixed to 1.0.
- A group of three modes (with neighbouring frequencies), with an $autoMAC_{i,j}$ value lower than 0.5 is considered as a *rather* critical case, so the $autoMAC_{i,j}$ penalty is fixed to 0.5.
- A group of more than three modes (with neighbour frequencies), with an $autoMAC_{i,j}$ value lower than 0.5 is considered as a *quite strongly* critical case, so the $autoMAC_{i,j}$ penalty is fixed to 0.7.
- A couple of modes i and j (with neighbouring frequencies) with an $autoMAC_{i,j}$ value higher than 0.35 is considered as a *rather* critical case. This risky situation is evaluated as critical but acceptable, so the $autoMAC_{criticity\ coefficient}$ penalty is fixed to 0.3.

If more than one critical condition exists, $autoMAC_{criticity\ coefficient}$ assumes the maximum value among them. If no such conditions occur, $autoMAC_{criticity\ coefficient}$ is set to zero.
The term *neighbour frequencies* means that, for each fiber configuration, to verify the presence of the previous critical situations the autoMAC matrix is analysed considering its first and second sub-diagonal.
Apparently the use of autoMAC can be judged as redundant with respect to the MSE calculation: if the mode shapes are well-reconstructed with a low MSE, it seems to be guaranteed that the autoMAC matrix is sufficiently equal to an identity matrix. Actually the autoMAC is implemented in the cost function definition to search particular criticism in a couple or small group of modes in the global range of frequencies selected as the targeted ones for the optimal sensor placement algorithm.

As stated previously, the main issue about $MSE_{weighted}$ is that it represents a *global* parameter able to describe the error in the reconstruction of *all* the modes, with proper weighting coefficients for each one of them. It is a sort of *average-quality* index among the resonances analysed. Practically, it can occur that the $MSE_{weighted}$ guides the optimization to a fiber solution with an high *average-quality* index but not all the modes have the same *reconstruction quality.* For that, it is possible that a couple of modes i and j have both *high* MSE_i and MSE_j values, similar frequencies and an high $autoMAC_{i,j}$ value. This means that there is the risk to *confuse* the modes in this critical set. It can occur that the real mode shape representation for that mode is not unequivocal.

Furthermore, a *low* MSE_i value does not always assure a right shape reconstruction. MSE value can be misrepresented by a very good shape reconstruction in some particular zones, hiding strong errors elsewhere. Usually, in plates, flap-wise and torsional modes are alternated: if a flap-wise mode is not well-described along the width, it is possible to confuse its acquisition with the neighbouring torsional mode.

The level of criticism of such cases must be not underestimated due to their deceptive and misleading nature: this is the reason why to introduce in the cost function the $autoMAC_{criticity\ coefficient}$ parameter.

- $\left(1-\frac{bends_{min}}{bends_{fiber}}\right)$ is the parameter that accounts for the progressive signal worsening caused by the non linear fiber path. This phenomenon is probably caused by a worst light reflection inside the fiber core when the fiber bends. The term $bends_{min}$ represents the theoretical minimum number of bends that the fiber should undergo depending on the geometry partitioning explained in 3.6.3 and Figure 3.21. The term $bends_{fiber}$ is the current number of bends.

Till now, fiber optimal arrangement has been computed processing strain data generated by FE-based modal analysis. These data have been assumed as completely reliable and valid to simulate a real measurement output. At this step, a further parameter that should be taken into account in the determination of the quality of a proposed fiber arrangement is an index that accounts for its *robustness*. In this context, the term *robustness* means that the candidate configuration (computed thanks to artificial data) have to be optimal even in a real situation: the shape reconstruction must be acceptable even if measured strain values differ from the expected one. A good configuration must prevent that discrepancies among the informations exploited in the optimal sensor placement algorithm and the concrete measurement could worsen the shape reconstruction. These discrepancies arise due to computer finite algebra, approximated physics, FE-model uncertainties, approximations and signal quality issues.

Given the computational weight in considering such *robustness-check* during each fitness computation, it has been tough to perform some considerations a-posteriori, comparing each-other a number of final candidate configurations. Two different sources of error are taken into account.

The first is correlated to the artificial nature of data employed in optimal sensor placement algorithm, so strain informations generated by FE-software can be somehow different from reality. For that, the optimisation itself is intrinsically carried on with potentially *wrong* data.
Strain data used to choose the optimal fiber configuration are different from real strains available in post-processing. To guarantee the solidity of the fiber arrangement with respect to computational modal analysis errors, a set of new FE cases have been created, each one characterised by particular features (i.e. localized masses on the surface) that make different the mode shapes of every model with respect to the others. Each model will be so characterised by different strain-eigenvectors. These different values simulate the occurrence of the difference between the informations that will be measured and the ones exploited during GA. What is done it is to compute the cost function value per each candidate configuration taken into account at this last step, virtually placed on each of the modified models. It is then computed the percentage variability of the fitness of any arrangement, in order to choose the fiber configuration that less affect the cost function value in case of data differences from computational modal analysis.

The second source of discrepancy among the quality of the shapes reconstruction in the *numerical case* and the experimental one depends from signal issues in real measurement: due to instrumentation criticisms, it will occur that some local strain informations measured by the acquisition system will be *meaningless*, as a matter of fact some data considered as available in the fitness computation will be neglected during the real post-processing. The optimisation is carried out with an higher availability of data. As a consequence, post-processing output could be much worse than expected.
Strain data used to choose the optimal fiber configuration are more than data available in real post processing. There are no ways to know a-priori which strain data will be unavailable, but clear trends allows to state some considerations and set up a robustness-check. It has been acknowledged that:

- Signal quality tends to worsen increasing the strain rate ($\mu\epsilon/sec$) and the excitation frequency. It means that the the quality of the data produced during the real experimentation is subject to variations, so in these circumstances it is possible that strain data belonging to one or more fiber-gauges become usefulness;

- Because of bends, as already stated, signal quality decreases. This reduction affects the quality of the strain measurement of every embedded sensor (i.e. the probability to exclude its values in post-processing increases) proportionally to its distance from fiber origin.

As a consequence the second robustness-check is performed in order to choose the candidate configuration that is more robust to data loss during acquisition, so that assure good shapes reconstruction even if are effectively available less data than expected.
Given a fiber configuration two parameters are determined.

The first concerns the overall minimum number of strain spatial informations required to avoid a decrease of the MSE value among the reconstructed shape and the reference one higher than 10%. The MSE variation is computed just for the mode shape at higher frequency in the range of interest. Starting from a situation in which are considered available all the informations (so the same condition in which the GA has worked), are progressively neglected a number of strain spatial values, chosen according to a random logic. The *removal* of usable sensor-data is concentrated in the last quarter of the fiber length. The choice to concentrate the sensor-data loss in the final part of the OF depends on the considerations carried out during the post-processing of some preliminary experimental measurements. Practically, the quality of the informations given by the sensors located in the fiber-end results to be really poor. For that, these data have usually to be discarded. This issue will be deeply investigated in the following chapters. At each *removal iteration* it is computed the MSE of the reconstructed shape: when the limit in the MSE value is achieved, it is known the minimum amount of sensors effectively required in the real post-processing to well reconstruct the highest-frequency shape (the most critical from a signal quality point of view). The best configuration among the candidates will be obviously the one with the minimum number of required sensors.

The second parameter provides an idea about the best mounting side. It determines the minimum number of strain spatial informations required just in the first and the last third of the fiber to avoid an MSE decrease above 10%. In this case the MSE variation involves all the mode shape reconstructions. As before, an increasing number of usable strain informations are randomly and progressively removed, then the MSE is computed. Because the last section of the fiber is the most critical one, it is better to exploit the mounting side that requires in the last part the lowest amount of data.

3.6.5 Coding and Decoding

The coding phase is a key-step of the GA theory. In this specific occurrence, the coding is performed by a standard binary-basis translation from decimal-basis of each individual DV. The interval of possible values that each DV can assume is discrete (composed by integer values) but without gaps.

Per each DV, the minimum and the maximum value it can assume must be stated: in this way it is performed a design variable *regularization.* This allow to well manage the coding procedure: it permits working with individuals composed by a set of DVs with different value-ranges and/or with a set of DV with a number of possible values smaller than the encodable range. Once the value has been converted into its *relative* integer value, which is meaningful inside the DV *max-min* interval, it is simply encoded by classical binary representation. A coded DV is called *gene.* The example in Table 3.2 clarifies the procedure.

Table 3.2: Coding example

-	Position index	Orientation
DV decimal value	235	3
Range (integer units)	$min : 1 \quad max : 900$	$min : 1 \quad max : 3$
Bits	10	10
Relative value (rounded) $\frac{value - min\ value}{max\ value - min\ value} \cdot (2^{bit} - 1)$	266	1023
DV binary value	$266 = 0100001010$	$1023 = 1111111111$

Table 3.3: Decoding example

-	Position index	Orientation
DV binary value	1001110111	0101100101
Relative value	$1001110111 = 631$	$0101100101 = 357$
Range (integer units)	$min : 1 \quad max : 900$	$min : 1 \quad max : 3$
Bits	10	10
DV decimal value (rounded) $\frac{relative\ value \cdot (max\ value - min\ value)}{2^{bit} - 1} + min\ value$	556	2

Once each DV of the individual is encoded, the chromosome is built up just concatenating all the *genes*. The chromosome is a $number\ of\ bits\ \cdot$

number of DVs long binary sequence. It is then performed the crossover and the eventual individual mutation.

The chromosome is now split again into genes, which needs to be decoded in decimal basis. The decoding procedure must follow exactly the logic of the coding (Table 3.3). At the end of the procedure, just valid sons values will be given back.

3.6.6 Crossover and Mutation

Once fitness and chromosomes of all the individuals of the population has been computed, the crossover occurs. Crossover *mixes* chromosome sections of individuals exploiting the favourable new bit-sequences that can arise. Just to remind:

- In each individual-chromosome the previously called *outstanding positions* and their orientations appears encoded. They represent the DVs of the optimisation problem. The chromosome itself does not contain direct informations about point connections and complete fiber arrangement. This information is implicit in DVs order and relative position in the chromosome. Crossover will involve the chromosome only.
- Per each individual (i.e. per each set of DVs) are tried four different DVs orderings. Only the best one is chosen as representative of the individual. Its fitness value is stored to be compared at this step, and the individual DVs are reordered according to the winning configuration in order to generate a meaningful chromosome for crossover.

Given m individuals, to proceed in crossover, $\frac{m}{2}$ couples of *parents* are collected. Each couple of parents generates a couple of *sons*. To determine the couples that will undergo crossover, each individual fitness is taken into account. Per each individual is assigned a probability to be chosen, computed as:

$$\frac{individual_i\ fitness}{\sum_{j=1}^{m} individual_j\ fitness}$$

It is then built up a conceptual *fortune wheel* (see Figure 2.11), in which the higher is the fitness value of the individual, the higher is the wheel area covered by its slice. Stated that the circumference length is 1, each slice has a sector length that correspond to its selection probability. Is then generated a random number (from 0 to 1) which corresponds to a position on the circumference. The individual in correspondence of that point is chosen. A second spin is required to perform a crossover.

Once two parents are chosen, the first half of their chromosomes is split in four sections, whose length is determined randomly. Four sections of the same random length are then generated in the second half of each chromosome. Remember that in the first half of the individual are stored the position indexes, in the second the orientations. Pairs of sections are now exchanged among the two individuals, so to virtually exchange *fiber segments*.

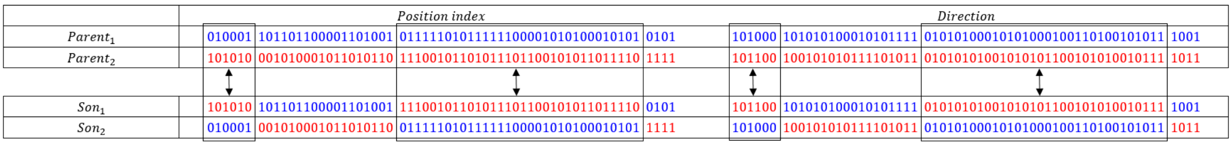

	Position index				Direction			
$Parent_1$	010001	101101100001101001	01111101011111100001010100010101	0101	101000	101010100010101111	01010100010101000100110100101011	1001
$Parent_2$	101010	001010001011010110	11100101101011101100101011011110	1111	101100	100101010111101011	01010101001010101100101010010111	1011
Son_1	101010	101101100001101001	11100101101011101100101011011110	0101	101100	101010100010101111	01010101001010101100101010010111	1001
Son_2	010001	001010001011010110	01111101011111100001010100010101	1111	101000	100101010111101011	01010100010101000100110100101011	1011

Figure 3.24: Crossover logic

The mutation process is managed after the crossover. Per each digit of each chromosome is assigned a random value, from 0 to 1. If the assigned value is smaller than the *mutation probability threshold* set by user, the digit switches its value.

The decoding of the chromosome occurs after this step.

3.6.7 Individual selection process

After crossover and decoding, a population of m new individuals is obtained. It can result to be *better* or *worse* than their parents one. To determine that, it is computed their fitness value, following all the steps described above (subsection 3.6.4).

Two approaches can be followed before advancing to the next generation. It is possible to take into account just the new population as parent-generation to perform a new reproduction process, or to select the best individuals (in terms of fitness) among old-parents and sons and build up a new hybrid population to provide the individuals that will represent the parents for the new generation. This last approach has been employed, since it guarantees a faster convergence speed.

3.7 Optimal Sensor Placement algorithm results

Several times the GA has been run till *convergence*. Convergence is claimed to be reached whenever for twenty-five consecutive generations no improvements in fitness value is noticed. Multiple runs are performed because the problem (and so its cost-function) is characterised by a huge amount of stationary points with comparable performances. For that, it must be determined which is the *candidate* fiber arrangement that is more convenient to employ.
This task should be performed just looking at their fitnesses. The configuration with the highest value must be chosen.
In this case, the fitness function that has been employed, is not the complete one. As explained in the second part of subsection 3.6.4, the *robustness*-check parameter inside the cost-function has been not implemented due to the computational weight. For that, having available a number of optimal candidate configurations, this kind of analysis is performed a-posteriori, behaving as the *discriminant* to be accounted to perform the choice. Here below are stated the specific values concerning the *candidate* configuration finally chosen as the best one:

Table 3.4: Best candidate fiber arrangement

Best connection strategy	1
$Fitness$	0.9318
$MSE_{weighted}$	0.3886
$\Delta F_{complete}$ %	10.6
$\Delta MSE_{weighted}$ %	10.7
Maximum allowed sensor loss	21

Each row has a specific meaning. The last three rows refer to the robustness analysis, as explained in subsection 3.6.4.

- Best connection strategy: referring to Figure 3.21, corresponds to the re-ordering logic which provides the best value of Fitness;
- $Fitness$: is the fitness value, according to Equation 3.14. More is better;
- $MSE_{weighted}$: is the weighted MSE among modes, according to subsection 3.6.4. In this case, each mode has the same weight. Less is better;
- $\Delta F_{complete}$ %: is the average percentage variation of fitness value when the configuration under exam is virtually *glued* on four *different* FE-models. Practically, it represents the variation in the *score* of cost function when the simulated strain data employed in the StD transformation undergoes some variations with respect to the *reference* simulation. It refers to the FE-model robustness check. Less is better;
- $\Delta MSE_{weighted}$ %: is the average percentage variation of MSE value when the configuration under exam is virtually *glued* on four *different* FE-models. It refers to the FE-model robustness check. Less is better;
- Maximum allowed sensor loss: is the maximum number of sensors that can be *lost* due to signal issues keeping the increase of the fitness value below 15% with respect to the *complete* configuration. It refers to the signal-quality robustness check. More is better;

Here below it is stated a short resume-list of the parameters considered to run the OSP algorithm, the GA convergence-trend concerning the chosen fiber arrangement, the fiber-path above the thin plate and its details and the expected shape-reconstruction output.

- Resume of GA input parameters:

Table 3.5: Resume of optimal sensor placement algorithm parameters for the final configuration

Target-modes considered in the optimisation	2, 3, 4, 5, 6, 7, 9
Modes weights for $MSE_{weighted}$ computation	unity per each optimised mode
Number of neighbouring modes considered in the $autoMAC$ risk-parameter computation	2
Number of *outstanding locations*	14
Number of population individuals	100
Bits for coding	15
Probability of mutation	0.4%
Minimum distance from clamp [mm]	30
Minimum sensor required per each measuring direction	3
Curvature radius [mm]	10
Maximum fiber length [mm]	1500
Plate sectioning for *connection-algorithm*	three bands along the width two bands along the length

- GA convergence trend:

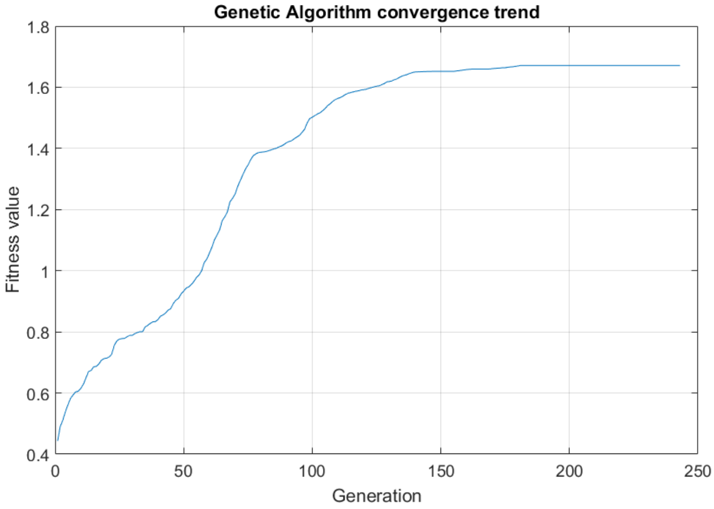

Figure 3.25: GA convergence trend

- Details of the chosen configuratio and configuration look:

Table 3.6: Configuration details

Theoretical fiber length $[mm]$	1379.8
Bends number	21
Overall theoretucal number of sensors	329
Sensors along x direction	235
Sensors along y direction	41
Sensors along $\angle_x 45°$ direction	53

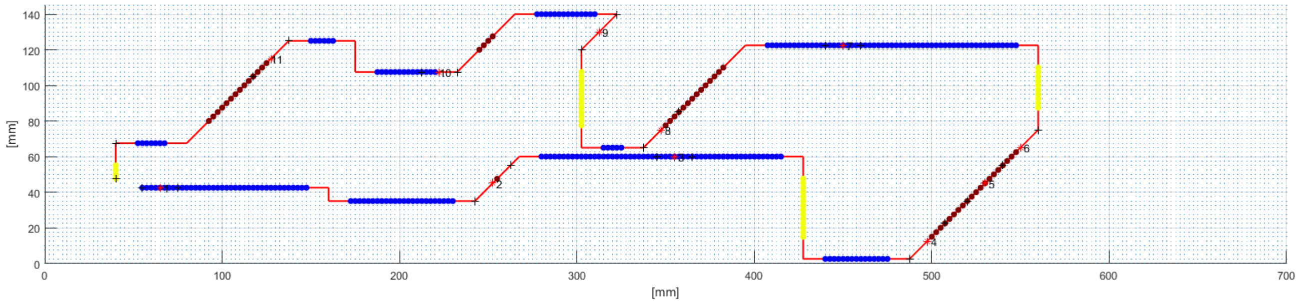

Figure 3.26: Definitive configuration

- Comparison among the exact mid-plane displacement w directly provided by FE-software and the reconstructed one. It is computed arranging *virtually* the fiber as explained before, considering in the strain-to-displacement conversion the simulated strains provided by the FE-analysis.
  Even mode 1 and 8 are shown to highlight the fiber arrangement effectiveness in their shape reconstruction.
  Modes till the 6^{th} are really well reconstructed given their simple shape.

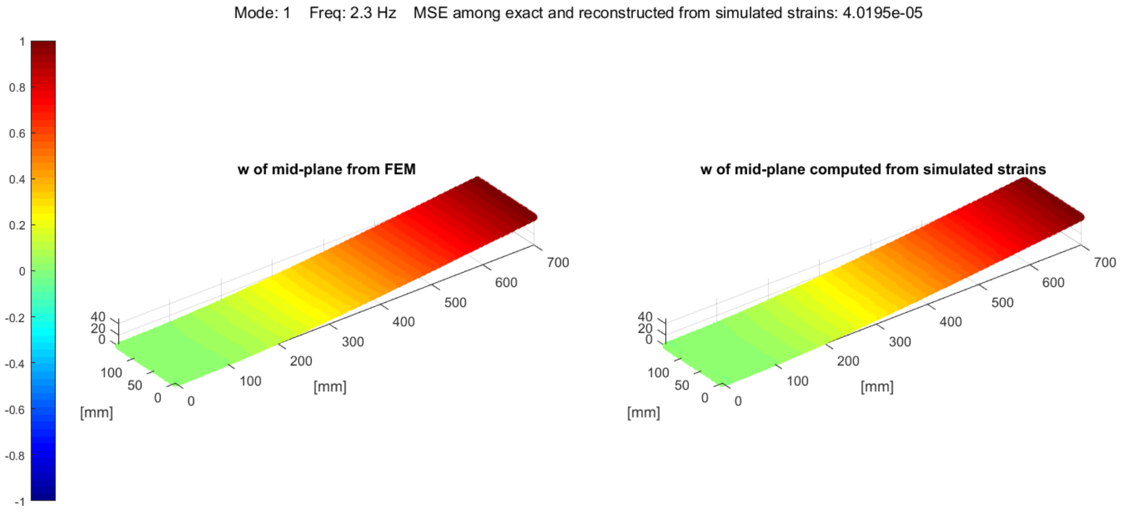

Figure 3.27: 1^{st} PC thin-plate reconstructed vibrating mode

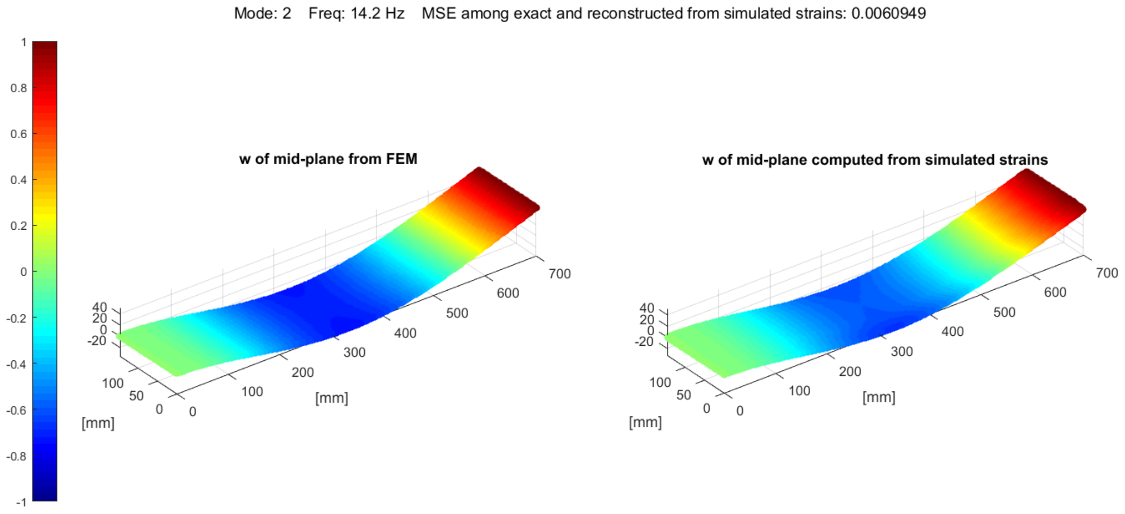

Figure 3.28: 2^{nd} PC thin-plate reconstructed vibrating mode

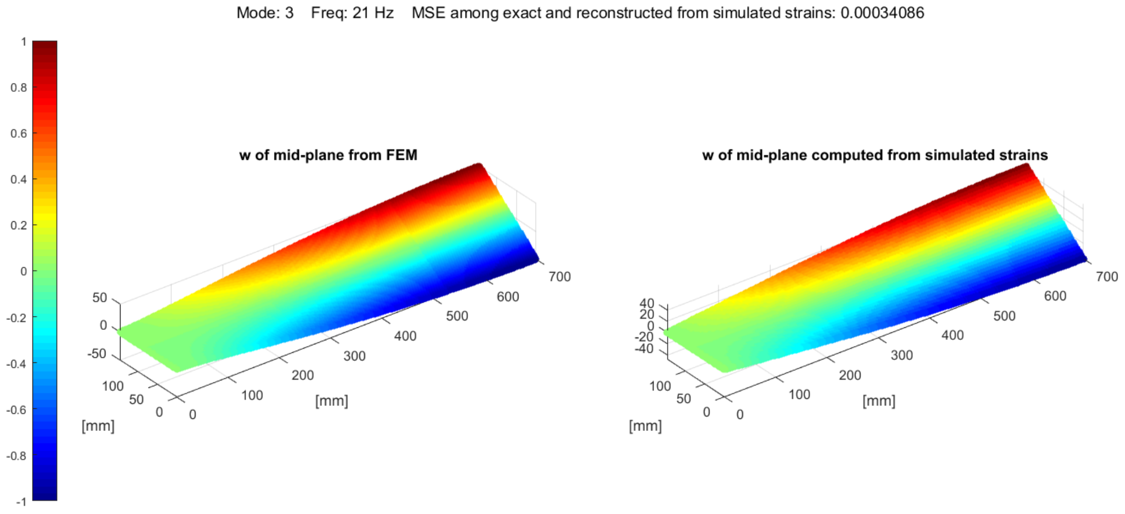

Figure 3.29: 3^{rd} PC thin-plate reconstructed vibrating mode

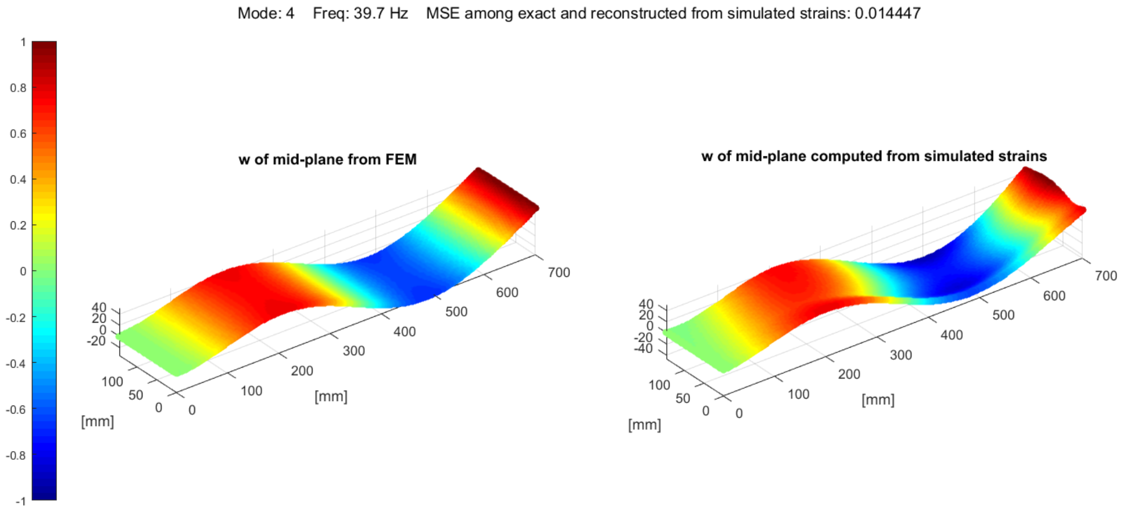

Figure 3.30: 4^{th} PC thin-plate reconstructed vibrating mode

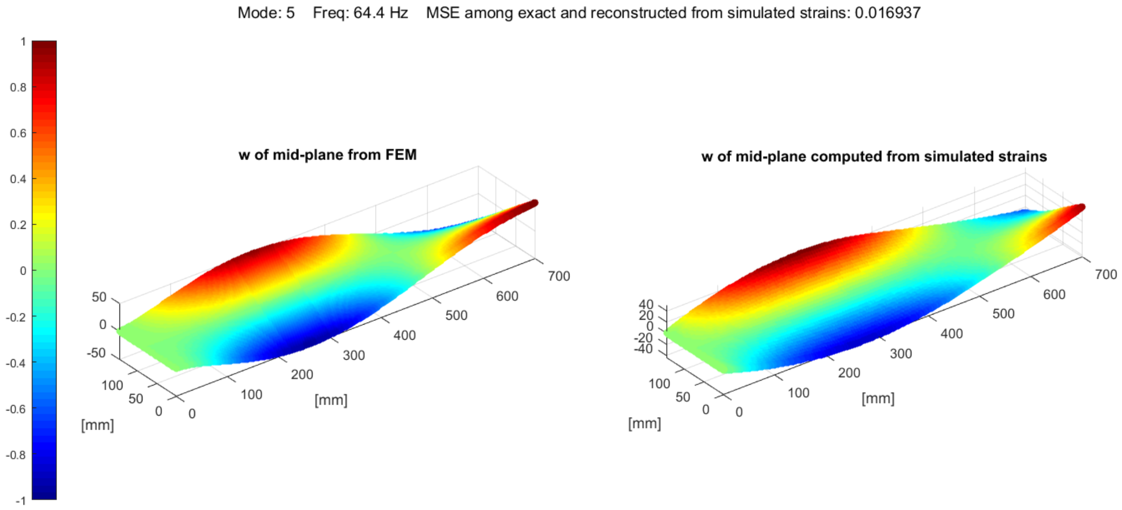

Figure 3.31: 5^{th} PC thin-plate reconstructed vibrating mode

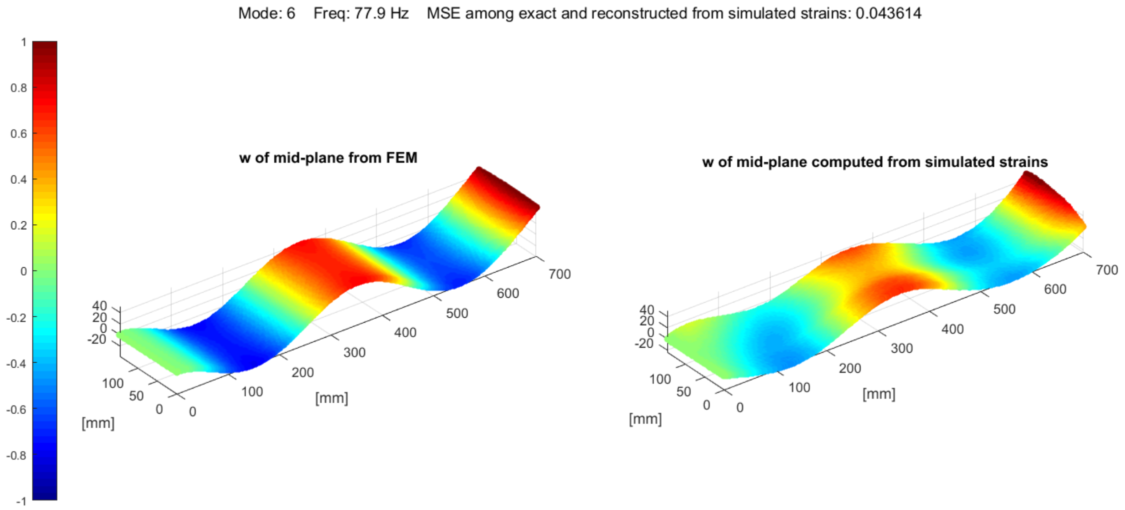
Mode: 6 Freq: 77.9 Hz MSE among exact and reconstructed from simulated strains: 0.043614

w of mid-plane from FEM

w of mid-plane computed from simulated strains

Figure 3.32: 6th PC thin-plate reconstructed vibrating mode

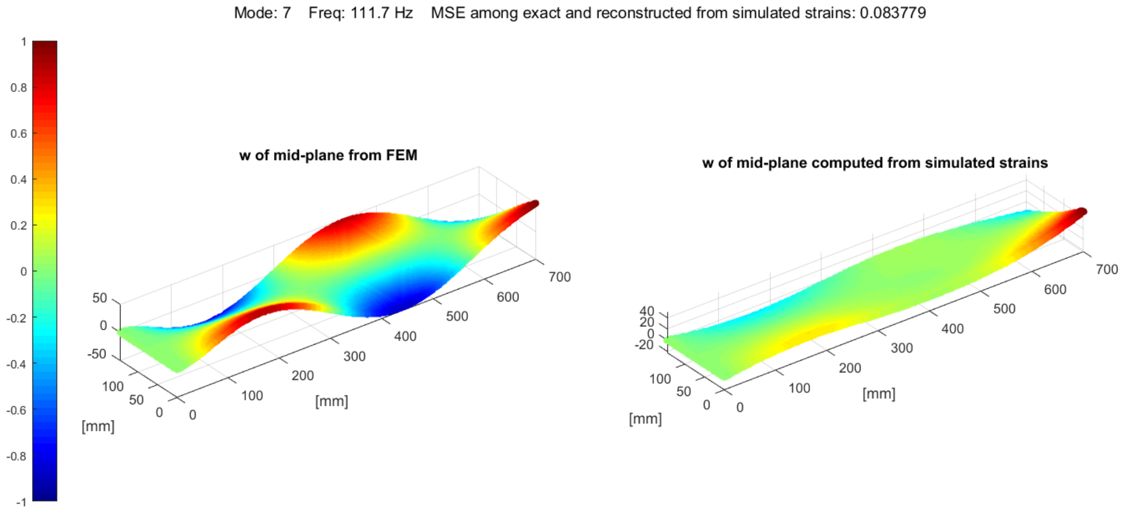
Mode: 7 Freq: 111.7 Hz MSE among exact and reconstructed from simulated strains: 0.083779

w of mid-plane from FEM

w of mid-plane computed from simulated strains

Figure 3.33: 7th PC thin-plate reconstructed vibrating mode

Mode 7, even if unequivocally recognisable, has a sort of *scaling* issue. Due to the eigenvector normalisation the bad reconstruction of plate *tip* displacement is reflected on the whole shape, *smoothing* its trend.

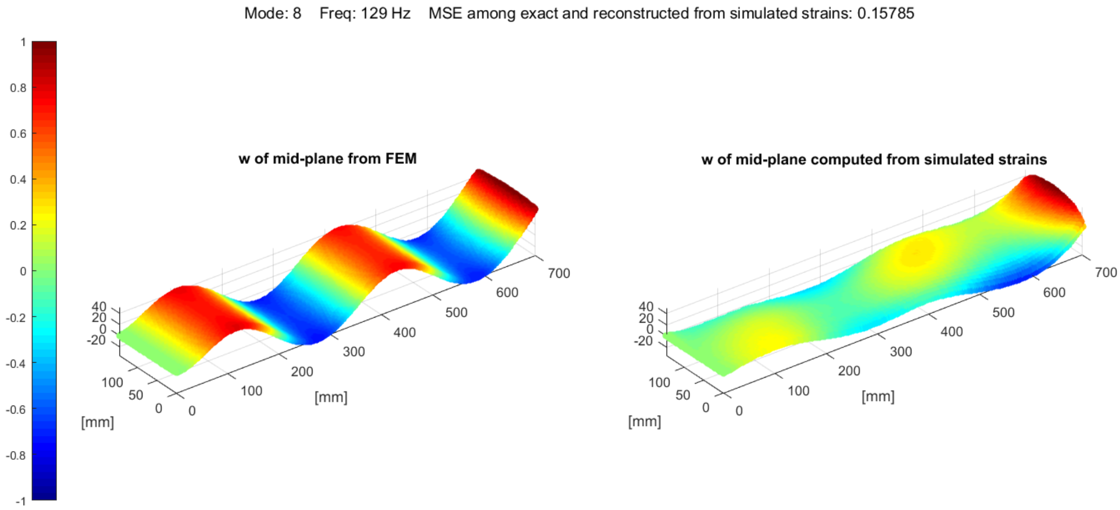

Figure 3.34: 8th PC thin-plate reconstructed vibrating mode

While mode 1, given its easy shape, is well reconstructed even if it is not introduced inside the target-modes for optimisation, mode 8, that is fairly more complex, due to the same reason results to undergo a very bad reconstruction.
Mode 9 has the same issue than mode 7.

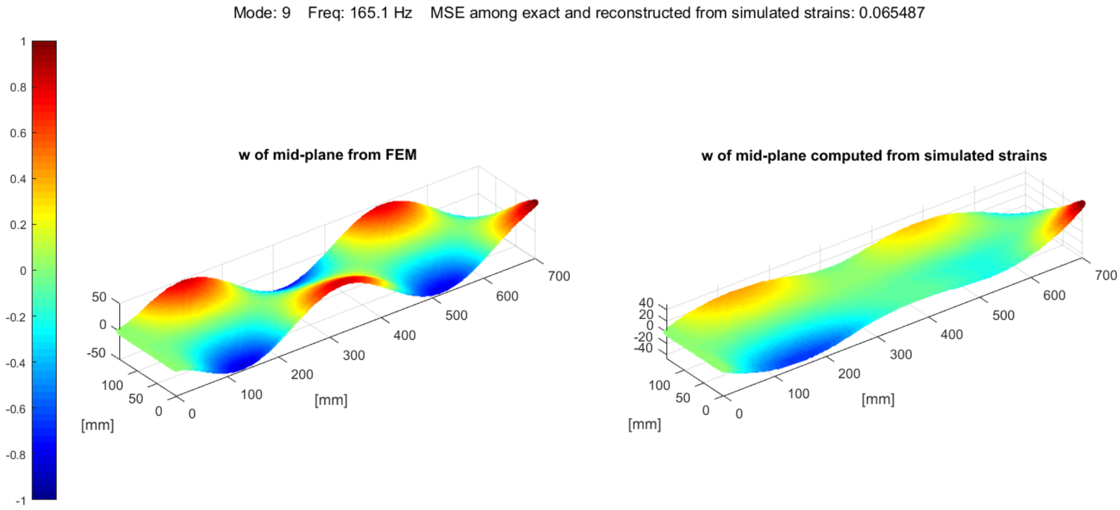

Figure 3.35: 9th PC thin-plate reconstructed vibrating mode

Chapter 4

Experimental set-up

The conclusive experiment concerning the bi-dimensional plate analysis manages to reconstruct the mid-plane displacement field w according to each vibrational mode, starting from the measured superficial strain-fields. The forcing input to the system will consist in the imposed displacement of the clamp, according to a mono-harmonic motion law. Each mode will be forced once at a time at its resonant frequency, according to a stepped sine forcing strategy. The nature of clamp imposed-motion will depend on the excited-mode expected shape, *flexural (or flap-wise)* or *torsional.*
This chapter will be closed by a brief resume concerning even the set-up of the three-dimensional case-study experimental session, scenario that will be deeply explained in the following chapter 7.

In a scenario of modal-analysis, a number of significant choices have to be performed during the design of the experimental set-up, depending on the particular features of the specific case, the requested output and the available instrumentation.

The experimental evaluation of the dynamic response of a mechanical system requires the application of some dynamic forces to the system itself. From a theoretical point of view, there are no restriction on forcing waveform or forcing strategy, but they must be determined accounting for the specific peculiarities of the case under exam. Wrong choices can result in complications during signal post-processing or can led to the impossibility to perform a successful modal analysis.

In this scenario, some considerations must be carried out:

- Surface strain monitoring is managed trough a system whose output must undergo a sensible *cleaning* procedure to provide reliable data. The deep *averaging* requires for many time samples to process.

- High baseline noise levels requires for sensible input forces to rise strain signal-to-noise ratio;

- Localised impact forces causes local strain spots that produce misleading strain fields in terms of displacement reconstruction;

Taking into account the particular features of the system-response measurement instrumentation and the geometry of the structure, the forcing strategy and the actuator type, the excitation wave-form and how to connect the system to the actuator must be determined.

The best forcing strategy that has been thought is an imposed motion of the clamp. Hammering the plate means to produce usefulness output measurements, because of the very reduced amount of energy introduced in the structure, the strong local deformation produced in the hit point and problems related to high-frequency signals acquisition (aliasing and limits in readable deformation speed). To punctually force the structure risks to locally deform the surface and changes system boundaries, instead.

The most suitable way to impose such an action is an electrodynamic shaker. This device is capable to generate highly controlled displacements along its slider axis. Depending on the electronic input it receives, it can generate different types of wave-forms: impulses, sine-swepts, stepped-sines, randoms, etc... . Its high bandwidth is counterbalanced by a small output force capability.
Severe loading limits must be respected to avoid damages on such device. This made necessary to employ a large size electrodynamic shaker.

Accounting for the same reasons, the best forcing wave-form is a pure sine. Each mode will be forced in its resonance, focusing the whole amount of input energy to obtain a *clear* system response. This approach allows to best post-process the signal, permitting to employ powerful specific cleaning algorithms that results to be essential in the case under exam . Furthermore, it would be impossible to obtain the same strain signal-to-noise ratio forcing the system with a signal composed by a wide amount of harmonics (i.e. controlled-random).

To excite the system so that the measured response contains an useful set of informations able to reconstruct the eigenvector of interest, it is necessary that the energy provided by the input force can actually *excite* the vibrating mode under exam. That depends on the coupling among forcing strategy and the system, being mode shapes determined by its features and constraints. Imposing just a linear motion to the clamp, a sort of *symmetric energy shape* is introduced into the system, that does not allow to excite *antisymmetric* modes (i.e. torsional) due to the physical and geometrical properties of the plate. This theoretically-based issue has been demonstrated even experimentally.

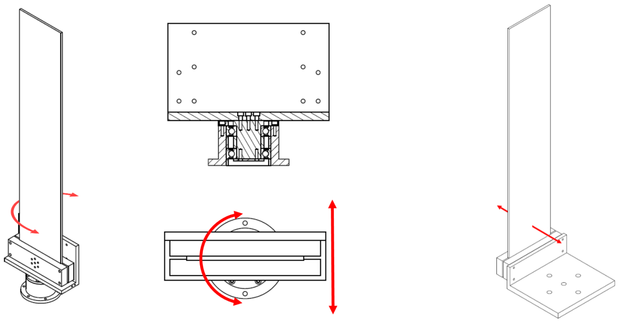

Figure 4.1: Actuator connections - torsional modes excitation and flap-wise modes excitation

For that reason, two different connections among the shaker and the clamped plate has been developed, Figure 4.1 and Figure 4.2. In the torsional modes set-up, the base is grounded and the force acts through a thin bar of spring-steel, producing the alternate rotation of the plate about its *axis*. In the flap-wise modes set-up, the squared base is directly bolted on the electrodynamic-shaker horizontal-slider.

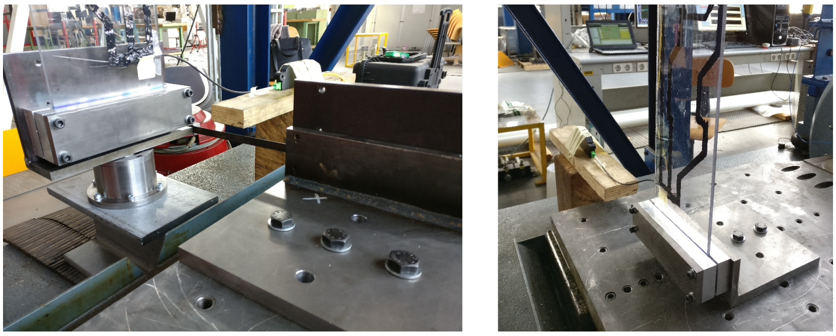

Figure 4.2: Real actuator connections - torsional modes excitation and flap-wise modes excitation

Due to plate small inertia moment about y axis and due to its own weight, if the plate is clamped horizontally it undergoes a strong static deflection. To avoid any issue related to this behaviour, the plate has been mounted vertically, as shown by the previous pictures.

4.1 Computational modal analysis experimental check

FE-software are extremely powerful tools. They are able to provide complete and essential informations in a fast and simple way. However, results reliability (especially in the case of dynamic analysis) is strongly affected by the huge set of intrinsic approximations and model uncertainties that are necessarily introduced.

In the case of a computational modal analysis of simple symmetric structures and materials, the consequence of computational errors mostly concerns modes eigenfrequencies. Shape is generally well determined instead.
This behaviour led to two issues:

- Structure resonance peaks can occur at slightly different frequencies than expected;
- The *mode-ordering* proposed by FE analysis can be misleading. It can occur that two modes, generally adjacent, are proposed with exchanged frequencies. At a given frequency system response can be totally different than expected.

The purpose of this work is to reconstruct the thin-plate mode shapes that resides below $200Hz$, due to the acquisition system limitations.

The dynamic excitation of the structure is performed by a stepped-sine approach: it means that is required a precise knowledge of the structure resonance frequencies to perform focused acquisitions.

The optimal sensor placement algorithm, extensively treated before, has been tuned to optimise optical-fiber arrangement such that it can successfully reconstruct all the mode shapes within that range. Whenever occurs that the FE-analysis mistakes modes ordering with respect to the real one, so occurs that a vibrational mode that in the computational modal analysis appears to be *out* of the bandwidth of interest is inside instead, fiber arrangement should still guarantee a good shape evaluation, because the *robustness factor* that should have been accounted in the fitness cost function computation (second part of subsection 3.6.4) assures sensor arrangement effectiveness even in this occurrence.

In this scenario it would be enough to evaluate just the exact frequency of the resonances (no informations about the mode-shape is required) before proceeding in real experimental session with a stepped-sine approach. This check can be performed with the help of an accelerometer and an impact hammer, or employing a sweep-sine waveform forcing or a random waveform forcing directly once fiber has been fixed.

As already explained in subsection 3.6.4, in the case under exam this particular *robustness-parameter* has not been implemented in fitness computation due to the high computational cost. Fiber arrangement would not be able to provide useful data about the *outer* mode in such occurrence.
For this reason the real mode ordering have to be inspected so that the sensor configuration can be optimised already over the *real* set of mode-shapes. As a matter of facts, it is necessary to perform a fast experimental check on the structure. In this study, a rough but meaningful analysis has been performed thanks to piezoelectric accelerometers and a series of localised impulse inputs. Here below, in Table 4.1, the frequency shift of each mode in the definitive case-study is stated:

Table 4.1: Comparison among FE-analysis modes ordering and experimental one - thin-plate case-study

Computational mode index	1	2	3	4	5	6	7	8	9
Computational eigenfrequency $[Hz]$	2.3	14.2	21	39.7	64.4	77.9	111.7	129	165.1
Experimental eigenfrequency $[Hz]$	2.4	15.8	23	44.6	70	87.3	121.6	144.6	181
Experimental mode index	1	2	3	4	5	6	7	8	9
Mode geometry	f-w	f-w	t	f-w	t	f-w	t	f-w	t

where:

- *f-w*: flap-wise (bending) mode;
- *t*: torsional mode;

Thanks to this preliminary test, it is obtained a clear information about the real modes order inside the frequency interval under exam (information required to well initialise the optimal sensor placement algorithm), and the right forcing frequency to apply in order to excite the wanted target-mode.

4.2 Experimental plan

Modes above $200Hz$ cannot be successfully monitored, modes below $10Hz$ cannot be forced. In this last occurrence, modes frequency is outside from electrodynamic-shaker bandwidth. In the first case mode frequency is too high to be successfully acquired by the measurement system.

Table 4.2: Experimental plan - thin-plate case-study

Experimental mode index	2	3	4	5	6	7	8	9
Forcing frequency $[Hz]$	15.8	23	44.6	70	87.3	121.6	144.6	181
Clamp max displacement $[mm]$ or [deg]	0.025	0.014°	0.015	0.0086°	0.005	0.0086°	0.005	0.0043°
Clamp max acceleration $[mm/s^2]$ or $[deg/s^2]$	246.4	5.1	1162	29	1504	87.6	4127	97
Sampling frequency $[Hz]$	∼250	∼250	∼250	∼250	∼250	∼250	∼250	∼250
Time samples	10000	10000	10000	10000	10000	10000	10000	10000

The chosen values in terms of clamp displacement *amplitude* are determined so to keep a considerable strain *signal-to-noise* ratio, without exceeding in *deformation speed* and structure displacements.

4.3 Instumentation

4.3.1 LUNA ODiSI-B

LUNA ODiSI-B delivers high speed, fully distributed strain and temperature measurements with high spatial resolution. The ODiSI-B system interrogates hundreds of sensing locations per meter on a single optical fiber simultaneously at a rate of up to $250Hz$.

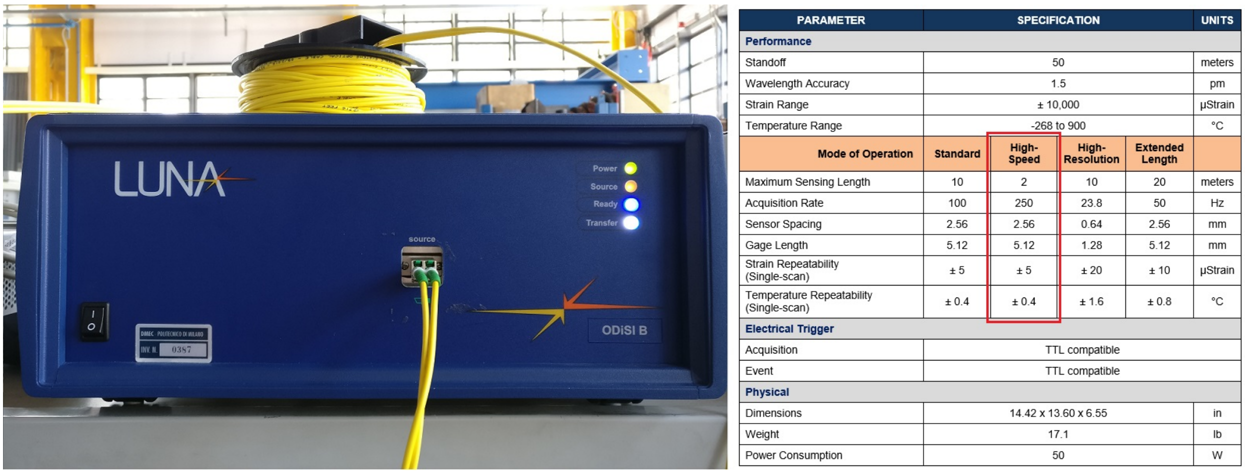

PARAMETER	SPECIFICATION				UNITS
Performance					
Standoff	50				meters
Wavelength Accuracy	1.5				pm
Strain Range	± 10,000				μStrain
Temperature Range	-268 to 900				°C
Mode of Operation	**Standard**	**High-Speed**	**High-Resolution**	**Extended Length**	
Maximum Sensing Length	10	2	10	20	meters
Acquisition Rate	100	250	23.8	50	Hz
Sensor Spacing	2.56	2.56	0.64	2.56	mm
Gage Length	5.12	5.12	1.28	5.12	mm
Strain Repeatability (Single-scan)	± 5	± 5	± 20	± 10	μStrain
Temperature Repeatability (Single-scan)	± 0.4	± 0.4	± 1.6	± 0.8	°C
Electrical Trigger					
Acquisition	TTL compatible				
Event	TTL compatible				
Physical					
Dimensions	14.42 x 13.60 x 6.55				in
Weight	17.1				lb
Power Consumption	50				W

Figure 4.3: LUNA ODiSI-B control unit and datasheet

A 2 *meters* fiber sensor has been employed.
ODiSI-B fiber sensors can be both LUNA stock fibers, both *adapted* commercial optical fibers. ODiSI home-made sensing fibers must be caracterised by a coating that allows to well transfer strains. Luna recommends polyimide-coated low-bend-loss fibers for strain measurement purposes. To use of standard fibers requires for curvature radii above $25mm$, and is however strongly discouraged.
According to LUNA platform requirements, sensing fiber must be characterised by:

- An LC/APC fiber optic connector, to be linked with the interrogator;
- A core-less end termination of about $80mm$, to generate a low reflection sensor-end.

LUNA Technologies provides an user-friendly software package to properly employ its acquisition system.

- Sensor-configuration software: allows to properly configure the OF sensor. It allows to determine which part of the fiber must be considered as *sensing*, so which section must be actually acquired (among the yellow and red line).

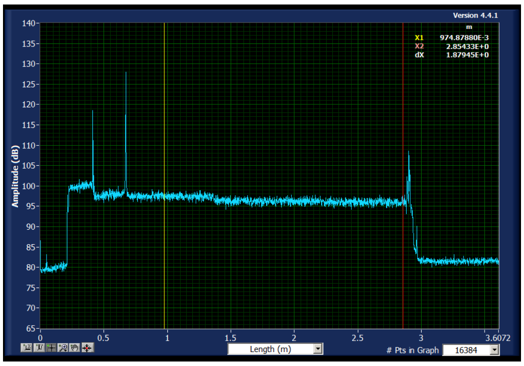

m
X1 974.87880E-3
X2 2.85433E+0
dX 1.87945E+0

Length (m)

Pts in Graph 16384

Figure 4.4: LUNA software - sensor configuration

- Acquisition software: allows to concretely acquire the fiber output converting it into a strain signal. The graphical output consists in a real-time representation of the strain the fiber is undergoing with respect to its length. In this scenario parameters like the *sampling frequency* are setted, and can be triggered the acquisition, whose informations are stored in an output database file *[.odb]*. To be noticed that the sampling frequency, even if setted, is not rigorously respected during the acquisition.

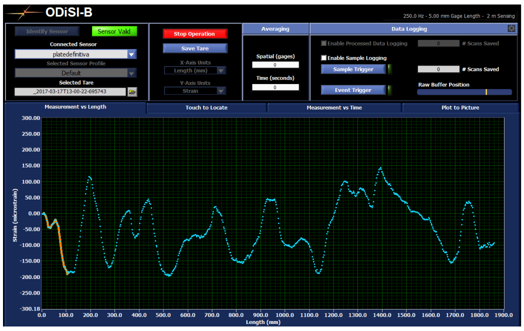

250.0 Hz - 5.00 mm Gage Length - 2 m Sensing

Connected Sensor: platedefinitiva

Selected Sensor Profile: Default

Selected Tare: _2017-03-17T13-00-22-695743

X-Axis Units: Length (mm)

Y-Axis Units: Strain

Spatial (gages): 0

Time (seconds): 0

☐ Enable Processed Data Logging 0 # Scans Saved

☐ Enable Sample Logging

0 # Scans Saved

Figure 4.5: LUNA software - acquisition

- Post-processor software: allows to convert the previously generated *[.odb]* output file into a readable text format output-file *[.txt]*, that will

be imported into MATLAB for further elaborations.
LUNA output file contains *rough* data, in the sense that no kind of signal cleaning is performed at this step. A LUNA tool is offered to remove *unreliable* time samples from output, but this procedure seemed to introduce more errors than benefits. This *cleaning* operation is performed by tuning a so called *qt (i.e.: quality threshold)* parameter. LUNA suggests a *qt* value equal to 0.38, probably referring to static applications. In this case *qt* is set to 0, entrusting in the signal cleaning developed in the post-processing chapter.

4.3.2 DM/PD005 Unholtz Dickie electrodynamic shaker

Electrodynamic shakers allow strictly controlled displacements. Shaker motion is governed by a dedicated PC software, which requires for the informations coming from a feedback loop-control accelerometer. In this way the shaker can generate various types of excitation wave-forms, imposing their amplitude in terms of acceleration, velocity or displacement, much easier to be managed than to a direct voltage-value input.

Figure 4.6: DM/PD005 Unholtz Dickie electrodynamic shaker

4.4 Fiber fixing on surface

After the best fiber configuration has been determined as described in chapter 3, it is necessary to physically fix the sensor on plate surface. Optical fibers are very thin and fragile transducers and require for careful handling. Strong tensile stresses, torsions or very narrow bends can damage fiber core. Materials required for a correct and effective fixing are:

- The fiber-path provided by the optimal sensor placement algorithm;
- A notches-free surface;
- The 3M Scotch-Weld™ EPX™ Adhesive DP490. DP490 is a black, thixotropic, gap filling two component epoxy adhesive. It is designed for uses where toughness and high strength are required. It guarantees high shear stress resistance even in case of composite assemblies

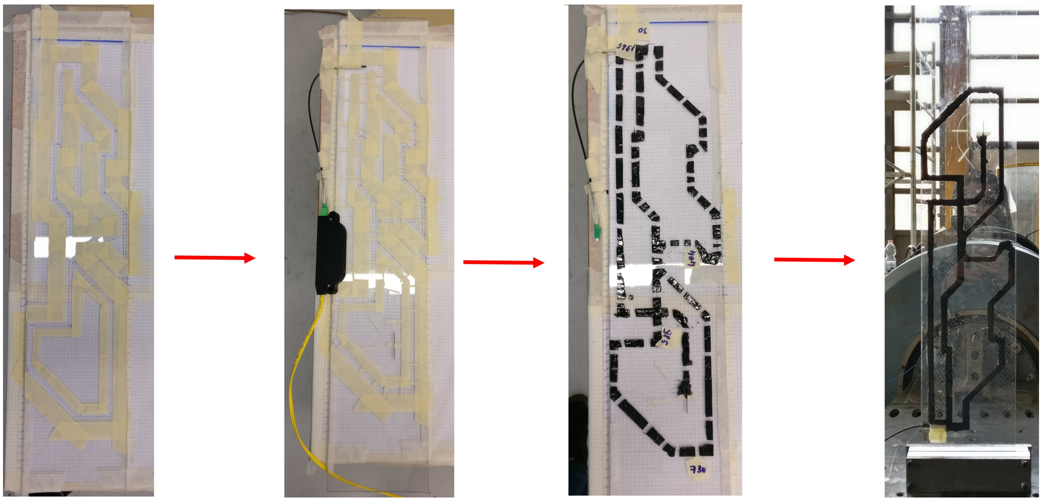

Figure 4.7: Glueing process

Some advices about this procedure are stated below:

- LUNA recommends to keep a 300mm strain-free region just after the connector. It can be done inserting the fiber in a low-friction polymeric sheath. Furthermore, the core-less end termination should be arranged along a bended path;
- To keep connected and switched on a fiber-fault detector during fiber glueing, allows to immediatly evidence *criticisms* during fiber handling;

- Sensor configuration must be performed after the fiber has been fixed and the glue is completely dried. However, to compare the fiber *signal amplitude* in the *sensor-configuration tool* before and after the glueing procedure allows to notice how bends have reduced signal strength. A good placement must be like Figure 4.4.

4.5 Three-dimensional case-study

All the considerations previously stated in chapter 4, section 4.1, section 4.4 and about the instrumentation itself, subsection 4.3.1, remain valid.
Given the strong asymmetry in the geometry of this structure, the distinction among *torsional* and *flap-wise* modes becomes less pronounced. For the same reason, the excitation will be provided just trough the not-rotating clamp (Figure 4.8).

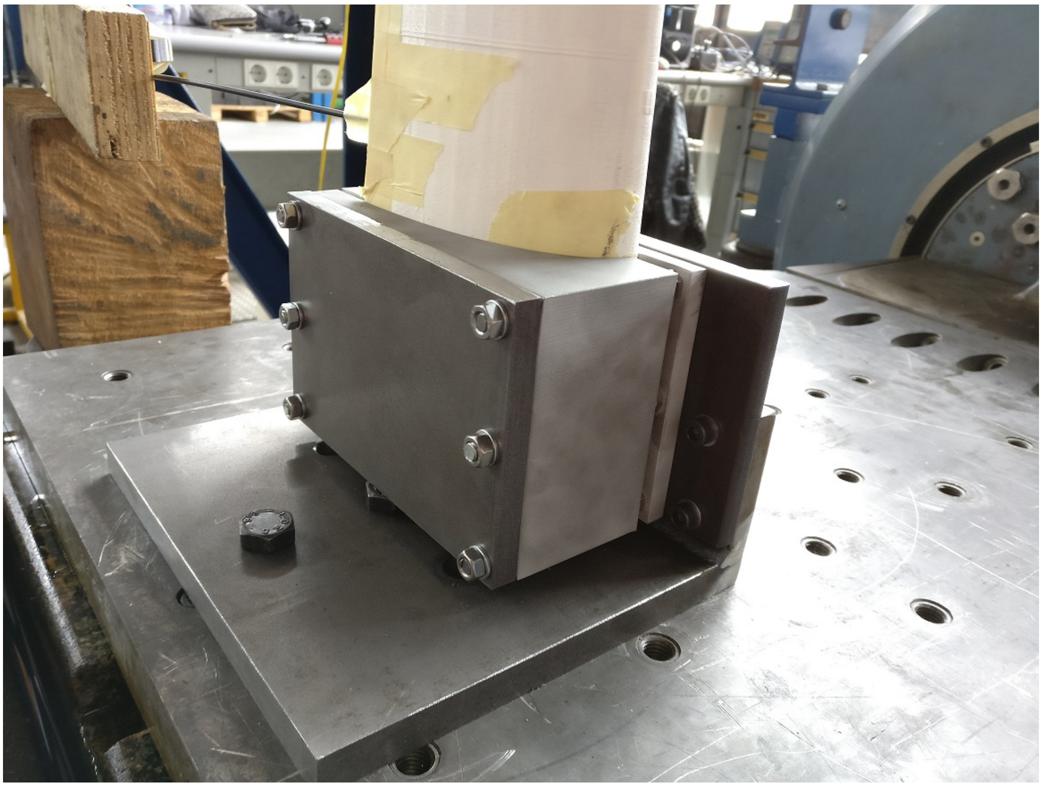

Figure 4.8: Actuator connection for the 3D case-study

Here below, similarly to Table 4.1, is shown the frequency shift of each mode of the three-dimensional blade with respect to the FE-analysis ones.

Table 4.3: Comparison among FE-analysis modes ordering and experimental one - 3D-printed blade case-study

Computational mode index	1	2	3	4	5
Computational eigenfrequency $[Hz]$	12.8	48.9	68.1	101.8	128
Experimental eigenfrequency $[Hz]$	15	58.8	83	117.5	147
Experimental mode index	1	2	3	4	5
Mode geometry	f-w	f-w	t	f-w	t

The experimental plan is the following:

Table 4.4: Experimental plan - 3D-printed blade case-study

Experimental mode index	1	2	3	4	5
Forcing frequency $[Hz]$	15	58.8	83	117.5	147
Clamp max displacement $[mm]$	0.02	0.03	0.025	0.005	0.01
Clamp max acceleration $[mm/s^2]$	177.5	4095	6800	2725.5	8531
Sampling frequency $[Hz]$	∼250	∼250	∼250	∼250	∼250
Time samples	10000	10000	10000	10000	10000

Modes beyond the 5^{th} have been not acquired because their eigenfrequencies was discovered to be well above $200Hz$, where LUNA interrogator performances are too low.

Chapter 5

Devised post-processing procedure and LUNA ODiSI-B investigation

The implementation of a proper post-processing tool results to be necessary to successfully manage the experimental acquisitions. The output of LUNA ODiSI-B CU has to be conveniently handled in order to extract the useful desired information. The strain data have to be opportunely imported and located in the structure. Consequently time signals have to be cleaned to extract reliable strain informations to proceed with the modal shape reconstruction.

5.1 Real fiber position identification

LUNA control-unit output is a list of strain values that represent the *punctual* deformation trend of the fiber in time. As already stated, the optical fiber behaves like a continuous strain sensor, in the sense that it contains an *high* number of sensing gauges along its length ($\approx 380\ \frac{sensors}{meter}$). Per each sensor and per each time step is acquired a strain value.

To proceed in the modal shape reconstruction, coherently with the pre-processing algorithm, it is necessary to define per each sensor:

1. Where it is located over the structure and its measurement direction;
2. If the sensor can actually provide the desired information. Practically if the sensor has effectively x,y or 45° as measure direction. Automatically the sensors which can not be related to any of the three directions are excluded.

LUNA output file provides just an ordered list of measured values. Strains are collected depending on the *sensor index* they come from and the acquisition instant. Sensors are indexed depending on their distance from first fiber sensing-point (the gauge that coincides with position X_0 in the sensor-configuration phase, subsection 4.3.1). Sensor spacing is $\approx 2.6mm$.

The acquired *strain-matrix* contains the strain data of each sensor physically placed between the *sensor zero,* X_0 and the *final sensor,* X_1. No spatial correlation among these informations and the real positions in the structure is provided by the acquisition system. It has to be externally implemented in a thought way. This is the first task of the proposed post-processing tool.

Remember that fiber fixing on surface must be as much coherent as possible with the one proposed by the optimal sensor placement (OSP) algorithm. However, real fiber gauges distribution and OSP fiber arrangement are totally uncorrelated. In this sense, even if real fiber path exactly coincides with GA configuration, must be understood in the most precise way where the i^{th} fiber sensor is located.
This procedure is performed with the help of a graphical interface that has been designed ad-hoc. An example of that is in Figure 5.1.

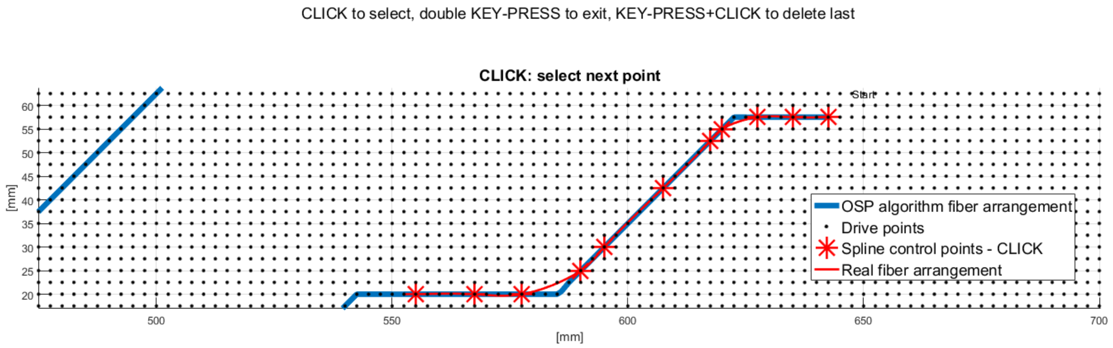

Figure 5.1: Example of real fiber path determination

By taking as a reference the OSP algorithm fiber arrangement and considering how the fiber has been concretely glued, by clicking on the *drive points* is tracked a spline that represent the real fiber arrangement. It must be as much coherent as possible with the real glued configuration.
Nevertheless some problems in this procedure can occur.

Any discrepancy among the parameters considered to run the OSP algorithm and the real scenario led to a different amount of strain data with respect to the ones assumed as *available* during pre-processing. In this case it is possible that a sensor, which is considered part of the *winner* fiber configuration, will not give its contribution in the real modal shape reconstruction due to its bend proximity or its uncertainty in the fixing direction. This step procedure has been *simulated* in the pre-processing where all the *simulated* sensors close to bends have been excluded. To reach satisfying results, the *elimination* process in the post-processing has to be as coherent as possible to the one *simulated* in the pre-processing. The same sensors along the fiber have to be *excluded* in order to make consistent and reliable the prediction of the mode shape reconstruction resulting from the OSP.

Practically, after having created the trace of the real fixed fiber configuration as shown in Figure 5.1, it is necessary to select the sensors which are wanted to be kept along its length.

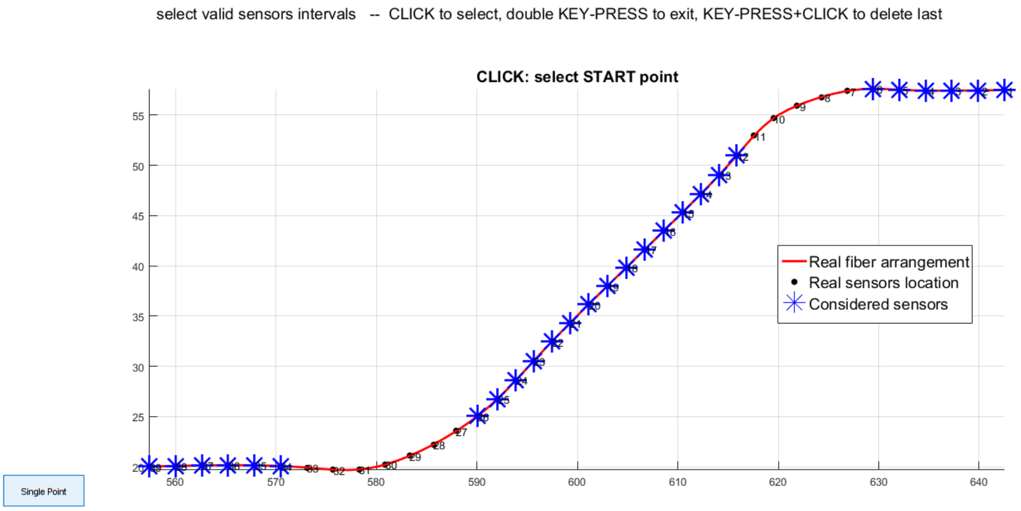

select valid sensors intervals -- CLICK to select, double KEY-PRESS to exit, KEY-PRESS+CLICK to delete last

CLICK: select START point

Figure 5.2: Example of *wanted sensors* selection process

This is performed with the help of another dedicated graphical tool described by Figure 5.2. Two consequences arise from the facts stated above.

Fristly, the number of usable sensors in the real measurement tend to be smaller than the one considered in the *virtual* fiber configuration provided by OSP algorithm.

Secondly, the amount of used gauges of the real fiber is always smaller than the overall number. Both the problems can be reduced, however the main issue is the first one.

A good pre-processing has to be able to predict the real number of sensors that will be available after the fiber gluing.
Obviously, if the manual glueing procedure of the fiber is substituted by an automatic and precise procedure, even the number of real sensors excluded due to their wrong orientation can be reduced and fiber bends can be much more regular. Furthermore, in this case it would be even possible to increase the angular degree of measure. The OSP algorithm would consider as possible measurement directions not just the x, y and 45°, but even other ones (e.g. 15°, 30° and 60°, and so on).
Even in this sense, it is clear the strong and intimate connection between the pre-processing tuning, the experimental set-up and the results.

The output of the whole procedure is the entire set of information concerning the spatial position over the plate of each real-fiber gauge and its orientation. In this way the informations coming from the LUNA strain-matrix can be effectively employed. Figure 5.3 is a graphical example of the difference among the position of fiber-gauges in virtual fiber arrangement and in the real one.

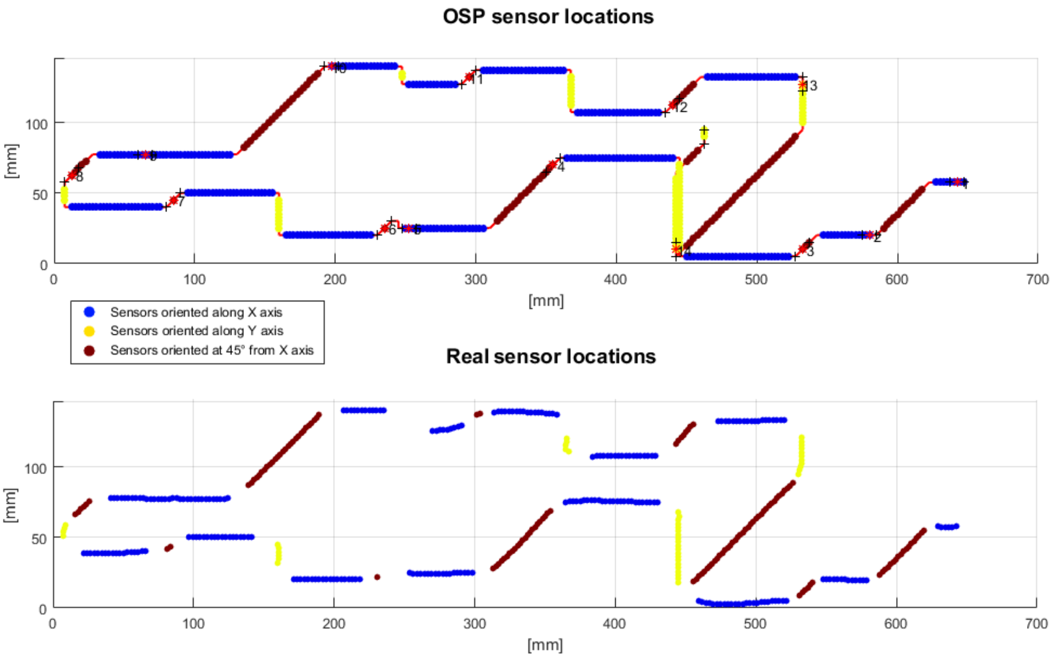

Figure 5.3: Comparison among *virtual* fiber arrangement and real fiber arrangement

5.2 Noise signal cleaning

After the definition of the physical coordinates and the measurement directions per each sensor acquired by the LUNA software, it is possible to proceed with the signal processing. At this point, the LUNA output data, are processed sensor by sensor. Each sensor has a signal time history to be analysed: it has to be properly translated in the frequency domain to perform the modal analysis.

The main issue is the noise suppression from the deterministic signal related to the deformation. *Noise* can be defined as any undesired signal. All the acquisitions are made in steady-state conditions. It has been observed that the acquired signals are affected by some irregularities:

1. Spikes values, that consist in time-samples with a module considerably higher than the Root Mean Squeare (RMS) of the signal. The cause of their presence is not related to a singular behaviour of the structure deformation. Spikes values have no physical meaning. It is presumable that these peaks come from a control-unit anomaly due to the dynamic nature of the measures. It will be interesting to analyse the presence of spikes in relation to different signal frequencies and its distribution along the fiber length;

2. Unreliable values, apparently physically plausible but really not coherent with the predictable sinusoidal output signal. This kind of undesired records is more critical due to its ambiguity, it represent untrustworthy signal values and practically decreases the quality of the Fast Fourier Transform calculation of each sensor. The causes of these unwanted irregularities are not extremely clear, however three general categories of possible sources of *unreliable values* can be found:

    - Wrong signal processing or wrong interpretation of the deformation value of a certain sensor in a certain time instant;
    - Uncorrelated electric noise, not so much probable with optical fibers;
    - Correlated and extrinsic noise caused by environmental susceptibility of the sensor.

    A deep analysis of the acquired data is necessary to understand the real disturbances origins.

    The first candidate cause consists in the possible difficulty of the CU to read the correct value of deformation or to associate it to the exact location along the fiber, or to insert the signal value in the right time-instant in the time-record. One of these faults, or even a combination of them, is the possible cause of the irregularities. In all these cases, the signal values classified as *unreliable values* are actually deformation proper to another sensor or proper to another instant of the time-record itself. This process is not necessarily random: the wrong values introduced in the signal-history of a gauge could be physically meaningful values, but related to other time-instant or other sensors. The process trough which the CU collects them is not necessary accidental. The faulty process comes from CU, fiber-CU interface or fiber measure bug, so it is probably a deterministic fault. It can be associated to a malfunctioning system with respect to the light reflection or the de-codifying capability of the system to follow a dynamic deformation. It is important to remember that LUNA ODiSI-B v4 is designed to work statically.

Nevertheless, it is possible that the signal disturbances origin can be even related to a more general noise issue. A noise random base-line can generates problems in particular with the resolve of small signal.

Probably it can be expected that if the origin of the *unreliable values* is an aberrant behaviour of CU and/or fiber sensor due to their employment in the dynamic field, the noise has to increase with raised frequencies. This analysis will be performed at the end of the cleaning-process explanation, with proper quality indexes to quantify and judge the phenomena.
Now that it is necessary to determine a significant methodology able to put in evidence which signal time-step belongs to the category of unreliable values. They have to be individuated and removed to perform a significant mode reconstruction;

The investigation of all these phenomena is required to carry out one of the main purposes of the thesis: understand the behaviour of ODIsI-B LUNA control unit in dynamic measurements. As explained, the fiber sensor and LUNA software are developed for static measures. The most critical aspect in their dynamic application is the presence of those not-coherent values in the output time-record, the noise. So, practically, the first scope of the signal processing has to be to eliminate all the not meaningful values.
While spikes can be eliminated with various methods, the real critical issue is the detection and removal of *unreliable values*.

In a traditional experimental acquisition, a simple time-averaging is usually capable to clean all the noise-dependent values. To achieve a clean acquisition of a deterministic phenomena a point-by-point mean is traditionally performed in the time domain among phased sub-records of the same length referred to the same phenomenon. This mean is finally divided for the number of the used records.

$$X(t) = \frac{1}{N} \sum_{k=1}^{N} x_k(t) \tag{5.1}$$

Usually the sampling frequency is fixed and properly imposed. If the forcing-waveform is a stepped sine, it is possible to perform a synchronous acquisition and always obtain the same number of points per period, in the same relative time instant. It would be easy to divide the entire acquisition in sub-records and perform time-averaging in order to eliminate any sort of noise. Actually, the procedure chosen to clean the signal and create a reliable time-history before applying the Fast Fourier Transform (FFT), is not a standard time-averaging. The most critical aspects related to signal averaging in the post-processing of LUNA output are:

- The sampling frequency is controlled by the LUNA CU and cannot be freely imposed. Furthermore, it is not strictly an constant in time. For that, the time *resolution* of the output signal is not exactly constant. As a consequence, to practically perform the time-averaging procedure, an interpolation of the signal in the time domain before the subdivision in sub-records would be needed. By interpolating time-samples of an entire time-record of a certain sensor, it would be possible to compute the previously explained point-by-point sum, with the certainty to compare values at same *relative time instant* per each sub-record. The critical aspect is the interpolation step: it generates the missing values of the time-histories and complete them where needed, so the interpolation introduces necessarily an approximated content of informations. If this *approximated informations* are averaged with the *exact acquired data*, the right signal can be tarnished by the averaging with the interpolated values. In conclusion, the final result is a not reliable signal cleaning.

- The disturbances nature is not necessarily random, because they are assumed to be produced mainly by CU faults as a result of the performed analyses. Due to the not-complete or not-strictly random time-dependence of the signal noise, the averaging process would not be effective. The average in the points would be affected by the presence of *unreliable values*. The discard of the unwanted values does not occur, because they are not purely random: they are included in the final result of the averaging and, in this way, alter some time-instant values of the final cleaned signal.

- A general disadvantage of the time-averaging is the impossibility to control the quality parameters during the process. The time-averaging is an optimal tool when there is the absolute certainty that:

    1. The time length has to be the same for all the sub records;
    2. The number of points to be averaged per each sub-record has to be the same;
    3. The records have to be *phases*, trigger acquisitions, cross-correlations or alignments of the sub records are required;
    4. The disturbances to be removed have to be completely random;

  Wherever some of the previous criticisms occur, it can be better to employ a less automatic and more *robust* cleaning method, with an higher level of control on the parameters that allows to evidence and judge the goodness of a post processing procedure. In this sense, it can be useful for instance to know the standard deviation variation during the execution of the average process, progressively considering more and more points. The importance to develop a new more controllable post-processing procedure is a key aspect to be taken into account to understand the final methodology employed to process LUNA data.

From this moment on, just one sensor at time is considered: a single time-signal has to be processed, in order to extract the strain mode-shape information-content of each gauge.
The developed data cleaning procedure is strictly dependant on the choice of the forcing waveform: in the experimental measures the structure is excited by a stepped sine action. As a result, the plate dynamic response is expected to be a sine at the same frequency of the force, with an amplitude and a phase that will result by the FRF. The final aim of the signal cleaning is, practically, to determine in a reliable way the strain amplitude and the phase of the response in correspondence of the measured location. This means that it is necessary to extract from the signal a *clean sine*, not influenced by spikes or wave-*distortions* given by disturbances.

As previously explained, the undesired disturbances in the signal can be ideally collected into two categories. The cleaning process is coherent with this noise scheme.
As a matter of fact the process includes two main steps:

1. Spikes elimination;
2. *Unreliable values* influence attenuation;

Both the analysis are performed in the time domain, considering sensor by sensor. The final aim is to define a single value of strain per each sensor, as much correct and reliable as possible.

The first issue concerns spikes individuation. The most efficient way to evidence the presence of spike values is to analyse the ratio between the signal peaks and the *actual* value of the signal in the time domain. The right index to be employed is the Crest Factor (CF) due to its ability to indicate how a peak is *extreme* in the relative signal waveform.

$$CF_x = \frac{max(|x(t) - \mu|)}{RMS_x} \tag{5.2}$$

Where $x(t)$ is the original acquired time signal, μ is the mean value of the signal. RMS_x is the root of the mean square and it is computed by the following equation:

$$RMS_x = \sqrt{(\frac{1}{n}\sum_{i=1}^{n}(x_i(t))^2} \tag{5.3}$$

The CF is used in the first cleaning step as *spikes detector*. Practically CF is calculated for the entire time-record, considering all the originally acquired time-samples. If the resulting CF is considered *excessive*, the sample with the maximum amplitude in the signal (in terms of absolute value) is removed. The CF value is defined *excessive* if higher than a *critical threshold value*. This procedure is re-applied until the signal CF is considered *satisfactory*. So the spikes cleaning step in post-processing has an iterative nature: the spikes are progressively removed in order to obtain a signal considered sufficiently spikes-free. It is fundamental to success in the procedure to correctly choose the *CF critical threshold value*. In this sense it is possible exploit the advantage given by the stepped-sine excitation: the signal acquired is a *dirty* sine with spikes. For that, it is possible to compare the CF of the acquired signal to an ideal CF value referred to an analytical sine.
The CF of an exact sine without off-set, is always $\sqrt{2}$, due to:

$$RMS_{sine} = \sqrt{\frac{1}{n}\sum_{i=1}^{n}(x_i(t))^2} = \sqrt{\frac{1}{n}\sum_{i=1}^{n}(A\cos(\omega t + \phi))^2} = \frac{A}{\sqrt{2}} \tag{5.4}$$

Where A is the amplitude of the sine and $x_i(t)$ is the i^{th} time-sample. In this way, for an analytical sine with $\mu = 0$, it is possible to substitute the presented RMS_{sine} in the 5.4, obtaining:

$$CF_{sine} = \frac{max(|x(t) - \mu|)}{RMS_x} = \frac{A}{RMS_{sine}} = \sqrt{2} \tag{5.5}$$

Actually the signal, even purified by spikes, is not a perfect sine: still persist the presence of the previously called *unreliable values*. So, due to the last consideration and in order to be precautionary, the *threshold value* for CF has been thought to be set as $4 \cdot CF_{sine}$, so $4\sqrt{2}$. When, during the cleaning iterations, the *threshold value* of CF is reached, the procedure can be considered as successfully completed. At this step the signal is sufficiently similar to an ideal sine, at least concerning the presence of spikes and irregular peaks. Each value that has been discarded from the time-record during the iterative process is the one that maximizes $max(|x(t) - \mu|)$ during that iteration. Practically, at each cycle the time-sample with the highest difference in terms of absolute value respect to the mean value μ is excluded. In this way the cleaning is performed spike-by-spike, till the desired *threshold value* of CF is reached.
The meaning of spike-value in the original time-record is clarified by the following figure:

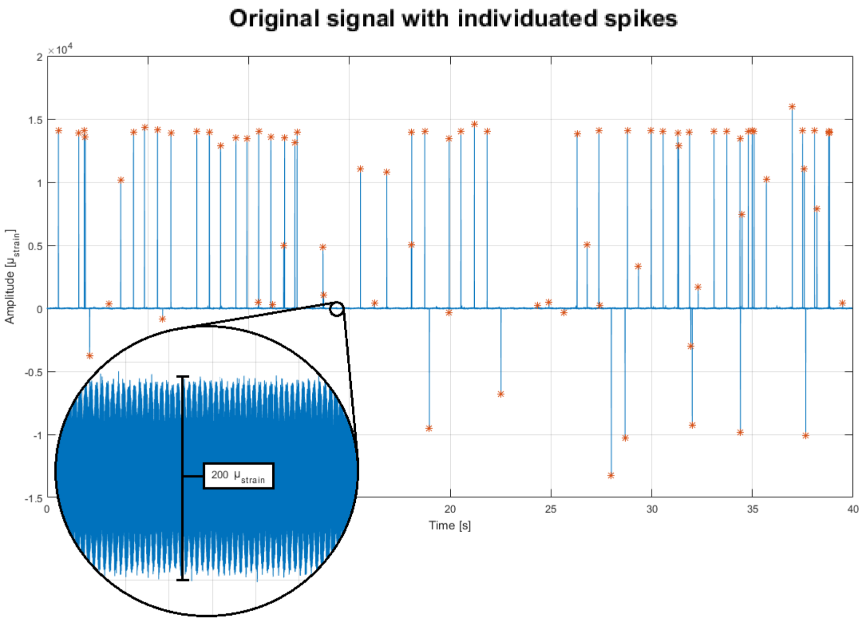

Figure 5.4: Original time history of the sensor 400 in the excited frequency of $84Hz$, number of individuated spikes: 79

At this step, it is possible to confirm that the spikes have been totally removed from the signal.

Now that the spike values are removed, it is possible to proceed with the second cleaning step: the elimination of the *unreliable values*.

As previously widely explained, a standard time-averaging procedure is not suitable to clean the LUNA output signal. As a matter of facts, the best approach can be represented by a *forced* sine reconstruction, point by point. It is possible, once again, to take advantage from the excitement-force waveform (stepped sine). Per each sensor the expected structure response is a sine and its frequency is known due to the stepped-sine forcing strategy. For that, it is possible to discretise each sine-period of the entire time-record into a certain number of time intervals. The period *time-discretization* is a free and user-dependant parameter.

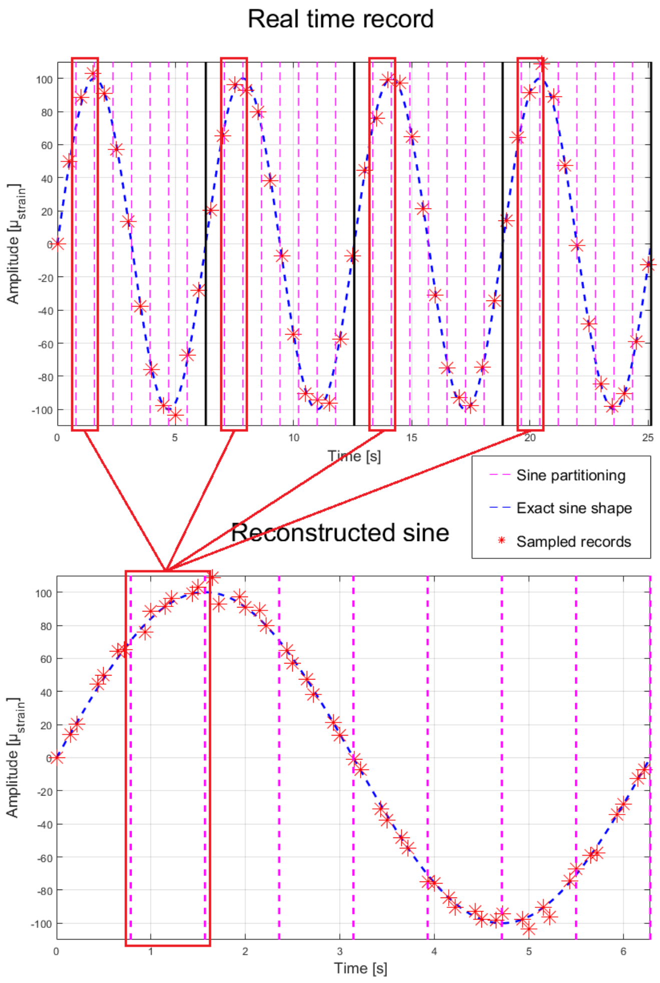

Figure 5.5: Representation of the *single sine response* reconstruction

According with this approach just one response sine-period is reconstructed, considering one time-sample at time and arranging it in the time interval of competence.
The time-discretization quality (i.e. the number of intervals that split each period) of the reconstructed sine is an input variable of the process. The smaller is the time interval, the smaller is the number of points that fall in the slice, but the probability to rebuild a sine-period with the same amplitude of the real one is higher. To use an higher time-discretization quality means to reduce the Δt where the real data of the original signal are aggregated. So the precision of the process is increased and the discretization error is reduced. However if the time-discretization quality is raised too much, the reliability of the average process in each reconstructed time-instant will be lower: a smaller number of data will be available per each time interval, so the statistical reliability of the averaging procedure decreases.
At this point, each time instant of the reconstructed response sine-period contains a group of values that comes from the original signal.

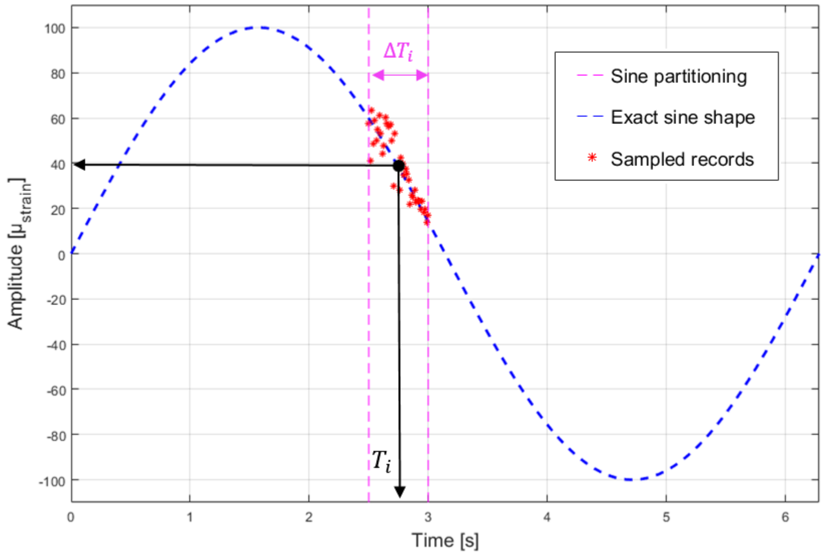

Figure 5.6: Representation of the values allocated in each i^{th} data cluster ΔT_i, before the second cleaning step

Actually, each cluster includes samples affected by all the disturbances: the *correct* values are *mixed* with the undesirable ones. For that, each set of samples has to be cleaned aiming to obtain a number of reliable values per each time interval. Once this task is performed, the remaining samples can be averaged. The applied procedure involves an average of all the strain data *allocated* inside each slice of the reconstructed sine-period. In this way each time-interval in the reconstructed sine will be characterised by a single value. It can even have no value, if the whole time-record of the sensor has no data in the corresponding slice

The main issue is that the value assigned to the time-interval under exam is calculated with a simple averaging process of the original time-samples, so it can be affected by the already explained disturbances. It is necessary to use a criterion able to guarantee the statistical reliability of the averaging process, trough the individuation of the intrusive values.

In statistical theory, Chauvenet's criterion offers the possibility to assess whether one experimental datum among a set of observations appears to be spurious. The use of such criterion permits to highlight the *unreliable values* in each class of data per each relative time-interval of the reconstructed sine.

Any unreliable disturbance-value is evidenced by the Chauvenet procedure. Per each ΔT_i time-interval the proper group of data has to be assessed. The *suspected outlier*, the time-sample under analysis, is called x_s. The required steps to be followed in such procedure are listed below:

1. Calculation of the mathematical mean of the data inside the slice, $\bar{x_i}$
2. Calculation of the Standard Deviation (STD) of these data, $\bar{\sigma_i}$
3. Calculation of the Z_{score}:

   $$Z_{score} = \frac{x_s - \bar{x_i}}{\bar{\sigma_i}} \tag{5.6}$$

   It corresponds the *times* $\bar{\sigma_i}$ that x_s differs from $\bar{x_i}$. Z_{score} is the *deviation* of x_s with respect to $\bar{x_i}$.

4. Calculate the probability that a single data belongs to the external interval $[(\bar{x_i} - Z_{score})(\bar{x_i} + Z_{score})]$. This is the probability that a single value stays *so far* from $\bar{x_i}$ in the data set distribution. It is the probability that a generic acquired value *deviates* from $\bar{\sigma_i}$ more than Z_{score}. To perform this step it is necessary to assume that data has a normal Gaussian distribution with mean $\bar{x_i}$ and the STD equal to $\bar{\sigma_i}$.

   From a practical point of view, it is necessary to calculate the Cumulative Density Function (CDF):

   $$CDF = \int_{-inf}^{\mu-|Z_{score}|} f(z) \tag{5.7}$$

To calculate the probability that a generic acquired value belongs to the external interval $[(\bar{x}_i - Z_{score})(\bar{x}_i + Z_{score})]$, the CDF has to be redouble. The $f(z)$ considered is the normal standardized probability density function:

$$f(z) = \frac{\exp(-z^2/2)}{\sqrt{2\pi}} \tag{5.8}$$

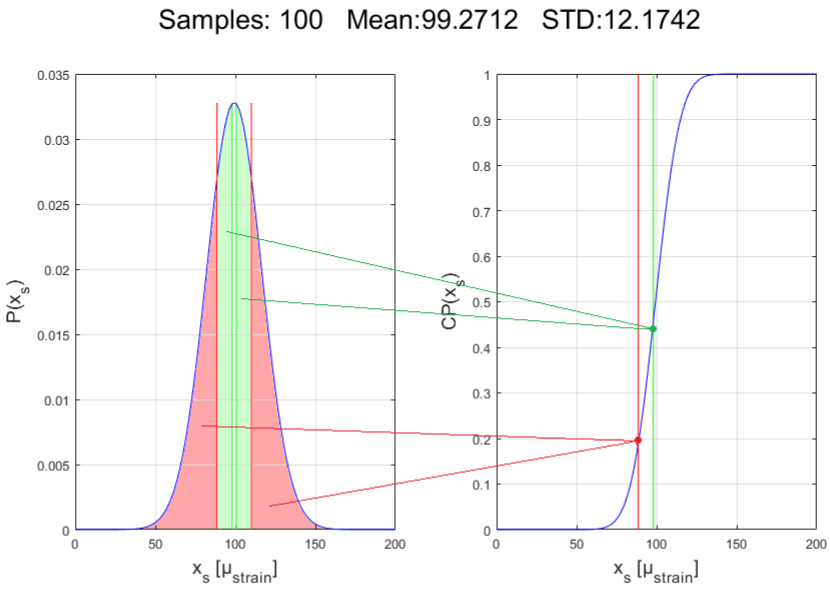

Figure 5.7: Graphical representation of the Chauvenet criterion

5. At this point the cumulative probability density function defined has to be multiplied to the number of data analysed in the group considered, n, in statistical terms the *number of observation*. According to the Chauvenet's criterion, if the calculated effected probability is lower than 0.5 the *suspected outlier* has to be considered as an effective outlier and has to be eliminated from the group of data in analysis. Probability lower than 0.5 means that there is low probability that the considered x_s belongs correctly to the data set considered and characterized by the calculated $\bar{x}_i$ and $\bar{\sigma}_i$. This means, practically, that x_s has no chance to belong to the group of data analysed, it is a spurious value. In statistical terms the probability of the *event* that a generic value *deviates* from $\bar{x}_i$ of Z_{score}, in n observations, is too low. x_s is a spurious value, with no chance to be reliable. It must be not considered during the averaging process.

The individuated outlier is an undesired value inside the original signal, it belongs to the category of the *unreliable values*. A simple iterative procedure is implemented. In each iteration the *suspected outlier* is called x_s. It is simply the maximum absolute value in the group of data considered. The Chauvenet procedure is re-applied until the iteration where the *suspected outlier* is considered *reliable*. At this point the $\bar{x_i}$ becomes the value of the response reconstructed sine associated to the instant T_i (Figure 5.6). After this step, the unreliable values are identified and removed from the usable ones. Per each process of averaging the final set of data used have a low STD and all the values belong to the internal interval $[(\bar{x_i} - Z_{score})(\bar{x_i} + Z_{score})]$. This guarantees an high quality level in the determination of each value $\bar{x_i}(T_i)$ of the reconstructed sine period.
In the first data-processing performed on real acquisitions the number of time-samples excluded by the Chauvenet criterion was around 4% of the complete amount (amount available after the spikes cleaning).
To conclude, it is possible to say that the noise is identified due to its contribution in the standard deviation determination and due to its spurious nature.

To sum up, with the iterative two-steps cleaning procedure the noise is mainly removed.

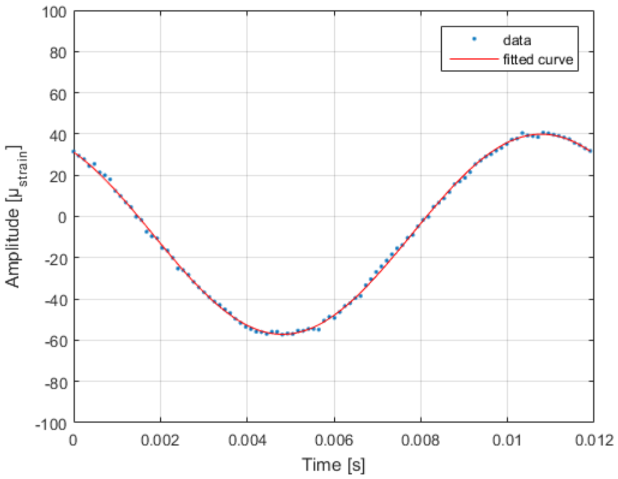

Figure 5.8: Final result of the cleaning procedure, reconstructed sine response at $84Hz$ for the sensor number 350

The spikes are removed from the time-record in the first sequence of iterations, till the *threshold desired* CF is reached. The remaining noise is eliminated by the second series of iterative-cycles in order to apply the

Chauvenet's criterion. The effectiveness of the procedure depends on the total amount of time-samples available: the longer is the time-record to process, the better is the quality of the cleaning procedure and the reliability of the result.
Figure 5.8 is a clear example of a well reconstructed sine-period once the whole procedure has been applied to the time-record of a specific fiber sensor.

5.3 Signal quality analysis

A remarkable advantage of the implemented cleaning procedure is the generation of quality indices dealing with the process of averaging. This represents a notable benefit with respect to the traditional time-averaging.
It is possible to analyse the post-processing results by means of three parameters. The first one is a real quantitative quality evaluator of the experimental acquired strain, while the others investigate the signal nature and the cleaning process.

The first quality estimator can be called *RMS quality factor*. It is practically the resulting difference between the RMS of the reconstructed cleaned sine and the *ideal* sine with the same amplitude of the reconstructed one. If this difference is appreciable, the sensor analysed has a reconstructed sine different from an ideal sine. This means that the cleaning process has not been able to extract a *well reconstructed* sine period. The cleaning process has tried to exclude all the unreliable values by searching in the data set a sine shape, but it has not reached a sufficiently coherent result. The time history values saved by the cleaning process are not enough to well define the reconstructed sine period or they are have no physical meaning. In those cases, the average process for each time interval is not reliable, because many instants in the reconstructed response have no survivor values associated of accurate and coherent value.
In the following Figure 5.9, how the RMS quality factor is able to describe the goodness of the reconstructed sine period of a single sine is explained.
It is clear that the RMS-difference index is able to define the quality of the signal sensor by sensor in all the fiber. In Figure 5.9 four sensor processed signals are compared, all the four reconstructed response sine refer to the same acquisition at $84Hz$ but in different fiber length positions. It is evident that the RMS-difference index represents the capability of the data of a single sensor to fit a pure sine. With ideal acquisitions the RMS-difference index would be theoretically zero. The higher is RMS quality factor the lower is the quality of sine reconstruction. When the RMS quality factor of

a sensor increases, no correlation among the sensor data and a period of a single sine exists. In this sense, the *points cloud* of the *worst* sensors has no similarities with a desired sine. The example of these kind of *sensor behaviour* is presented with the sensor 406 at $84Hz$ (Figure 5.9). In this case the RMS quality factor strongly increases. Theoretically the *point cloud* is *infinitely* different from a sine shape. For these reason, all the sensor with a RMS quality factor higher than 3000 can be considered as *worst sensors*, this makes more readable the following graphs. Such sensors have to be excluded from the effective modal shape reconstruction.

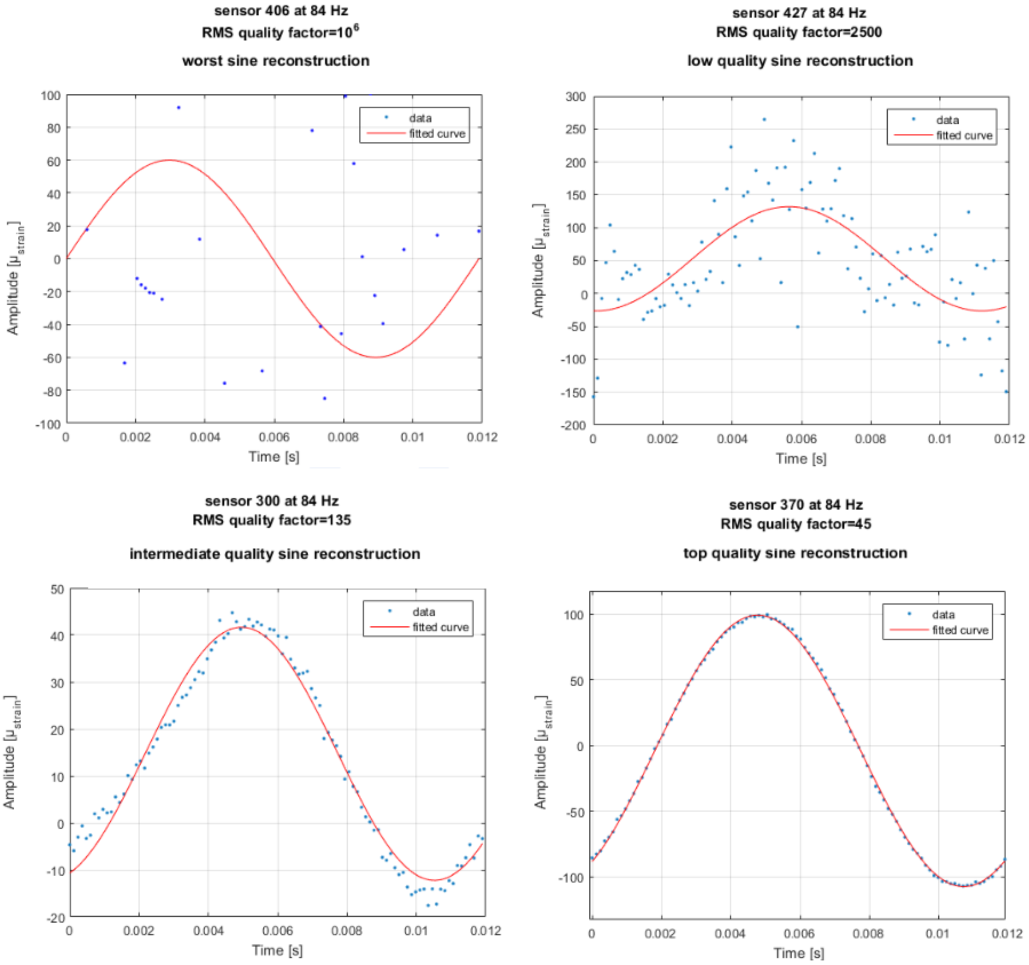
sensor 406 at 84 Hz
RMS quality factor=10^6
worst sine reconstruction

sensor 427 at 84 Hz
RMS quality factor=2500
low quality sine reconstruction

sensor 300 at 84 Hz
RMS quality factor=135
intermediate quality sine reconstruction

sensor 370 at 84 Hz
RMS quality factor=45
top quality sine reconstruction

Figure 5.9: Comparison among different signals RMS quality factor

It is possible to analyse the RMS quality factor along the fiber length, in order to understand which are the sensor with the worst quality. Generally the sensor quality decreases in the last part of the fiber. Considering a fiber length of 1.8 meters in the preliminary optimized configuration, the RMS-index is quite constant in the first three quarter of the fiber, while in the final part the index increases dramatically (the considered length is lower than 2 meter due to the low-friction polymeric sheath section 4.4). This trend can be well represented by the analysis of the following acquisition at $84Hz$ (Figure 5.10):

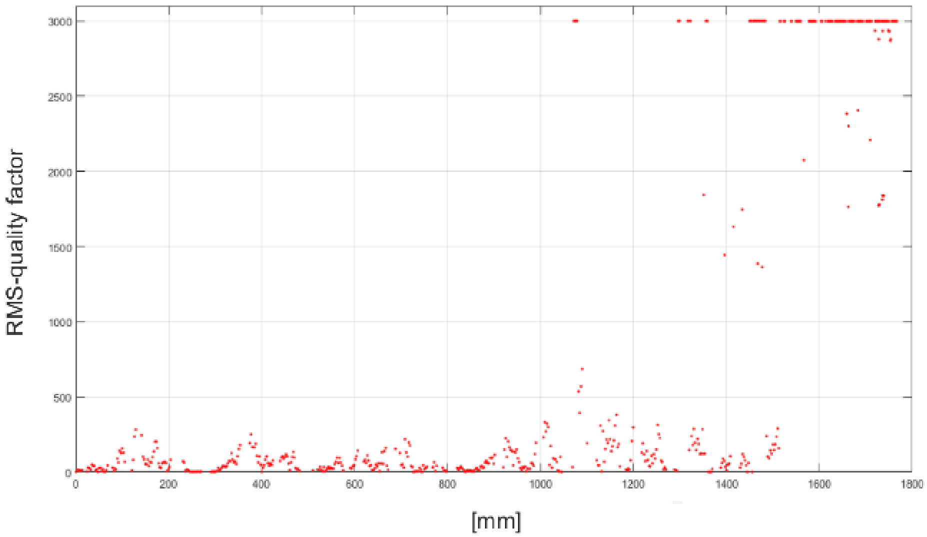

Figure 5.10: RMS quality factor along the fiber length at $84Hz$ in the preliminary configuration

In Figure 5.10, all the sensors with a RMS quality factor higher than 3000 are set to 3000 just to better present the results. As previously said, the sensor set to 3000 can be all categorized as *worst sensors*. It is evident that the RMS quality factor saturates in the final part of the fiber. Generally it is clear the positive trend. In figure Figure 5.10, some smooth amplifications of the RMS quality factor can be found around $150mm$, $390mm$, $450mm$, $700mm$ and $900mm$. These very low peaks of the RMS index are not related to a *local loss of quality*, but are caused by the increase of the amplitude of the physical signal. The RMS quality factor tends to be more sensitive to the *disturbances*, in case of sensor with considerably high sine amplitude. To conclude, surely the most reliable sensors will be in the first $1500mm$ of the fiber length.

This kind of analysis has been performed with a preliminary $1800mm$ length fiber configuration. In the final OSP algorithm, the length considered as *effectively available to be optimized* is reduced to 1.5 meters due to the individuated RMS quality factor trend along the fiber. This pre-processing

choice is considered to avoid the arrangement of necessary sensors where the experimental quality data would be too low in the optimized fiber configuration.
To properly reconstruct the modal shape, it is fundamental to consider as input for the StD process just the sensor with an elevated signal quality. For that, not all the strains acquired are effectively considered in the modal shape reconstruction: the sensors that present too low quality in the frequency of interest are excluded. Practically the sensor with higher RMS quality factor have to be kept out.
This result is coherent with the robustness-check used in the pre-processing to search the best fiber configuration: in the OSP algorithm used, each fiber positioning in the genetic algorithm is processed with a progressive decrease of sensor number. In that case the cost function is computed with the elimination of a part of the original set of conflagration sensors. In GA even the fiber behaviour respect to the *loss of sensor* is tested. The winner configuration would be the one that gives the best modal shape reconstruction even with a considerable sensor loss. So it is better to eliminate the *bad* sensor and proceed with less sensors available than use *wrong* strain information.

The second quality index that can be computed is the *final mean-number of used time-samples* in the averaging process of strain values allocated in the same *relative time interval.*

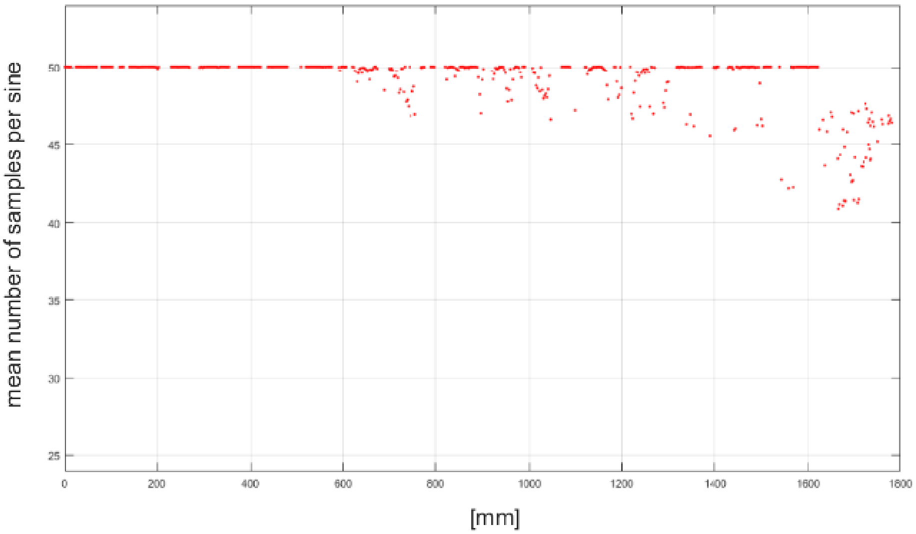

Figure 5.11: Mean usable data number per sine along the fiber length, after the cleaning process at $84Hz$ in the preliminary configuration

This parameter practically states the number of data used, as *average*, to calculate the $X_{strain} sin(t_i)$ in each single i^{th} time instant. It is a *mean among the number of values* that are accounted in the averaging process in each relative time interval in the final reconstructed sine period. This gives an idea about the reliability of the average process performed to obtain the final reconstructed sine, and about the reliability of the Chauvenet statistical approach to clean the data.
Actually, the *final mean-number of used time-samples* is affected by the presence of spikes: if the original signal contains spikes, the final mean-number of used time-samples has to decrease. So this estimator gives a global idea about the amount of survivor data after the two-step cleaning: it is not able to distinguish among the two categories of *undesired values*, previously called *spikes* and *unreliable values*.

The third indicator is the *number of spikes* found in the original signal. This index does not affect the quality of the modal shape reconstruction since the spikes can be completely removed. This is clear from an analysis of the RMS quality factor in the sensor with the highest number of spikes: the group of sensors with many spike values have a good quality in the sine response reconstruction. This means, practically, that the presence of spikes does not affect the final quality of the mode shape definition.

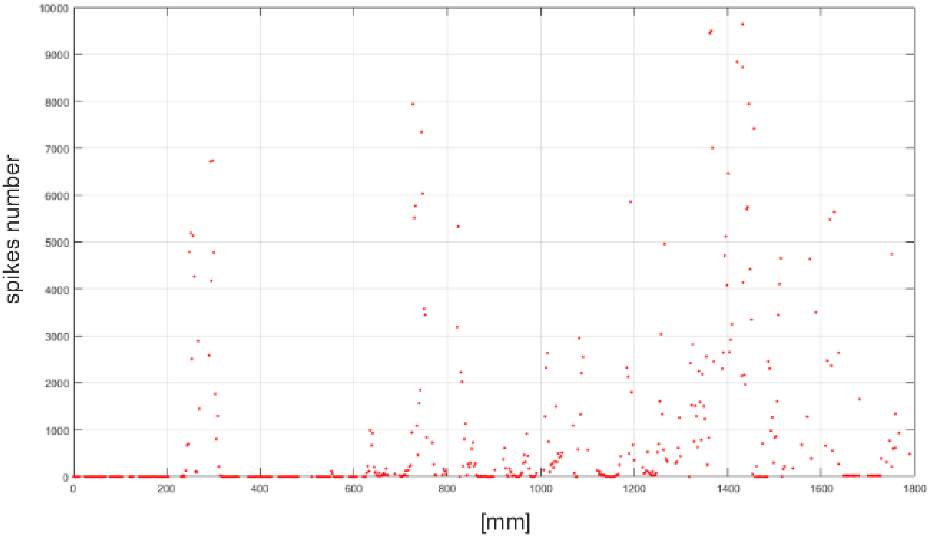

Figure 5.12: Spikes number in the original signal along the fiber length at $84 Hz$ in the preliminary configuration

Nevertheless an evident spikes presence compromises the number of usable data. If many acquired time-samples in the signal are spikes, the number of strains with reasonable values is lower. To sum up, the spikes values are not e real criticisms in the LUNA output since their elimination can be performed efficiently and no disturbances originated by the spikes remains the final clean signal. The only consequence is in the reduction of usable data in the time acquisition. This can be easy compensated with longer acquisitions.
It can be possible to investigate the evolution of the *number of spikes* along the fiber looking at Figure 5.12. In the previous figure it is evident that the number of spikes has no a real trend along the fiber. It does not clearly increases with the length. Nevertheless it presents some considerable peaks in some distinct fiber positions. These positions are the locations where the fiber configuration exhibits the most critical series of curves. This analysis has been made with the *preliminary* configuration, where the optimization does not include any considerations to limit the criticism regards the radius of the curves. In Figure 5.13 it is evident the relation among the spikes presence and the curve criticism.

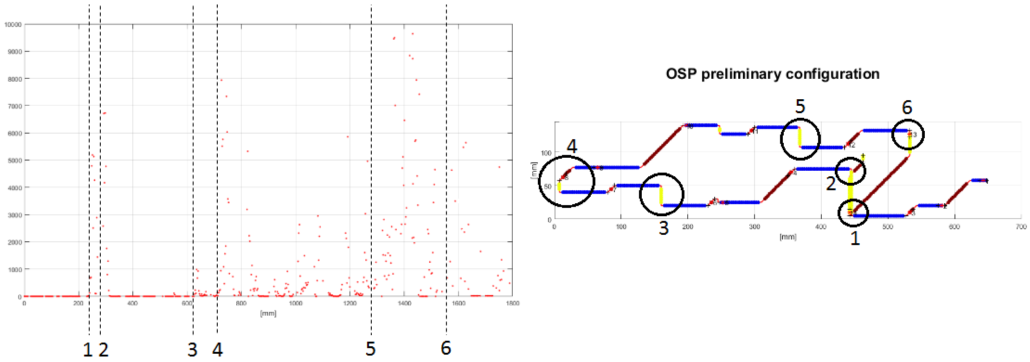

Figure 5.13: Spikes number in the original signal along the fiber length at $84Hz$ correlated to fiber bends

In the preliminary OSP configuration, the critic curves are situated around $200mm$, $270mm$, $600mm$, $770mm$, $1300mm$ and $1520mm$. In Figure 5.13 it is underlined that the spikes number increases considerably after those fiber locations. The sensors with the highest number of spikes are those located after the critic curves. This is extremely coherent with the considerations regards the minimum permitted fiber radius explained in the subsection 3.6.2.

It must be noticed that the last two indices are able to evidence the kind of disturbance on the original signals. They are not real *quality estimator*, like the *RMS-quality* factor. They make possible to analyse the nature of noise

on the sensor at a certain excitation frequency.
On the contrary, it is possible to affirm that the *RMS-quality* index is the quality estimator of the *final goodness* of the sensors. So the index that evidences the presence in each sensor of a certain *residual noise* on the final reconstructed signal.

It is generally possible to find sensor with an inadequate *RMS-quality* index, and characterized by a low number of relived spikes. This can be easily explained as following. The sensor with a *bad RMS-quality* index would be the sensor with a more *dirty* time-record. Actually this *filth* can be related to the presence of the so called *unreliable values*. In these sensors the original signal, even without the spikes, is not similar to a sine.
So the first cleaning step based on CF is not able to find and evidence the occurrence of *dirty* values inside the record. If the time history is not similar to a sine, the method to individuate the spikes based on CF can not be effective. It is not able to remove efficiently and coherently the spikes. In these cases the initial time signal is too damaged, CF cleaning and the Chavenuet cleaning can not be applied. The Chavenuet criterion does not work properly mainly because there is no kind of sine to *search* in the signal, but even because the CF has not been able to prepare the data set of each time interval where Chauvenet is used. For Chavenuet cleaning the cluster of values considered has to have Gaussian distribution. These *dirty* sensors will have the worst RMS-quality index, as evidenced by Figure 5.9. However it has to be noted that this inability of the CF cleaning-step comes from a strong presence of *unreliable values* in the signal.

It is clear that no sine-like distribution can be seen in the first reconstructed sine period of Figure 5.9. *RMS-quality* is a good detector of this criticism as can be seen by the same figure.
As previously anticipated, the sensors with such a critical *RMS-quality* index are really not reliable and have to be excluded. In order to obtain a satisfying modal shapes reconstruction, these critical fiber positions have to be kept out by both the optimization and post processing.

At this point some final consideration concerning LUNA signal output can be elucidated. The most critical nature of noise is the one initially called *unreliable value*, so value physically plausible but statistically unreliable and, at the end, not usable. This kind of disturbances on signal can make *ineffective* the implemented cleaning procedure and not employable the sensors more affected. This is the main issue evidenced in the LUNA CU investigation.
Now it is deepen to analyse how this LUNA criticism depends on the frequency and on the bend matter. This analysis is performed by studying the results collected with OSP preliminary configuration. As anticipated, the genetic

code that generates this configuration does not include any optimization to compensate LUNA criticisms, any expedient to reduce the *unreliable values*, any precaution regards the bends presence and risks. The scope is to investigate LUNA criticism causes and relations, in order to implement a final OSP algorithm able to reduce the sensor with such awful *RMS-quality* index.

First of all it is necessary to understand the role of the fiber curvatures in the decrease of signal quality. As previously explained, by observing the Figure 5.9, it is possible to affirm that the quality of the signal decreases in the last part of the fiber and it is not associated *directly* to fiber bends. No correspondence is evident among the bend positions and RMS-quality factor amplifications. Bends, as explained in the Figure 5.13, are mostly related to spikes and generally the spikes can be easily removed. They influence *just* the number of available time samples for each sensor, but this issue can be surpassed with long acquisitions. Nevertheless, the fiber bends role in the final *RMS-quality* index is however fundamental: the higher is the number of critic curves and the lower is the radius of the bends, the worse the *RMS-quality* index will be in the last part of the fiber. So the bends generates directly the spikes, but influences indirectly the signal quality of the last sensors along the fiber. The effect of the bends on the RMS quality factor in the last sensors invalidates heavily the mode shape reconstruction.

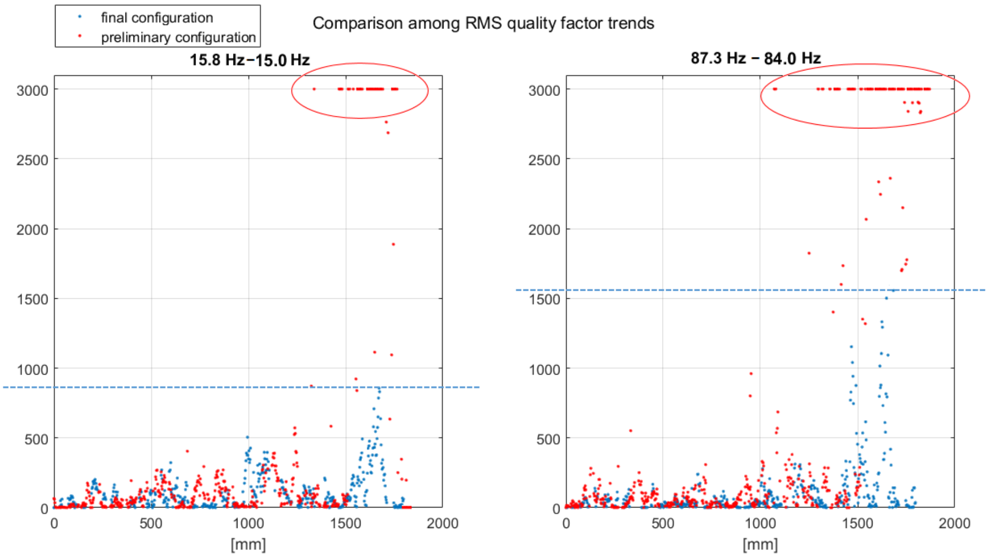

Figure 5.14: Comparison among two different configurations in terms of RMS quality factor along the fiber length

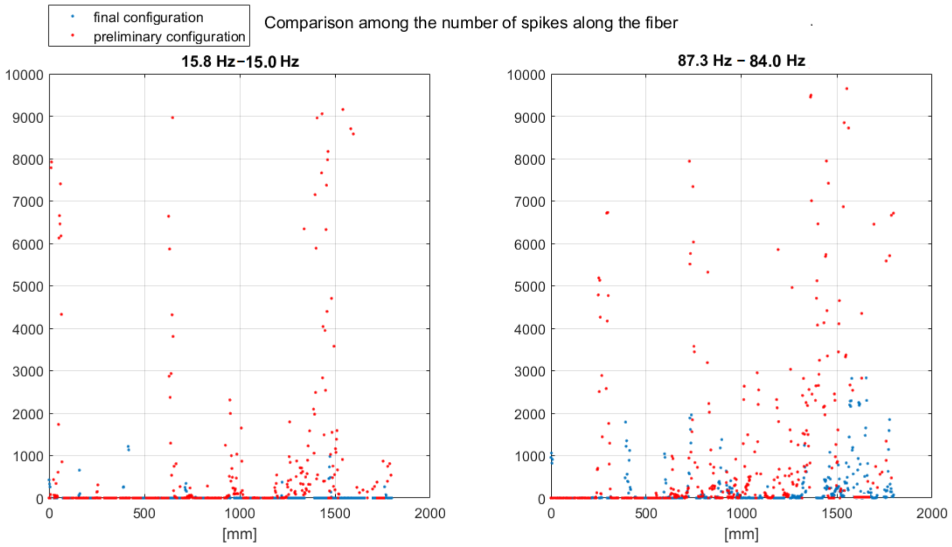

Figure 5.15: Comparison among two different configurations in terms of signal spikes number along the fiber length

If thigh curves in the fiber configuration are avoided two effects will be obtained:

1. The global number of spikes along the fiber length is reduced;
2. The worsening of the *RMS-quality* index in the last part of the fiber is limited;

Figure 5.14 and Figure 5.15 will explain these two important successful results. The *RMS-quality* factor is reduced especially in the last part of the fiber. In the preliminary configuration many sensors have the *RMS-quality* factor superior than 3000 and the slope trend of the index of *bad-quality* versus the fiber length is higher. While in the new OSP configuration all the sensors have a *RMS-quality* factor lower than 900 at $15.8Hz$ and lower than 1600 at $87.3Hz$. No sensors have *saturated* the RMS-quality factor scale, no sensors have RMS index higher than 3000. A sufficient high signal quality is obtained for all the sensors. All the 1.8 meters fiber length can be considered as usable and reliable for the mode shape reconstruction. This is an important result obtained with the final OSP implemented algorithm. The minimum permitted radius has been finally fixed to $10mm$.
At this point it is explained how to obtain a satisfactory signal quality along quite all the fiber.

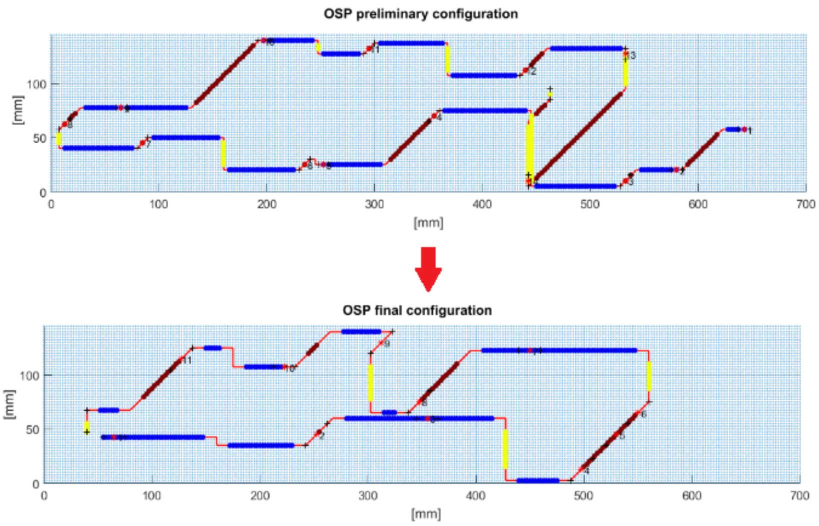

Figure 5.16: Comparison among the preliminary optimized configuration and the final optimized configuration

Now it is possible to investigate the behaviour of the noise and of the signal quality in the frequency domain. The dependence on frequency of the spikes number can be described by Figure 5.17.

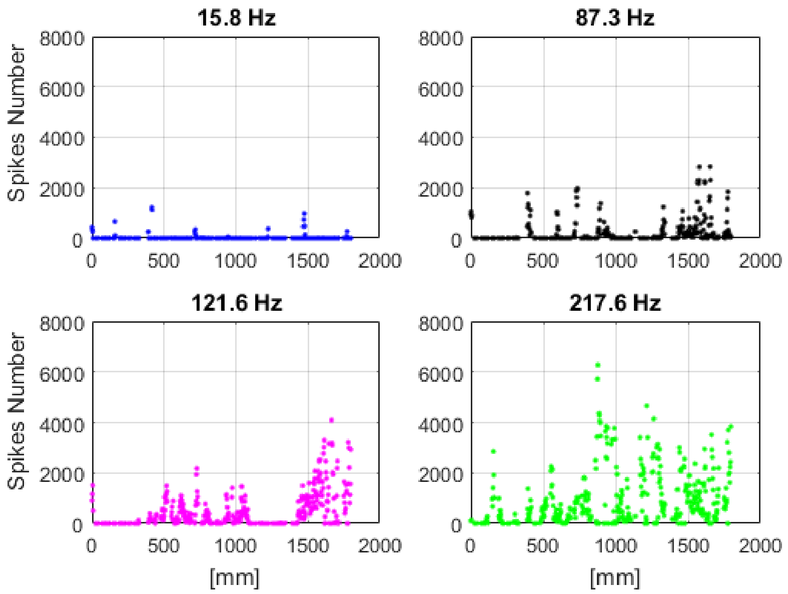

Figure 5.17: Comparison among the signal spikes number distribution along the fiber length at different frequencies

Just four frequency acquisitions graphs are reported, but the trend is clear: the spikes number increases at high frequency.
Now the behaviour in frequency of the *RMS-quality* factor can be analysed through Figure 5.18.

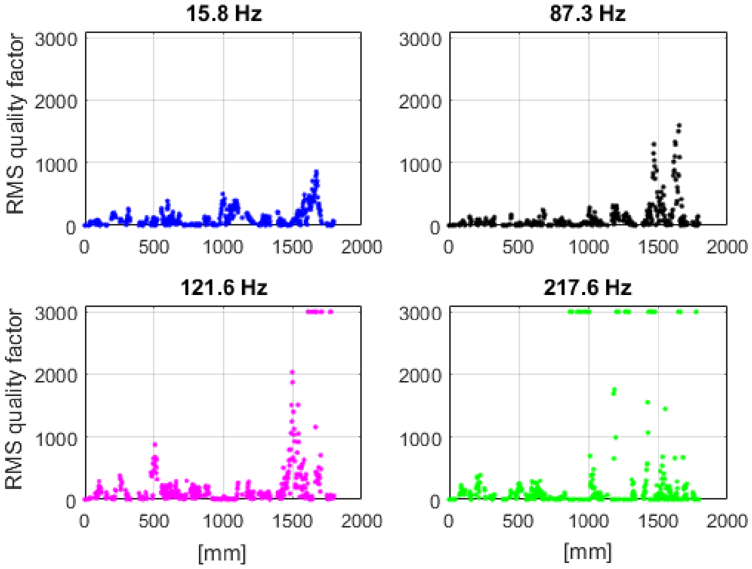

Figure 5.18: Comparison among the RMS quality factor distribution along the fiber length at different frequencies

This is one of the most important parts of the considerations regarding the signal quality. The results are presented for the final OSP configuration, where the bends issue has been already limited by the optimization code. It is evident that the quality of the acquired time histories remains sufficiently high until the mode at $87.3Hz$. In the acquisition at $121.6Hz$, the *RMS-quality* factor of the sensors in the last part of the fiber begin to *saturate* at 3000. At the frequency of $121.6Hz$, some of the sensors in the last part of the fiber start to behave as *awful* sensor. Their reconstructed sine is similar to the data representation of the so called *worse* sensor of Figure 5.9.
Nevertheless for the mode at $121.6Hz$ it is still possible perform the modal reconstruction. It is sufficient to eliminate the sensor with such *worse quality*. It will be shown in the following chapter. Finally at frequency $217.6Hz$ many sensors lose completely the coherence. The *RMS factor* goes to infinite for many fiber locations, even at $900mm$ along the fiber length. In this case to many sensors have to be discarded and so no modal shape reconstruction can be completed.

It possible to define $220Hz$ as the upper limit where the LUNA CU can be considered reliable in dynamic acquisitions.

This limit concerns the OSP final configuration, the available physical fiber and the available manual fixing-glueing method. Actually the real limit is not just related to the frequency, but it is caused by a more general limitation in the fiber deformation velocity $\mu\epsilon/sec$. This strain variation velocity is directly proportional to both the frequency and the amplitude of the structure response. In this sense, the amplitude of the strain response has to be modulated during the experimental tests to compensate the growing frequency and obtain a satisfying signal quality. In particular the amplitude has to be reduced when the frequency arises.
As a matter of fact, the main issue at high frequency is the necessary considerable reduction of the signal amplitude required to maintain an acceptable deformation velocity value. Above $90Hz$, the signal amplitude has to decrease so much to obtain a satisfactory value of deformation velocity that the physical response signal energy becomes seriously low. In these cases, to attempt to preserve a good strain data quality, the signal becomes too less reliable. Its amplitude arrives to be comparable to the measure instrument uncertainty. Anyway this produces a useless strain acquisition. For this reason the mode shape reconstruction for the high frequency modes is so critical. The desired amplitude of the response would be too low to maintain reliability in the strains management. As a consequence, a decrease in signal quality has necessary to be accepted for the modes at higher frequency than $90Hz$. As explained many sensors will have a $RMS - quality$ index too *bad* and have to be excluded. Their number increases when the frequency arises. With the explained minimum limitation of the signal amplitude, the upper limit in frequency is represented by $220Hz$, as affirmed.

The high frequency analysed-modes show another obstacle: the complexity of these modal shapes causes a more *stressed and deformed* fiber configuration during the acquisition and this can produce a more *disturbed* output signal.

To conclude, the deformation velocity limit has to be increased in order to obtain a satisfying quality of the mode reconstruction, in particular at the high frequency. In this way even the upper limit of $220Hz$ would be surpassed. Reliable acquisitions with a sufficient signal amplitude would be performed. In this sense proposing prospective are offered by the new version of LUNA OBR fiber technology which has been recently put on the market. This new acquisition system is effectively designed for dynamic applications and it promises to be able to reach considerable deformation velocity values. With this new upgrade of the investigated LUNA measure system and the proper innovative proposed OSP algorithm, it will be possible to extrapolate structure vibration modes with a simpler post-processing and high reliability results. The quality of the signals will be enhanced and the upper limit in frequency probably will result improved.

5.4 Mode-shapes reconstruction procedure

The reconstruction of the response sine, starting form the time history of each fiber gauge, is fundamental since it permits to calculate the module of strain in correspondence of the fiber sensor considered. The cleaned module of the strain per each sensor is the input of the integration algorithm to reconstruct the modal shape. So, practically, the cleaning-process output gives the necessary informations to start with the complex procedure to determine the final displacement modal-shape of the whole surface of the structure.

At this point, a reliable reconstructed response-sine is obtained per each sensor: the amplitude of the sine is the measured strain in the considered location when the structure is excited with the stepped sine approach. The phase of the sine is used to impose the relative right sign to the strain fields. At the end of the process to acquisition, sensor position localization and signal cleaning, the available information for each sensor in the fiber are:

- The spatial position (coordinates x,y) of the considered sensor;
- The strain value associated to the modal shape excited;
- The measure direction of the sensor considered;
- An index of *reliability* of the acquired strain value in the considered sensor.

The final phase of the post-processing is the actual the mode shape reconstruction. The main idea of the pre-processing was to *simulate* the strain-based modal-shape reconstruction, in order to obtain the best fiber configuration to optimize the resulting mode determination. In this sense, it is fundamental the application in the post-processing of the same *strain to displacement* procedure used in the pre-processing. This assures the effectiveness of the optimization of fiber arrangement even with respect to the *integration and interpolation* processes included in the mode re-building operations.
To conclude the available data experimentally measured are interpolated on surface to generate three continuous strain fields, exactly as in the pre-processing simulation: $\epsilon_x = \epsilon_x(x, y)$, $\epsilon_y = \epsilon_y(x, y)$, $\epsilon_{45} = \epsilon_{45}(x, y)$. At this point all the procedure explained in section 3.5 can be applied to complete the

post-processing of the acquired strain and arrive to generate the displacement vibrating modes.
To sum up, the final mode shape reconstruction is exactly the same of the procedure implemented in OSP algorithm, except for the input data that in the post processing are the measured strains while in the pre-processing were the FE model output.

Chapter 6

Results - thin plate mode-shapes reconstruction

In this chapter the experimental results are presented. The $w(x, y)$ field, whose reconstruction is the main task in this scenario, is obtained starting from the surface acquired strains.
All the information concerning the experimental set-up can be found in chapter 4. The fiber arrangement employed is the one in section 3.7, generated by the optimal sensor placement (OSP) algorithm.
After a proper signal processing (chapter 5) the strain-to-displacement transformation is performed relying on the interpolation-integration procedure explained in section 3.5.

6.1 Experimental mode-shapes reconstruction result

The reconstructed mode-shapes will be presented through a comparison among three w fields. The experimentally obtained mode-shapes (on the right) are compared with the *exact* ones provided by the FE-analysis (on the left). In the middle it is proposed the shape reconstructed by the *simulation* of the measurement process, starting from the *virtual* strain-fields generated by the FE-software. This represents the result coming from an *ideal* measurement.
Mode-shapes till the 6^{th} mode (Figures 6.1 to 6.5) are well reconstructed. The ones of modes 7, 9 and 8 (Figures 6.6 to 6.8) have some criticisms that will be explained step-by-step.

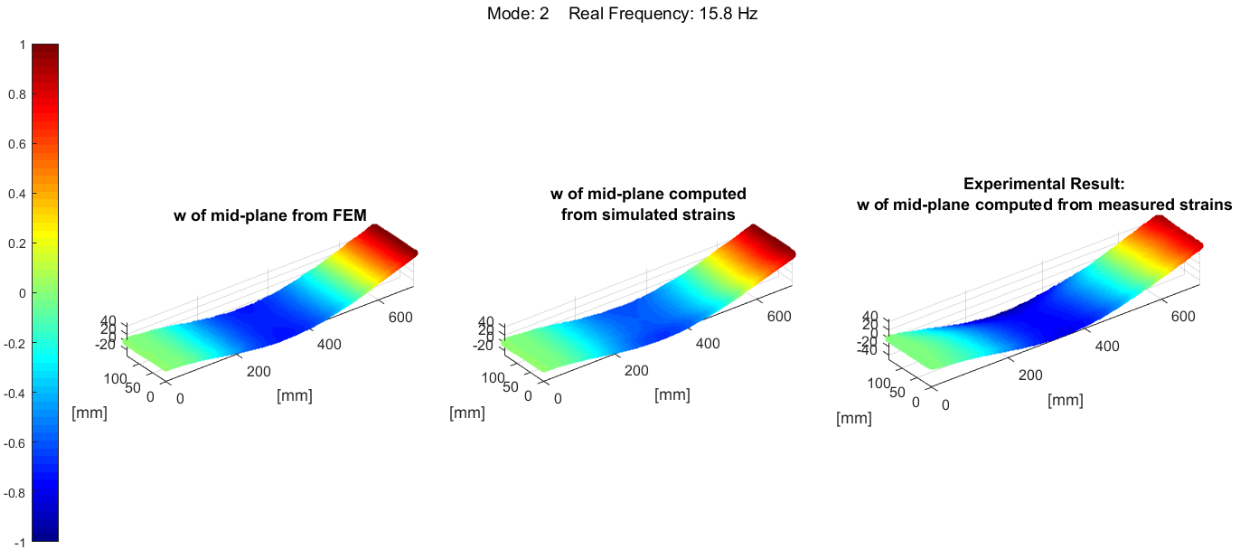

Figure 6.1: Experimental 2^{nd} mode-shape at $15.8 Hz$

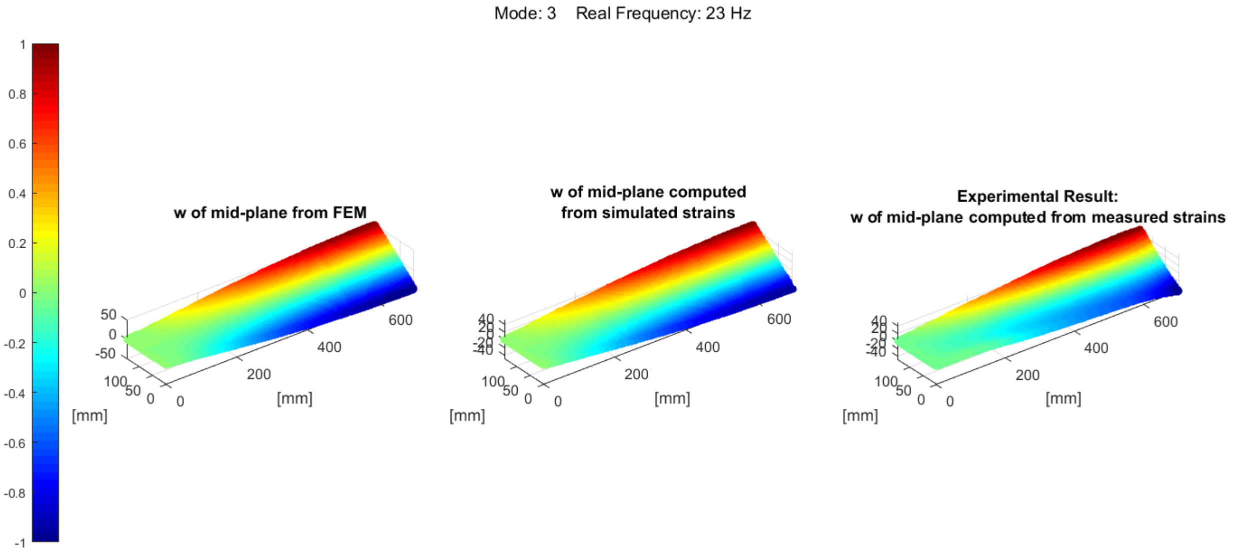

Figure 6.2: Experimental 3^{rd} mode-shape at $23 Hz$

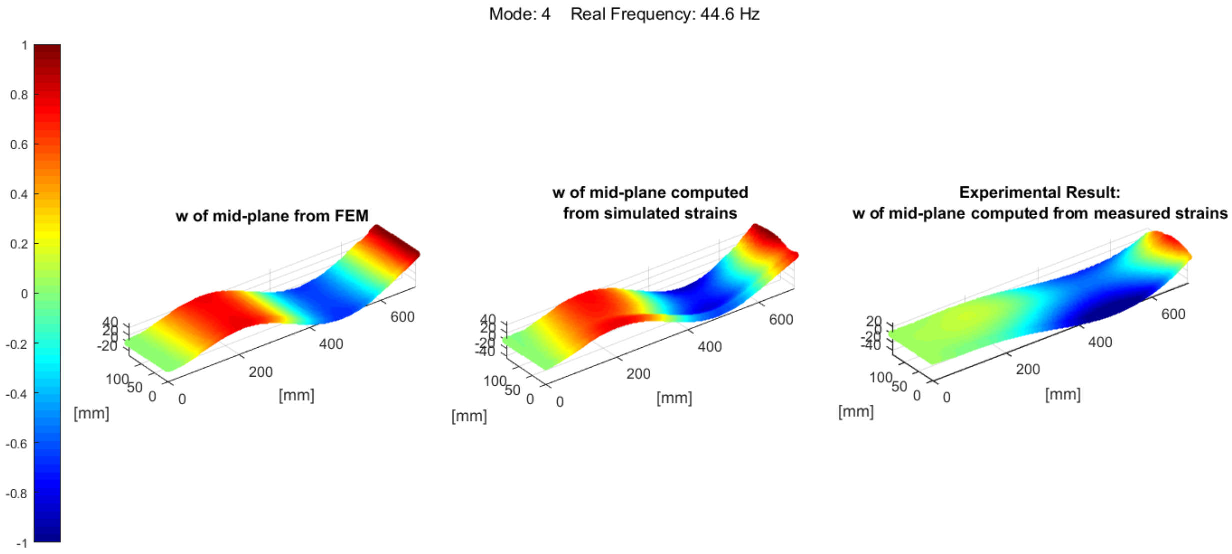

Figure 6.3: Experimental 4^{th} mode-shape at $44.6Hz$

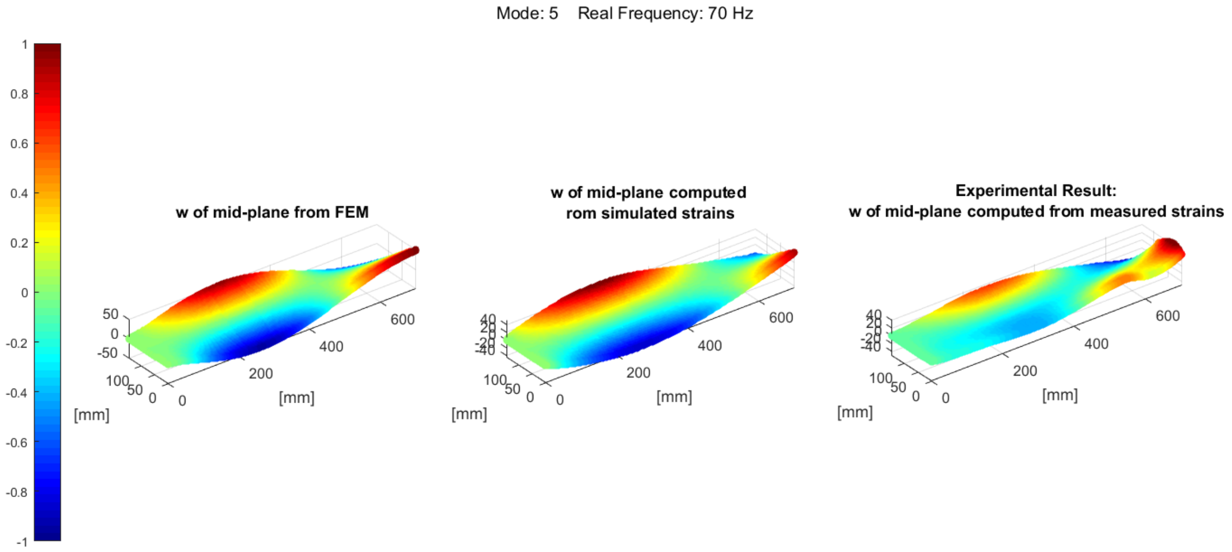

Figure 6.4: Experimental 5^{th} mode-shape at $70Hz$

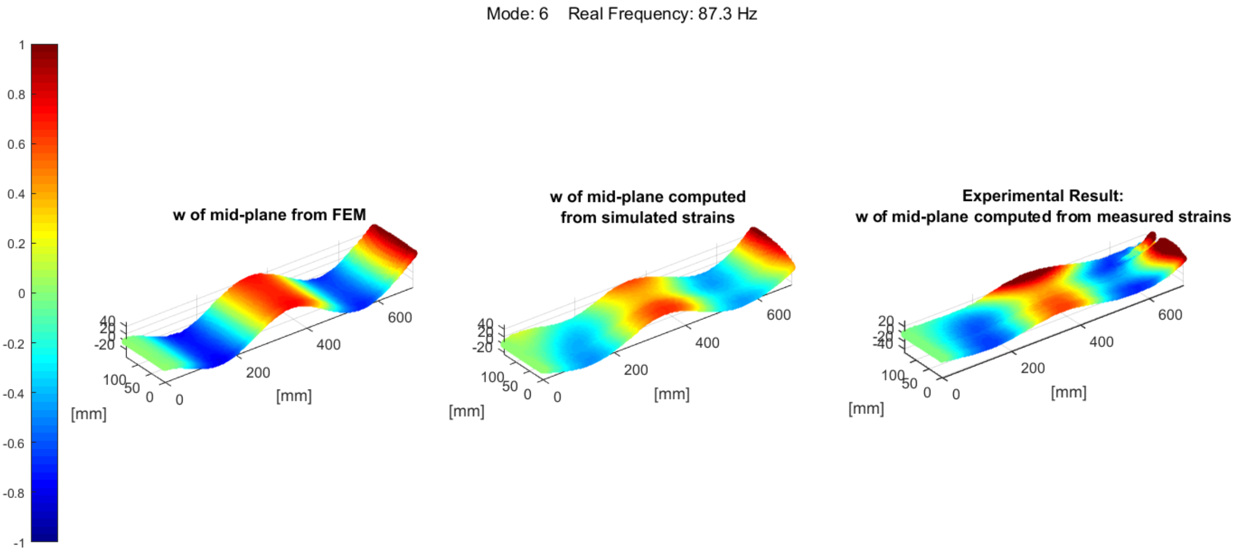

Figure 6.5: Experimental 6th mode-shape at $87.3Hz$

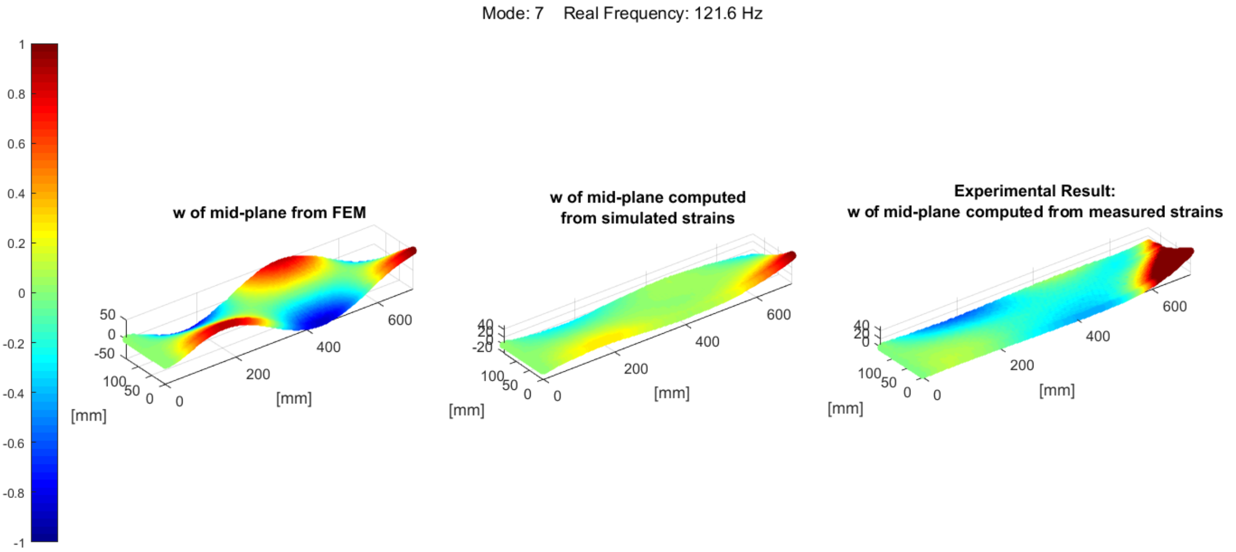

Figure 6.6: Experimental 7th mode-shape at $121.6Hz$

The 7^{th} mode, Figure 6.6, has some difficulties to be sufficiently and completely reconstructed. This issue is obviously related to its considerably high frequency, next to the Nyquist one according to LUNA control unit CU limit. Actually, it is possible to observe that the mode shape reconstruction is really well determined in the first part of the plate, until $600mm$. Being the value of w normalised with respect to its maximum absolute value, due to the strong singularity next to the plate *tip* the real trend of the displacement in the other zones is somehow *hidden*.
The error concentrated next to the plate tip can be caused by the fiber configuration (Figure 3.26): the chosen fiber disposition has no sensors in that zone. In the plate tip-area the mode-shape reconstruction totally relies on interpolation and extrapolation procedures of the strain fields.
According to the initial strain-field *simulation* with the FE-analysis to perform the optimal sensor placement (OSP), this interpolation-extrapolation procedure to define the $w(x, y)$ at the tip was not critical. Mode-shape was well reconstructed. As a matter of fact, strains were the *correct and ideal* ones, and the fiber disposition was optimized to *work* as well as possible to maximize the quality of the interpolation according to these data. In that scenario, the interpolation resulted to be sufficiently effective to reconstruct the deformation field all over the plate, even where the fiber was not fixed. Nevertheless, the experimental strains are not the same *correct and ideal* than before but affected by some variabilities, and can even be different from the FE-model ones. So the extrapolation can be no longer effective.

To resume, if an entire area of the surface is not covered by any *sensing-gauge*, the interpolation has an heavier role in the procedure. In this case, the interpolation itself is a part of the proposed method, making the procedure sensitive even to small variations in experimental strain.
This problem can be easily limited introducing the *robustness-check* with respect to the FE-model parameters (subsection 3.6.4). If this *robustness-parameter* is considered in the cost function, the best fiber configuration produced will be less sensitive to the variation of the measured strains in respect to the FE-model simulated ones. As explained in chapter 3, this aspect has been not implemented due to its computational weight.
An additional solution to limit this specific error is to increase the *placeable* sensing fiber length in the OSP algorithm parameters. This can be done due to the noticeable increase in signal quality obtained in the last part of the fiber-length: this is the result of the optimization process performed focusing even on the LUNA CU criticisms compensation. As explained in chapter 5, the signal quality is considerably increased by a fiber configuration that reduces *bends-related* issues. According to this occurrence, the fiber length that can be *optimally-placed* on surface can be more than the one used in the presented

results ($1500mm$ of the $1800mm$ theoretically available, see Table 3.5).

The considerations that can be stated concerning mode 9 are the same done for the 7^{th}. The error is always concentrated next to the tip.

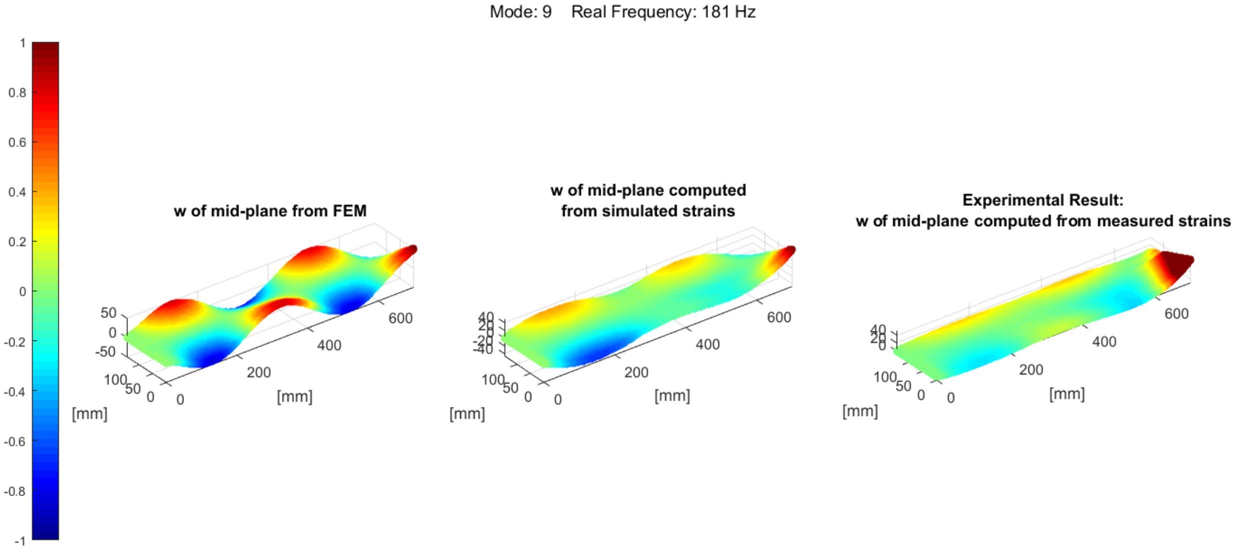

Figure 6.7: Experimental 9^{th} mode-shape at $181Hz$

Particular attention must be devoted to mode 8 and to the fact that it was not a target-mode considered in the optimization.
As a matter of fact, differently from what expected thanks to the *first* preliminary analysis performed through a *first* plate and the *first* prototype of plate-support, the mode corresponding to the 8^{th} was found shifted at a frequency higher than mode 9, so that it cannot be assumed successfully measurable due to LUNA limits. As a consequence, the logical choice was to optimize fiber arrangement for modes 7 and 9, by excluding the 8^{th} one. Actually, in the *final* tests with a *new* plate and the *definitive* clamping structure, the mode corresponding to the 8^{th} is found at 144.6 Hz, before mode 9. As a consequence, it has been however acquired even if the fiber arrangement was not optimized for its good reconstruction. The result is shown in Figure 6.8.

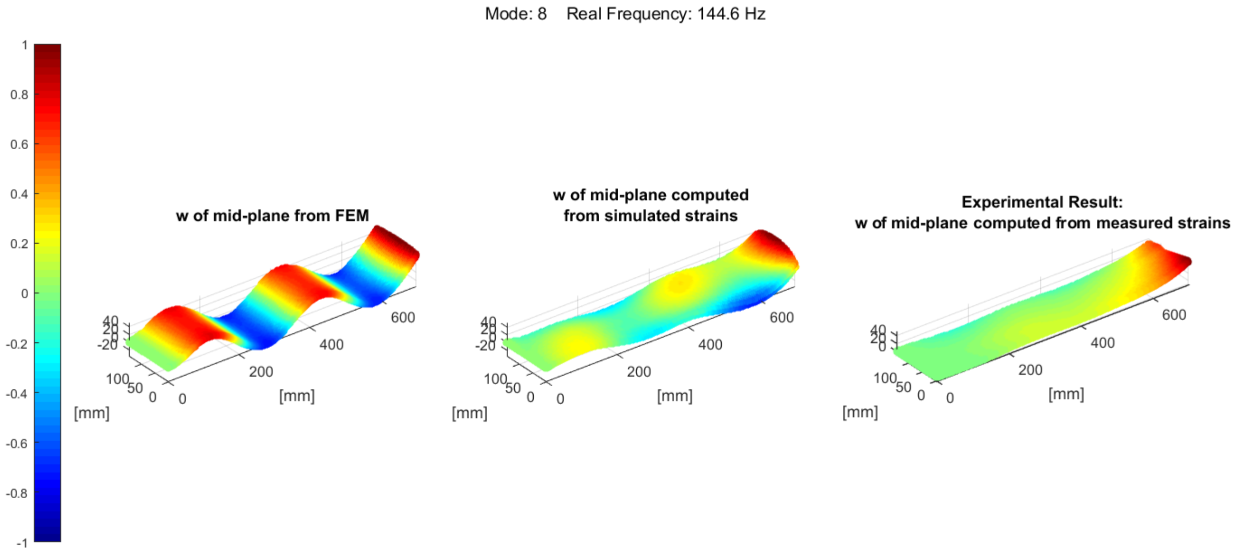

Figure 6.8: Experimental 8^{th} mode-shape at $144.6Hz$

It is evident that in this case the mode-shape reconstruction is not satisfactory, neither in the case it is computed from simulated strains, neither in the case of real measurement. This confirms the effectiveness of the fiber-placement optimization algorithm.

6.2 Comparison among the DST method and the proposed integration-based approach

As explained in chapter 2, strain measures about a structure are traditionally translated into its displacements by means of the DST-matrix method. This thesis work has proposed a method completely independent from the use of that procedure. The purpose is to avoid the use of FE-generated data in the transformation of strain informations into displacements.

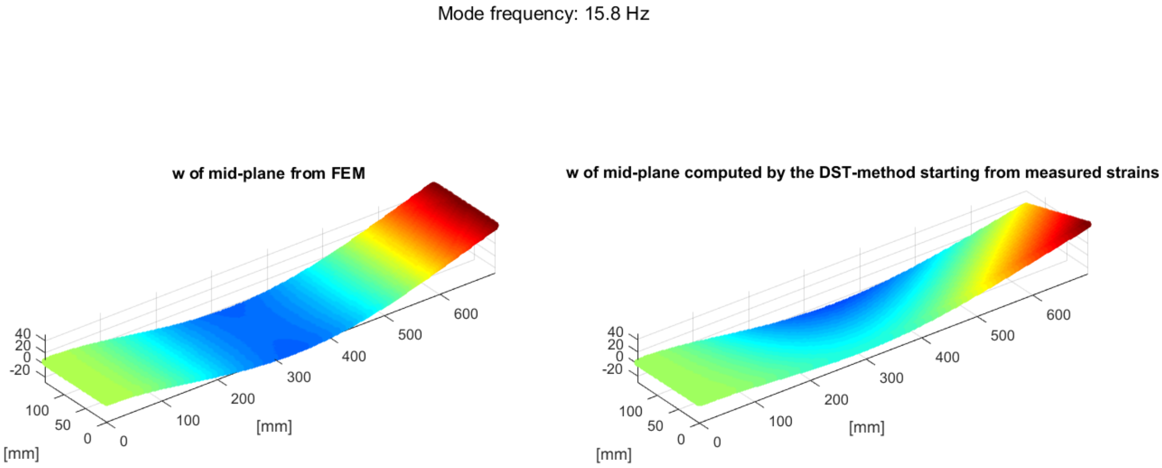

Figure 6.9: Experimental 2^{nd} mode-shape reconstruction by means of the DST-matrix method

As a comparison, the result obtained thanks to the DST-matrix method in generating displacements from the acquired strains is presented in Figure 6.9. The processed strains to obtain the previous figure are exactly the same than Figure 6.1. From the analysis of the mode-shape reconstructed by applying the DST-matrix (Figure 6.9), it is clear that, with the same fiber configuration and the same acquired strain signal, the output obtained by the DST approach is worse than the integration one.

As first consideration, the two results comparison proves that a different *strain-to-displacement* translation methodology provides different quality results in the modal shape definition.

However a deeper investigation about the *strain to displacement* method must be performed.

As extensively explained, one of the main issues related to the use of the fiber strain-sensor is the necessity to convert the acquired strain information in displacements. This is fundamental especially in the turbomachinery field, where the aerodynamic forces are applied to the blade surfaces and can excite their vibration in resonance.

The purpose of the thesis is to develop a strain-displacement translation method as independent as possible from the FE-analysis. The proposed method will deal with a series interpolations and integrations that aims to exclude the requirement of FE-based data in the strain to displacement step. However, another aspect has to be considered. Actually it is necessary to examine in depth the *error-introduction* issue.

The final results are affected by errors, both relying on the *integration-based* method or the DST-matrix one. In order to understand how it is possible to reduce the *error*, it is necessary to determine *how* this error is introduced in the final results and which steps of the process are the critical ones. As a consequence, the reason that stays behind the choice of the strain-to-displacement conversion approach will be even more clear.

At this point the two different possible strain-to-displacement translation processes have to be accurately compared. The scope is to evidence how each algorithm introduces errors in the reconstructed experimental modal-shape and how it is possible to reduce it.

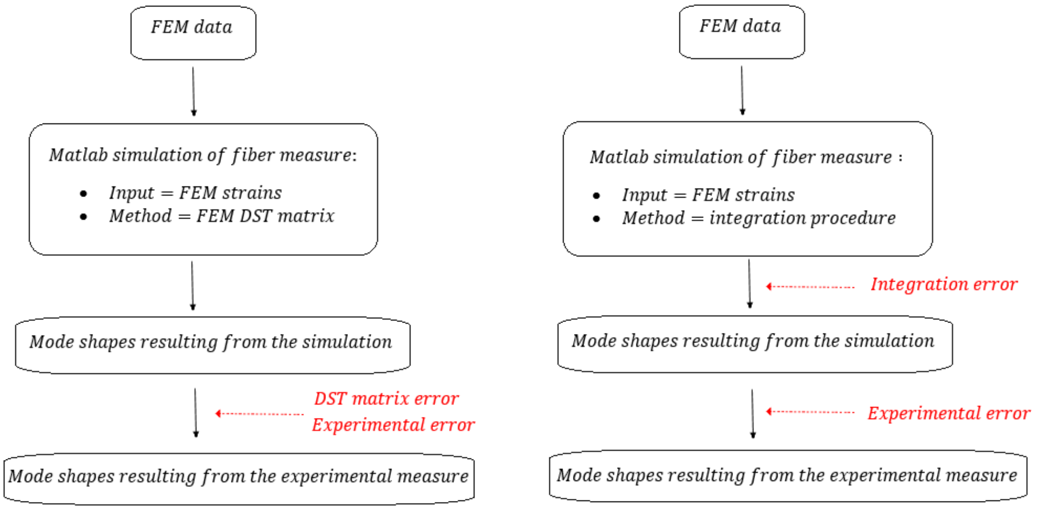

Figure 6.10: Conceptual comparison among the two strain-to-displacement translation methods

Figure 6.10 resumes the two different methodologies of strain transformation, putting in evidence where, along each algorithm, the error is introduced.

In the integration-based approach, the error arises from two distinct sources and its introduction occurs during two different passages:

1. Error associated to the strain-to-displacement translation procedure:
   It is present even in the mode-shape reconstruction achieved by the *simulated* strains (section 3.7). It is an error strictly dependent from the interpolations and the numerical integrations employed in the processing of the strains. As widely explained, in this work an OSP algorithm where the experimental measure is simulated by a virtual simulation the fiber measurement is implemented. For that, the error related to the interpolations-integrations is present both in the computation of the fitness of genetic algorithm GA, both in the modal-shape reconstruction based on the experimentally acquired strains. This error can be called *integration error*;

2. Error introduced by the experimental session:
   The acquisition is not *ideal* and the *manual* fiber fixing process cannot be exact. The experimental results are necessarily different from the simulation-based ones implemented in the GA in order to find the best fiber configuration. Some not-cleaned disturbances, some glueing inaccuracies, some carelessness in the fiber local orientation or some local fiber singularities can introduce errors in the experimental results. It must be considered that the experimental uncertainties are amplified by the integration-interpolation process. In general, this kind of error can be called *experimental error*;

In the DST-matrix method, the error introduction is *concentrated* in just one algorithm step, in correspondence of the experimental measure. In the truth, the error affecting the mode-shapes reconstruction has two origins even in this case. The main difference with respect to the integration-based method is that in this new scenario the error is introduced completely and *exclusively* at the final step of the algorithm and introduction does not occur in two different moments. The two sources of error, in this case, are:

1. Discrepancy among the FE-model and the *real* structure:
   This entails an inadequacy of the DST-matrix application in the strain-to-displacement transformation step. The DST-matrix is a re-elaboration of the ϕ and ψ matrices of the FE model (the displacement modal-matrix and the strain modal-matrix, see chapter 2 for further details). If the DST is used to compute displacements with the experimental

strains, inevitably the result will be affected by error. Theoretically, the experimental strains have to be processed with the DST of the *real structure* to reach an exact result. This part of the error can be defined as *DST-matrix error.*
To sum up, the *DST-matrix error* comes from the intrinsic discrepancy among the FE-model and the real structure;

2. Error introduced by the experimental session:
   Exactly as in the integration-based method, signal disturbances, sensor positioning imprecisions, some carelessness in the fiber local orientation or some local fiber singularities introduces errors in the measurement and in the mode-shape reconstruction. As a consequence, this part of the error can be called, even in the DST-matrix approach, *experimental error.*

As previously explained, if the DST approach is chosen to convert strains into displacements, the error will be *introduced* in the results just in one step, the experimental-test step.
At this point, a proper comparison between the two strain-to-displacement methods can be performed. In particular, now it is clear how the error in the two approaches is introduced.

First of all, in the DST procedure the two causes of the error can not be distinguished: it is impossible to understand if the mode shape quality decrease is a consequence of LUNA signal quality reduction or of FE-model discrepancy with respect to the real structure. The *experimental error* cannot be distinguished from the *DST matrix error.* An inadequate modal shape reconstruction can be related to a low experimental signal quality but even to FE-model errors. This inability to analyse the final error source decreases the result observability.
This problem has not to be underestimated. One of the main purposes of this work was to investigate the OBR fiber technology. The reduction of the modal-shape result observability complicates the possibility to examine the fiber measure application and the CU behaviour at high frequencies. With an innovative measure or acquisition system, the DST-matrix method does not offer the complete opportunity to extensively study the new instrument and its eventual peculiar criticisms.
In the chosen integration-based strain-to-displacement approach the *experimental error* is clearly distinguished from the *integration error*, instead. So it is easier to understand the behaviour of the sensor used in the experimental set up and isolate the criticisms caused by the instrumentation. In conclusion, it is easier to understand how to reduce the measurement-system criticisms, as done in this work.

Secondly, the choice to use an integration-based strain-to-displacement approach is coherent with the purpose to implement the OSP-algorithm. In particular, the error separation concept peculiar to this method, permits to *work* to reduce the *integration error.* As explained, in the OSP-algorithm a measurement simulation is implemented and the integration-based strain-to-displacement method is applied per each fiber-configuration individual of GA. The optimal sensor placement algorithm defines which is the best fiber arrangement. The consequence is that the *integration error* is minimized by the OSP code, because the integration step *belongs* to the optimization process itself. The best configuration proposed by the genetic algorithm guarantees the minimization of the *integration error.*
This is the main advantage of the integration-based approach with respect to the DST-matrix method use.

With the application of the integration-based approach instead of the DST one, a part of the error affecting the reconstructed mode shape can be minimized by the OSP-algorithm.

Actually the DST-matrix method overall error can be reduced too. It is possible to limit the *DST matrix error.* Differently from the integration-based procedure, this error reduction can not be obtained with a sensor positioning optimization. To reduce the *DST matrix error* an *iterative validation* of the FE-model must be performed. Practically, it is necessary to *modify* the FE-model in order to *fit* the experimental data collected from the real structure. The iteration can be interrupted when the FE-model validation reaches convergence, so when the reconstructed mode-shapes obtained applying the DST-matrix to the measured strains *coincides* directly with the FE-model ones. Nevertheless, this procedure has many criticisms:

- The iterative procedure that modifies the FE-model to fit the experimental data to make the DST application consistent is less automatic than the implementation of an OSP-algorithm based on the GA convergence;
- The FE-model iterative validation practically substitutes the genetic OSP. The lack of an OSP implementation excludes the possibility to optimize the fiber to miminimize the *experimental error.* In this thesis work, the designed OSP algorithm compensates the LUNA CU disturbances and dynamic criticisms. In case of DST-matrix method, an additional OSP should be created to reduce the fiber experimental problems. Practically the FE-model validation would be followed by an OSP code, and this procedure would have to be applied iteratively. It is certainly heavy and complicated. One of the purposes of this research project was to understand how the LUNA CU can been applied in dynamic acquisition

with a consistent signal-frequency. For this reason, in the proposed GA a part of the cost function is dedicated to the minimization of the number of bends and to the noise robustness. All these considerations can not be done in a DST approach where no OSP code has to be implemented.

- In the FE-model iterative validation, the parameters are modified to fit the experimental acquisitions. Nevertheless, the LUNA strains are surely affected by the *experimental error*. So there is the real risk to change the parameters of the FE-model in order to fit *wrong or dirty* experimental data. This complicates the validation process. The iterative FE-model validation strictly depends on the measurement process. This passage is particularly dangerous in case of innovative acquisition systems, as the OBR LUNA OdISI-B. The higher is the uncertainty of the measurement system, the more critical is the FE-model iterative modification to successfully apply the DST-matrix.

In conclusion, the main advantage of the proposed strain-to-displacement procedure, which is innovative with respect to the approach offered by literature resides in its independence from any FE-analysis. Furthermore, with the integration-based approach a part of the error concerning the mode-shape reconstruction can be reduced by the OSP-algorithm. For this reason, considering the OSP *integration error* minimization, it is possible to state that the overall error of the DST-approach (which accounts for *DST matrix error + experimental error*) is higher than the integration-based one (*integration error + experimental error*).

6.3 General considerations about LUNA interrogator

The choice of a simple geometry (the bi-dimensional thin plate) was performed even to ease the study of the behaviour of the LUNA interrogator in an *off-design* measurement environment. For this reason, to conclude the analysis of the results concerning the plate case-study, it is possible to state some conclusions concerning the LUNA OBR instrumentation. Making reference even to the considerations made in chapter 5, it can be stated that:

- Bends represent the main criticism with respect to the OBR fiber measurements. Bend radius has to be higher than $10mm$ in order to obtain a satisfactory signal quality. With this care, the effective fiber length with a good signal quality can be increased considerably;
- According to the experimental tests, it can be assumed that the precision in the fiber fixing procedure affects the measurement results. The more automatic and accurate the glueing process will be, the best will be the reconstructed mode shapes.
- It has been proved that, with the proposed OSP algorithm, the LUNA CU can have a satisfying signal quality at least till $220Hz$.

Chapter 7

Three-dimensional blade problem

The original purpose of this work was the turbine blade modal-analysis through the application of the OBR fiber-sensor technology. As extensively explained, the plate case-study has been implemented to better investigate the fiber strain measurement process and the LUNA CU behaviour in dynamic applications. The developed fiber positioning optimization algorithm and the devised *strain-to-displacement* procedure are successfully applied to the bi-dimensional structure. For the plate case-study the targeted modes are completely experimentally reconstructed and a satisfying results-analysis has been performed. At this point, all the considerations related to the bi-dimensional simplified case have to be applied to attempt the real-blade modal-shape reconstruction.

As initially explained, one of the main challenges regarding the use of the LUNA system in modal analysis, is the frequency upper bandwidth-limit: the system is designed for static measurements, while the reliability in its dynamic application is not guaranteed by the manufacturer. In the bi-dimensional plate modal-analysis the maximum frequency where LUNA output has been considered as *reliable* was approximatively $220Hz$. In this scenario, the real steel-blade has considerably *high* natural frequencies. As a matter of fact, the blade has only two resonances in the frequency range where LUNA CU can be effectively employed. To face this occurrence, it has been thought to act on the blade physical properties aiming to *shift* the resonances by *scaling* in the frequency domain the FRF of the original steel blade. This task has been achieved thanks to a material change and some tolerable geometrical modifications. An ABS 3D-printed model has been manufactured. In this way the new stiffness and material density of the system result in a structure

with more suitable eigenfrequency values.
The experimental modal analysis will be performed on the 3D-printed blade.

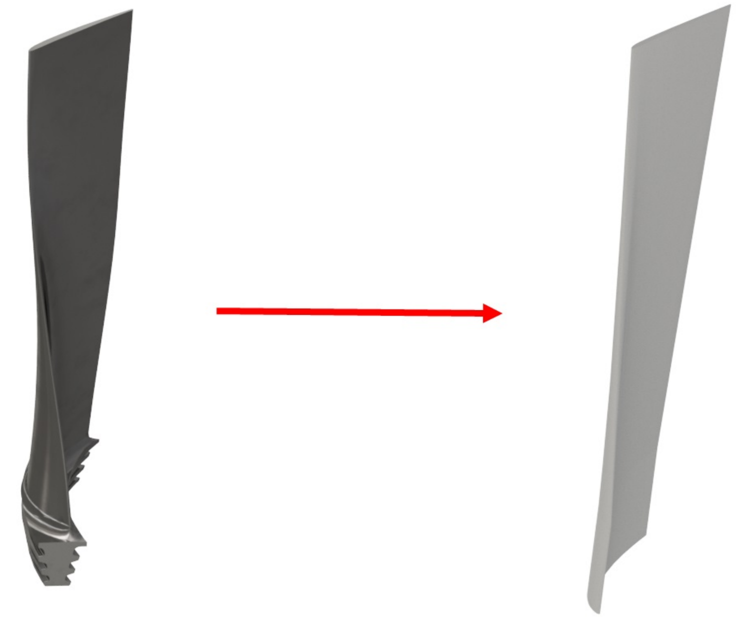

Figure 7.1: Comparison among real blade and 3D-printed model

A FE-model of the modified blade has been created, both to generate the required files for *printing*, both to permit its computational modal analysis. The blade is modelled by means of a *blade-alone model*, described in subsection 2.1.2 and in the Figure 2.3. The nodes on the blade cross section on the hub are clamped, the rotor is not modelled.
The ABS material is modelled as stated in Table 7.1:

Table 7.1: ABS data-sheet

-	quantity	unit
Density	1.1	g/cm^3
Young modulus	2000	MPa
Poisson ratio	0.37	$-$

The mesh is structured and hexaedral. The approximate mesh global size is set to $2.5mm$. Elements are 8-node linear bricks (type C3D8). Analysis is performed with full integration and with second order accuracy.

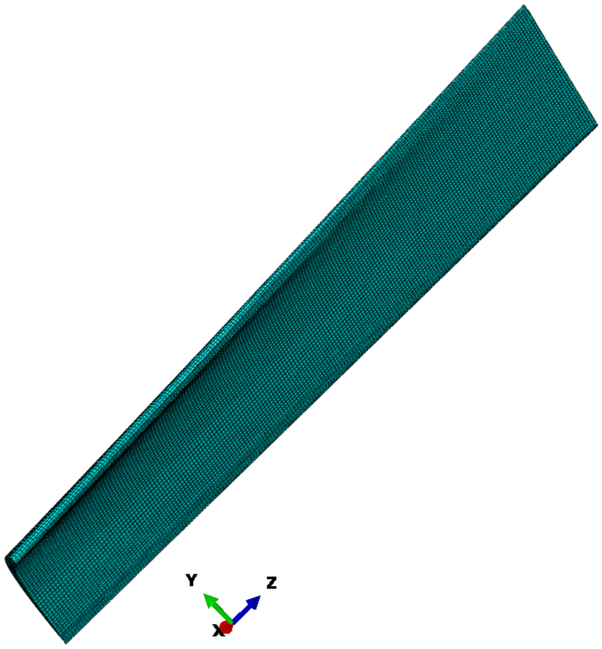

Figure 7.2: FE-model of the 3D-printed blade

The modal parameters in Table 7.2 are extracted by a CMA of the structure under exam.

Table 7.2: 3D-printed blade eigenfrequencies from FE-analysis

Computational mode index	1	2	3	4	5
Computational eigenfrequency $[Hz]$	12.8	48.9	68.1	101.8	128
Mode geometry	f-w	f-w	t	f-w	t

Where *f-w* stands for flap-wise, while t indicates torsional modes. Thanks to the modifications that has been made with respect to the steel-blade, it is theoretically possible to investigate till five vibrating-modes by means of the LUNA acquisition system. In addition to this, the development and the use of a 3D-printed ABS model is coherent with the future technological use of the fiber as embedded sensor, as anticipated in chapter 2.

As previously stated, one of the most challenging goals of this work resides in the development of a strain-to-displacement procedure as independent as possible from the FE-model simulation. The idea is to achieve the reconstruction of the displacement mode-shapes just by an elaboration of the experimentally acquired strains. The *desired* algorithm, which has to perform the modal-shape reconstruction, has to consider as input values only the surface strains given by the fiber, and anything else. This kind of approach was implemented successfully in the bi-dimensional thin-plate analysis: the strain-to-displacement translation was based on a sequence of interpolation and integration procedures.

In section 6.2, the advantage of this integration-based approach with respect to the traditional DST-matrix method has been already explained, especially in terms of FE-model independence, immediacy of the results, optimization code performances and fiber-technology management.
The scope is to devise a software able to manage the acquired strain-data and reconstruct the three-dimensional surface displacement mode-shapes just monitoring the surface itself.
It will be demonstrated that in the three-dimensional case study the surface strains are not sufficient to reconstruct the displacement field by means of a 3D-*integration* process.

First of all, the reason why this *interpolation-integration* procedure can not be applied to the available 3D-printed blade will be widely explained. A mathematical demonstration will be reported, section 7.1.

Secondly a practical an immediate solution based on a dedicated DST-matrix method will be described. Experimental results will be shown, section 7.2.

Finally a new methodology will be proposed, with the scope to create an algorithm to extrapolate the blade displacements from the measure strains, completely avoiding FE-model *help*. This would permit in future to exploit all the advantages (section 6.2) of a strain-to-displacement conversion method involving just an *integration* procedure and not the DST-matrix application.

7.1 Strain-to-displacement procedure based on integration

The absolute reference system in which the structure is considered and its origin are stated in Figure 7.3.

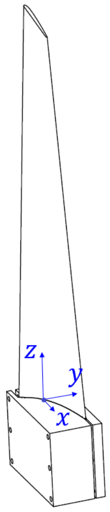

Figure 7.3: Absolute reference system for the 3D case-study

In order to approach the three-dimensional case-study, the first issue is to evidence which are the physical variables to be estimated and which is the measured information.

Firstly, the surface can be seen as composed by a set of *surface points*. The whole set of surface points are the only entities that will be considered undergoing the *modal-displacement*. Each surface point is characterized by spatial-coordinates in the absolute frame of reference. In addition to this surface categorisation, it is possible to set-up a *relative surface mapping* where each point has its proper set of planar coordinates x_R and y_R. This will be described and motivated in the following sections.
The fiber sensor will necessarily pass through some of these surface points. In the use of optical fiber sensor, as previously extensively explained, the measured data are the surface strains. In particular, it is possible to measure the strains in all the directions arranged in the plane tangent to the local surface orientation. Practically, the strain acquired with the fiber sensors are the *in-plane* deformations, where *planes* are the local entities characterized by a normal equal to the local normal to the surface. Each i^{th}-point of the

surface has its proper normal direction.
In this way the directions where the strain are experimentally known are dependent on the local surface orientation. The strain ϵ_{l_i} acquired in correspondence of the surface i^{th}-point has the generic orientation θ_{x_i}, θ_{y_i} and θ_{z_i} with respect to the absolute spatial reference system x, y and z. Obviously ϵ_{l_i} belongs to the plane tangent to the local surface in the i^{th}-point. In addition to this, it is fundamental to consider that the fiber has even a *local* orientation in the plane where is fixed, called θ_{l_i}: this local direction is the angular position of the measure ϵ_{l_i} with respect to a bi-dimensional reference system *built-in* to the local surface.

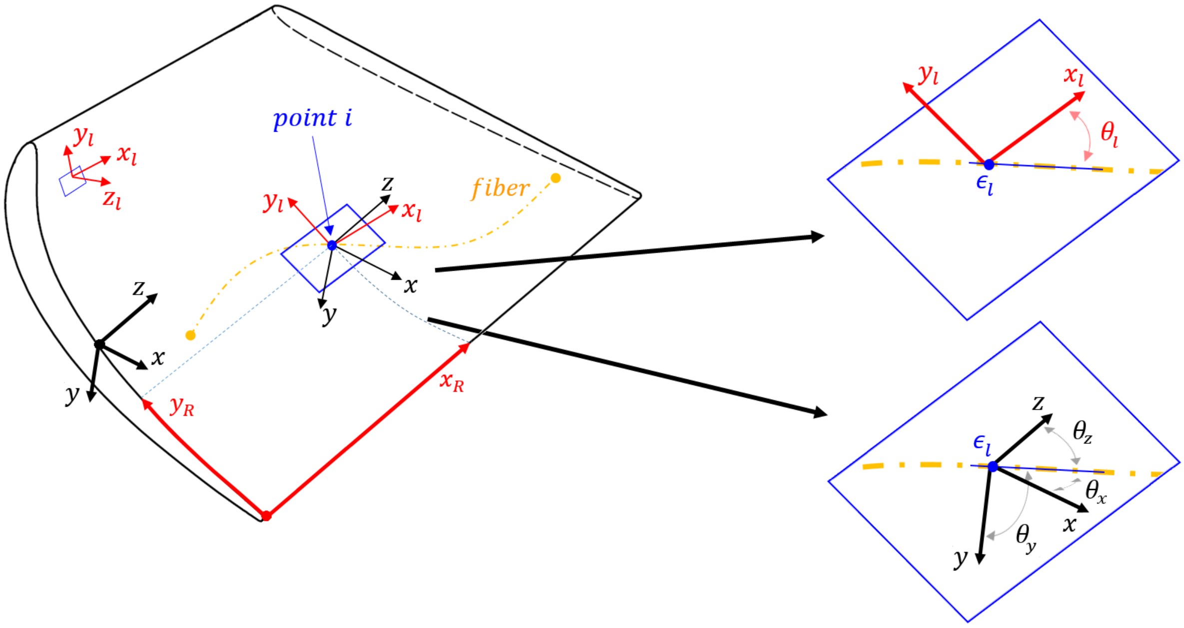

Figure 7.4: Relative reference system and nomenclature for the 3D case-study

Practically each fiber-gauge is characterized by:

- A set of absolute spatial coordinates x, y and z, in order to locate the sensor in the global reference system;
- A set of absolute angular coordinates θ_x, θ_y and θ_z;
- A set of bi-dimensional relative spatial coordinates x_R and y_R, in order to locate the sensor in a relative frame of reference. In this way the fiber positioning can be performed considering the x_R and y_R of each sensor, starting by some fixed reference edges of the surface of the structure to

measure. In addition to this, if such a *mapping* procedure is performed per each point, a *relative* coordinate system over the surface is available;

- A value of local orientation (an angular coordinate θ_l). It is the angular orientation of the fiber *on* the local surface plane.

At this point, it is necessary to implement the strain-to-displacement three-dimensional *integration procedure* in order to transform the strains in the final displacement mode shapes.

The main difference between the thin-plate analysis and the 3D case is the wanted output. In the plate case-study the final purpose is the definition of $w(x, y)$, the surface displacement-field normal to the plate middle plane. This case-study physics is reduced to a single DoF-model, so just one displacement-field is the final modal result. This is allowed by the possibility to consider as reliable a physical model where some assumptions are made, as described in the chapter 3. In particular can be assumed that $w_{mid-plane} = w_{surface}$. The complexity of the inner physical-laws is reduced by the plate-like model: the mid-plane displacement w is the only variable and completely describes the three-dimensional behaviour of the whole structure.

In this scenario, the blade is a complex 3D body and no physical simplifying models can be realistically introduced. The blade case can not be considered as a thin-structure mainly due to its considerable spatial twist, and its not so much low and regular thickness. In addition to this, in the word of turbomachinery, many blades proper to different machines or stages, have a more stocky shape. A quite general approach is desired. So, in the blade investigation the request is the computation of three distinct displacement fields *u(x,y,z)*, *v(x,y,z)* and *w(x,y,z)*. These are the displacements of all the surface points in respect to the absolute reference system.
To resume:

- Thin structures can be modelled as plates, so the only variable and wanted result is just $w(x, y)$;
- Blade-like structures are complex three-dimensional systems, so the wanted results are $u(x, y, z)$, $v(x, y, z)$ and $w(x, y, z)$.

For this reason the mathematical procedure to find the final mode-shapes can not be exactly the same employed in the plate study-case. The 3D problem is more complex. Nevertheless the logical nucleus is the same: to apply a set of interpolations and integrations to achieve the displacement-fields definition starting from the strain values measured along the fiber, without relying on any FE-model of the structure.

As previously anticipated, the surface is considered as *discretized* in *surface points*. It is just a way to manipulate the acquired strains and to represent the final global displacement fields. Measurements will be performed in correspondence of some of the surface points.
First of all, to calculate per each surface i-point the final amounts u_i, v_i and w_i, it is necessary to compute $u_l i$, $v_l i$ and $w_l i$, the projection in the local reference system of the absolute displacement components. This need arises from the necessity to measure the *local* strains on the surface. The passage from the *local* displacements to the absolute ones is simply governed by a T *rotation matrix*. It is composed by the direction cosines of the local reference system. For each i-location it is possible to write the following rotation equation:

$$\begin{bmatrix} u_i \\ v_i \\ w_i \end{bmatrix} = \begin{bmatrix} l_{1i} & m_{1i} & n_{1i} \\ l_{1i} & m_{2i} & n_{2i} \\ l_{1i} & m_{3i} & n_{3i} \end{bmatrix}^T \begin{bmatrix} u_{li} \\ v_{li} \\ w_{li} \end{bmatrix}$$

The directional cosines are related to the angles between the absolute reference system and the local reference system, described by the axis x_{li}, y_{li} and the local surface normal z_{li}. The T matrix has to be computed for every surface point, so where the modal shape has to be reconstructed.

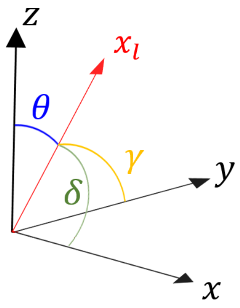

Figure 7.5: Directional angles of x_l

At this step it is important to evidence that just m surface locations are really measured by the fiber sensor, exactly as in the bi-dimensional plate. Practically the input of the algorithm is a set of m measured strains. Nevertheless the modal-shapes have to be determined all over the surface. As a consequence, it is evident the need of interpolating the measured strains: to complete the displacement definition it is necessary to have strain informations in all the positions where the modal shapes have to be reconstructed, as in the plate case. The strains values are calculated per every surface point employing interpolations.

To determine nodes u_l, v_l and w_l it is necessary to consider the following strain-displacements relations, extensively explained in chapter 3:

$$\epsilon_{x_l} = \frac{\partial u_l(x_R, y_R)}{\partial x_l} \tag{7.1}$$

Where $u_l(x_R, y_R)$ can be easily calculated by integrating ϵ_{x_l} with the proper clamp boundary condition $u_l = 0$ in $x_R = 0$.
The others useful strain-displacements equations are:

$$\gamma_{xy_l} = \frac{1}{2}(\frac{\partial u_l}{\partial y_l} + \frac{\partial v_l}{\partial x_l}) \tag{7.2}$$

$$\gamma_{xz_l} = \frac{1}{2}(\frac{\partial u_l}{\partial z_l} + \frac{\partial w_l}{\partial x_l}) \tag{7.3}$$

From these two equations it is theoretically possible to explicit $\frac{\partial v_l}{\partial x_l}$ and $\frac{\partial w_l}{\partial x_l}$.
To *extract* $\frac{\partial v_l}{\partial x_l}$ and $\frac{\partial w_l}{\partial x_l}$ from the Equation 7.2 and Equation 7.3, it is necessary to have previously determined the values of $\gamma_{xz_l}(x_R, y_R)$ and $\gamma_{xy_l}(x_R, y_R)$. To successfully reach the determination of $\gamma_{xz_l}(x_R, y_R)$ the *plane stress* condition has to be imposed on the surface.
The final $v_l(x_R, y_R)$ and $w_l(x_R, y_R)$ can be computed by integrating both the previous derivative scalar fields ($\frac{\partial v_l}{\partial x_l}$ and $\frac{\partial w_l}{\partial x_l}$) with the clamp condition $v_l = 0$ and $w_l = 0$ in $x_R = 0$. All these mathematical procedure will be accurately described in the following paragraph.

The three-dimensional *integration procedure* to extract the surface mode-shapes from the acquired strains is summarised below:

- Measure the local strain ϵ_{x_l} or ϵ_{y_l} or ϵ_{45_l} in the gauge locations (so where the fiber is fixed). In other words, for the i-point where the fiber is attached, the strain ϵ_{li} is acquired along a proper θ_l (θ_{l_x} or θ_{l_y} or θ_{l45}) that depends on the local fiber orientation;

- Interpolation of the fiber acquired values ϵ_{x_l}, ϵ_{y_l} and ϵ_{45_l} *all-over* the surface. The result is the determination of those quantities per each i-point: $\epsilon_{x_l}(x_R, y_R)$, $\epsilon_{y_l}(x_R, y_R)$ and $\epsilon_{45_l}(x_R, y_R)$;

- Calculation of $\gamma_{xy_l}(x_R, y_R)$ by using the three scalar fields previously defined $\epsilon_{x_l}(x_R, y_R)$, $\epsilon_{y_l}(x_R, y_R)$ and $\epsilon_{45_l}(x_R, y_R)$:

$$\gamma_{xy_l} = \frac{\epsilon_{45_l} - cos(45°)^2\epsilon_{x_l} - sin(45°)^2\epsilon_{y_l}}{sin(45°)cos(45°)} \tag{7.4}$$

The formula is exactly the same of the bi-dimensional thin plate case-study (Equation 3.10);

- For the sake of completeness, the imposition of a *plane stress state* condition (which implies null σ_{z_l}, τ_{xz_l}, τ_{yz_l} and null γ_{xz_l}, γ_{yz_l}) guarantees the validity of the following equation:

  $$\epsilon_{z_l} = -\frac{\nu}{1-\nu}(\epsilon_{x_l} + \epsilon_{y_l}) \tag{7.5}$$

  At this point, the knowledge of the full tensor composed by the *relative strains* is achieved:

  $$\begin{bmatrix} \epsilon_{x_l} & \gamma_{xy_l} & 0 \\ \gamma_{xy_l} & \epsilon_{y_l} & 0 \\ 0 & 0 & \epsilon_{z_l} \end{bmatrix}$$

- Now the computation of $\frac{\partial v_l}{\partial x_l}(x_R, y_R)$ and of $\frac{\partial w_l}{\partial x_l}(x_R, y_R)$ is possible. It is sufficient to impose, in the Equation 7.2 and Equation 7.3, $\gamma_{xz_l} = 0$ due to the plane stress hypothesis on the surface and the calculated scalar field $\gamma_{xy_l}(x_R, y_R)$;

- The calculation of $u_l(x_R, y_R)$ can be completed through the direct integration of ϵ_{x_l} with the clamp boundary condition;

- The calculation of $v_l(x_R, y_R)$ and $w_l(x_R, y_R)$ can be performed through the integration along x_l-axis of $\frac{\partial v_l}{\partial x_l}$ and $\frac{\partial w_l}{\partial x_l}$;

- Finally, the computed set of u_{l_i}, v_{l_i} and w_{l_i} can be rotated with the T_i matrix, so to obtain for all the surface points u_i, v_i and w_i in the absolute reference system.

At the end of the procedure the vectorial displacement field

$$\bar{u}(x,y,z) = \begin{bmatrix} u(x,y,z) \\ v(x,y,z) \\ w(x,y,z) \end{bmatrix}$$

is defined.

The presented algorithm aims to process LUNA strain-data referred to the surface only, to reconstruct just the surface displacements in the absolute frame of reference.

All the mathematical passages are feasible, except for one: the criticism is evident in Equation 7.3, where the term $\frac{\partial u_l}{\partial z_l}$ appears. As a matter of fact, to complete successfully the previous scheme of modal shape determination the w_{li} has to be calculated in order to apply the rotation-matrix and determine the absolute nodal displacements u_i, v_i, w_i. Practically all the *local displacements* have to be known to find the absolute ones. Actually the calculation of w_{l_i} depends on the computation of $\frac{\partial u_l}{\partial z_l}$. Practically, to reach w_{li} is required $\frac{\partial u_l}{\partial z_l}$.

It arises that the procedure requires the knowledge of $\frac{\partial u_l}{\partial z_l}$. This means that the procedure needs to know the gradient of u_l along the normal direction to the surface. This is required to have a sort of three-dimensional *description* of $u_l(x_R, y_R, z_R)$. Actually it is necessary to know the behaviour of u_l not just *over* the structure surface, but even in its *depth*. z_l is the *local normal* to the surface, so it is the direction that *penetrates* locally the body. To sum up, the three-dimensional strain-to-displacement integration-scheme cannot be completed due to the impossibility to define $\frac{\partial u_l}{\partial z_l}$ disposing just for the *external single* surface strains.

A general final conclusion can be stated: it is not possible to reconstruct the displacement-fields of a three-dimensional body surface employing informations just about its surface strain-state.
The presented algorithm is coherent with the original purpose to not employ informations except for measured strains. Just integrations and interpolations are used to achieve the displacements: no FE-model data are considered. The use of an approach such as DST-matrix is completely avoided.
This is the innovative aspect of the proposed procedure.
Nevertheless, the presented strain-to-displacement procedure requires for the *gradient* of u_l along the third direction. In other words, it requires an additional information about what is *happening* along the thickness. Obviously, this information cannot be experimentally obtained if the fiber is attached just over the blade surface.
In other words, due to the bi-dimensional assumption in the plate case-study, the surface is somehow *representative* of the entire body, while in a more complex full-3D body (such as the blade under exam) a set of surface informations does not suffice nether to reconstruct the displacement of the surface itself.
Where the plate-assumption is not applicable, the surface cannot be *representative* of the structure and some informations regarding the body *inner* has to be available.

As a matter of facts, when dealing with a full three-dimensional problem the solutions to obtain surface-displacements starting from measured strains are mainly two:

- To somehow measure the body internal strains, so to dispose of the missing information about the u_l gradient along the *third-direction*, in order to employ a strain-to-displacement procedure independent from the FE-model;
- To use *external* informations regarding the solid inner, so abandon the idea to use just the measured surface strains and resort to the DST-matrix method that relies on FE-model based data. In this way the strain-to-displacement procedure will not be based just on interpolations and integrations of the acquired experimental strains, but needs FE-model informations.
  Employing the DST-matrix method is like providing all the missing informations about the body inner starting from *computationally generated* data.

7.2 Devised DST-matrix formulation

In this section the 3D-printed blade mode-shapes definition is carried out according to the DST-matrix approach. The acquired strains on the surface are re-elaborated in order to reconstruct the surface displacements.
The theoretical background that states the formulation of the DST-matrix approach has been already treated in subsection 2.3.4.
Consider to dispose of an experimental set of strain-data acquired on the surface of a structure, and a FE-model of the whole structure itself. Considering K the amount of nodes on the surface, N is the number of their displacement-DoFs. m is the amount the strain-DoFs that are actually monitored. Finally, n is the number of modes accounted in the modal approach.
Here the DST-matrix method is recalled in its complete formulation:

$$\begin{aligned} \bar{u}(t)_{N\times1} &= [\Phi]\ ([\Psi]^T\ [\Psi])^{-1}\ [\Psi]^T\ \bar{\epsilon}(t)_{m\times1} \\ &= DST_{N\times m}\ \bar{\epsilon}(t)_{m\times1} \end{aligned} \tag{7.6}$$

A resume on the terms that are accounted by this approach is carried out below.

- $\bar{u}(t)_{N\times1}$ is the vector that accounts for the *displacement* time-responses of the overall amount N of *displacement-DoFs* of surface nodes:

  $$\bar{u}(t)_{N\times1} = \begin{bmatrix} u_1(t) \\ v_1(t) \\ w_1(t) \\ \vdots \\ w_K(t) \end{bmatrix}$$

  $\bar{u}(t)_{N\times1}$ is the unknown to be determined;

- $\bar{\epsilon}(t)_{m\times1}$ is the vector which contains the *strain* time-responses of the m monitored *strain-DoFs*:

  $$\bar{\epsilon}(t)_{m\times1} = \begin{bmatrix} \epsilon_{x_{78}}(t) \\ \epsilon_{y_{235}}(t) \\ \epsilon_{y_{536}}(t) \\ \vdots \\ \epsilon_{x_{965}}(t) \end{bmatrix}$$

  For example, it is assumed that node 78 is monitored and the obtained strain information lies along x-direction.

$\bar{\epsilon}(t)_{m\times 1}$ contains really measured strains. Measurements must be performed so that the m_i strain data in $\bar{\epsilon}(t)$ can be *physically* linked to the m_i strain-DoF of the FE-model;

- $\Phi_{N\times n}$ is the *displacement modal matrix* accounting for n eigenvectors and the N DoFs:

$$\Phi_{N\times n} = \begin{bmatrix} u_{1,1} & u_{1,2} & \cdots & u_{1,n} \\ v_{1,1} & v_{1,2} & \cdots & v_{1,n} \\ w_{1,1} & w_{1,2} & \cdots & w_{1,n} \\ \vdots & \vdots & \vdots & \vdots \\ w_{K,1} & w_{K,2} & \cdots & w_{K,n} \end{bmatrix}$$

  This matrix is provided by the FE-analysis;

- $\Psi_{m\times n}$ is the *strain modal matrix* accounting for n eigenvectors and the m monitored DoFs:

$$\Psi_{m\times n} = \begin{bmatrix} \epsilon_{x_{78,1}} & \epsilon_{x_{78,2}} & \cdots & \epsilon_{x_{78,n}} \\ \epsilon_{y_{235,1}} & \epsilon_{y_{235,2}} & \cdots & \epsilon_{y_{235,n}} \\ \epsilon_{y_{536,1}} & \epsilon_{y_{536,2}} & \cdots & \epsilon_{y_{536,n}} \\ \vdots & \vdots & \vdots & \vdots \\ \epsilon_{x_{965,1}} & \epsilon_{x_{965,2}} & \cdots & \epsilon_{x_{965,n}} \end{bmatrix}$$

  This matrix is provided by the FE-analysis;

Equation 7.6 allows to reconstruct, from a reduced set of m acquired strain signals $\bar{\epsilon}(t)_{m\times 1}$, the displacement of the entire surface in terms of $\bar{u}(t)_{N\times 1}$. As a matter of facts, m can be much smaller than N.

Practically, $\bar{u}(t)_{N\times 1}$ comes from an hybrid procedure that mixes computational modal analysis (CMA) generated data and really measured strains, making the strong dependence of the procedure from the FE analysis clear.

The Φ and Ψ matrices are built by extracting, from the *complete* $\tilde{\Phi}$ and $\tilde{\Psi}$ matrices of the CMA, the values u, v, w associated to each surface node K (in the case of Φ) and the values ϵ associated to each surface monitored DoF (in the case of Ψ).

The complete $\tilde{\Phi}$ and $\tilde{\Psi}$ matrices account for the entire set $\tilde{K}$ of FE-model nodes and for the overall amount of strain and displacement DoFs, $\tilde{m}$ and $\tilde{N}$. In the complete formulation, per every vibrational mode, each node is linked to three displacement-DoFs (u, v, w) and to six strain-DoFs that compose the nodal strain-tensor (ϵ_x, ϵ_y, ϵ_z, ϵ_{xy}, ϵ_{yz}, ϵ_{xz}).

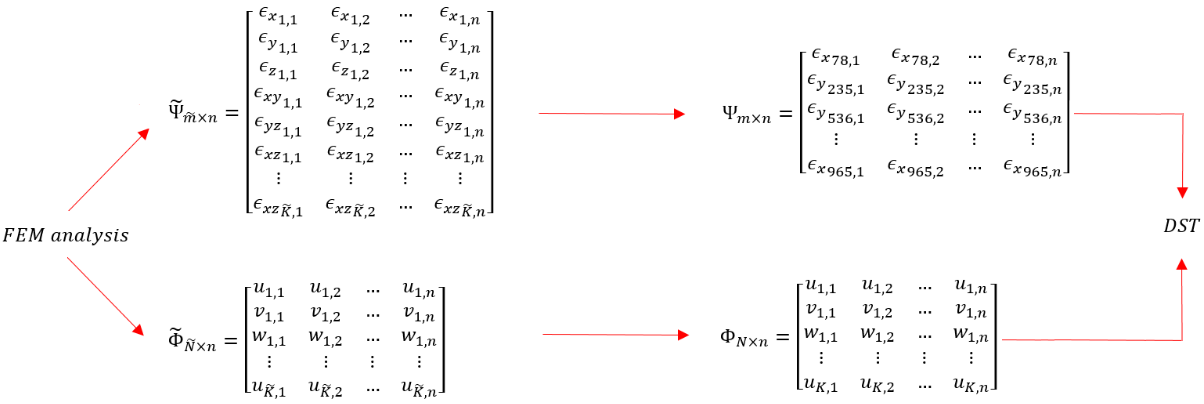

Figure 7.6: DST-matrix formulation

At this step, the available information are:

- $\Psi_{m\times n}$ and $\Phi_{N\times n}$, that are extracted from FE-analysis and are required to formulate the DST matrix;
- $\bar{\epsilon}(t)_{m\times 1}$ that comes from a real measurement session;
- The surface nodes spatial coordinates and the $\tilde{\Psi}$ matrix which comes from FE-analysis and contains per each node the informations about the local strain-tensor;

It must be stated that to have a meaningful Equation 7.6, the m strain-DoFs monitored must be coherent with the FE-model mesh. As a matter of facts, the $m_{i^{th}}$ DoF measured must have its *physical-twin* in the i^{th} row of Ψ matrix. For this reason the sensor must be fixed so that it passes in the same locations where in the FE-model there is a mesh-node, or vice-versa. For that, it is required a coherence among the mesh-nodes spacing and sensor-gauges spacing. Summarising, the m DoFs of $\bar{\epsilon}(t)_{m\times 1}$ must be from a physical point of view the same inside $\Psi_{m\times n}$.

It has been already faced that OF measures the axial-strain that its *embedded gauges* undergo. Being the fiber fixed on the surface, the obtained data-set consists in a sequence of *on-surface* strains.

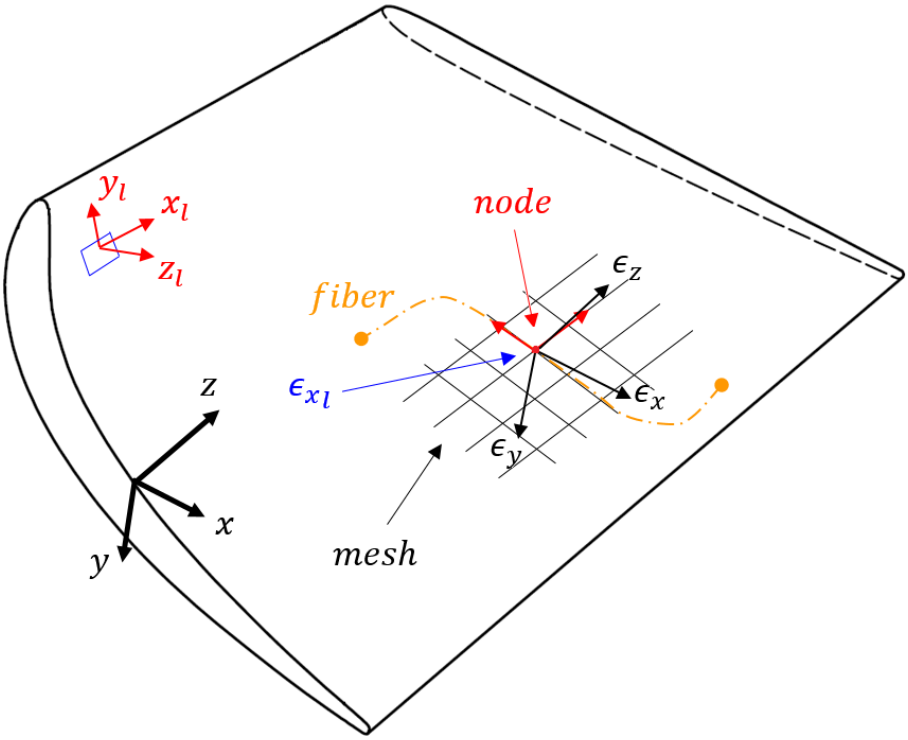

Figure 7.7: Difference among simulated-strains reference system and measured-strains reference system

Making reference to Figure 7.7, consider the red node. The fiber measures, in its correspondence, a superficial strain value named ϵ_{x_l}. The fiber is measuring ϵ along the y_l direction of that frame.

As stated, it is necessary to acquire a vector $\bar{\epsilon}(t)_{m\times 1}$ so that the m strain-DoFs monitored are coherent with the m accounted by $\Psi_{m\times n}$.
Being Ψ formulated in the absolute frame of reference, while each measured ϵ_l is referred to the local surface in the local measuring direction, it is necessary to proceed in a strain *rotation*.
What is rotated is the CMA-based nodal tensor contained in $\tilde{\Psi}$, so to generate a set of rotated strain values coherent with ϵ_l that will be *replaced* inside $\tilde{\Psi}$ itself. Actually, according to FE-analysis, $\tilde{\Psi}$ contains per every node six strain values (per each mode). They represent the terms of its *vibrational* strain-tensor in the absolute coordinate system.
To perform the rotation, the three directional cosines that represent the surface-dependent local reference system with respect to the absolute coordinates (Figure 7.7) must be computed. Once directional cosines are computed, strains

are rotated so that they assume a *meaning* with respect to the surface. Their values will be re-elaborated to represent the strain-tensor with respect to x_l, y_l and z_l, where x_l and y_l are locally tangent to the surface and z_l is normal instead.

Once this procedure is performed per each monitored node, $\tilde{\Psi}$ can be *rewritten*. Thanks to $\tilde{\Psi}$, a $\Psi_{m\times n}$ coherent with each ϵ_l (and the entire $\bar{\epsilon}(t)_{m\times 1}$) is generated, and $\bar{u}(t)_{N\times 1}$ can be computed.

First of all, to perform a strain-tensor rotation the *directional cosines* that states the new coordinate system are required. They depend on the *discrepance*-angles among the original frame of reference and the rotated one.

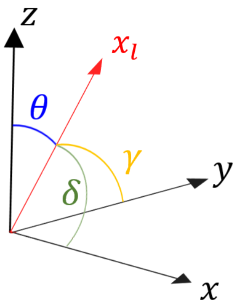

Figure 7.8: Directional angles of x_l

The rotation matrix referred to node k can be formulated as:

$$T_k = \begin{bmatrix} cos\delta_{x_l} & cos\gamma_{x_l} & cos\theta_{x_l} \\ cos\delta_{y_l} & cos\gamma_{y_l} & cos\theta_{y_l} \\ cos\delta_{z_l} & cos\gamma_{z_l} & cos\theta_{z_l} \end{bmatrix} = \begin{bmatrix} l_1 & m_1 & n_1 \\ l_2 & m_2 & n_2 \\ l_3 & m_3 & n_3 \end{bmatrix}$$

For each surface-node of interest the three vectors that states the orthonormal basis x_l, y_l, z_l of the local reference system must be determined. In this way the T matrix can be computed. The logic to determine the surface-dependent reference system has been defined a-priori. From this moment on, just one node k will be accounted.

The z_l axis will be collinear to the surface outer-normal. To compute this direction, the four neighbouring nodes are searched, then the plane interpolating these spatial points by a least squared error approach is computed. Given the plane formulation, the normal to the plane passing through the node under exam is easily extracted.

The y_l axis determination has required a deeper analysis, because an approach that permits to generate a local reference system somehow *consistent* per each node has been thought. A straight line (in this case the trailing-edge because well fit this requirement) has been taken as *invariant*. For the node under exam, the plane that passes through the node and normal to the straight line is tracked. Then, the curve that arises by the intersection among the plane and the surface is numerically computed . The vector y_l that states the y local direction associated to the node is computed by considering the segment that links the two points which reside just *before* and *after* the node on the intersection curve. y_l will be conceptually tangent to the surface, the positive direction tends *far* from the trailing-edge.

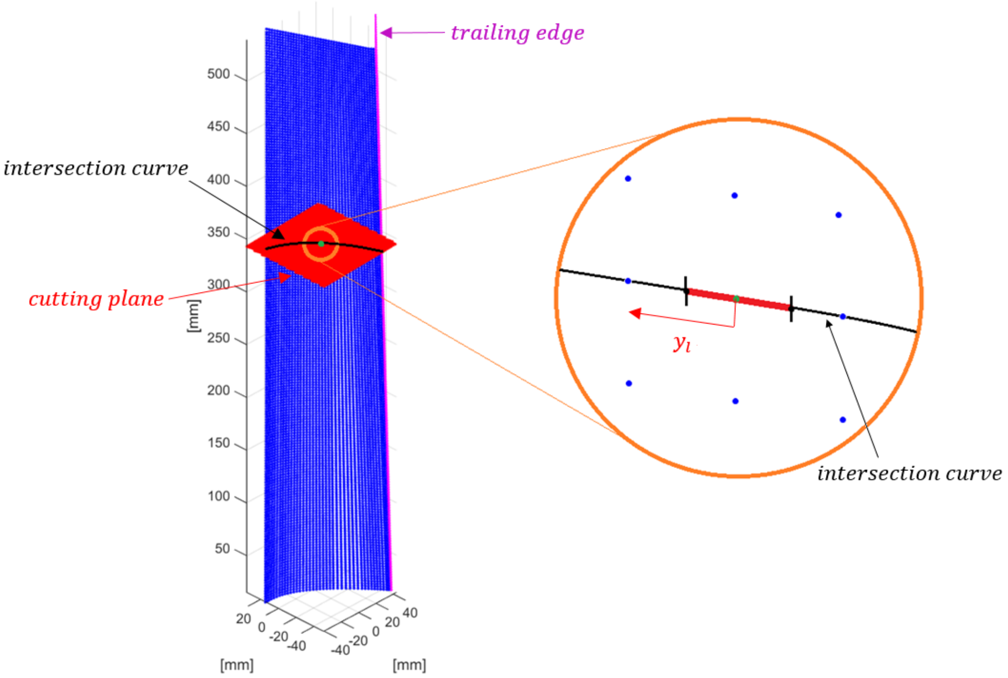

Figure 7.9: y_l definition

The x_l axis depends on the vectorial product among z_l and y_l. x_l is conceptually tangent to the surface, too.

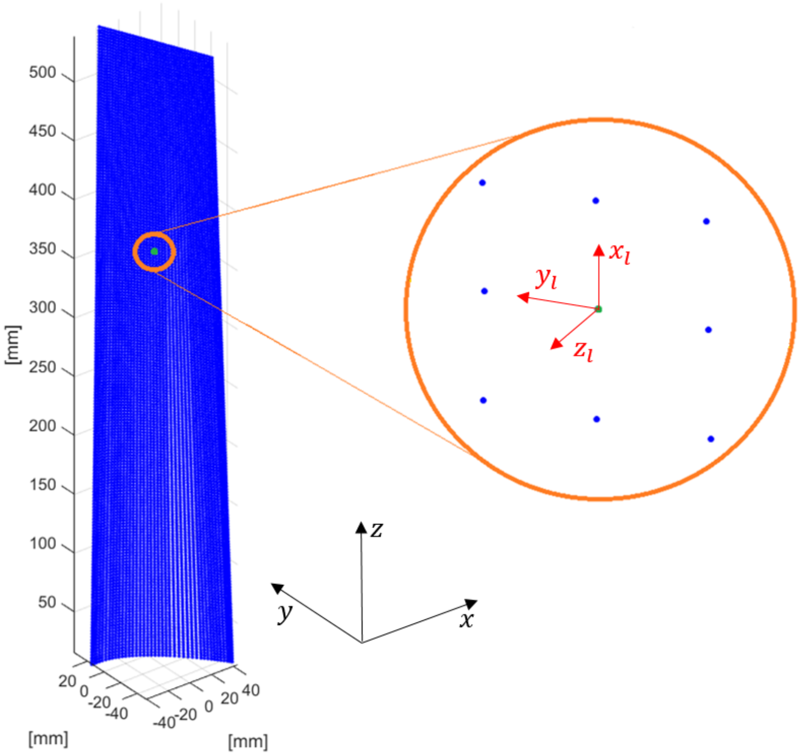

Figure 7.10: Example of local reference system

At this point the rotation matrix T has been calculated per each node of interest.
Now, to practically compute the rotation, the strain-tensor referred to node k and mode g in the absolute reference system has to be considered. This tensor has been extracted from $\tilde{\Psi}$, according to the general procedure described by Figure 7.6:

$$E_{\ k,g} = \begin{bmatrix} \epsilon_{x\ \ k,g} & \epsilon_{xy\ \ k,g} & \epsilon_{xz\ \ k,g} \\ \epsilon_{xy\ \ k,g} & \epsilon_{y\ \ k,g} & \epsilon_{yz\ \ k,g} \\ \epsilon_{xz\ \ k,g} & \epsilon_{yz\ \ k,g} & \epsilon_{z\ \ k,g} \end{bmatrix}$$

To perform the rotation and obtain $E_{l\ \ k,g}$, the strain-tensor in the local frame referred to k and g:

$$E_{l\ \ k,g} = \begin{bmatrix} \epsilon_{x_l\ \ k,g} & \epsilon_{xy_l\ \ k,g} & \epsilon_{xz_l\ \ k,g} \\ \epsilon_{xy_l\ \ k,g} & \epsilon_{y_l\ \ k,g} & \epsilon_{yz_l\ \ k,g} \\ \epsilon_{xz_l\ \ k,g} & \epsilon_{yz_l\ \ k,g} & \epsilon_{z_l\ \ k,g} \end{bmatrix} = T_k\ E_{k,g}\ T_k^T$$

At this step, $E_{l\ \ k,g}$ terms will replace $E_{\ k,g}$ ones in $\tilde{\Psi}$.

Reached this point, all the steps required to properly employ the DST-matrix method has been faced. The last task to be performed is to physically fix the sensor according to a *well* known path. Each fiber-gauge must be placed on the surface so that its location can be brought back to a specific node and its measuring direction attributed to x_l or y_l. This passage can be eased relying on a relative surface-dependent coordinate system.
The three-dimensional nature of the surface requires for a *bi-dimensional* mapping of nodes coordinates. This procedure allows to switch from an in-space nodal position to an in-plane nodal location. The reasons that stay behind this choice are two:

- In the case of a *manual* fiber fixing, it is extremely difficult to understand the real spatial path of the fiber. To understand which are the FE-model nodes in correspondence of sensor arrangement, or viceversa, to make the fiber pass along a pre-determined track, is a critical task if the path is a set of x, y and z coordinates;
- In the case it is possible to proceed with the *layers fiber-embedding* procedure (section 7.4), the integration stencil employed must be handled in *surface* coordinates;

The choice of the mapping criteria is defined according to ease the recognition of sensor real path. The easiest method is to perform a *physical distance measurement* on the surface from some fixed references.

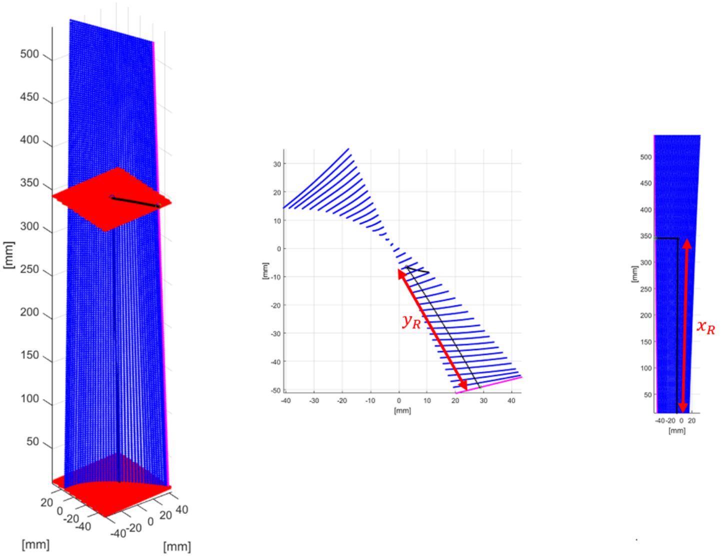

Figure 7.11: Example of mapping procedure

Each node is processed and linked to a couple of relative coordinates x_R and y_R. This task is carried out with the same logic expressed in section 7.2. The straight line of the trailing-edge has been taken as fixed reference. For each node, the plane that passes through the node and normal to the line is tracked. The curve that comes from the intersection among the plane and the surface is then numerically evaluated. The cumulative sum of the distances among all the points within the trailing edge and the node that lies on the intersection curve give the relative coordinate y_R.

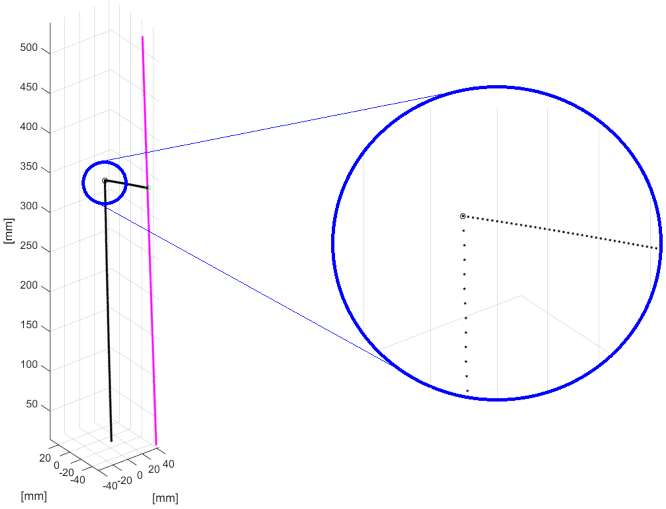

Figure 7.12: Mapping procedure

The x_R coordinate is computed by the cumulative sum of the distances among the points that can be found descending from the node till the *zero-plane* keeping fixed the distance y_R *stepped* on the surface from the straight-line. The *zero-plane* is the plane normal to the trailing-edge passing through the *origin-node*, that resides in $x_R = 0$ and $y_R = 0$.
These steps are exemplified by Figure 7.11 and Figure 7.12.
At this point, to find on the real structure a FE-model node position it is sufficient to take its x_R and y_R and physically measure the distances on the surface.

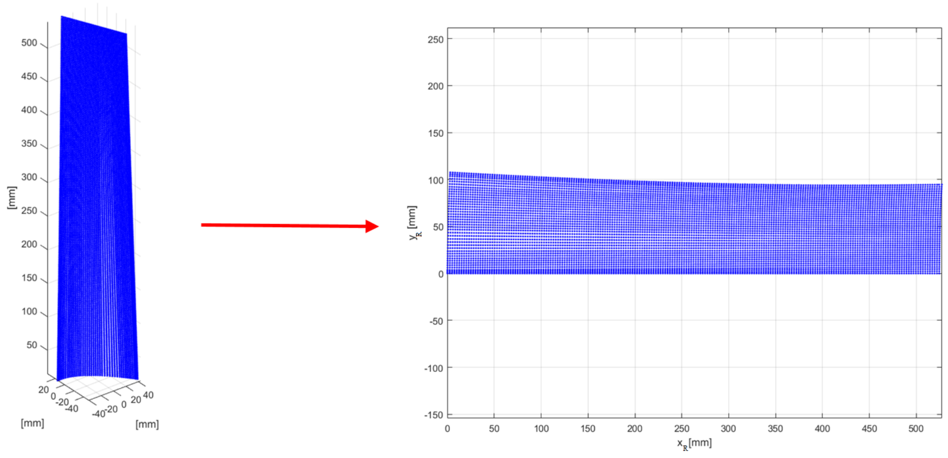

Figure 7.13: Mapped surface

7.3 DST-matrix method experimental results

Once the DST-matrix has been derived, it is necessary to physically *link* the real fiber arrangement to the FE-model nodes to complete the procedure. Once the mapped surface is available, it is virtually tracked on the bi-dimensional map the wanted sensor arrangement and the sections that are wanted to be actually acquired. Figure 7.14 and Figure 7.15 exemplify these steps.

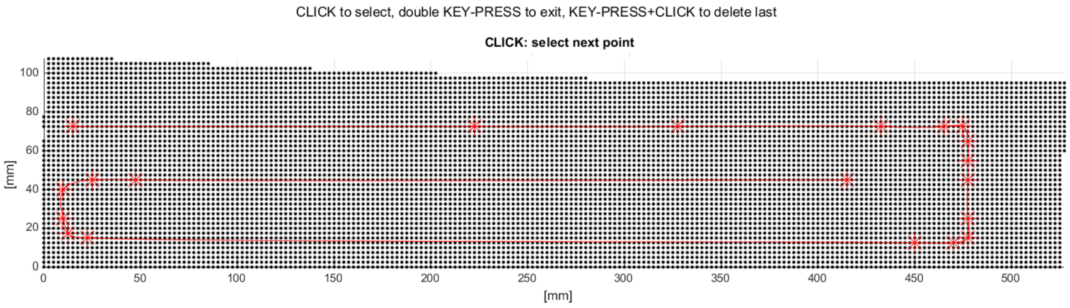

Figure 7.14: Example of fiber path selection

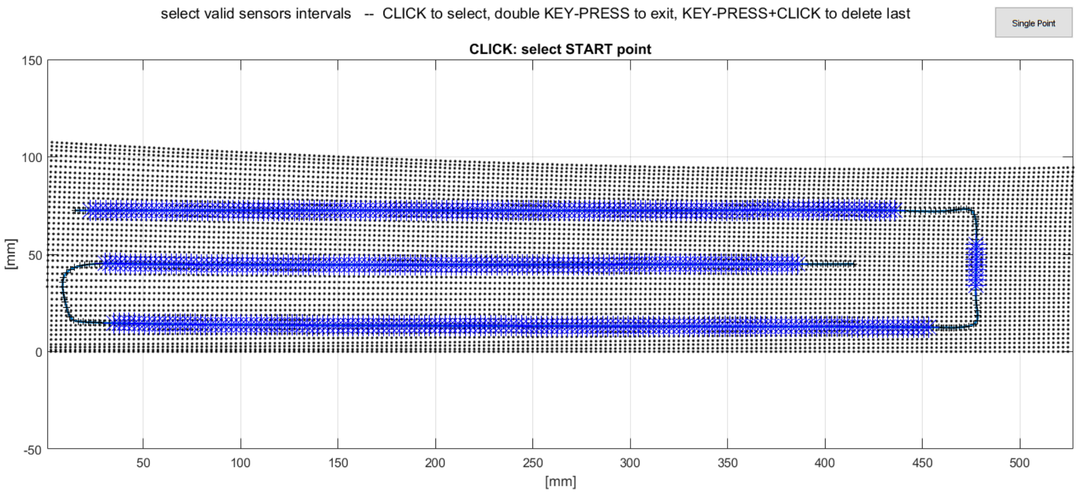

select valid sensors intervals -- CLICK to select, double KEY-PRESS to exit, KEY-PRESS+CLICK to delete last

CLICK: select START point

Figure 7.15: Example of selection of the wanted section

In this way the relative locations where the fiber must pass through are clear, and the fixing procedure can be carried out.

The acquisition can be performed. The strain signal is processed by the same *cleaning-procedure* treated in chapter 5, in order to generate a reliable $\bar{\epsilon}$ vector. In this scenario, $\bar{\epsilon}$ contains the *cleaned* amplitudes of the harmonics of the strain signals of the m monitored locations.

By the *virtual* fiber placement on the bi-dimensional map, and the knowledge of the sensors eventually discarded by the signal-processing algorithm, the code generates the Ψ matrix already re-elaborated to be coherent with the measured strains.

$$\begin{aligned} \bar{u}_{N\times 1} &= [\Phi]\ \left([\Psi]^T\ [\Psi]\right)^{-1}\ [\Psi]^T\ \bar{\epsilon}_{m\times 1} \\ &= DST_{N\times m}\ \bar{\epsilon}_{m\times 1} \end{aligned}$$

Vector $\bar{u}$, which accounts for the complete displacements of the structure displacement-DoFs, can be computed.

The output of the previously explained procedure, according to the experimental plan and the considerations presented in section 4.5, will be shown below. A comparison among the surface displacements coming from the FE-analysis and the reconstructed ones according to the DST-matrix method is carried out. Colours represent respectively the displacements along x, y and z directions with respect to the un-deformed condition. Displacement colours are scaled according to their maximums.

While the first two mode-shapes are reconstructed with a sufficiently good quality, the more complex ones are progressively shaped in a worse way.

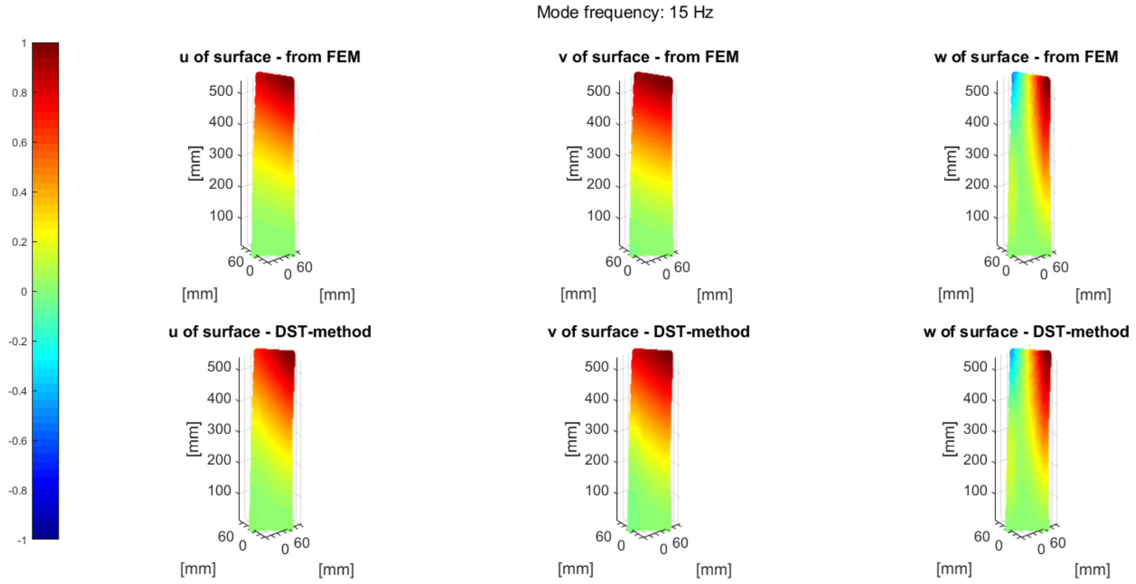

Figure 7.16: 3D-blade experimental 1^{th} mode-shape at 15 Hz

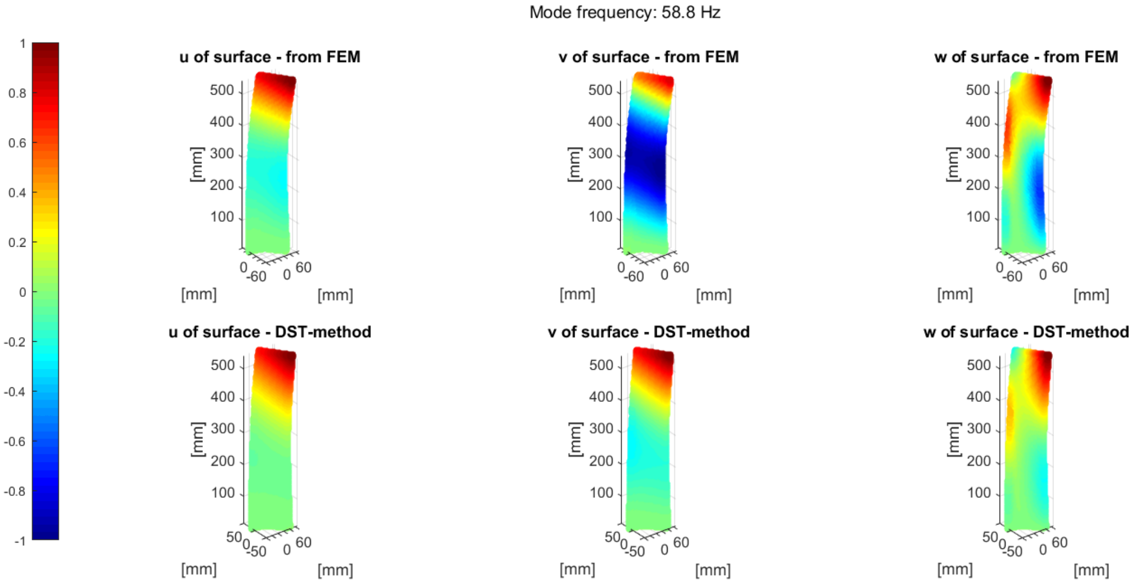

Figure 7.17: 3D-blade experimental 2^{th} mode-shape at 58.8 Hz

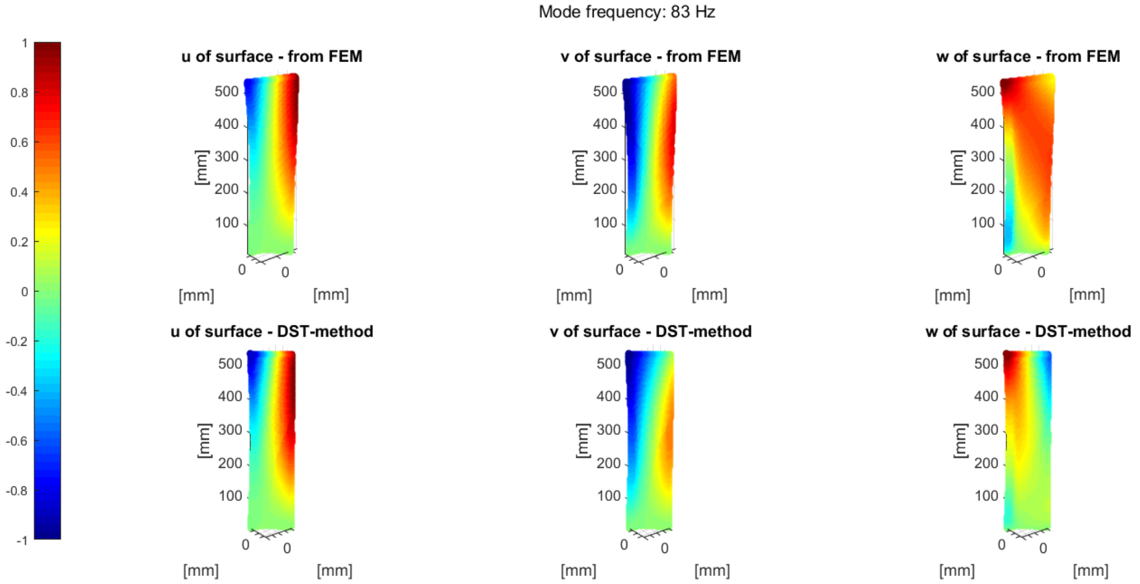

Figure 7.18: 3D-blade experimental 3^{th} mode-shape at 83 Hz

Here it becomes evident that displacements along x and y are acceptable, while w shape start to be misleading.

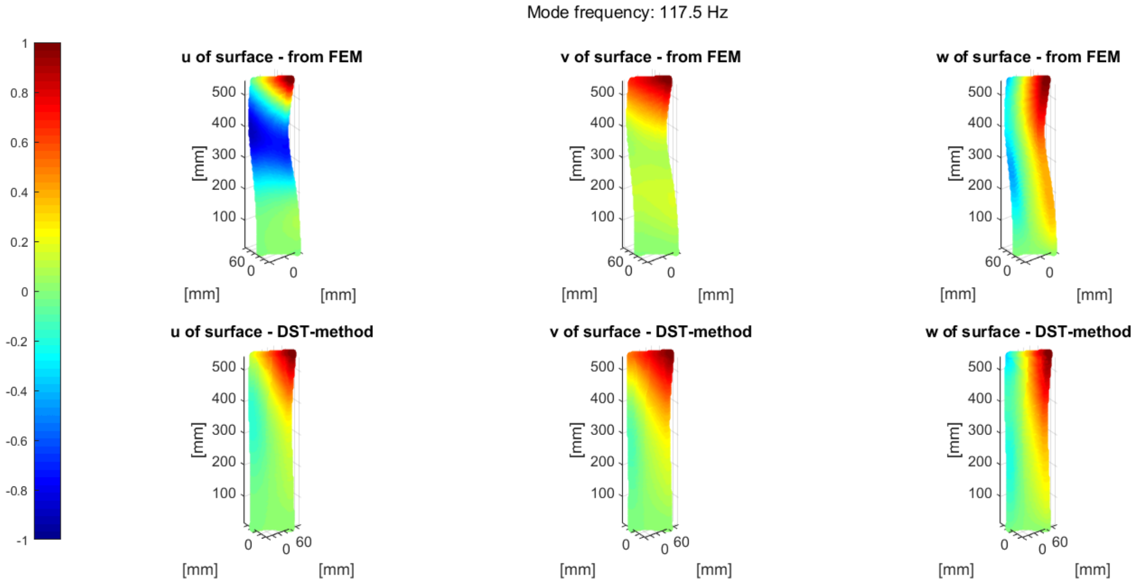

Figure 7.19: 3D-blade experimental 4^{th} mode-shape at 117.5 Hz

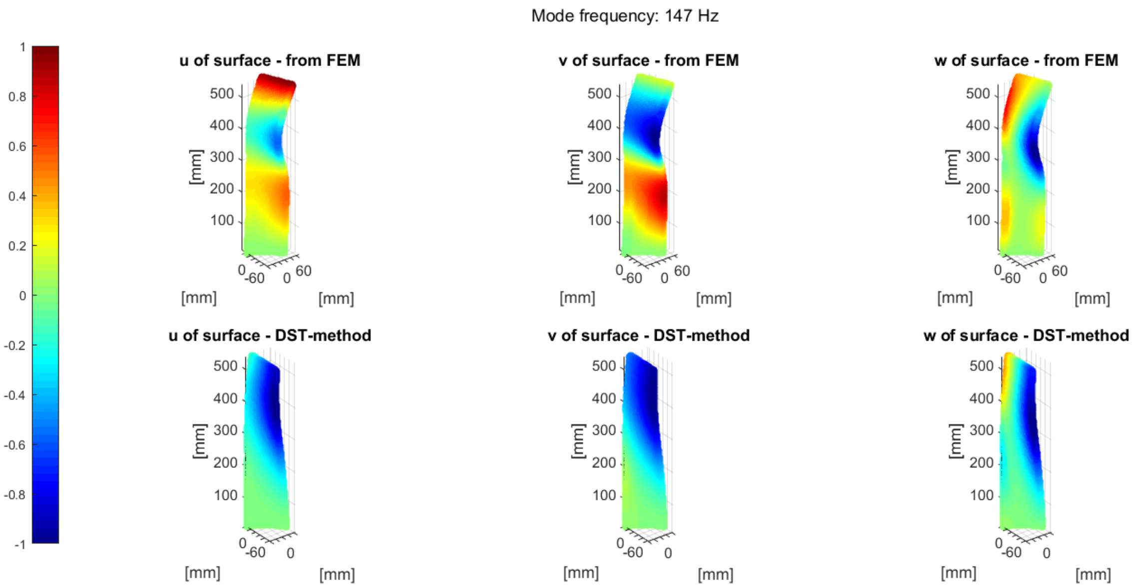

Figure 7.20: 3D-blade experimental 5th mode-shape at 147 Hz

The progressive worsening in mode-shape reconstruction has become more and more evident, resulting in a totally meaningless output.

The reasons that determine such a globally non-acceptable result are linked to the ones already anticipated in section 6.2
The strain-to-displacement transformation approach here employed fully relies on the output of a FE-analysis. It means that each *inaccuracy* accounted in the computational model *moves* from the simulation to the final output, usually influencing the result in a non-predictable manner. The uncertainties that affect each single parameter inside the FE-model arise or from *approximations* of the reality, which can be compensated by a more accurate modelling, or from a concrete *lack* of knowledge about, for example, the structure inner. Furthermore, the finite algebra of computers introduces numerical errors and truncations.

To improve results, a parameters-tuning should be performed to achieve a *convergence* among the reconstructed shape obtained according to DST-matrix method and the eigenvectors directly generated by the FE-software. Once this task is completed, two goals are reached. The experimental modal analysis is accomplished and the FE-model has been consequently *validated*. Its output should be now claimed as *reliable*.
This process of *convergence-research* is however tricky and can led to misleading results.

First of all, it is generally not an easy task to *modify* the computational model in a very focused way in order to improve FE-simulation reliability.
Secondly, a concrete risk exists in tuning parameters so that *convergence* is reached modifying the model in a *wrong* manner. It can be tuned so to *fit* errors that do not depend on simulation-faults but from *external* factors. All the criticisms concerning the acquisitions system and the signal-related issues have been widely explained in chapter 5.
Last but not least, even if the fiber arrangement can however undergo an optimisation procedure, its implementation would result much more complex (section 6.2).
As a matter of fact, a genetic algorithm (GA) could be developed in order to face an optimal sensor placement (OSP) problem even in case of the DST approach usage, through a dedicated *cost-function*.
Being the OSP result strongly related to the FE-model, at each *tuning-iteration* a new run of GA would be required. For that, a number of different fiber arrangements should be glued on the surface during the whole convergence process. The *weight* of such procedure arises immediately.

7.4 Proposed fiber embedding solution

The fiber embedding solution responds to the original ambitious scope of the thesis: to elaborate a mode-shape reconstruction algorithm by avoiding the DST-matrix use.
Taking into account all the considerations in section 7.1, in the following part the proposed method to experimentally acquire the necessary information about u_l along the third direction is explained. This will complete the description of the devised idea of a feasible three-dimensional *integration* procedure.

Previously, in section 7.1, a three-dimensional strain-to-displacement procedure able to convert the acquired strains into 3D displacement modal-shapes has been proposed. Nevertheless, there was a complication: the missing term $\frac{\partial u_l}{\partial z_l}$. The fiber embedding solution is able to solve this leak without requiring the use of any FE-model.

To be able to calculate the gradient of u_l in the z_l direction, the definition of $u_l(x_R, y_R, z_R)$ is theoretically necessary. Some informations regarding $u_l(z_R)$ has to be built. As previously explained, $u_l(x_R, y_R)$ is computed over the external blade surface by simply integrating ϵ_{x_l} in the x_l direction, with the clamp boundary condition. To know the behaviour of u_l in the z_l direction, the blade has to be sectioned with surfaces *approximately parallel* to the external one. Practically the blade thickness is divided into *inner surfaces*, as shown by Figure 7.21.

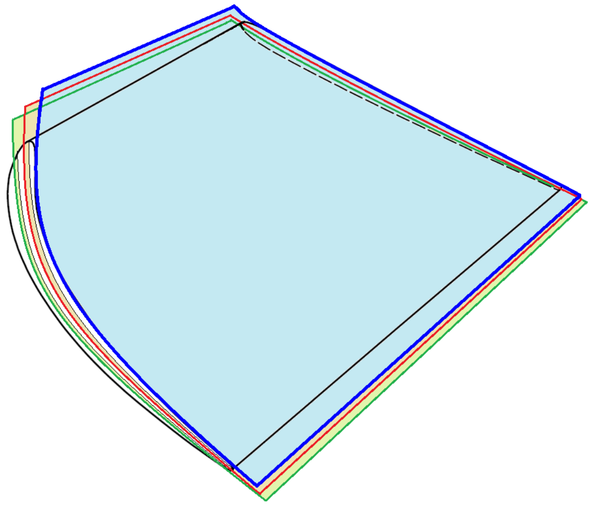

Figure 7.21: Blade sectioning into *layers*

The following procedure can be performed:

- To acquire ϵ_{x_l} *into* the blade thickness. So it is possible to collect a group of $\hat{\epsilon}_{x_l}$ data, where each group of $\hat{\epsilon}_{x_l}$ is related at a different $\hat{z}_l$ value. Practically, $\hat{\epsilon}_{x_l}$ is measured at different blade *thickness*;
- To interpolate $\hat{\epsilon}_{x_l}$ in the layer surface (x_R, y_R) for each $\hat{z}_l$, the result will be $\hat{\epsilon}_{x_l}(x_R, y_R, \hat{z}_R)$;
- To calculate $\hat{u}_l(x_R, y_R, \hat{z}_R)$ for each $\hat{z}_l$, always though the integration along $\hat{x}_l$ of $\hat{\epsilon}_{x_l}(x_R, y_R, \hat{z}_R)$ with the clamp boundary condition, applied for each layer;
- At this point it is possible to compute $\frac{\partial u_l}{\partial z_l}$.

The proposed method is coherent with the general geometry of blades. Since the thickness of the 3D body can be successfully and easily *sectioned* into layers. Generally all the 3D structures with a quite smooth surface are suitable to the *layer sub-division*, it would be sufficient to be careful to consider as parallel as possible the layer-surfaces.

In this innovative approach the fiber has to be arranged *inside* the blade *along* the previously called *inner surfaces.*

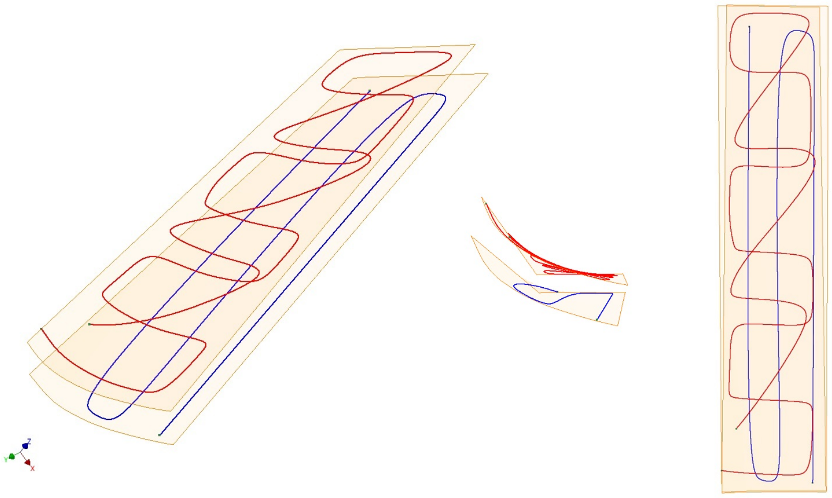

Figure 7.22: Fiber arrangement on *layers*

Over the external surface the fiber can be fixed in the desired directions: x_l, y_l or $\angle 45^\circ_l$. The angular orientation of fiber fixing and its global positioning

can be optimized, similarly to the optimization implemented in the plate study-case.
For what concerns the inner-layers measured strains, the fiber has to be arranged just in one direction (x_l direction), as described in Figure 7.22.

The reason why the *inner surface* has to be measured just in one direction is explained by the formulas in section 7.1. To sum up, in the *inner surface* is enough to acquire ϵ_x due to the fact that ϵ_x field is sufficient to calculate, by means of an integration, $u(x, y)$ in the inner-layer and so to compute $\frac{\partial u_l}{\partial z_l}$ as finite difference. The resulting fiber arrangement just along x_l direction is peculiar of the 3D case-study considered, the blade geometry. As a matter of fact, the blade structure is clamped in $x_R = 0$, so all the integrations can be conveniently performed along x-axis through the proper clamp condition. All the formulas and the mathematical algorithm presented in section 7.1 exploit the typical blade boundary condition. The result is that just ϵ_x has to be measured in the inner-layer. Generally, if the structure has a different shape or different boundary conditions, it could become necessary to define both $u(x, y)$ and $v(x, y)$. In these cases, once again, the fiber arrangement can be optimized even for the *inner-surfaces*, always with an optimal sensor positioning algorithm very similar to the one proposed in this thesis for the bi-dimensional plate structure.

A great advantage of this procedure can be noticed: just *one* inner measured surface is theoretically strictly necessary to calculate successfully $\frac{\partial u_l}{\partial z_l}$. Ideally, the closer to the external surface is this inner layer of measurement, the more precise is the calculation of the required u_l gradient along z_l. So, notionally, it is sufficient to embed the fiber over just one layer in the blade solid inner. In practice, due to the possible technological issues that can arise, a more practical solution could be to dispose two or more fiber-layers next to the external surface. In this way, practically, there will be not the necessity to *monitor* the strain-state next to the *core* of the body. The fiber has not to be arranged neither in many inner layers and neither really in depth. This represents an enormous advantage in terms of technological manufacturing and modal-shape reconstruction quality.

Really the proposed method is not the unique procedure relying on fiber embedding. In literature, [31], can be found another solution.

Luna OBR sensor is integrated in a smart composite structure during the manufacturing step. In that case the structure was a simple cantilever beam. In that scenario the fiber is embedded along two directions: the main direction of the beam and the transversal direction z along the thickness of the beam itself. It would be theoretically feasible to apply the same logic even in a full three-dimensional blade structure. In this sense the fiber has to be arranged in all the three absolute directions x, y and z.

In this occurrence, it would be necessary to interpolate each group of deformations to obtain the three 3D absolute strain fields ϵ_x,ϵ_y and ϵ_z. Finally, from the *reconstructed* strain-fields all over the entire body, it is possible to calculate the 3D displacement-field of the entire solid, due to an integration in the volume.

In this way the approach described by [31] can be theoretically applied to a 3D case-study. Actually, in such an approach, many meters of fiber has to be employed to accurately measure and interpolate the strains along the three directions. In addition to this, the procedure requires three strain-data interpolations in the volume of the structure. Considering the same number of strain-data initially available, the interpolation of these strains to obtain three three-dimensional strain fields inevitably introduces more errors. A supplementary error component can be added by the presence of three volumetric numerical integrations.

To conclude, in the proposed *layer-embedding* method there are some innovative aspects, even with respect to other existing approaches that consider fiber-embedding too:

- Minimization of the required fiber length;

- Simplification of the technological manufacturing process that permits the fiber integration in the structure. In the proposed method it is sufficient to measure ϵ_{x_l} over some *inner layers* of the blades. It does not require any ϵ_{y_l} or $\epsilon_{45^{\circ}_{l}}$ measurement along these surfaces. So the fiber physical embedding can be eased during a 3D-printing relying on this approach;

- As explained, the acquisition of ϵ_{z_l} is not necessary;

- It is possible to *section* the thickness of the blade in few *layers*, or just in *one* as close as possible to the external surface. So a small amount of *embedded measurement* are really required to complete successfully the determination of $\frac{\partial u_l}{\partial z_l}$;

- Just the real strictly necessary physical quantities to determine the surface modal-shapes are subjected to the processes of interpolation and integrations. So a limited error is inserted.

In addition to these *technological* and *computational* advantages, the *layer-embedding algorithm* proposed has a main conceptual advantage with respect to the three-dimensional traditional embedding methods proposed by [31]. In the blade modal-analysis, the final scope of the measures is the *surface* displacement determination, not the displacement or the deformation of the entire 3D body. In the proposed strains processing, the gradient $\frac{\partial u_l}{\partial z_l}$ is what is strictly necessary to be determined along the *inner* of the blade, and no other variables. The gradient of u_l is the only variable that has to be reconstructed *inside* the body. So there are no informations wasted in the definition of not-interesting parameters, the *sensor disposition* is concentrated where it is really necessary. Just the surface displacement has to be determined, for that only the surface and its closest 3D area are measured. In this sense, the method optimizes the use of available strains.

The original purpose of the 3D study-case was to reconstruct the displacement field of a three-dimensional *surface*, just measuring the surface itself. With the proposed integration algorithm (which requires the fiber layers embedding) the initial goal is reached: the *surface* modal shapes can be determined by measuring just the area next to the surface of the 3D body.
For all these reasons, the proposed solution can be considered a successful method to determine the surface modal shapes of the blade by means of strain measures. Actually, this technology cannot be tested, due to its unavailability. Nevertheless, the theoretical procedure has been extensively explained.

At this point, to however obtain the blade modal-shapes the only solution in the actual scenario is the DST matrix method. So it is necessary to abandon the idea to employ just the measured surface strains and rely on the FE-model.

Chapter 8

Conclusions

The purpose of this work was to reconstruct the displacement mode-shapes of a turbine blade, in order to develop a methodology potentially able to evidence the possible resonant criticisms and to monitor the vibrating modes as accurately as possible. The turbines are machine considerably exposed to catastrophic failures, so real-time mode-shapes knowledge would even permit a satisfying preventive maintenance. In this research project, the mode-shapes are experimentally extracted by means of an innovative measurement system, the LUNA ODiSI-B v4. In particular, the local surface strains are acquired by OBR fiber and properly manipulated to define the whole displacement field of the structure surface. Through this new kind of sensor, many limits of the traditional measurement systems presented in the state of the art are overcome. The most interesting feature of such technology resides in the *spatial continuity* of the measurement it can provide. Being a new device, specifically designed for static measurements, an important task was to investigate its behaviour in monitoring dynamic phenomena and to exploit its potentialities through an advanced optimal sensor placement (OSP) algorithm.

The technologically advanced LUNA ODiSI-B system exploits the OBR principle to *convert* a commercial-grade optical-fiber into an innovative strain-sensor. OBR-based fibers are handled by LUNA device so that any *point* of the fiber itself behaves as a *strain-gauge*. For this reason, the fiber can be assumed to be somehow a *continuous* strain sensor.

The huge number of available informations together with the features of the strain-to-displacement implemented procedure permit to reconstruct the displacement field of the whole surface. This is a remarkable advantage with respect to traditional direct displacement acquisition instruments, as accelerometers or LDV systems, which output few discrete displacements.

The first important result is the analysis of the application of LUNA ODiSI-B v4 in measuring dynamic phenomena.
All the considerations concerning the signal quality are drawn by means of experimental tests analysis. The investigation of the dynamic behaviour of LUNA ODiSI-B v4 evidences the presence of signal disturbances. Nevertheless the developed cleaning procedure has limited successfully their effects.

The fiber bends radius has been identified as the main cause to the limit of the signal reliability. In particular it has been proved that the signal presents a coherence-loss localized just after the critical bends and a distributed quality signal decrease in the final part of the fiber length, always proportional to the curves sharpness. At high frequency, the signal quality reduction in the last section of the fiber becomes more emphasized. The maximum frequency processed has arrived at about $220Hz$, a significant result considering that the used CU is designed just for static measurements. This evidences the considerable potentiality of the OBR technology even for dynamic applications.

The main limitation at high frequency of LUNA ODiSI-B v4 stays in the deformation velocity $[\mu\epsilon/sec]$. This inconvenient restriction could be overcome with the new LUNA acquisition system just put on the market. This upgrade of the technology, differently from system employed in this thesis, is designed in particular to enhance its dynamic performances. Many improvements in the modal analysis applications by exploiting OBR potentialities are expected.

The other fundamental result is the design of an innovative optimal sensor placement (OSP) algorithm. Differently from the optimisation techniques available in literature, the developed procedure is able to manage successfully the *continuous* nature of the OBR sensor and to maximise its advantages.

The best fiber arrangement to optimize the mode-shapes reconstruction has been found through the implementation of a proper *genetic algorithm*. In the devised approach the fiber measurement continuity property has been fully exploited by optimising each embedded fiber-gauge position. This represents a remarkable discrepancy with respect the FBG optical-fiber technology. The proposed OSP code can work even with the FBG measurement systems, nevertheless it express all its potentiality with a *continuous* sensor as the OBR fiber. With the implemented algorithm even complex mode-shapes can be detected and a wide range of modes can be considered.
All the physical limits concerning OBR fibers arrangement have been effectively solved. The OSP algorithm was also thought so to be able to compensate the issues arisen from the dynamic *off-design* usage of LUNA interrogator.

Some precautionary conditions are introduced in the OSP to guarantee a global satisfying reliability of the experimental acquisitions. The smart and preventive expedients inserted in the described OSP and the completed performed analysis on LUNA sensor behaviour offer interesting prospectives for the dynamic potentiality of such innovative *continuous* fiber.
To resume, the developed OSP algorithm has been focused on enhancing the mode-shape final reconstructions but it is even able to maximize the quality of the experimental acquisitions performed with LUNA ODiSI-B v4.

The first experimental success deals with the bi-dimensional case-study.
A new method to convert the structure surface strains into displacements has been developed. The strong innovative aspect is the complete independence from any FE-models and the traditional DST-matrix method. The proposed *strain-to-displacement* algorithm is based on a sequence of interpolations and integrations of *physical quantities*. Through the proposed methodology the acquired surface strains can be transformed into displacements information without using any FE-models.

The experimental results reached for the thin plate case-study demonstrate the effectiveness both of the proposed bi-dimensional strain-to-displacement procedure, both the potentialities and the power of the OSP algorithm that has been implemented. The best fiber configuration found by the developed sensor positioning algorithm has been exploited. A first numerical simulation with the devised strain-to-displacement procedure has been performed for each investigated mode, then an experimental displacement mode-shape reconstruction has been successfully completed. As a matter of fact, a *spatially-continuous* shape reconstruction has been well assessed for the first six target-modes. The two modes at highest frequency present some difficulties, nevertheless they can be clearly distinguished. According to this evidence, it arises that the genetic algorithm works properly, *arranging* the fiber in a thought manner to achieve the wanted results.

The final outcome of the thesis is represented by the experimental vibrating mode-shapes reconstruction of the turbine blade surface. The experimental dynamic tests carried out on the 3D-printed blade show that the DST-matrix approach has been effectively implemented on a full three-dimensional structure. This represents a satisfying result, since in literature its application is however restricted to far simpler geometries. Moreover, DST-matrix method *limits* have also been put in evidence.
The first five vibrating mode-shapes of a turbine-blade model has been reconstructed, nevertheless their quality is acceptable just in case of the less complex ones. This issue could be overcame by an hard FE-model iterative

tuning.
As a matter of facts, a new approach which involves fiber embedding inside the structure to reconstruct the three-dimensional mode-shapes has been described. Once again, the devised procedure consists in a proper sequence of interpolations and integrations, in order to complete the strain-to-displacement conversion relying just on physical correlations. The main advantage, exactly as in the bi-dimensional explained and tested method, arises from the FE-model independence. Consequently, it results in a more *reliable* and *controllable* approach.
Even if the proposed method needs for fiber embedding, it does not require for tricky three-dimensional paths. It has been shown that just the surface and its underlying layer must be simultaneously monitored, without requiring to *go* more in depth, easing the technological manufacturing. The impressive progress in 3D-printing technology will permit to automatically manage such an embedding process. Furthermore, composite material blades result to be the most promising perspective for this innovative approach.

The described research work fully responds to the recently increasing requests concerning the shape estimation and monitoring, in particular for more complex geometries. The original scope of this thesis was the reconstruction of the displacement mode-shapes of a turbine blade, nevertheless in all the structures with aerodynamic forces interaction the surface shape-changes influence directly the performance of the system. The presented OBR technology with its proper mode-shape extraction method offers the possibility to provide an accurate real-time vibration monitoring. In particular, the embedding methodology presented in this research work concerning the mode-shapes definition of three-dimensional structures offers a feasible solution to develop 3D-printed or composite-material *smart* structures including embedded fiber. This innovative health-monitoring solution avoids to alter the surface fluid interactions and to be resistant to critical temperature conditions. Practically the future development will be the realization of bi-dimensional and three-dimensional smart structures with a smart sensor embedding, which guarantees an intrinsic health-monitoring capability. The first obvious success would be the clear improvement in the components maintenance and failure analysis management. Furthermore, the OBR-integrated smart structures would be able to collect data concerning their shape modifications and eventually react to the environment by means their mode-shape monitoring system. In all the applications which require high aerodynamic efficiency, the proposed shape-estimation approach can give in the future the possibility to enhance the performances. Especially for the wind turbines this technological solution is not so distant to now. In this sense the OBR fiber technology offers many versatile and proposing solutions.

In the aerospace, turbomachinery, wind turbines and many other three-dimensional structural analysis researches, the presented shape estimation strategy, based on interpolations and integrations of strain data, associated to the innovative *continuous* OBR fiber system, presents many interesting future perspectives.

Acronym

autoMAC Modal Assurance Criterion

BCs Boundary Conditions

CDF Cumulative Density Function

CF Crest Factor

CMA Computational Modal Analysis

CU Control Unit

DST Displacement Strain Transformation

DV Design Variable

DVs Design Variables

DoF Degree of Freedom

DoFs Degrees of Freedom

EB Entropy Based

EFI Effective Indipendence

EMA Experimental Modal Analysis

FBG Fiber Bragg Grating

FE Finite Element

FFT Fast Fourier Transform

FIM Fischer Information Matrix

FRF Frequency Response Function

GA Genetic Algorithm

HCF High Cycle Fatigue

KE Kinetic Energy

LDV Laser Doppler Velocimeter

MAC Modal Assurance Criterion

MC Monte Carlo

MIMO Multiple Input Multiple Output

MSE Mean Squared Error

ObF Objective Function

OBR Optical Backscatter Reflectometer

OF Optical Fiber

OSP Optimal Sensor Placement

PC Polycarbonate

RMS Root Mean Squeare

SA Simulated Annealing

SE Strain Energy

SIMO Single Input Multilple Output

STD Standard Deviation

StD Strain to Displacement

SWI Swept Wavelength Interferometry

Ringraziamenti

Scrivere in poche righe tutto quello che questi anni hanno racchiuso è difficile. Cercherò di procedere con ordine, ma so già che non riuscirò ad essere molto sintetica quindi mi scuso in anticipo.

Prima di tutto, ringrazio Gabriele per tutto il tempo speso soprattutto negli ultimi giorni, per i suoi consigli, ma anche per la fiducia. Grazie per i tuoi modi sempre gentili, per niente scontati. E' stato davvero un piacere poter lavorare con te.
Ringrazio Prof. Pennacchi per avermi dato la possibilità di fare ciò che davvero mi piace nell'ultimo anno, per avermi proposto un progetto così interessante e per me coinvolgente. Lo ringrazio anche per essere stato sempre disponibile, pronto e mai banale.
Ringrazio tutti quelli che hanno contribuito direttamente e indirettamente alla tesi, ringrazio il mio compagno di tesi Andrea per aver sopportato il lavoro e la fatica degli ultimi mesi. Grazie a Iacopo, Emanuele e Carlos con cui ho condiviso il laboratorio e che hanno reso molto più leggere le giornate.

Grazie a Loris per le parole e l'ascolto negli anni passati trascorsi insieme, grazie a Matteo e Francesca per la comprensione e per i sorrisi con cui mi hanno aiutata soprattutto nei momenti meno facili. Grazie a Riccardo che mi è stato vicino in cose più importanti di esami e libri. Perché tu lo hai sempre saputo che le cose che contano sono fuori da un'aula di università. Grazie per il tempo e i momenti che mi hai dedicato, eri tu che più c'eri quando avevo più bisogno.

Grazie a te Stefano. Quando ancora diciottenne ti ho detto che avrei fatto ingegneria, sorridendo mi hai fatto gli auguri. Non sapevi ancora quante volte mi avresti dovuto sopportare. Grazie per i consigli, per avermi risposto al telefono ad orari assurdi, per le pause caffè e per le chiacchiere comprese quelle più serie. Sono sicura che riceverai quello che meriti.

Devo ringraziare tutti quelli che ho incontrato in questi cinque anni, inclusi tutti quelli che non mi hanno capita, che non ci credevano, che non mi hanno aiutata. Perché sono le difficoltà, gli sguardi perplessi, le sofferenze e gli errori che più mi hanno fatto crescere. La motivazione stava anche lì, non ho scelto questa strada per brillare. L'ho scelta per confrontarmi, per dimostrare che l'impegno paga, per dimostrare che una scelta giusta spesso non è quella più facile. L'ho scelta per ispirazione.

E ora posso dire grazie alla cosa più importante e più preziosa che io abbia trovato qui. Grazie a te Simo. Perchè nei momenti più bui può arrivare la luce e la mia luce io l'ho trovata qui tra i tavoli del dipartimento. Grazie a tutto quello che mi hai insegnato, a tutto quello che mi hai mostrato. Grazie alla forza che mi hai dato. Grazie per avermi fatto scoprire quanto sono stata coraggiosa e quanto lo posso essere. Venuti dallo stesso posto, con le stesse motivazioni, abbiamo dimostrato che si può fare. Orgogliosa di essere accanto a te.

Grazie alla mia famiglia e a tutti quelli che per me ne fanno parte, anche senza un legame di sangue. Grazie a te nonna per avermi sopportata e capita.

Grazie alla mia mamma. Per la tua pazienza, per le cure e per l'amore che ci hai messo sempre. Mi eri vicino anche quando nessun altro poteva capire. Sei sempre di più il mio esempio, prima di ogni altra cosa come donna.

Infine grazie al mio papà. E' soprattutto merito tuo se io oggi sono qui. Grazie per le tue parole e per il tuo aiuto. Per avermi sostenuta anche mentre soffrivo. Mi hai insegnato la determinazione e la costanza nell'affrontare le difficoltà, l'ordine e la calma nel risolvere i problemi. Grazie per avermi preparata senza mai spaventarmi. Non mi hai mai nascosto che sarebbe stato complicato, ma mi hai sempre ricordato quale sarebbe stata la ricompensa. E più di ogni altra cosa, grazie per avermi mostrato cosa potevo diventare ma anche cosa dovevo sempre rimanere, una bella persona.

Dove sono oggi è anche un vostro successo, per tutti i sacrifici che avete fatto per permettermi tutto questo e per tutti i momenti che avete dovuto affrontare accanto a me.

Infine, grazie a questi cinque anni per quello che mi hanno fatto diventare e per quello che mi hanno mostrato di me, grazie per avermi fatto scoprire *tutto ciò che muove il mondo.*

Martina

Ringraziamenti

Se alla fine è stato messo un punto anche all'ultimo capitolo di questa tesi, il primo grazie va a Gabriele, che con la sua pazienza e i suoi suggerimenti ci ha costantemente consigliato, aiutato e spesso indirizzato verso le scelte più appropriate.

Un grazie speciale anche al Prof. Pennacchi, per averci offerto la possibilità di portare avanti questo lavoro ed averci seguito nel corso dei mesi con i suoi preziosi consigli e la sua competenza.

Grazie infine ai ragazzi dell'officina, ai responsabili del magazzino in C4, a Luciano e a tutti coloro che ci hanno permesso di arrivare sin qui, per l'aiuto e l'attenzione dimostrata nei confronti nostri e della nostra tesi.

Non è facile capire da dove cominciare quando, spostandosi nella sfera più personale, ci si chiede chi abbia in un modo o nell'altro contribuito a farmi raggiungere questo traguardo.
Premetto che non sono bravo con le parole, ma cercherò di fare del mio meglio.

Certamente, scontato ma non banale, il primo grazie va ai miei genitori, che hanno reso materialmente possibile questa giornata. Grazie ai loro sacrifici, non solo io, ma tutti i loro figli hanno potuto intraprendere il proprio percorso, seguire le proprie aspirazioni e raggiungere i propri obiettivi, senza che il supporto di mamma e papà venisse mai meno.

Grazie poi ai miei amici di sempre, con cui ho condiviso tantissimi momenti di felicità e di spensieratezza, che non mi hanno mai tolto il saluto nonostante il peso dello studio e forse l'eccessivo zelo li abbia costretti a sentirsi dire fin troppe volte "no ragazzi, stavolta ho da studiare".

Grazie alla mia amica e co-tesista Martina, per l'impegno e la pazienza dimostrati durante questi mesi di lavoro, e grazie a Emanuele e Stefano, per la contagiosa allegria diffusa quotidianamente in laboratorio.

Grazie ai miei amici dell'Università, anche a quelli che ormai persi un po' di vista non leggeranno mai questa pagina, per aver reso unici gli anni universitari, dal primo ormai lontano a quelli più recenti.

Lascio per ultimo il pensiero dedicato alla persona che più di chiunque altro merita un ringraziamento speciale, per il modo in cui ha saputo capirmi e starmi vicino anche nei momenti più difficili.

Grazie Marta, per aver sempre avuto una parola di incoraggiamento e per non aver mai perso la pazienza, per non avermi fatto mai mancare la tua comprensione e il tuo supporto. Grazie, per avermi accompagnato fin qui.

Andrea

Bibliography

[1] Carlo Osnaghi. *Teoria delle turbomacchine*. Società Editrice Esculapio, 2013.

[2] Halkon Ben. “Turbomachinery blade vibration analysis”. In: 2002, pp. 1–12.

[3] McComb Patrick. “Turbomachinery blade and stage vibrations”. In: 2013, pp. 1–17.

[4] Murari P. Singh. “Safe Diagram - a design and reliability tool for turbine blading”. In: pp. 94–101.

[5] Benjamin Gwashavanhu, Abrie J. Oberholster, and P. Stephan Heyns. “Rotating blade vibration analysis using photogrammetry and tracking laser Doppler vibrometry”. In: *Mechanical Systems and Signal Processing* 76-77 (2016), pp. 174–186.

[6] B. J. Halkon and S. J. Rothberg. “Vibration measurements using continuous scanning laser Doppler vibrometry: theoretical velocity sensitivity analysis with applications”. In: *Measurement science and technology* (2003), pp. 108–9.

[7] Rastogi P. K. “Holographic interferometry”. In: (1999).

[8] Howard Fein. “Applications of holographic interferometry to structural and dynamic analysis of an advanced graphite-epoxy composite component”. In: *Smart Structures and Systems* 13.3 (1998), pp. 389–406.

[9] Andrea Cusano et al. “Experimental Modal Analysis of an Aircraft Model Wing by Embedded Fiber Bragg Grating Sensors”. In: *IEEE sensors journal* 6.1 (2006), pp. 781–800.

[10] Stephan Rappa, Lae-Hyong Kanga, Uwe C. Muellerb, Jae-Hung Hana, and Horst Baierb. “Dynamic shape estimation by modal approach using fiber Bragg grating strain sensors”. In: *SPIE 14th Annual Symposium Smart Structures and Materials*. 2007.

[11] Lae-Hyong Kang, Dae-Kwan Kim, and Jae-Hung Han. “Estimation of dynamic structural displacements using fiber Bragg grating strain sensors”. In: *Journal of Sound and Vibration* 305 (2007), pp. 534–542.

[12] Stephan Rapp, Lae-Hyong Kang, Jae-Hung Han, Uwe C Mueller, and Horst Baier. “Displacement field estimation for a two-dimensional structure using fiber Bragg grating sensors”. In: *Smart Materials and Structures* 18 (2009), pp. 534–542.

[13] Armen Derkevorkia and Sami F. Masri. “Strain-Based Deformation Shape-Estimation Algorithm for Control and Monitoring Applications”. In: *AIAA journal* 51.9 (2013).

[14] Geng Lu, Zhu Xiaojin, Zhang Hesheng, Gao Zhiyuan, and Liu Kaining. “Optimal Placement of FBG Sensors for Reconstruction of Flexible Plate Structures Using Modal Approach”. In: *34th Chinese Control Conference*. 2015.

[15] D. S. Li, H. N. Li, and C. P. Fritzen. “The connection between effective independence and modal kinetic energy methods for sensor placement”. In: *Journal of Sound and Vibration* 305 (2007), pp. 945–955.

[16] Rafael Castro-Triguero, Senthil Murugan, Michael I. Friswell, and Rafael Gallego. “Optimal Sensor Placement for Structures under Parametric Uncertainty”. In: (2012).

[17] Meo M. and Zumpano G. “On the optimal sensor placement techniques for a bridge structure”. In: *Engineering Structures* 27 (2005), pp. 1488–1497.

[18] Papadimitriou C., Beck J. L., and Au S. K. “Entropy-based optimal sensor location for structural model updating”. In: *Journal of Vibration and Control* 6 (2000), pp. 781–800.

[19] K. H. Tong, Norhisham Bakhary, A. B. H. Kueh, and A. Y. Mohd Yassin. “Optimal sensor placement for mode shapes using improved simulated annealing”. In: *Smart Structures and Systems* 13.3 (2013), pp. 389–406.

[20] Hao Sun and Oral Büyüköztürk. “Optimal sensor placement in structural health monitoring using discrete optimization”. In: *Smart Materials and Structures* 24 (2015).

[21] Goldberg D. E. *Genetic Algorithms in Search, Machine Learning and Optimization*. Addison-Wesley, 1989.

[22] Can He et al. “A Combined Optimal Sensor Placement Strategy for the Structural Health Monitoring of Bridge Structures”. In: *International Journal of Distributed Sensor Networks* 2013 (2013), p. 9.

[23] U. Muthuraman et al. “An Approach for Damage Identification and Optimal Sensor Placement in Structural Health Monitoring by Genetic Algorithm Technique”. In: *Circuits and Systems* 7 (2016), pp. 814–823.

[24] Kammer D. C. “Sensor placement for on-orbit modal identification and correlation of large space structures”. In: *Journal of Guidance, Control, and Dynamics* 14.3 (1991), pp. 251–259.

[25] Minwoo Chang and Shamim N. Pakzad. “Optimal Sensor Placement for Modal Identification of Bridge Systems Considering Number of Sensing Nodes”. In: *Journal of Bridge Engineering* (2014).

[26] Wei Liu, Wei-cheng Gao, Yi Sun, and Min-jian Xu. “Optimal sensor placement for spatial lattice structure based on genetic algorithms”. In: *Journal of Sound and Vibration* 317 (2011), pp. 175–189.

[27] Heo G., Wang M. L., and Satpathi D. “Optimal transducer placement for health monitoring of long span bridge.” In: *Soil Dynamics and Earthquake Engineering* 16 (1997), pp. 495–502.

[28] James L. Beck and Siu-Kui Au. *Entropy-Based Optimal Sensor Location for Structural Model Updating.* 1999.

[29] Holland J. H. *Adaptation in Natural and Artificial Systems.* MIT press, 1975.

[30] Timoshenko S. and Woinowsky-Krieger S. *Theory of plates and shells.* New York: McGraw–Hill, 1959.

[31] Matt Castellucci, Sandra Klute, Evan M. Lally, Mark E. Frogatt, and David Lowry. “Three-Axis Distributed Fiber Optical Strain Measurement in 3D Woven Composite Structures”. In: (2013).